Origin of Creep-Fatigue Back Stress and its Effect on Deformation and Damage

Thesis

Origin of Creep-Fatigue Back Stress and its Effect on Deformation and Damage

By

Abdullah Al Mamun

Department of Engineering and Innovation

The Open University

This dissertation is submitted for the degree of

Doctor of Philosophy

November 2016

To my parents, for your everlasting love and support …

Preface

I hereby declare that except where specific reference is made to the work of others, the contents of this thesis are original and have not been submitted in whole or in part for consideration for any other degree or qualification in this, or any other University. The work reported in this thesis was conducted under the supervision of Dr. Richard Moat and Professor John Bouchard at the Open University between December 2012 and November 2016. This thesis is the result of my own work and includes nothing which is the outcome of work done in collaboration, except where specifically indicated in the text.

Abdullah Al Mamun

November 2016

Abstract

Creep deformation of metals operating at a high temperature in electricity generation plant can limit the lifetime of components and pressurized systems. Assessment of a structure's creep life under power plant operation conditions is a complex problem due to materials being exposed to cyclic load variations. The creep life of high-temperature steels can be significantly affected by the generation of internal back stress during monotonic and cyclic plastic loadings, originating from inhomogeneous deformation at grain and sub-grain length scales. This thesis examines origins of back stress developed in austenitic stainless steel and their influence on subsequent material deformation behaviour.

In-situ neutron diffraction and transmission electron microscopy techniques were employed to study the contributions of intergranular and intragranular incompatible strains to the back stress that is introduced in type 316H austenitic stainless steel under monotonic and cyclic loading at room and elevated temperatures. The scope of testing included load controlled and displacement controlled creep dwells introduced at peak and intermediate positions of the cyclic loading curves. The origin of kinematic hardening in the same material was also examined by systematic loading interruptions during tension-compression cyclic loading, from which the observed variations in macroscopic yield stress were correlated with corresponding changes in intergranular strains. In addition, development of creep cavitation damage was characterized using small angle neutron scattering (SANS) and high-speed atomic force microscope (HS-AFM) techniques.

Intergranular strains were found to significantly affect the minimum creep deformation rate of type 316H austenitic stainless steel, whereas no evidence of that for intragranular strains was observed, at the early stage of creep deformation studied here. It was found that, during tension-compression cyclic loading, the magnitude of intergranular strains not only depends on the stress and strain in the material but also on its loading path history. Intergranular strains were found to increase during the primary stage of load controlled creep, remain unchanged during the secondary stage and reduce during displacement controlled creep relaxation. A strong correlation between the evolution of intergranular strains and the

kinematic hardening of this material were observed during interrupted cyclic loading test at room and elevated temperature, suggesting, that the observed Bauschinger effect in this material originates from the intergranular strains. SANS and HS-AFM were found to be powerful quantitative techniques for studying the nucleation and growth of creep cavities in stainless steel. The HS-AFM work also revealed that the cavities were faceted which highlights the oversimplification of current creep cavitation models that are based on an assumed spherical morphology.

The experimental results have highlighted the significance of the effect of plasticity generated back stress on the creep and cyclic deformation of type 316H austenitic stainless steel. This demonstrates the importance of allowing for the evolution of back stress in high-temperature life assessment procedures.

Acknowledgements

First and foremost, I would like to thank my supervisors Dr. Richard Moat and Professor John Bouchard for offering me the opportunity to undertake this PhD degree at the Open University. Richard was the friendliest of supervisors any PhD student could ask for. John was extremely supportive throughout the course of the PhD and was always there to guide on any technical and non-technical issues of the project. Without his guidance and continuous encouragement, completion of this work would not have been possible.

I acknowledge the financial support from the EDF energy, UK and the Open University. I would like to thank Dr. David Dean and Mr. Mike Spindler of EDF energy for their useful discussions in shaping the research project. My special gratitude to Dr. Shirley Northover and Dr. Hedieh Jazaeri for reviewing and helpful discussions on part of the thesis. I am grateful to the instrument scientists of the Engin-X instrument, Dr. Shu-yan Zhang, Dr. Joe Kelleher, Dr. Saurabh Kabra and instrument scientist of the SALSA instrument, Dr. Thilo Pirling for their assistance with the neutron diffraction experiments.

I would like to thank Mr. Damian Flack and Mr. Peter Ledgard for their help with the specimen machining, Mr. Gordon Imlach for his assistance in using SEM, Mrs. Heather Davies for her assistance in using TEM. My special thanks to Mr. Stan Hiller for his assistance with the mechanical testing and for all the good discussions we had. I would also like to thank Mrs. Olivia Acquah for her assistance with the administrative works throughout the PhD and for her friendship.

I would like to thank the past research students of my department, Yeli, Sanjoo, Shah Karim, Jino, David, Gerrardo, Jeferson, Khader, Shan, Rudelpho, Needa and the current research students Anas, Mushfiq, Rahul, Eleyis, Yadu, Stephen, Beverly for all of their help, guidance and most importantly their friendship.

Finally, I can’t thank enough my family; without the sacrifices of my parents, I wouldn’t be able to accomplish this work. Thanks to my brother Rony, my sister Nasrin, my grandmother, my mother in law and other in-laws for their support, motivation and prayers.

Last but not the least, I would like to thank my wife, Nazmus Sakiba, for looking after me in the last year of my PhD and for her unconditional love before and beyond that.

Table of Contents

List of Figures

List of Tables

Nomenclature

Symbol	Description
Tm	Absolute melting temperature
Q_c	Activation energy for creep
λ	Angle between the axis of the applied stress and the direction of slip plane in Schmid's law
φ	Angle between the axis of the applied stress and the normal to the slip plane in Schmid's law
D	Average length in mm of the diagonals of the indentation
β	Back stress
d_c	Creep damage per cycle in R5
CF	Contrast Factor
A	Constant in creep power law
ε_c	Creep strain
ε_f	Creep strain at failure
A	Constant in Ramberg-Osgood power law
β	Constant in Ramberg-Osgood power law
D	Diameter
E	Elastic Modulus

ε_{el}	Elastic strain
F	Force
θ_{hkl}	Incidence angle of the beam
$I_H(\lambda)$	Incident beam current
σ_i	Internal stress
d_{hkl}	Inter-planer spacing
Q_{sd}	Lattice self-diffusion energy
m	Mass
P_1	Material constant in ductility exhaustion
L	Mean linear intercept grain size
H^-	Negative hydrogen ions
$N(D)$	Number fractional distribution
N	Number of intercepts
R	Number of rows scanned
P	Number of pixels
h	Planck's constant
ε_p	Plastic strain
ε_p	Plastic strain range
δ	Scan step distance between pixels
Q	Scattering vector
$I_M(\lambda)$	Scattered beam current
ε_s	Secondary creep strain

ε	Strain
σ	Stress
n	Stress exponent in creep power law
$d_{0\,hkl}$	Stress-free reference measurement
$\Delta\sigma$	Stress range
T	Temperature
D_c	Total fractional damage by creep
D_f	Total fractional damage by fatigue
ε_t	Total strain
R	Universal gas constant
u(	Variation of steady-state creep strain rate with stress
v(t)	Variation of steady-state creep strain rate with temperature
V	Velocity in De Broglie's equation
HV	Vicker's hardness number
C(D)	Volume fraction distribution of cavities
V(D)	Volume fraction distribution of scatterers
λ	Wavelength in Bragg's law of diffraction
σ_y	Yield stress of the crystal

Abbreviations

AFM	Atomic Force Microscope
AGR	Advanced Gas Cooled reactor
AISI	American Iron and Steel Institute
AKA	Also Known As
BF	Bright Field
CBED	Convergent Beam Electron Diffraction
CRSS	Critical Resolved Shear Stress
DIC	Digital Image Correlation
EBSD	Electron Backscattered Diffraction
EDM	Electric Discharge Machining
EDS	Energy dispersive X-ray spectroscopy
EPSC	Elastic Plastic Self Consistent
FCC	Face Centred Cubic
FE	Finite Element
FIB	Focused Ion Beam
FWHM	Full Width at the Half Maximum
HCP	Hexagonal Closed Packed
HOLZ	High Order Laue Zone
HS-AFM	High Speed Atomic Force Microscope
ILL	Institut Laue-Langevin
IR	Intergranular
MLI	Mean Lineal Intercept
MUD	Multiples of Uniform Density
OES	Optical Emission Spectroscopy
OM	Optical Microscopy
PID	Proportional Integral Derivative
RAL	Rutherford Appleton Laboratory

SANS	Small Angle Neutron Scattering
SEM	Scanning Electron Microscope
SFE	Stacking Fault Energy
SINQ	Swiss Spallation Neutron Source
TEM	Transmission Electron Microscope
TOF	Time of Flight
TWIP	Twinning Induced Plasticity
μSANS	Ultra-High Resolution SANS

Chapter 1 Introduction

1.1 Overview

Electricity generation fuelled by gas, oil, coal and nuclear sources account for almost three-quarters of the total electricity generation in the UK [1]. The life of utility scale power generation plant is limited by the endurance of the materials from which they are made which may be exposed to harsh service operating conditions. For example power generation plant operating at high temperature under pressure for prolonged periods of time is subjected to variable tension-compression cyclic loadings owing to routine start-up and shutdown operations or sudden rise or drop in electricity demand, or an unplanned shut-down. Moreover, there is a growing need for large power plants to operate in 'load-follow' mode to fill the gaps created by low carbon power generation (for example solar and the wind) which can be intermittent in nature. The load-following requirement imposes even more frequent load cycles on components. A realistic plant life assessment procedure has to capture the effects of these complex loading sequences on the deformation and integrity of structures operating at high temperature. Moreover it's important that such procedures are not so conservative such that plant is retired prematurely or do not impose unnecessary inspection and maintenance costs.

In the context of UK nuclear power generation, the robustness and accuracy of plant life assessment procedures are of crucial importance. This is because, design lifetimes of most of the nuclear power plants currently operating in the UK (14 advanced gas cooled reactors, AGRs) have been exceeded [2]. With increasing demand for electricity and commitment to large-scale reductions of carbon emissions, the UK's electricity supply is in a potential cliff-edge situation [3, 4] in the next few years until power supplies from plants under construction are added to the grid. To overcome the potential short-term gap between supply and demand of electricity, lifetime extension assessments of currently operating AGRs are being

undertaken. A robust and reliable life assessment procedure is required to justify and ensure that the continued operation of nuclear power plants is safe and commercially viable during proposed extended periods.

Two components, which are irreplaceable in nuclear power plants, are the reactor core and the boiler. The lifetime of the entire plant is essentially limited by the life of the materials of these components [3]. AISI type 316H austenitic stainless steel has been used in the construction of the steam systems (pipes, steam headers and boiler) of the AGRs. In service, these components operate at temperatures in excess of 500°C. At these temperatures creep of type 316H stainless steel is an important deformation mechanism which has been widely studied for many decades. The creep life of simple components under steady state loading can be predicted from laboratory data with a reasonable accuracy. However, in operation, complex structures are subjected to cyclic operational loads where material creep behaviour is less easy to predict because of the load history. For example, creep deformation during dwell periods at constant load or displacement can be influenced by a type of internal stress known as the 'back stress'. The back stress can be defined as a self-generated stress which equilibrates over a finite length-scale in the material. Such stresses generate from the inhomogeneity of deformation at various length scales, for example, due to elastic and plastic anisotropic deformation of grains (intergranular stress) and due to the development of an inhomogeneous distribution of dislocations within the grains (intragranular stress). The concept of back stress is long known and has been widely established by various macro observed phenomena in the material such as anelasticity [5] and the Bauschinger effect [6].

In plant life assessment procedures, for example, the R5 high-temperature life assessment procedure developed by EDF energy [7], the effect of back stresses generated by monotonic and cyclic loading on the creep deformation is not taken into full account. In order to incorporate the effect of back stresses in the estimation of material's deformation, first the origin and evolution of back stress in the material during cyclic and creep loading sequences need to be understood and then the effects of these on the material's deformation need to be quantified, which are the aims of this research project. The main objectives of this thesis are:

- To enhance understanding of the origin and evolution of back stresses in AISI type 316H austenitic stainless steel during monotonic and cyclic deformation at room and high temperatures.

- To quantify the effect of back stresses on creep deformation and damage development, of type 316H austenitic stainless steel during high-temperature creep-fatigue loading.
- To evaluate the role of intergranular strains on the kinematic hardening (i.e. the Bauschinger effect) observed in type 316H austenitic stainless steel.
- To enhance understanding of the nucleation and growth mechanisms of creep cavitation in type 316H stainless steel using novel experimental techniques.

1.2 Structure of the thesis

The thesis consists of 10 chapters in total as summarised below.

Chapter 1 provides a general introduction to the study.

Chapter 2 provides a literature review. First, the relevant theories concerning deformation mechanisms in stainless steel are described. Secondly, significant publications relevant to this project are critically reviewed and research gaps highlighted.

Chapter 3 describes the experimental techniques used in this project covering the instruments, experimental set-up, the design of specimens and test procedures.

Chapter 4 presents experimental results showing the generation of intergranular strain during tensile, compressive, load-unload and tension-compression cyclic loading of type 316H austenitic stainless steel at room and high temperatures. Results of material characterization tests are also described in this chapter.

Chapter 5 presents experimental results illustrating the effect that back stresses have on the creep deformation of type 316H stainless steel and how they evolve during load-controlled and displacement controlled creep dwells.

Chapter 6 presents experimental results showing how intergranular strains control kinematic hardening (known as the Bauschinger effect) in type 316H austenitic steel during tension-compression cyclic deformation at room and high temperatures.

Chapter 7 presents experimental results showing a quantitative measure of creep cavities and a subsequent ex-situ measure of intergranular strains in two sets of creep interrupted specimens.

Chapter 8 critically evaluates the key findings of the research and discusses their relevance to engineering applications. Moreover, the conceptual development of a novel stress rig for conducting longer term creep-fatigue tests in the neutron beamlines is described.

Chapter 9 describes overall conclusions arising from the research and suggests future work plan that could be envisaged from the findings.

Chapter 10 lists the key findings of the study.

Chapter 2 Literature Review

2.1 Overview

The aim of this chapter is twofold; first to introduce the concepts and theories that were used in this thesis and then to review the current state of knowledge in the area of back stress. The chapter begins with a brief introduction to stainless steel and its elastic, plastic and creep deformation mechanisms. Deformation in a single crystal is described in order to explain the deformation mechanisms at the atomic scale in the material; these mechanisms are then used to explain deformation mechanisms in the polycrystalline material. The concept of back stress is explained and sources contributing to its existence are identified. Published works relating to the generation of back stress in material and its effect on macroscopic deformation are reviewed in order to describe the current state of knowledge in this area and to highlight the research gaps.

2.2 Austenitic stainless steel

In its most basic form, steel is an alloy of carbon and iron. Figure 2-1 shows an iron-carbon phase diagram, it can be observed that the austenite phase of steel is stable only at temperatures above 723°C. However, various alloying elements such as Nickel and Manganese stabilise the austenite phase of steel making it possible to have austenitic steel at room temperature [8]. The specific grade of steel investigated in this project is AISI type 316H austenitic stainless steel. This grade of steel has been widely used in many components of power generating plants since the 1950s, for example in boiler headers and steam piping [9]. Type 316H stainless steel possesses good high-temperature properties such as good resistance to oxidation and creep deformation [10]. The average melting temperature of this steel is ~1400°C. The main alloying elements of the steel are Fe, Cr, Ni, Mo, Si, N and C.

The function of these elements in the alloy can be found in the textbooks, for example in [8, 11].

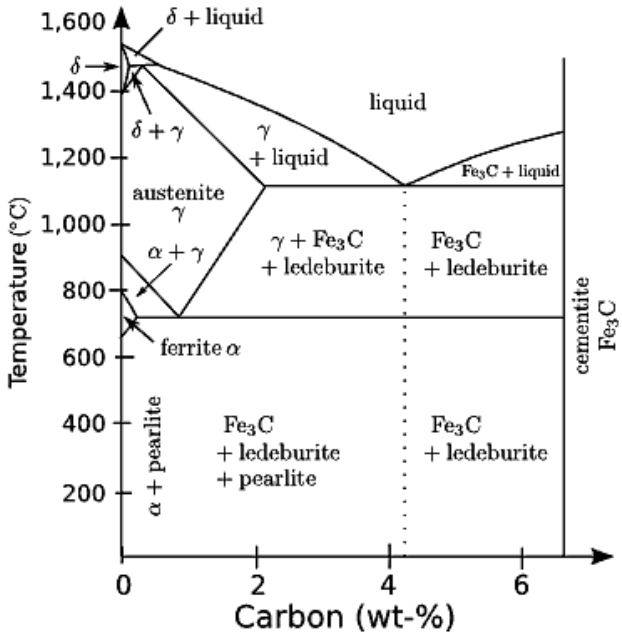

Figure 2-1: Fe-C phase diagram showing various phases of steel existing as a function of temperature and carbon content

2.2.1 Precipitation in type 316 stainless steel

316H austenitic steel contains a large number of alloying elements and therefore, a number of different precipitates such as carbides and intermetallics are formed in this material at high temperatures. The formation of precipitates significantly affects the creep resistance and strain hardening of the material. Figure 2-2 [12] shows the formation of various precipitates and phases in 316 austenitic steel as a function of time and temperature. It can be noticed that $M_{23}C_6$ is the most abundantly formed precipitate in this material and more readily so at higher temperatures. The $M_{23}C_6$ carbides are usually $Cr_{23}C_6$ carbides, because of the high affinity of carbon for chromium but M can also be substituted by Fe, Ni and Mo [13]. The formation of $Cr_{23}C_6$ is chromium diffusion controlled [14], therefore, such precipitations only occur at high temperatures. As the diffusion rates of carbon and chromium are higher at the grain boundaries than inside the grain, these precipitates are first formed along the grain boundaries resulting in chromium depleted zones in the material. This precipitation process is commonly known as sensitization and may result in intergranular corrosion in the material. A schematic of the sensitization phenomena is shown

in Figure 2-3. At about 600°C, the M_6C precipitates are also observed to form in this material; elements for M are Mo, Ti, Nb, V and Fe.

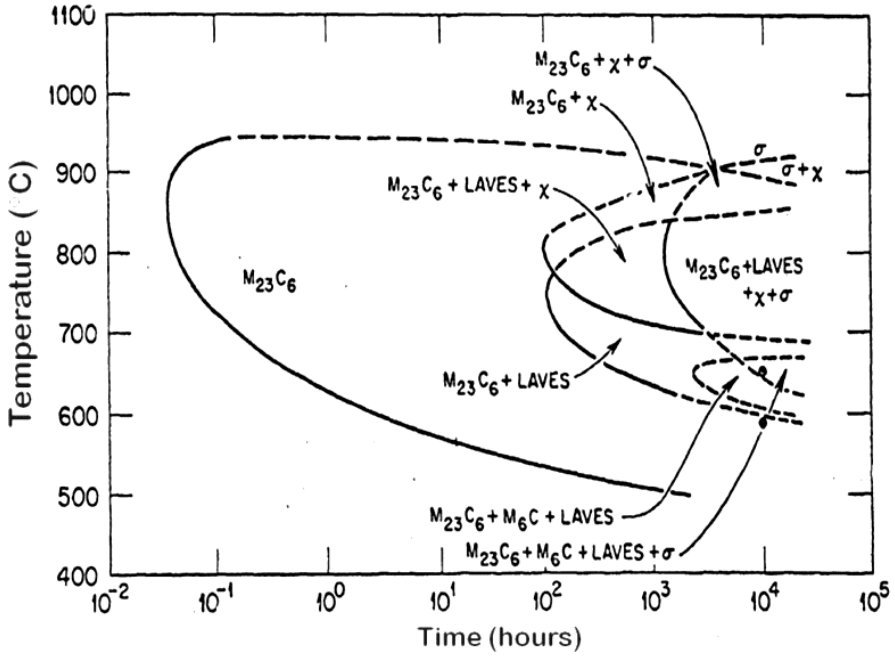

Figure 2-2 Formation of precipitates in 316 austenitic steel at various temperatures and time lengths during the ageing process [12]

A number of intermetallics are formed during the ageing process of type 316 austenitic steel; these mostly have a deleterious effect on the deformation of this material. Sigma and Chi phase form at about same temperature and both of these phases are chromium and molybdenum rich.

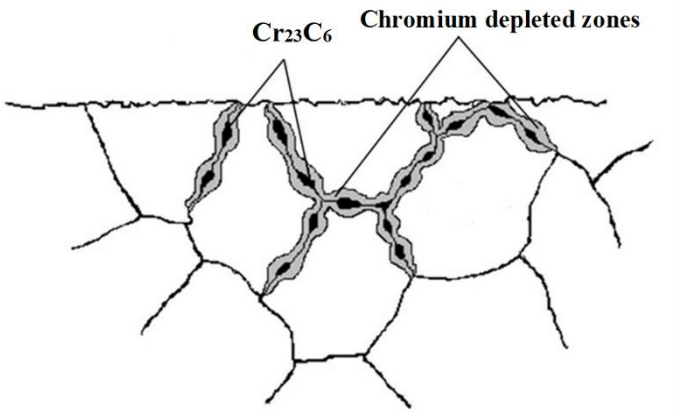

Figure 2-3 Schematic showing formation of Chromium carbides in the grain boundaries creating chromium depleted zones which are prone to corrosion, this phenomenon is known as sensitization

2.3 Deformation mechanisms in austenitic stainless steel

Deformation of a material refers to the change of shape of a body due to applied load. Upon application of increasing uniaxial load, like most other metals, stainless steel undergoes elastic deformation followed by plastic deformation. Elasticity arises from short-range interatomic forces, which maintain the atoms in regular patterns when there is no load applied. With the application of a small magnitude of the load, these bonds stretch and the material gets elongated in the direction of loading. When the load is removed the material goes back to its original shape. On the other hand, during plastic deformation the bond stretches and the lattice planes shear. Such shear of lattice planes occurs through movement of dislocations which requires breaking and rejoining of atomic bonds. Therefore, when the external load is removed the material cannot go back to its original shape any more. In the context of this thesis, it is necessary to describe the deformation mechanism in a single crystal first, to better describe the deformation mechanism in the polycrystalline macroscopic material.

2.3.1 Deformation in a single crystal

Type 316H austenitic stainless steel has a Face Centred Cubic (FCC) crystal structure. Upon application of an external load, the spacing between lattice planes of the crystal gets stretched and elastic deformation occurs. When the load exceeds the yield stress of the crystal, specific parallel lattice planes slip over one another in a specific direction and plastic deformation occurs. Although slip is the most common mechanism of plastic deformation in type 316H stainless steel, plastic deformation by twinning can also occur. Increase in the shear stress for slip and reduction of stacking fault energy due to high solute concentration can cause twinning in the FCC materials [15].

Slip in a crystal occurs by the movement of dislocations and can only happen when the shear stress in a slip direction of a slip plane exceeds the critical resolved shear stress (CRSS). The CRSS is related to the stress required to move dislocations in a slip plane and can be determined analytically using Schmid's law [16]. Figure 2-4 shows a schematic of the plastic deformation of a single crystal by slip. Uniaxial tensile force is applied along the F direction through the longitudinal axis shown at the centre of the crystal. Slip in the lattice occurs in the plane marked in blue, having a normal that lies along C. The direction of slip is along B.

Schmid's law can be applied to determine the critical resolved shear stress in this slip system as described by equation 2.1.

$$\tau_C = \sigma_y \cos \varphi \cos \lambda \qquad (2.1)$$

Here, τ_C = Critical resolved shear stress

σ_y = yield stress of the crystal

φ = Angle between the axis of the applied stress and the normal to the slip plane

λ = Angle between the axis of the applied stress and direction of slip

In this equation, cos φ cos λ is known as the Schmid factor.

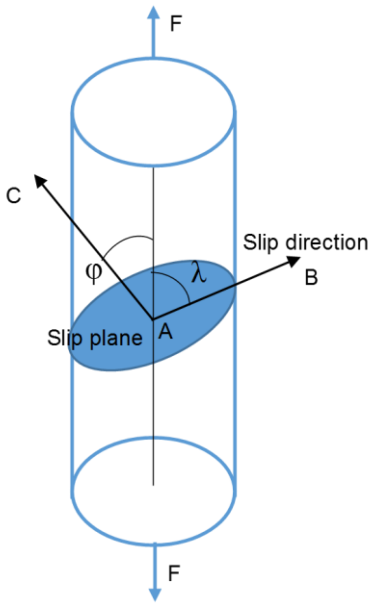

Figure 2-4 Schematic illustrating the formulation of Schmid's law.

The shear stress required to move a dislocation increases exponentially as the inter-planer spacing decreases among lattice planes [17] and therefore slip tends to occur on the closest packed planes, which have the highest inter-planar spacing [18]. So, crystal planes in which slip occurs are well-defined and parallel to each other. The direction of slip occurring in those planes is also consistent. The lattice plane in which slip occurs and the direction of the slip makes up a crystallographic slip system. The closed packed directions of an FCC unit cell are along the diagonals of each face. Therefore, in 316H stainless steel, the preferred slip systems are the twelve {111} <110> system.

If an external load is applied to a single crystal of FCC structured material, shear stress will increase in each of the available slip systems, until it reaches the CRSS in one of the systems. This system will be the one with the highest Schmid factor. The slip will occur in that system first and may occur in the other systems when the load is increased further. The Schmid factor in equation 2.1 shows that the magnitude of the CRSS depends on the angles between the loading axis and slip system of the crystal. In other words, in a polycrystalline material, the plastic deformation of an individual crystal is highly dependent on the orientation of the crystal with respect to its loading axis.

2.3.2 Dislocations

A dislocation can be generally defined as a geometric imperfection (defect) in the regular lattice of the crystal. Geometrically, dislocations could be of edge type, screw type or a mix of these two types. Upon application of a shear load, edge dislocations move parallel to the direction of the shear stress while the screw dislocations move in a direction perpendicular to it [19].

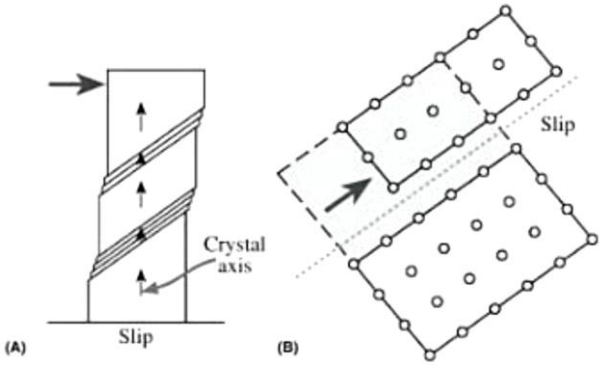

Figure 2-5 Schematic of dislocation glides (A) Macroscopic (B) Atomic [20]

Dislocations can move in the crystal by two distinctive processes known as glide and climb. In glide motion, the dislocation line and burgers vector both stay on the surface in which it moves, therefore, glide movement of an edge dislocation is limited to a specific plane. On the other hand, a screw dislocation does not have a specific slip plane assigned to it, and therefore, can glide to another slip plane. For example, in a FCC material like 316H austenitic steel, glide of edge and screw dislocations will generally occur in {111} crystallographic planes, however, only the screw dislocation can move from one {111} type plane to another. Such movement of a screw dislocation is called cross-slip. At room

temperature, deformation by slip in the crystal occurs predominantly by glide motion of dislocations. At high temperatures, dislocations can also move by climb process; that is, an edge dislocation can move out of its slip plane. This process requires mass transport by diffusion of vacancies or interstitial atoms [21]. In climb motion, the dislocation line remains perpendicular to the Burgers vector. Further details of the motion and nature of dislocations can be found in textbooks, for example in [19].

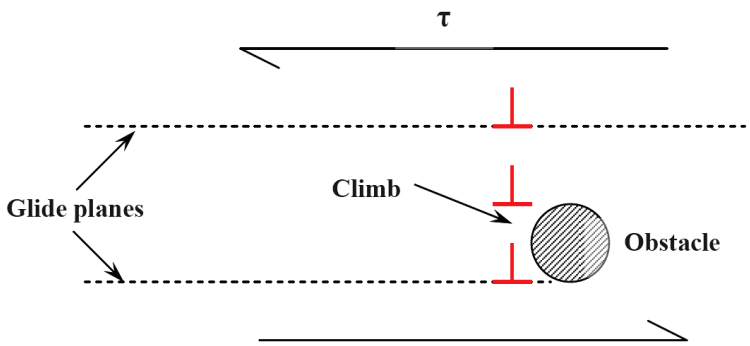

Figure 2-6 Schematic of dislocation climb [20]

2.3.2.1 Stacking fault

Faults in the stacking of lattice planes are produced by plastic deformation and are generally termed as a stacking fault [22]. A stacking fault is a planar defect in the crystal, unlike the dislocations which are line defects. A stacking fault introduces a thin layer of a different crystal structure within a structure, for example, stacking faults in FCC crystal structure may create an atomic thin layer of HCP crystal structure [23], which ultimately affect the deformation behaviour of the crystal. The energies due to the irregularities in the lattice plane sequence can be expressed in terms of stacking fault energy (SFE). Different materials with the same crystal structure may have very different SFE, for example, despite having the same FCC crystal structure, the SFE of austenitic steel is much smaller than that of Aluminium and Nickel. The SFE affects various mechanical properties of metals, for example, strain hardening, the formation of dislocation structures etc. Due to lower SFE, 316H stainless steel strain hardens rapidly compared to Nickel and Aluminium and thus although the yield stress of 316H stainless steel is low, the ultimate tensile strength is comparatively higher [24]. Dislocation type sub-structures are formed more readily in metals with higher SFE due to easy occurrence of cross slip [25].

2.3.3 Strengthening mechanism in austenitic stainless steel

Strain hardening is the main strengthening mechanism in type 316H austenitic steel which arises from the interaction of dislocations with other dislocations, solute atoms, precipitates and grain boundaries. The density of dislocations is found to increase with increasing plastic strain, which occurs by a number of processes, for example, by the emission of dislocations from a high angle grain boundary, by multiple cross slip mechanisms and by Frank-Read mechanisms [26]. Dislocations glide in their respective slip plane and combine with other dislocations gliding on intersecting slip planes. The combination of dislocations can make a new dislocation which is not in the slip plane with lowest CRSS, and therefore, become immobile or sessile. These sessile dislocations act as an impediment to other dislocations until the shear stress in that plane is raised. One particular type of such dislocation interaction can be noticed in type 316H stainless steel and in other FCC metals when dislocations from different {111} plane combine each other and become sessile, such formation is known as Lommer-Cottrell dislocation structure. Other types of dislocation interactions can also lead to strain hardening in the material, for example, when one dislocation cuts through other dislocations in the intersecting plane, in a mechanism known as the forest intersection of dislocations [27]. Such interactions of dislocations may form steps or jogs [28] in the dislocation line, which further contribute to the strain hardening of the material. Formation of jogs impedes the movement of screw dislocations but not that of the edge dislocations.

Movement of dislocations can also be hindered by the grain boundaries in a mechanism known as dislocation pile-up. Pile-ups produce a ‘back stress’ in the crystal which opposes the applied stress on the slip plane [23]. Strain hardening can arise from the interaction of dislocations with solute atoms and precipitates. Due to the difference in size of solute atoms compared with base atoms, a distortion is generated in the lattice plane close to the solute atoms. Dislocations interact with this stress field of the solute atoms. The strain hardening from precipitates arises from dislocation movement being hindered by a pinning process, which can be overcome either by cutting through the precipitates or by moving past in a bowing and looping process [29], as shown in Figure 2-7.

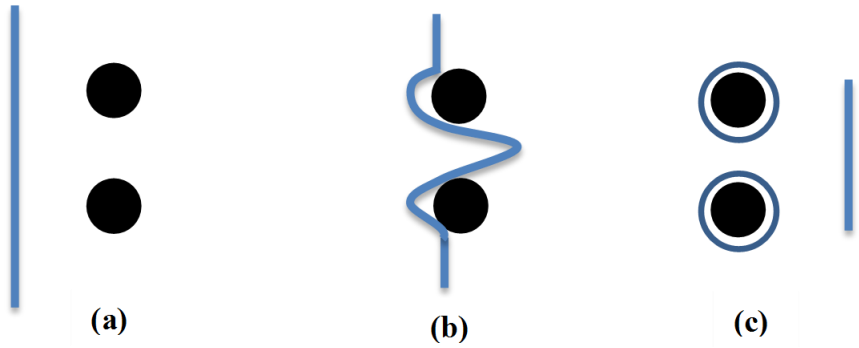

Figure 2-7 Schematic showing dislocation bowing and looping process. (a) a dislocation is gliding towards two point obstacles (such as precipitate) (b) the dislocation bowed to move around the obstacle (c) dislocation left the looping marks around the obstacle and became shorter in length

Strain hardening due to dislocation pile-ups occurs over a long distance (relative to the lattice spacing) while strain hardening due to the cutting of dislocations occurs over a small atomic distance. The short range forces associated with dislocation cutting process can be influenced by temperature fluctuations and the strain rate but the long range forces associated with dislocation pile-ups are relatively uninfluenced by these factors. This difference can be used to distinguish the strain hardening mechanisms in the material.

The evolution of dislocation structures with increasing plastic strain can be systematically described in a FCC crystal using few general assumptions [30]. If a FCC structured single crystal is pulled in tension, at first stage, it will undergo a small magnitude of strain hardening, which implies that the dislocations are able to glide over a long distance without facing impediments. At this stage, the dislocations glide in only one slip system. With further increase of load, the slips start to occur in multiple planes and therefore the strain hardening increases quickly with the formation of more Lomer-Cottrell barriers. Due to slips occurring in a number of slip systems, the dislocations start to tangle at this stage which leads to the formation of a dislocation cell type sub-structure. The interior of these sub-structures is almost free of dislocations while the walls have much higher dislocation densities. These dislocation sub-structures have been referred to as a source of back stress contributing to the Bauschinger effect in a single crystal [31] and will be discussed in detail later in this thesis. With further increase of load, dislocation mechanisms (such as cross slip) which were not possible at lower applied stress, get activated. Due to cross slip, dislocations can escape the pile-ups and therefore at this stage the strain hardening is reduced.

2.3.4 Polycrystalline deformation

A polycrystalline material like Type 316H austenitic stainless steel consists of an aggregate of single crystals oriented in different directions. When an external load is applied to the polycrystalline material, differently oriented grains deform elastically differently, as illustrated using Schmid's law. When the load is increased, some crystals are oriented such that slip initiates in those whilst others remain elastic until the external load increases further. Therefore, the deformation of a single crystal in a polycrystalline aggregate depends on the orientation of the crystal itself and its neighbouring crystals. To describe such complex deformation of crystals, plasticity models are useful. A number of such models have been developed, among which the ones by Sachs [32], Taylor [33] and Bishop-Hill [34-36] are most noteworthy.

In one of the earliest polycrystalline plasticity model developed by Sachs [32], it was assumed, upon application of an external load all grains sustain equal stress, as in the bulk material, and each grain deforms by single slip similar to an unconstrained single crystal. This suggests activation of different slip system in grains with similar crystal orientation and independent deformation of grains irrespective of their neighbouring grains, none of which is realistic. Based on this assumption, upon application of a finite strain, gaps and overlaps will be created in the boundaries between grains [37]. In 1938 Taylor [33] proposed, upon application of a load, all grains do not sustain equal stress but equal plastic strain as in the bulk material. The initial Taylor model was limited to large plastic strain only. Bishop and Hill [35] extended this model to account for polyaxial stress state [38] and Lin [39] extended the model to account for both large and small strains. If all the grains in a polycrystalline material deform equally, it will satisfy the compatibility requirement in the grain boundaries. However, as different stress is required to activate multiple slips in each grain, it will violate the stress equilibrium at grain boundaries. Taylor's model assumed plastic deformation in single grain occurs by multiple slips. The Sachs model provides a lower bound to the polycrystals yield stress, while the Taylor model provides an upper bound [18].

A major limitation of the above-described models is that none of these takes elastic anisotropy of grains into account [40] which is crucial to understanding the micromechanics during the initial stage of plastic deformation. Elastic anisotropy can be represented by self-consistent models. A self-consistent model was first developed by Kroner [41] and,

Budiansky and Wu [42] where they considered the variation of stress and strain in each grain upon application of an external load. In anisotropic polycrystalline material, each grain is surrounded by a number of randomly oriented grains which are deforming by slip in random directions. Each of these grains was considered as a spherical inclusion in an infinite homogenous matrix. The stress and strain in a single crystal surrounded by its plastically deformed neighbours are approximately obtained by considering the deformation of this inclusion [43]. The problem of stress and strain in the inclusion can be solved using a modified version of Eshelby's ellipsoidal inclusion solution [44]. Although the initial formulation of Eshelby was limited to elastic interactions only, Kroner [41] has proposed a modified version of the formulation which includes the effect of plastic strain in the surrounding matrix. Further to this, Hill [45] incorporated elastoplastic interaction of the matrix in his proposed general formulation. The elastic-plastic self-consistent (EPSC) model is based on this modified Hill's model which was initially formulated by Hutchinson [38].

2.3.5 Creep deformation

Creep of metals results in permanent deformation. Creep is a time dependent deformation mechanism and thus is somewhat different to plastic deformation. Creep deformation in Type 316H stainless steel is significant usually at temperatures above 0.4 T_m, where T_m is the homologous melting point of the alloy. Above this temperature threshold, the atoms become sufficiently mobile to allow time-dependent rearrangement of the structure [46]. Creep is the most critical deformation mechanism of materials operating at high temperature [47, 48]. It has attracted widespread industrial and academic research interest in the past century and continues to be of relevance as materials are required for ever more demanding high-temperature applications.

2.3.5.1 Representation of creep data

High temperature creep curves are usually expressed in terms of a strain vs time graph. The shape of the creep curve is found to be same for many pure metals and alloys. A schematic of a typical creep curve for type 316H stainless steel is shown in Figure 2-8. The material sustains an instantaneous strain when the load is applied. At the beginning of creep process, the creep rate decreases until it becomes almost zero. After a duration of time, the creep rate increases leading to fracture of the material. Based on the changes in strain rate, creep

deformation can be divided into three stages, although in many materials all these three stages are not distinguishable. Also, the extent to which different stages of creep can be distinguished depends on the temperature and applied stress [23] of a particular test.

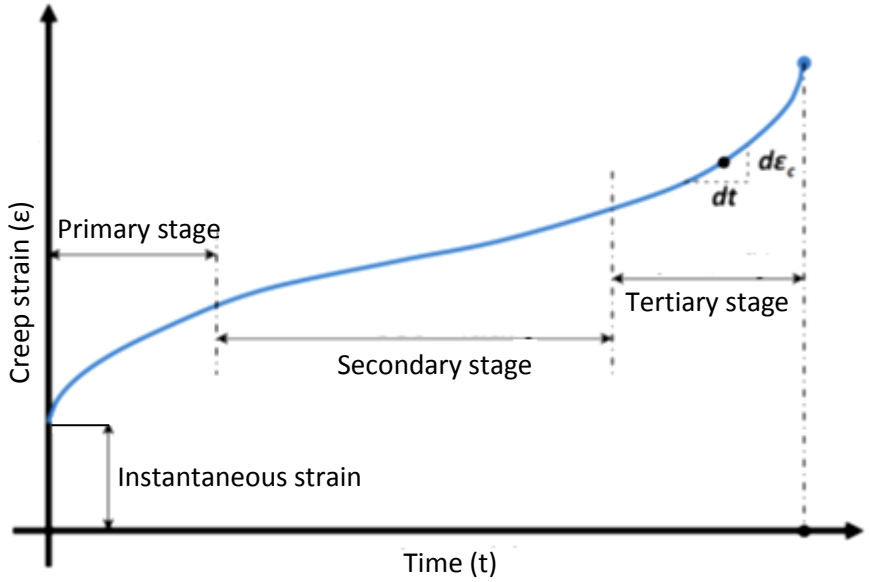

Figure 2-8: Schematic showing typical creep curve of 316H stainless steel and different stages of creep deformation

In the primary stage of creep, the creep strain rate decreases with time. This decrease of creep rate occurs mainly due to work hardening in materials. Dislocation movement and stress-induced dislocation generation in the crystal structure of the material is the main source of work hardening in type 316H stainless steel. Impediments created from the increasing dislocation densities eventually decrease the flow of dislocations by decreasing the number of available mobile dislocations. In most materials, the secondary creep stage is significantly longer than the primary and tertiary stages [49]. So, 'secondary' or 'steady-state' creep rate is one of the most significant parameters of a creep curve. At this stage, the rate of work hardening balances out the rate of annealing (thermal softening) which brings the creep strain rate to a minimum. However, significant microstructural changes of materials take place due to both diffusion and dislocation movement. At the final stage of deformation, known as the tertiary stage, the creep strain rate increases with time and eventually leads to failure of the material. This behaviour is the result of a combination of several mechanisms operating independently, such as strain hardening, recovery, precipitation of carbides, cavity formation and necking [50]. Failure due to creep generally leads to intergranular fracture of materials.

2.3.5.2 Mechanisms of creep

There is no single theory of creep which satisfactorily predicts the creep rate of all metals at all stresses and temperatures, understandably so, as the inherent creep deformation process could be very different in a material itself, depending on the temperature and stress applied. On the other hand, different materials with very different properties (in terms of crystal structure, types of dislocation etc.) often exhibit a similar creep curve [46]. So, it should be possible to capture the creep deformation process in a general framework, at least within specific loading conditions.

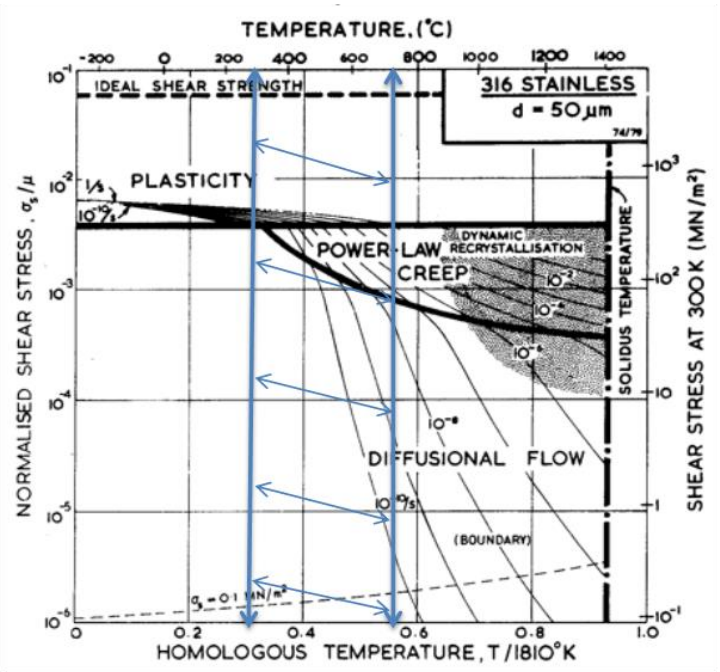

Figure 2-9: Deformation mechanisms map for type 316H austenitic steel with a grain size of 50 microns [51] The blue arrow shaded region is the main area of interest for this project, based on nuclear power plant operating temperature range.

Deformation mechanism maps for various materials have been constructed by Frost and Ashby [51] which indicate the activation of different creep mechanisms at different stress and temperature. The map for steady state creep of type 316H stainless is shown in Figure 2-9. At lower applied stress, diffusion based creep is the dominant deformation mechanism in this material while at a higher applied stress dislocation based creep becomes dominant. These two creep processes are discussed below in brief.

2.3.5.3 Diffusion Creep

Diffusion creep occurs by transport of material via diffusion of atoms within a grain. Under an externally applied stress, the vacancies or point defects within a crystal structure can diffuse in a certain direction through the crystal or around grain boundaries. Free surfaces and grain boundaries are usually sources and sinks of vacancies. Vacancy movement is the dominant diffusion mechanism in most metals and alloys [46]. Theories of diffusional deformation mechanisms proposed by Nabarro-Herring [52] and Coble [53] are the most widely accepted.

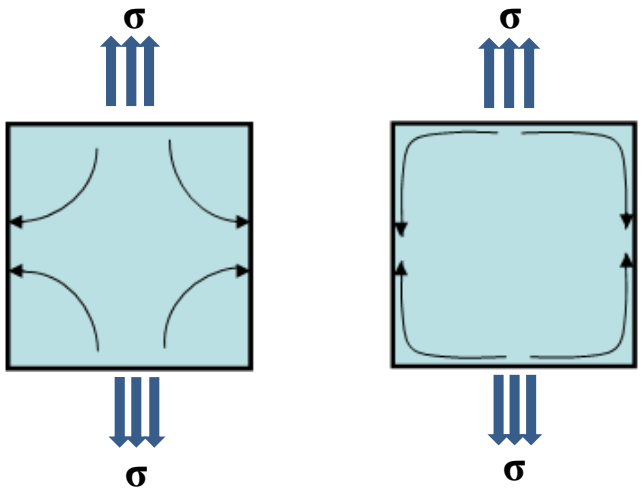

Figure 2-10 Schematic showing flow of vacancies in a crystal by (a) Nabarro-Herring and (b) coble creep. When creep occurs by stress directed flow of vacancies, the vacancies may flow through the grains and along the grain boundaries.

Frank Nabarro and Conyers Herring [52] explained the creep processes in a polycrystalline material, which simply involve diffusional transport of atoms. When an external stress is applied, the vacancies generated in grain boundaries experience tensile stresses and thus diffuse to the boundaries under compression. This creates a counter-flow of atoms to the tensile boundaries. This process is equivalent to picking atoms from boundaries under compression and placing those to the boundaries under tension. This causes the elongation of the grain size in the direction of tensile loading and reduces the size in the transverse direction. Another type of diffusion creep mechanism has been postulated by Coble [53] in which creep takes place by the diffusion of vacancies along the grain boundaries.

2.3.5.4 Dislocation creep

Diffusion creep processes can provide a prediction of the creep rate for pure polycrystalline material at low stresses. However, at higher applied stresses, the prediction from diffusional creep theory cannot satisfy the experimental findings. Therefore, an alternative theory of creep deformation processes has been postulated in terms of generation, movement, and annihilation of dislocations during creep process. Later, electron microscopy has provided the evidence of alterations of dislocation density and arrangement of dislocation structures as creep continues [46]. Similar to plastic deformation, in creep, dislocation within a material can move by 'glide' or 'climb'.

During the secondary stage, the creep rate remains constant with increasing time i.e. the 'steady state' creep rate depends only on stress and temperature but not on creep strain or time [46]. So, the steady-state creep strain rate $\dot{\epsilon}_s$ can be expressed as

$$\dot{\epsilon}_s = u(\sigma).v(T) \qquad (2.2)$$

Here, $u(\sigma)$ = variation of steady-state creep strain rate with stress

$v(T)$ = variation of steady-state creep strain rate with temperature

The dependencies of secondary creep rate on temperature and stress are independent of each other that is the change in creep rate with increasing/ decreasing temperature should be same for all stresses and vice versa. By conducting creep tests at different temperature but at the same stress, an independent relation between creep strain and temperature can be established based on Arrhenius's law, as shown in equation 2.3.

$$\dot{\epsilon}_s \propto \exp - \left(\frac{Q_C}{RT}\right) \qquad (2.3)$$

Here, R is universal gas constant and Q_c is the activation energy for creep. On the other hand, from creep tests at the same temperature, but at different stress, several different relationships could be found between creep strain rate and applied stress. However, generally a good relationship is often observed when log $\dot{\epsilon}_s$ is plotted against log σ [46] suggesting that,

$$\dot{\epsilon}_s \propto \sigma^n \qquad (2.4)$$

Substituting equation (2) and (3) in equation (1), the power law behaviour of creep can be generalised as follows:

$$\dot{\epsilon}_s = A\sigma^n \exp - \left(\frac{Q_C}{RT}\right) \qquad (2.5)$$

Here, A is a constant. This power law can be used to predict creep strain rate for a number of pure metals, ceramics and many alloys in steady-state creep region. The value of the constant n is found to be about 5 for most of these materials and the activation energy Q_C is found to be equal to lattice self-diffusion energy (Q_{sd})of specific materials. However, this is only true for a certain range of temperature/stress and power law breaks down outside the regime where generally the value of n increases and the value of Q_C decreases [54]. In fact, the constants A, Q_C and n themselves are found to be functions of stress and temperature [55].

2.3.5.5 Creep cavitation damage and measurements

Creep damage in the metals occurs by the nucleation and growth of creep cavities. Study of creep cavities and the role of cavities in limiting creep life of materials was first reported by Greenwood [56, 57]. Creep damage is usually associated with tertiary stage of creep, however, creep cavities are nucleated at relatively early stage of creep and gradually grow during the creep deformation [58]. A lot of research has been conducted since the identification of the creep cavities, however, the mechanisms of cavity nucleation are still not completely understood [59], particularly in engineering alloys with complex secondary particles [60]. Among the creep cavity nucleation mechanisms described in the literature, those based on the accumulation of vacancies [61], grain boundary sliding [62] and dislocation pile-ups [63] are the most widely established.

In creep deformation, nucleation of the cavities occurs usually at the grain boundaries oriented normal to the principal stress direction [64, 65], although, cavities can nucleate within the grains as well, particularly under higher applied stresses. Cavitation in the commercial alloys, such as that in type 316H stainless steel, is appeared to be associated with the second phase particles [66]. The cavities grow in number and size with increasing creep deformation. Different mechanisms of creep cavity growth may prevail depending upon the stress and temperature [67] in the material; most notable of the creep cavity growth

mechanisms are the diffusion controlled movement of vacancies, plasticity and constrained cavity growth.

Cadek [68] theoretically predicted the critical size of the creep cavities to be in the range of 2-5 nm. Such smaller size cavities are not detectable using a conventional optical microscope (OM), therefore, most of the study of creep cavities using OM is limited to later stages of cavity damage. Creep cavities in the size range of ~20 nm have been reported [69] to be measured using Scanning electron microscope (SEM) and those as small as ~3 nm is reported [70] to be measured using Transmission electron microscope (TEM). Apart from the destructive microscope based techniques, non-destructive measurements such as small angle neutron scattering (SANS) and density measurements are also employed in measuring creep cavities in metals. SANS is capable of measuring creep cavities as small as of <10 nm diameter, although the works reported in the literature, measuring cavities in metals using SANS are very limited. Page et al. [71] first reported such measurements of the size and volume distribution of cavities in a fatigue deformed specimen. Following that work, similar measurements of creep cavities are reported in creep deformed 304 stainless steel specimens [72-74], in reheat crack specimen of type 316H stainless steel [75, 76] and in recent times in type 316H stainless steel weld and creep cavity growth specimens. [77, 78].

2.4 Back stress

Back stress can be termed as a stress generated internally in a material upon application of an external load, which opposes the external load. In the literature, various other terms have been used, sometimes interchangeably, to describe the concept of back stress, such as internal stress [18], threshold stress [79] , friction stress[80], residual stress [81] and long range internal stress [54].

The existence of back stress can be observed from various deformation phenomenon, for example, anelasticity and the Bauschinger effect during creep and cyclic deformation of metal respectively. An example where the influence of back stress is observed is illustrated in Figure 2-11. A stainless steel specimen was deformed in creep at high temperature under an applied stress. When the specimen was unloaded after being crept for a period of time, a portion of the permanent creep strain was found to recover with time, this phenomenon is known as anelasticity. This anelastic recovery of strain suggests that a stress was generated

within the material during the forward creep deformation which pushes the deformation back, as evident by the recovery of strain when the external load is withdrawn.

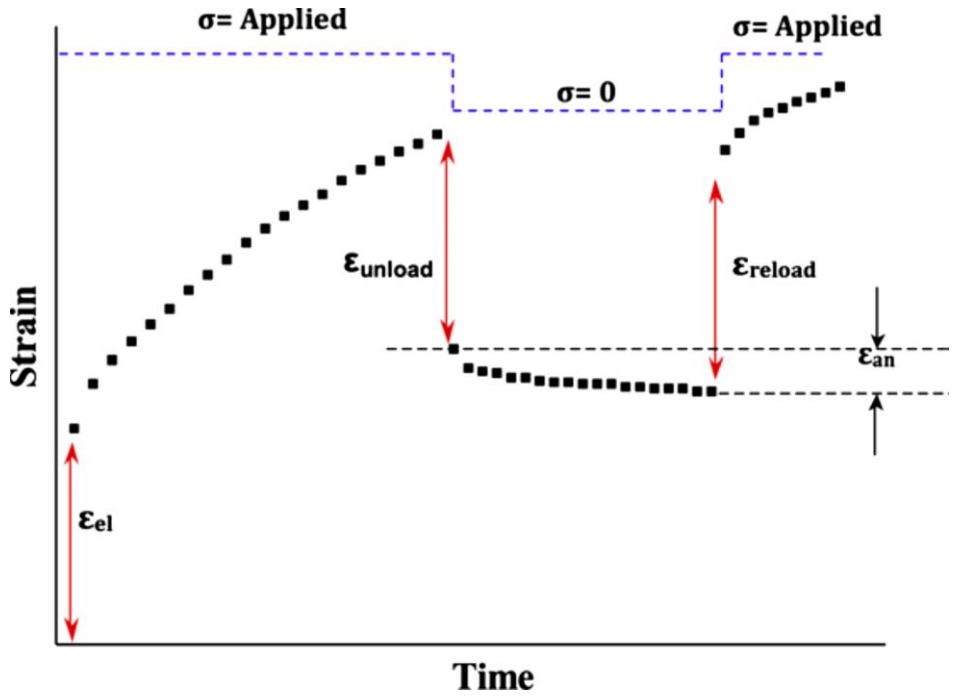

Figure 2-11 Schematic illustrating the observation of back stress during anelastic recovery of creep strain [81]

Another example where the influence of back stress can be observed is the widely known Bauschinger effect in metals. The effect was first described by Bauschinger [82] in 1886. Bauschinger effect can be described as the lowering of yield stress in compression during a tension-compression cyclic loading, if the specimen is loaded in tension first and vice versa. Figure 2-12 shows a schematic illustrating the Bauschinger effect. The specimen is first loaded in tension from point A and starts deforming plastically approaching point B. If the specimen's load is reversed, there will be an elastic unload to the zero stress (point F) followed by compressive deformation as shown by locus C-F-G, where the yield stress in compression is at point G. If no prior tensile load was applied, the material would deform in compression at a similar magnitude to that of tensile deformation as shown by the dotted line from point A to E and therefore the yield stress would be at point H. However, due to prior tensile loading, the material has yield at a stress lower than the monotonic yield stress of the material in compression. Therefore, the material's yield in the reverse cycle is assisted by a stress which is generated during the tensile deformation that is a generation of a stress acting opposite to the direction of the applied stress.

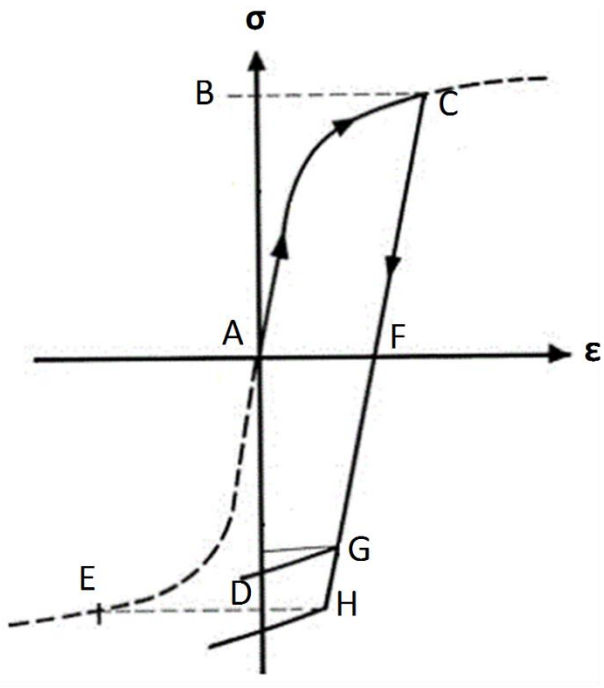

Figure 2-12 Schematic illustrating the Bauschinger effect in metals

2.4.1 Origin of back stress

The back stress originates from the inhomogeneity of deformation at different length scales within the material. Contributors to the back stress can be classified according to the area over which they self-equilibrate, similar to that of the residual stress classification [83]. Stress equilibrating over a number of grains is known as intergranular stress and stress equilibrating within a grain is known as intragranular stress.

2.4.1.1 Intergranular stress

Intergranular (IR) stress originates from elastic-plastic anisotropic deformation. Deformation in single and polycrystals has been described above in 2.3.1 and 2.3.4 respectively and it is clear that elastic and plastic deformation in Type 316H stainless steel is highly anisotropic. Due to this, upon application of a load, differently oriented grains deform differently. This inhomogeneity of deformation further increases, when the applied stress is increased further such as to cause slip in grains, as some grains are oriented more favourably for slip than others. These heterogeneities in deformation of the grains create an internal pull and push between the grains, which is termed intergranular stress.

An example of the generation of intergranular strain is illustrated in Figure 2-13. The figure shows the result of a tensile test of type 316H stainless steel carried out at 650 °C where the development of volume averaged elastic lattice strains in different grain families were measured in-situ by neutron diffraction. With the diffraction technique, an average deformation can be measured in the set of grains having similar crystallographic orientation, which are often termed a grain family. As the load increases, differently oriented grain family starts to deform differently. For example, in the macroscopic elastic zone of the material, at the same applied stress, the {200} grain family has more lattice strain than the {220} grain family. The discrepancies in the deformation increase further when the material starts to deform plastically at the macroscopic scale. Some grain families start to deform plastically while others are still deforming elastically. The onset of plastic deformation cannot be measured with neutron diffraction directly, however, it can be assumed that a grain family started deforming plastically when the elastic lattice strains of that grain family stopped increasing with increasing load. For example, in Figure 2-13 for the {220} grain family, the elastic lattice strain stopped increasing with increasing load at ~100 MPa, implying that those grains are deforming plastically. At the same applied stress, the other two grain families, that is the {200} and the {311} grain family, are still deforming elastically. As a result of these incompatible strains in the neighbouring grains, internal pull and push forces are generated between the grains, which create the intergranular stress.

An average measure of this intergranular strain in each grain family can be taken from the deviation of the elastic lattice strains from the ideal linear elastic lattice strain line [14]. The ideal linear elastic lines are based on the diffraction elastic constants (DEC) that is the elastic modulus of an individual grain family within a polycrystalline aggregate. Thus it is seen that significant IR strains develop in the {220} and {200} grain families whereas the {311} grain family behaves elastically for the macroscopic stress range applied. Another way to measure the intergranular strain at the point of loading is to elastically unload the macroscopic material and measure the residual strain in each crystallographic grain family. In Figure 2-13, such elastic unloading of the grain families is shown with the dotted line. It can be observed that, after unloading, the {200} grain family possess tensile residual strain, the {220} grain family possess compressive residual strain and the {311} grain family possess almost negligible residual strain.

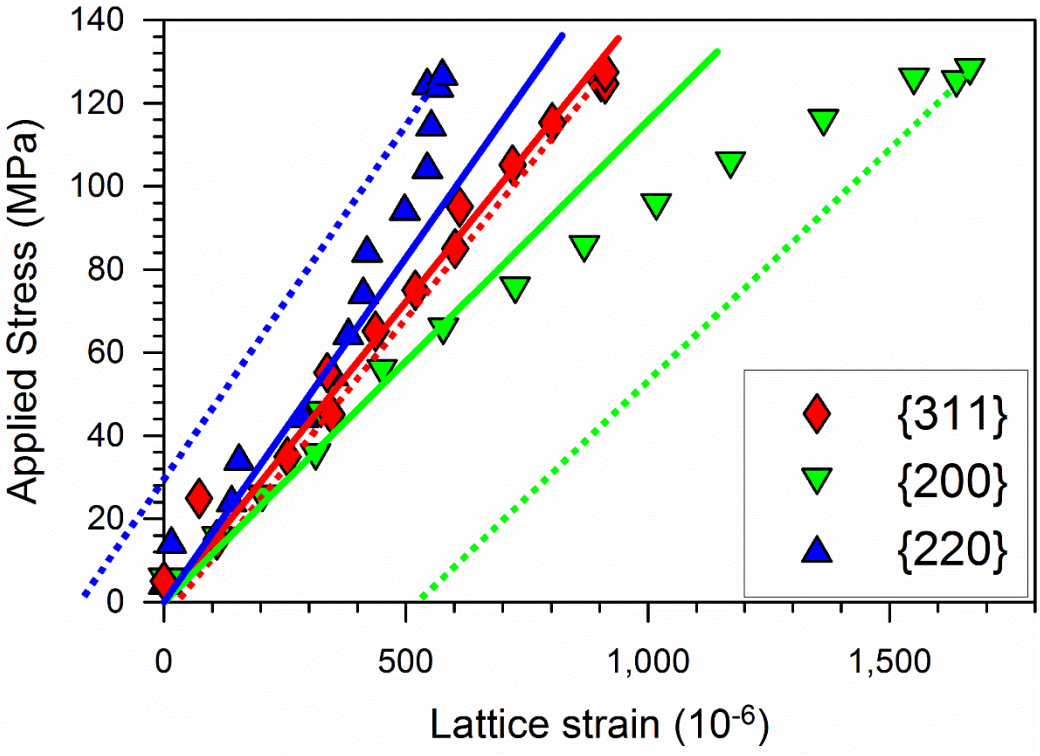

Figure 2-13 Tensile test of 316H stainless steel at 650° C shows origin of intergranular stress due to inhomogeneities of deformation of variously oriented grains. The graph is plotted using experimental results of this project, described in details later in section 4.3.

2.4.1.2 Intragranular stress

Intragranular stresses are generated in the material due to inhomogeneity of deformation within a grain. The concept can be explained with the heterogeneous dislocation sub-structure model proposed by Mughrabi [31, 84]. The schematic of the model is shown in Figure 2-15. The model is based on the formation of a dislocation cell type sub-structure in the grain, Figure 2-14 shows an example of such a cell structure formation. In Figure 2-14 (a), a random distribution of the dislocations can be observed, which after deformation transformed into a cell type structure, as shown inFigure 2-14 (b), where the walls of the cells have a higher dislocation density compared to the interior of the cells, implying, the wall of the cells is harder compared to the interior of the cells.

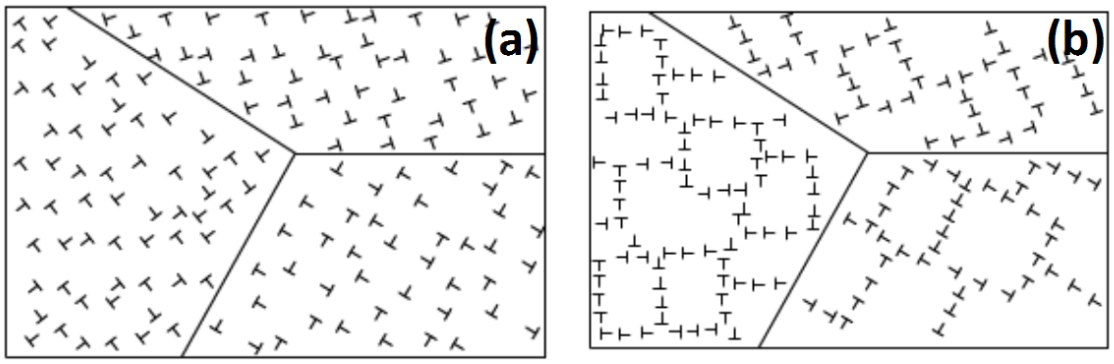

Figure 2-14 (a) Random distribution of dislocations within the grains (b) systematic arrangement of dislocations by formation of cell type dislocation sub-structure upon deformation [85]

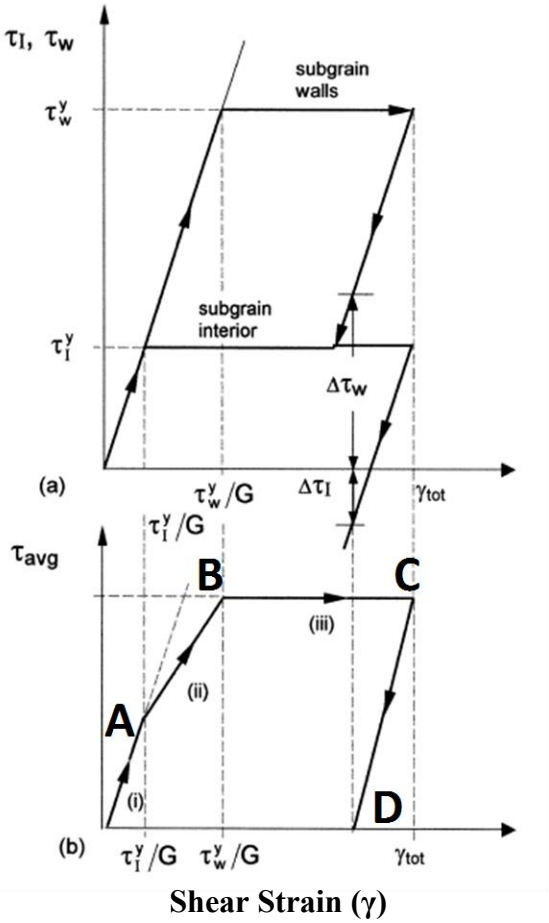

Figure 2-15 Mughrabi's [31] model of inhomogeneous deformation in grains show (a) deformation of sub-grain walls and sub-grain interior and (b) deformation in the corresponding total grain

In Mughrabi's model, for a simplistic explanation, it is assumed that both the cell wall and the cell interior are elastic-perfectly-plastic. If a load is applied to the grain, the interior of the grain being softer will start to deform plastically while the deformation in the cell wall

is still elastic (point A of Figure 2-15). With increasing load, the harder cell wall also starts deforming plastically at point B. If the grain is unloaded at point C, the cell wall and cell interior will unload elastically. Therefore, at point D, with macroscopic load reaching to zero, the harder cell wall will be in tension driving the softer cell interior into compression. This leads to the generation of internal pull and push within the grains, which creates the intragranular stress in the material.

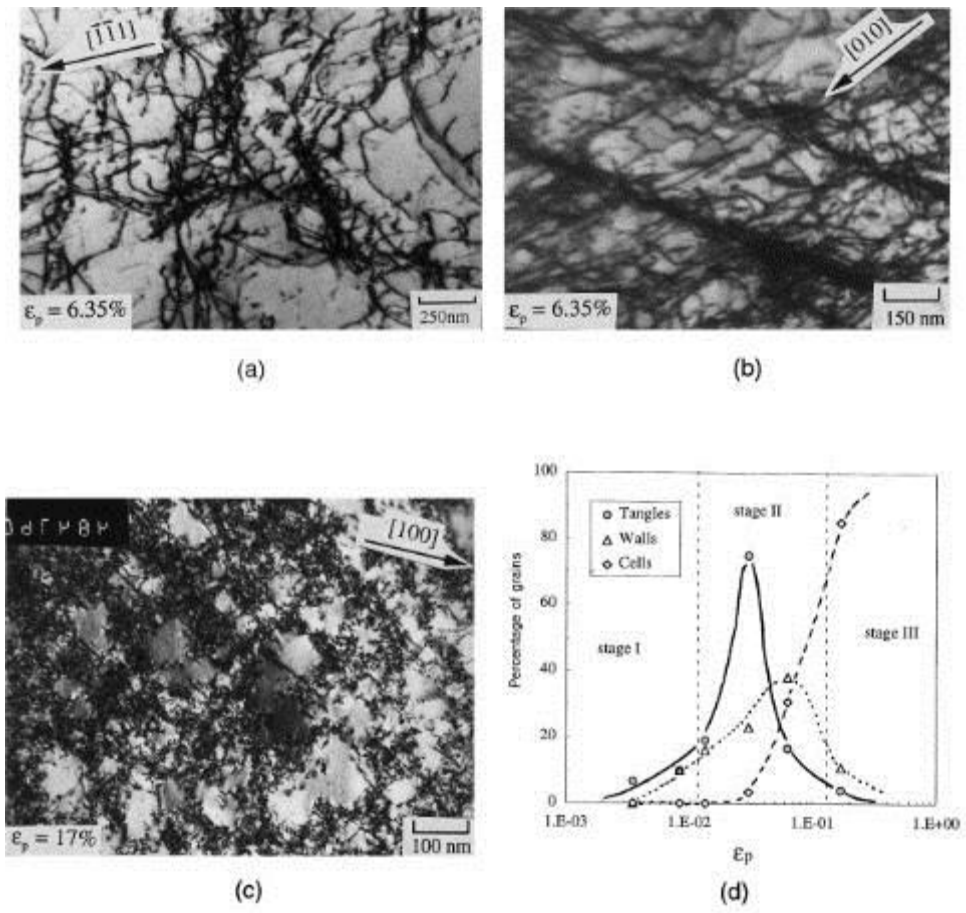

Figure 2-16 Formation of heterogeneous dislocation substructure in 316L during uniaxial tensile test at 300K; (a) dislocation tangles (b) walls (c) cells (d) formation of these structures as a function of plastic strain [6]

In a low SFE material like Type 316H austenitic stainless steel, the formation of dislocation cell type structures does not occur readily, particularly at the low plastic strain. Feaugas [6] conducted a uniaxial tensile test of AISI type 316L stainless steel at 300 K, and observed the formation of various heterogeneous dislocation structures in the material as a function of plastic strain, as reported in Figure 2-16. Formation of cell type structures in a significant percentage of grains can only be noticed after 3% of plastic strain. Other heterogeneous

distributions of dislocations that contribute to the intragranular stresses are dislocation pile-ups, stacking faults, Lomer Cottrell locks and hexagonal dislocation networks [6].

2.5 Back stress and the Bauschinger effect

A number of investigations have been conducted in both single and polycrystals of various materials to unfold the mechanisms of the Bauschinger effect, however, the number of models or theories that have been developed to explain the Bauschinger effect is almost equal to the number of investigations [86]. Different mechanisms controlling the Bauschinger effect may prevail in different materials, depending upon the microstructure, texture, dislocation structure etc., however, a macroscopically similar Bauschinger effect has been observed in a number of different metals [87] [88] and therefore it is possible to bind the mechanisms of the Bauschinger effect in metals within a general framework.

Theories of the Bauschinger effect can be divided into two overarching groups; the continuum theories and the microstructure based theories. Continuum theories describe the Bauschinger effect in terms of back stresses, generated due to inhomogeneous deformation in the material while microstructure based theories describe it in terms of interactions of dislocations in the material's microstructure. In 1914 Heyn [89] explained the concept of generation of macroscopic internal stresses due to inhomogeneous deformation in the material such as by unequal cooling or heating, swelling, phase transformations. Later, the inherent mechanisms of internal stress generation in the polycrystalline material were investigated by Wood et al. [90] using X-ray diffraction. They observed internal stress generation due to elastic and plastic anisotropy of the grains and termed them intergranular stress. Constitutive models [16] [91] have also been developed to explain the kinematic hardening in metals based on this concept of internal stress generation in metals.

Sachs and Shoji [92] demonstrated the existence of the Bauschinger effect in single crystals and therefore, microstructure based theories of the Bauschinger effect were necessary. Orowan [93] proposed one of the most widely accepted mechanisms of the Bauschinger effect, where he discarded the idea of internal stress and described the Bauschinger effect as the easier reverse movement of dislocations during load reversal. As explained in 2.3.3, in solid solution strengthened alloys, mobile dislocations encounter increasingly effective obstacles with increasing plastic strain. Therefore, when a metal is plastically deformed, the

dislocations have to overcome more effective obstacles on further forward deformation compared to an undeformed metal. On the other hand, if the metal is deformed in the reverse direction, the dislocations have to encounter the obstacles which they have already surmounted. Therefore, the elastic limit increases in the forward loading direction and decreases in the reverse loading direction. Sleeswyk et al. [94] added to this theory by studying the hardening behaviour of various metals during room temperature cyclic loading. Their study shows, hardening behaviour during cycling loading can be predicted by subtracting an amount of reversible strain associated with each reversal from that of monotonic loading in these materials. Therefore, they concluded, lowering of elastic limit due to reverse loading is a manifestation of the easy reverse movement of the dislocations. In continuum theories, observation of the Bauschinger effect in single crystals can be explained by transferring the idea of inhomogeneous deformation of material to inhomogeneous deformation of crystals, for example, due to the formation of dislocation pile-ups, tangles and cell type structures. As described in Section 2.4.1.2, such types of dislocation structures generate intragranular back stresses.

It is well evidenced that formation of cell type structures induces internal stress in the material [95-97], and a number of investigations have been conducted correlating the effect of such stresses with the Bauschinger effect [31, 98-100]. Moreover, a large number of semi-phenomenological theories [98, 100-109] have described the correlation between the changes in dislocation structures during reverse loading and the material's hardening behaviour. These models postulate formation of dislocation structures, and dissolution of the structures during reverse loading as the primary cause of the Bauschinger effect in metals. To give a few examples, Hasegawa et al. [108] conducted stress reversal tests with polycrystalline aluminium and observed, at the start of the stress reversal, that the dislocation density reduced significantly and the dislocation cell walls dissolute. Therefore, they postulated, for metals in which dislocation cell structures are formed during pre-straining, the Bauschinger effect originated from the changes in dislocation structures and not from intergranular internal stresses. A similar observation of changes in dislocation sub-structure during reverse loading, was also made by Kocks et al. [109] where they concluded that the polarity of the cell walls may cause the Bauschinger effect in the material.

Such theories of dislocation cell type structures to explain the Bauschinger effect in polycrystalline materials have been contradicted by other works. Experimental findings by

Kassner et. el [110] show that the Bauschinger effect in steel does not show any significant difference with the formation of dislocation sub structures compared with random dislocation distribution. In other experiments, Kassner et al. [111] have also shown that a significant Bauschinger effect can be observed at very low plastic strain in Al single crystals when the formation of a dislocation substructure is not expected. Therefore, they concluded that there is no obvious evidence for internal back stresses generated from the dislocation sub-structure assisting plastic deformation on the reversal of the stress [112]. They have reasoned that the Bauschinger effect in this material is a combination of the unbowing of dislocations and easy reverse movement of the dislocations.

Vincze et al. [113] have conducted reverse loading test with an aluminium alloy and a low carbon steel. Pre-straining the Al sample created a dislocation cell type structure while the dislocation distribution in the steel sample was homogeneous even after pre-straining. However, they observed similar stagnation of hardening upon reversal of load, concluding that, the evolution of a cell structure or dislocation cell disintegrations during load reversal are not responsible for the hardening transient and are merely correlated with the reverse loading. Rauch [114] conducted a tension-compression reverse experiment with two mild steel samples, one with a cell structure and the other one without. Although he found a significant difference in load during reverse loading of these two samples, he attributed the variation to the differences in the dislocation densities rather than the cell type structure formation, concluding that structural changes of dislocations during reverse loading are not responsible for causing the Bauschinger effect in the material. In another experiment with low carbon steel and aluminium alloys Rauch et al. [102] reported similar findings and again related the stagnation of hardening during reverse-loading to the dislocation density rather to their distribution.

Therefore, in light of the recent publications, it can be stated that dislocation cell type structures and those that change during the loading path change have no unique relationship with the observed Bauschinger effect and thus cannot be a primary mechanism for the Bauschinger effect in polycrystalline material.

Abel et al. [115] reviewed various theories proposed to explain the Bauschinger effect and compared the internal stress theories with the dislocation based theories by performing reverse loading experiments using low carbon steel samples. He concluded that the back stress is not a significant contributor to the Bauschinger effect in this material, as the creation

of mobile dislocations can solely explain the effect. However, there is no contradiction that both intergranular stress and dislocations exhibiting directionality in their resistance to further motion acquired as a result of pre-strain, can combine to contribute to the back stress of the material.

Although the role of intergranular stresses in the Bauschinger effect has been known for a long time, very limited quantitative works have been reported on this topic so far, mainly, due to difficulties in quantitatively measuring the intergranular stresses in the bulk of the material. With the advent of in-situ experimental capabilities at a number of neutron diffraction engineering instruments, it's now possible to measure the evolution of intergranular stresses as a function of applied load and strain path. Using these facilities, the generation and evolution of intergranular stresses have been studied in a number of materials and the results used to validate polycrystalline plasticity models, however, most of these studies are limited to uniaxial tension and compression only [116]. The limited number of studies conducted incorporating in situ neutron diffraction to investigate hardening of polycrystalline material during strain path changes are reviewed below.

James et al. [117] conducted room temperature cyclic tests of type 316L austenitic steel using in situ neutron diffraction and compared the experimentally measured intergranular stresses in various grain families with the prediction of EPSC models with and without taking the intragranular component of back stress into account. Their model shows an improved prediction of intergranular stresses when the intragranular component is taken into account, implying the combined role of intergranular and intragranular stresses in the Bauschinger effect of this material. Chen et al. [118] conducted room temperature forward and reverse loading tensile tests with a high-temperature pre-strained specimen of type 316H austenitic steel using in situ neutron diffraction. They reported a decrease of measured intergranular stresses with the diminishing transient softening of the material implying that kinematic hardening of this material originated from the misfit stresses (intergranular stresses) between the grains. Saleh et al. [119] conducted a Bauschinger test of twinning induced plasticity (TWIP) steel using in-situ neutron diffraction. From the experimental findings, they postulated the Bauschinger effect in this material is due to a combined effect of intergranular stresses and intragranular stresses originating from microstructure based mechanisms such as pile ups of dislocations.

Highlights

1. In literature, a number of mechanisms explaining the Bauschinger effect have been identified, however, the relative contribution of these mechanisms to the Bauschinger effect is still debatable.
2. The widely accepted and agreed primary source of the Bauschinger effect is the easy reversibility of dislocations upon reversal of load and it is generally accepted that a large part of the Bauschinger effect comes from dislocation behaviour within grains, and not from intergranular stresses.
3. There is a live debate in the literature about the contribution of the cell type dislocation sub-structure and changes during reloading to the Bauschinger effect. Recent literature suggests that correlations between dislocation cell structures and the Bauschinger effect are not unique.
4. Early theoretical explanations suggest that intergranular stress contributes to the Bauschinger effect, however, limited experimental works have been conducted in quantifying the evolution of intergranular stresses during Bauschinger tests and how they contribute to the phenomenon.

2.6 Back stress and creep deformation

Back stress in Type 316H stainless steel can arise from a number of sources at different length scales during creep deformation. It is difficult to experimentally quantify the magnitude of internal/back stress originated from inhomogeneity of deformation at the microscopic scale. An alternative approach is to measure the macroscopic back stress from the change of creep deformation rate after a reduction of applied load and then theoretically establish a correlation between the rate change and the observed microstructural changes. These type of tests are known as stress dip test or load reduction tests and were originally proposed by Mitra et al. [120] and Davies et al. [121] and later applied to many different metals and alloys. These tests are conducted by simply reducing the applied stress during a creep test and observing the corresponding change of creep strain rate and changes in the dislocation microstructure at a lower stress/unloaded state.

In early experiments, one common observation of the dip tests was that upon reduction of the stress, for a period of time, the creep deformation rate remains zero. Based on this

observation, Mitra and Mclean [120] proposed a model which explains back stress during creep in terms of formation of a three-dimensional dislocation network. The links of this network bow when an external load is applied and unbow when the load is removed, due to dislocation line tension. This dislocation line tension can cause the links to bow in the opposite direction and contribute to the backward strain observed in the macroscopic material. In this model, it is assumed that the effective stress is negligible compared to applied stress. Later, Dip tests by Gibbs [122] and Ahlquist and Nix [123] showed that, there is actually a critical magnitude of the stress reduction and the creep rate immediately after the stress reduction could be zero, positive or negative if the stress reduction is equal, less or more respectively than this critical value. The observation of positive creep rate after stress reduction implies that the effective stress for dislocation glide during steady state deformation is a measurable fraction of the applied stress and must not be neglected [124], therefore, the dislocation network theory's assumption is not valid.

In explaining the origin of back stress during creep deformation, first, 'particles' generated during the creep process were reported to be the primary source of back stress. The stress exponent in power law creep was found to be much higher in determining the creep rate of solution strengthened material compared to pure metals. Therefore the particles were considered to inhibit the recovery process and thus to reduce the creep rate [125]. The model calculates the secondary creep rate of the solution strengthened metal using a modified power creep law, $\dot{\epsilon}_s = A(\sigma - \sigma_i)^n \exp - \left(\frac{Q_C}{RT}\right)$, in which σ_i is the internal stress. An average value of internal stress has been used in this model and the dislocations are represented with an average velocity and density. However, neither dislocation structure can be represented solely by an average density [126] nor the velocity of dislocation by an average. Morris [127] reported these drawbacks and proposed, as the majority of dislocations are immobile at any given time, therefore, that creep back stress mainly originates from the unbowing of bowed dislocations when the load is reduced or taken off. He has shown experimentally that the creep rate in type 316H stainless steel can be estimated by measuring the dislocation link lengths. One assumption of this model is that the total applied stress operates on the dislocation links and that only those links greater than a stress dependant critical value are capable of becoming mobile.

Nix et al. [5] studied the anelastic recovery of Al single crystal and observed the magnitude of anelastic strain recovery to be much larger than the elastic strain in the material. Such

magnitude of anelastic strain cannot be explained by simple models of dislocation unbowing, which invariably predict recoverable strains about equal to the elastic strain. Moreover, the anelastic recovery was much slower than the unbowing process of dislocations. He rather postulated that the heterogeneous dislocation sub structure formed during primary creep is the primary source of creep back stress. Due to inhomogeneous stress-state, upon removal of the load, the dislocations tend to move back from cell walls to the cell interior, causing anelasticity. Experimental observations of Hasegawa et al. [128] supported this theory, in which they measured anelastic strain recovery of a Cu-Al alloy upon unloading during both primary and secondary creep. This particular alloy exhibits sigmoidal creep characteristics, which means, during primary creep the dislocation density of this material is low and distribution is homogeneous. Upon reaching to secondary creep, the dislocation density increases rapidly and forms dislocation sub-grain type structures. The measurements showed that anelastic recovery during primary creep was much lower compared to secondary creep. Creep strain recovery has also been attributed to the migration of the boundaries of these dislocation cell type structures [129] and [130] and dislocation cross-slips [131].

Among other notable explanations of creep back stress, Gibbons et al. [132] described the anelasticity in Ni-Cr alloy in terms of viscous bowing and unbowing of dislocations with help of the unzipping of the dislocation networks. Lupnic and Gabrielli [133] observed an instantaneous recovery followed by a slow recovery of plastic strain during stress drop tests of IN597 alloy. They postulated two separate mechanisms of anelasticity taking place in this material, matrix glide and jog generation. Bueno [134] postulated two stage recovery mechanism. The first stage is the quick unbowing of the bowed dislocations and in the second stage, the material trying to reach to an equilibrium state.

In more recent publications, the role of intergranular stresses has been discussed on the anelastic recovery of creep in type 316H stainless steel. Rao et al. [81] have conducted in-situ neutron diffraction creep tests in which they observed, time-dependent changes of the intergranular stresses in various grain families, during anelastic recovery of strain upon unloading after creep. They argued that dislocation type sub-structures are not expected to form at the temperature and loading conditions (under 180 MPa at 650°C) at which they conducted the tests, and therefore anelasticity in type 316H stainless steel under these conditions probably originates from the relaxation of intergranular stresses. Chen et al. [135-138] studied the evolution of intergranular stresses during creep deformation of type 316H

stainless steel. They reported [136] the magnitude of intergranular stresses to be a function of the total inelastic (creep + plastic) strain in the material. However, in a later publication [137] concluded contradictorily, that intergranular stresses in various grain families do not change during steady-state creep deformation of this material.

Highlights

1. In the literature, generation of back stress during creep is largely described in terms of dislocation structures and how those interact with the microstructure of the material.
2. Recent publications indicate that intergranular stress may play a significant role in generating back stress during creep deformation and could be more significant than the intragranular stresses in particular loading conditions.
3. There hasn't been any work reported on quantifying the effect of intergranular stresses on creep deformation rate and its influence on creep life.

2.7 Intergranular stress and neutron diffraction

The origin of internal stress due to the elastic and plastic anisotropy of grains (intergranular stress) were reported as early as in 1914 by Heyn [89]. The first experiments reported to confirm the existence of intergranular stress were conducted using X-ray diffraction by Greenough [139] and Wood et al. [90]. In their experiments, they investigated the generation of intergranular stress in a number of metals and observed correlation between the magnitudes of intergranular stresses and pre-strain in the material. One major limitation of studying intergranular stresses using X-rays is its limited depth of penetration in metals. With the advent of neutron diffraction having larger penetration depth, the study of intergranular stresses in metals has progressed quickly. The capability of neutron diffraction to measure intergranular strains was reported by Allen et al. [140, 141] with an example of measurement in a plastically bent mild steel bar.

Generation of intergranular strains during in-situ tensile loading in aluminium [142] and steel alloy [143] has been studied by Pang et al. In both studies, the specimen was loaded in tension under strain control while neutron diffraction measurements were recorded by stopping at the peak tension strain. Between each strain increment, the specimen was

unloaded and the residual strain of various grain families at the unloaded state was measured. Aluminium has a low degree of elastic anisotropy, therefore, when deformation in the aluminium sample was fully elastic, no intergranular strains were found to generate. Significant intergranular strains were generated when the macroscopic loading exceeded the yield limit of the material. The important conclusion of the study was, if not taken into account, intergranular stress can introduce significant error in the measurement of the residual stress using diffraction techniques. Measurements from the grain family least affected by the intergranular strain or a texture weighted volume average of all the grain families can be considered for avoiding such error in residual stress measurement. In this study, they also tested the validity of the elastic plastic self-consistent model developed by Turner and Tome [144] against the experimental results and found only qualitative agreement. In a similar in-situ neutron diffraction tensile test using 309H stainless steel, they observed that the increment of intergranular strains was large only in case of the first load-unload cycle and after which it gradually reduces during subsequent loading. With the increase of applied stress, slip systems of the grains which are non-favourably oriented for slip to occur also get activated, therefore, plastic deformation is initiated in a greater number of grains. As a result, the discrepancies of strain between elastically and plastically deformed grains reduce, which eventually reduces the increment of intergranular strain. They also compared the results of the experiment with EPSC predictions and found good agreement only up to the elastic loading of the material. One limitation of the model was the use of linear hardening for the slip system, which assumes the critical resolved shear stress of a slip system increases with the rate of plastic deformation increase. This was addressed by Clausen et al. for aluminium [145] and steel [146] and by Pang et al. for aluminium alloy [142] in which they incorporated non-linear hardening for the slip system. Clausen et al. [40] have studied the generation of intergranular stresses in a number of FCC polycrystalline materials including stainless steel, copper and aluminium, during uniaxial tensile loading using in-situ neutron diffraction and EPSC modelling.

Generation of intergranular strain during cyclic loading of polycrystalline material has also been studied using in situ neutron diffraction. In one study [147], a stainless steel sample was cyclically loaded between fixed strain limits of ±0.4% for eight successive cycles. Near linear elastic deformation of the (111) reflection and non-linear plastic deformation of the (200) reflection with respect to the loading axis was observed. The authors also reported an increase of anisotropic strain in the material with repeated cycling. The evolution of

intergranular strains during fatigue deformation of type 316 stainless steel was studied by Korsunsky et al. [148] and Wang et al. [149] [150] using in situ neutron diffraction. Large intergranular stresses were found to develop after the initial few cycles of loading and then it was observed to gradually decrease when micro-cracks were formed. The intergranular stresses disappeared completely when the sample reached failure in fatigue. Generation of intergranular strains during tensile deformation of type 316H stainless steel was studied by Daymond et al. [151] at a number of elevated temperatures up to 650°C. EPSC modelling showed a good correlation with the experimental data up to 0.4 T_m of the material but the correlation broke down at higher temperatures, implying that a slip based deformation mechanism alone is not sufficient to describe deformation at these temperatures.

Recently, a two level self-consistent model has been reported by Jamal et al. [152] where they showed improvement in prediction when 316L stainless steel grains are considered as a two-phase material with cell walls and cell interiors. Dissolution of dislocation cell structures during reverse loading is also incorporated in the model. A number of crystal plasticity models with neutron diffraction measurements have also been developed, for example, by Gonzalez et al. and Ahmed et al. [153, 154]. These models account for the combined contribution of intergranular and intragranular stresses to yield asymmetries upon strain path changes. Jinan hu et al. [155, 156] developed a three-dimensional multi-scale self-consistent model based on a crystal plasticity approach. The model takes detailed dislocation kinetics into account and thus is useful in understanding the physical process of intergranular stress evolution during plastic deformation.

Highlights

1. Generation and evolution of intergranular stresses during room temperature uniaxial loading in conventional FCC materials has been well studied. Self-consistent and Crystal plasticity models have also been developed which can satisfactorily predict the generation of intergranular stresses during such loading conditions.
2. A limited number of studies of the evolution of intergranular strains during cyclic loading of material have been reported but an understanding of the evolution of intergranular strains, particularly during cyclic loading at elevated temperature is incomplete (which is the main focus of this thesis).

2.8 Summary

Type 316H austenitic stainless steel is widely used in many engineering applications, particularly where high-temperature strength is required. The plastic and creep deformation mechanisms of this material were reviewed in this chapter. The back stress phenomenon and its effect on the deformation behaviour of metals has been known for a long time but an ambiguity exists in the literature about the definition and origin of back stress. Macroscopically, the effect of back stress on material's deformation can be quantified by standard laboratory tests, for example by conducting creep dip tests and Bauschinger type cyclic loading tests for creep and cyclic deformation respectively. In creep tests, the approximate magnitude of back stress can be measured by measuring recovery of anelastic strain or by recording instantaneous changes of creep strain after changing the load. On the other hand, back stress can be measured by measuring the change of yield stress in the material during reverse loading during a tension-compression cyclic test. Back stresses originate from inhomogeneity of deformation at various length scales; that is contributions from grain-scale misfits (intergranular) and sub-grain misfits (intragranular). The ambiguity arises from knowing the relative contributions to the back stress under particular loading conditions.

Intragranular stress originates from the inhomogeneous distribution of dislocations in the materials microstructure. Intragranular stresses are widely studied and often mistakenly referred as the sole source of back stress. In the literature, generation of back stress during creep deformation is largely described in terms of dislocation structures and their interactions with the material microstructure. In the case of cyclic loading, it is widely accepted and agreed that the primary source of the Bauschinger effect is the easy reversibility of dislocations upon reversal of load. Intergranular stresses are generated from the inhomogeneous deformation of grains with different orientations. The generation and evolution of intergranular stresses have been reported for simplistic loading conditions, but not so much for complex tension-compression cyclic loading, particularly at elevated temperatures where creep deformation mechanisms prevail. Moreover, limited work has been published quantifying how intergranular stresses affect the macroscopic deformation of materials at room and elevated temperatures.

Chapter 3 Experimental techniques

3.1 Overview

In this chapter, the experimental techniques used throughout this project are described in detail. Mechanical tests including room and high temperature tensile, cyclic, load-unload and creep tests are described in Section 3.2. Microscopic based techniques such as optical microscopy (OM), scanning electron microscopy (SEM), transmission electron microscopy (TEM) and atomic force microscopy (AFM) are described in Section 3.3. Finally, neutron diffraction and neutron scattering-based techniques are described in Section 3.5. A comparison of the techniques available to measure internal stress at various length scales of material is provided and choice of one particular technique over others is justified.

3.2 Mechanical testing

Mechanical tests were conducted to characterise the stress-strain properties of the material and to introduce various degrees of mechanical deformation for comparative studies. Most of the tests were conducted at the high-temperature laboratory of the Open University (OU). Specialist mechanical tests with in-situ neutron diffraction measurements were conducted using the Engin-X diffractometer at the Rutherford Appleton Laboratory (RAL), as described later in Section 3.6.6.1.

3.2.1 Tensile and cyclic tests

The room temperature mechanical tests were conducted according to the BS EN ISO 6892-1:2009 standard [157] and high-temperature tests were conducted according to the BS EN 10002-5:1992 [158] standard. Two different designs of the specimen were incorporated for mechanical tests; one for the uniaxial tensile and load-unload tests and the other for the

tension-compression cyclic tests. Figure 3-1 shows schematic of designs of these two specimen with dimensions marked up. The diameter to gauge length ratio was increased for the cyclic tests specimen, in order to avoid the occurrence of buckling during tension-compression cyclic loading. The specimens were machined using a wire electric discharge machine (EDM) available in-house.

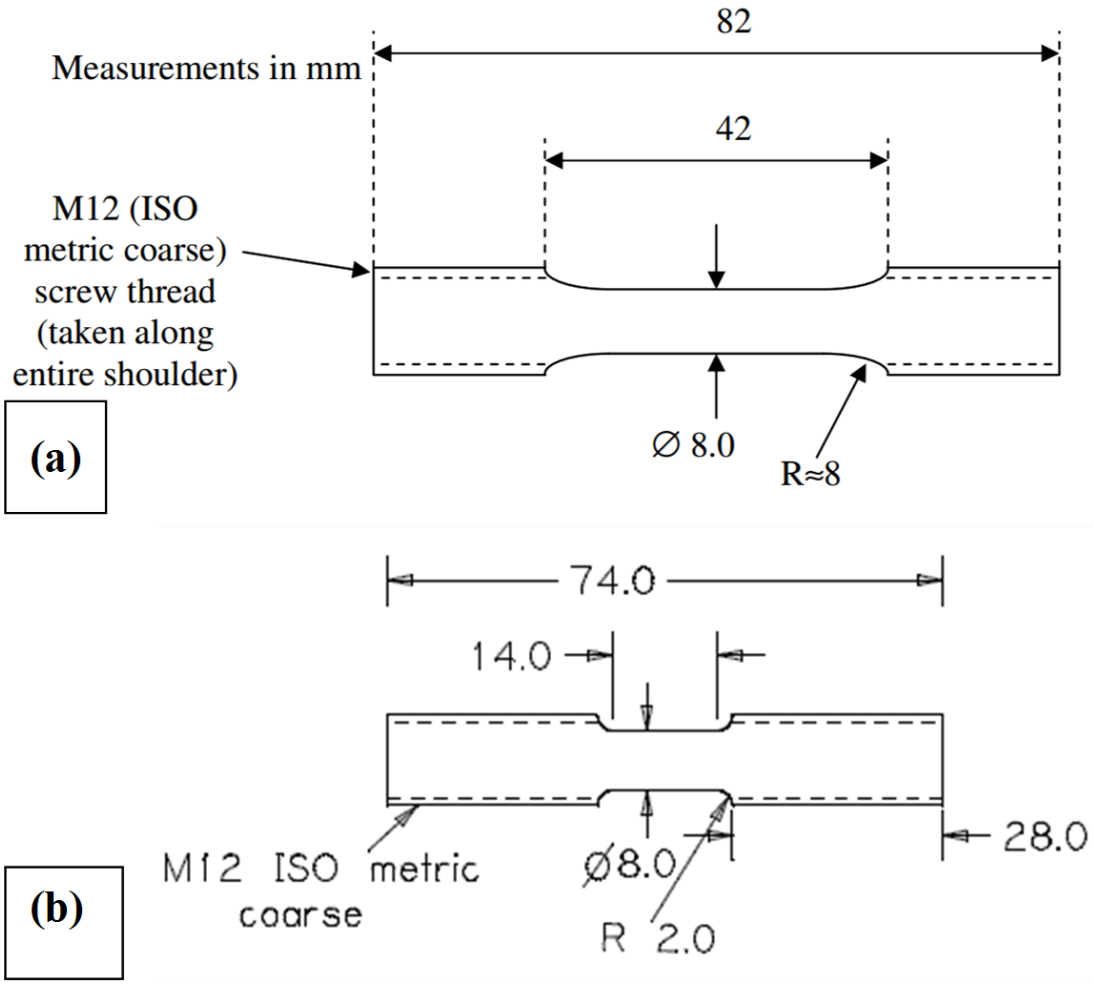

Figure 3-1 Schematic of design showing dimensions of the specimens used for the (a) tension and load-unload tests and (b) tension-compression cyclic tests. All dimensions are in mm.

An Instron 8862 slow strain rate machine was used for conducting the mechanical tests. This is an electricity driven mechanical tester with a maximum load capacity of ±100 KN. The machine consists of a single screw electromechanical actuator, load cell, pull road, external frame and detachable split furnace. The built in Instron Bluehill software was used for machine control, test design and data recording. The machine is capable of conducting tests in load, displacement and strain control.

Two collets and threaded specimen holders were used for clamping the specimens in the upper and lower jaws of the stress rig. An Instron 2632-054 high temperature extensometer was used to measure strain, directly from the gauge length of the specimen. The extensometer has a gauge length of 12.5 mm (this is the distance between the two jaws of the extensometer when the strain is zero) and can measure strain up to 20% in tension and 10% in compression. It can be attached to the specimen with a simple spring and ceramic string combination. The legs of the extensometer (made of either glass or ceramics) have grooves such that they do not slip during the test. The extensometer was calibrated using an Instron extensometer calibrator unit before the start of a test. The calibration was done by attaching the extensometer to the jaws of a micrometre, revolving the micrometre to a known length, and checking the distance read by the extensometer. The attachment of the extensometer and thermocouples to the specimen for a high-temperature test is shown in Figure 3-2.

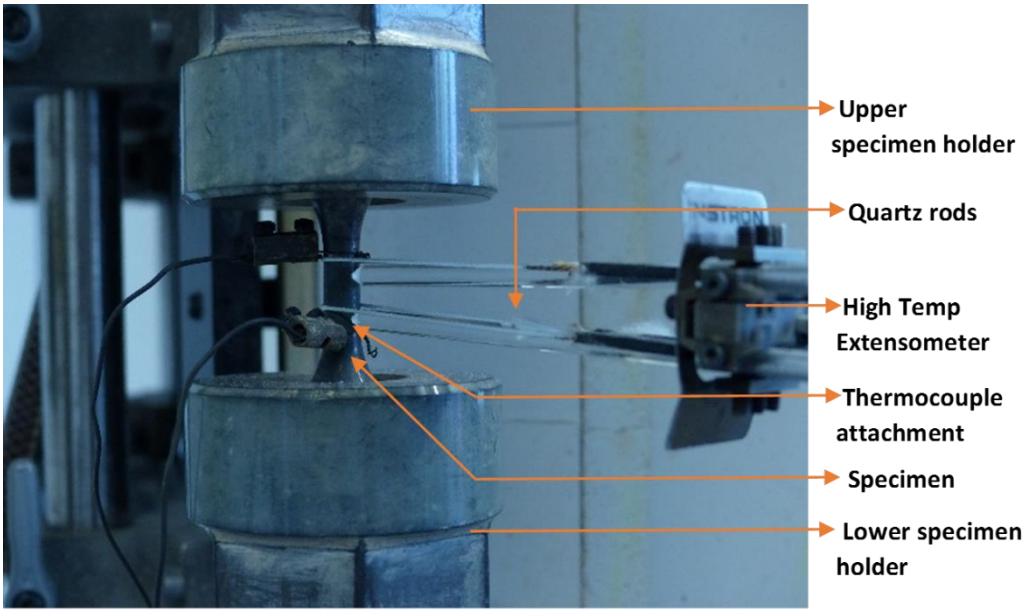

Figure 3-2 Attachment of the thermocouples and the extensometer on the specimen before the start of a high-temperature test

An electric resistance split furnace was used for the high-temperature tests. The furnace is clamped to the stress rig such that its height can be adjusted to place the specimen in the middle section of it. The specimen inside the furnace is heated uniformly by controlling the temperature of the furnace's upper, middle and lower zone separately. A Eurotherm 3216 controller was used to control the temperature of the furnace. A water cooling system

attached to a refrigerator was used for cooling the pull roads of the machine and thus protecting the temperature sensitive parts of the machine (for example the load cell) from overheating. The furnace has a small window on the front side, through which an extensometer can be set to the gauge length of the specimen. An additional small fan was used, placing it close to this window to avoid overheating of the extensometer. The temperature of the specimen was monitored using 2 or 3 N-type thermocouples clamped to the gauge length of the specimen by a combination of a wire and a screw, as shown in Figure 3-2. Before starting a new set of tests, the reliability of the readings of the thermocouples was checked using an Isotech thermocouple calibrator. If the temperature reading from any thermocouple differed by more than ±1° C from the calibrating alumina thermocouple, then it was replaced with new. Before the start of each high-temperature test, the specimens were held at the intended test temperature for 1 hour to allow the temperature to homogenise in the specimen. By fine tuning the temperature of the furnace, it was ensured that the gradient of temperature along the gauge length of the specimen was less than 1°C. The temperature variation during the test was maintained within ±1°C by insulating the open parts of the furnace using ceramic fibre and by maintaining a stable laboratory temperature (air conditioned).

3.3 Microscope analysis

Four different types of microscopes were used in this project. The suitability of a specific microscope depends upon the type of specimen, type of investigation and the scale of the measurements required. In this project, optical (OM) and scanning electron microscopes (SEM) were mainly used to characterise the material and a transmission electron microscope (TEM) was used to study the changes in dislocation structures post-deformation in the material. An atomic force microscope (AFM) was used to characterise the carbides and cavities in creep deformed specimens.

3.3.1 Optical Microscope (OM)

An optical microscope uses rays of light and compound lenses to create an enlarged image of an object. An objective lens is usually used to collect light rays from the object, which focuses inside the microscope. Another lens (or a set of lenses) is then used to generate an enlarged inverted virtual image of this focused image, which can be viewed using the

eyepiece. A Leica DMI 5000M reflected light microscope was used for optical microscope investigations in this project. A Leica DFC280 digital camera and Leica application suite software were used with the microscope to capture and analyse the images respectively. The microstructural images were taken in the bright field (BF) mode. In this mode, the polished specimen surface appears bright and all other irregularities in the surface (for example precipitates, grain boundaries, cavities etc.) appear dark. The microscope has a fitted digital camera that can capture and process the optical images.

3.3.2 Scanning electron microscope (SEM)

An electron microscope uses a beam of electrons for microscopic viewing. The wavelength of the electron beam used is usually much smaller than the wavelength of visible light, allowing the scanning electron microscope (SEM) to image with a much higher magnification than the OM. In SEM, a beam of electrons is generated using an electron gun situated at the top part of the microscope. The electron beam passes through a number of lenses focusing the beam before it reaches the specimen. During operation, the SEM chamber is kept under vacuum so that the beam of electrons is not obstructed by any particles. The focused electron beam scatters from the surface of the specimen and emits 4 different types of electrons as, X-rays, secondary electrons, backscattered electrons and auger electrons. Different detectors can be used to detect different electron signals. Typically, secondary electrons are used for imaging and backscattered electrons are used for crystallographic studies.

A Zeiss Supra 55VP high-resolution SEM was used in this project. This microscope has a wide range of electron volts, although images for this project were usually taken at a fixed electron volt of 5 KeV. The specimen stage of the microscope has a 3-dimensional movement and tilting capability. The microscope is equipped with a dispersive x-ray spectrometer (EDS) and an Electron backscattered diffraction (EBSD) system. EDS can be used for composition analysis and EBSD can be used to study the texture, crystal orientation, phase mapping of materials. EBSD has also been reported to characterise the plastic and creep strain in the material by measuring the changes in the lattice misorientations [159].

3.3.2.1 Specimen preparation for OM and SEM

Specimen preparation undertaken for the OM and SEM imaging was similar except for the final stage; the basic steps include sectioning, mounting, grinding and polishing. A final step of etching was conducted for the OM and a final step of electropolishing was conducted for the SEM and the EBSD investigations. The specimen preparation steps for the OM and SEM are described below briefly.

The specimen was sectioned from undeformed and deformed cylindrical specimens using either a wire EDM machine or a Struers cutting wheel machine. The cut was made radially such that the plane normal to the macroscopic loading direction of the specimen could be observed with the microscope, as shown in Figure 3-3.

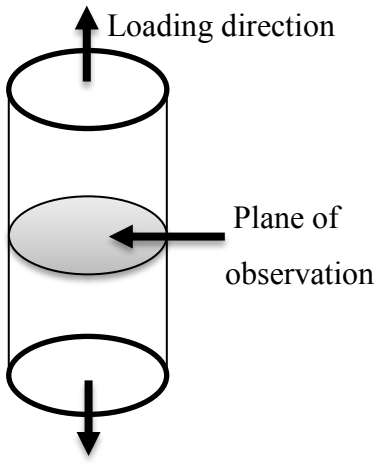

Figure 3-3 Schematic showing the plane of the cylindrical specimen that has been sectioned for the microscopic analysis

Care was taken such that the cutting speed was slow enough not to plastically deform the surface of the sectioned specimen. The specimen was water cooled throughout the cutting process. Following sectioning, samples were hot mounted using a Struers Citopress machine. Phenolic thermosetting resin with a small amount of iron powder was used as the mount. The mount was conductive and as such readily allowed electropolishing of the samples.

The mounted specimens were ground using different grades of SiC papers using a Buehler semi-automatic grinding machine. Twelve mounted specimens can be ground simultaneously using this machine. Water was continuously sprayed on the grinding paper

during the process. The samples were washed and rinsed thoroughly during the change of the grinding papers to avoid any contamination. The grinding was conducted according to Table 3-1. Occasionally, a Struers hand-held grinding machine was used. A Struers Tegraforce-5 automatic polishing machine was used for polishing. Polishing removes the small scratches from the finest grinding stage and thus provides a smooth surface finish reflecting maximum light. Polishing was conducted in 4 steps according to Table 3-2. In between each polishing stage, the specimen was washed in soap, soaked in isopropanol and dried in air.

Table 3-1 Specimen grinding guidelines used in preparation of the specimen for OM and SEM analysis

Grinding paper	**Grit size (µm)**	**Force (N)**	**Time (minutes)**
P120	78	27	3
P240	68	27	3
P500	30	27	3
P800	22	27	3
P1200	15	27	5
P2500	8.5	27	5

Table 3-2 Specimen polishing guidelines used in preparation of the specimen for OM and SEM analysis

Polishing tray	**Diamond particle (µm)**	**Force (N)**	**Time (minutes)**
MD-nap	9	30	20
MD-nap	6	30	20
MD-floc	3	30	20
MD-floc	1	30	20

Etching was the final step in preparation for the OM imaging. Selected chemical etchants reveal the microstructural features in the material by attacking the high energy regions, for

example, grain boundaries and precipitates. A 60% nitric acid solution was used; this particular etchant reveals the grain boundaries of type 316H stainless steel. The etching process was conducted electrolytically using a 2V current for at least 20 seconds.

Electropolishing was the final step of preparation for SEM imaging. Electropolishing removes the thin surface deformed layer introduced by earlier preparation steps (grinding and polishing). A Struers A21 solution, that is a mixture of 2-butoxyethanol, perchloric acid and water with ethanol, was used as the electrolyte during the process. Optimum parameters for the electropolishing process were determined using a trial and error process; a 22V current for 60 seconds was found to give best results for this material.

3.3.3 Transmission electron microscope (TEM)

In the transmission electron microscope (TEM), a beam of electrons is transmitted through the sample and therefore can reveal the internal microstructure (for example dislocation arrays). In this microscope, the beam of electrons is generated from an emission source, such as from a single crystal, using a supply of high voltage electric current. The beam of electrons is focused by passing through different lenses and directed to the sample. As the electron beam transmits through the sample, so the TEM images have very limited depth resolution. Moreover, the specimen under the microscope has to be extremely thin in order for electrons to transmit through it.

A JEOL JEM 2100 microscope was used in this project for the TEM investigations. The microscope has a maximum magnification of >1000000 X. The imaging for this project was conducted using an accelerating voltage of 200 KV, in the Bright field (BF) mode. In this mode, the contrast in the image is formed by the absorption of the electrons in the specimen where thick areas appear dark and thin appear bright.

In TEM imaging, microstructural features in the direction of the beam may overlap each other which may hide important information. To overcome this, a double tilt specimen holder was used in this project and imaging was conducted by tilting the specimen at various angles. Due to the small volume of the specimen that could be investigated in the TEM, at least 4 specimens for each condition were investigated to improve the statistical significance of the observations.

3.3.3.1 Specimen preparation for TEM

Foil specimens of ~100 μm thickness were prepared for TEM imaging. A thin foil of about 300 μm thickness was first sectioned from the cylindrical specimen using a Struers cutting machine. It was not possible to section the specimen any thinner without introducing significant bending in the foil. The section was cut radially off the cylindrical specimen as indicated in Figure 3-3. The disc grinder shown in Figure 3-4 was used to reduce the thickness. The foil was mounted on the grinder using a specialised glue which melts at high temperature. Grinding was conducted in three steps using three different grit size papers. The process was continued until the foil's thickness was reduced to 100-150 μm. Thereafter, smaller diameter discs were punched out of the bigger diameter foil using a puncher. The diameter of the punched out discs was ~3 mm.

A metal thinner was used to further reduce the thickness of the discs by electropolishing. The discs were inserted in a specimen holder, interior of which is made of platinum. The holder with a disc inside it was submerged in a solution of 5% perchloric acid in methanol. The holder has a small hole in the middle section of it by which the foil can come in contact with the solution. The temperature of the solution was brought down to -60° C by pouring liquid nitrogen into the system. The temperature was monitored using a thermometer and maintained throughout the electropolishing process by a continuous supply of liquid nitrogen. Reaching the desired temperature, a 20V electric current was supplied to thin the foil down. During the thinning process, a small hole in the middle of the sample was created. A photo detector with variable sensitivity was used as a sensor to monitor the creation of the hole in the specimen. As soon as the hole in the foil is created, the sensor detects light passing through the hole and automatically turns off the thinning process. As a final step, the specimen was cleaned thoroughly using methanol. This was to ensure that no perchloric acid remained on the specimen.

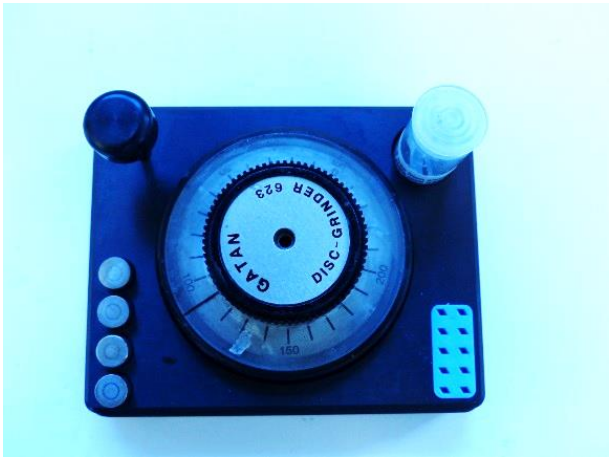

Figure 3-4 The disc grinder used to reduce the thickness of the foil by gradual grinding for TEM analysis

3.3.4 Atomic Force Microscope (AFM)

An AFM [160] uses detection of forces between a probe and the specimen surface to obtain a 3D profile of the surface. A cantilever with a very sharp tip is used for scanning. The cantilever deflects towards the surface as it's brought close to the surface due to the attractive force between the surface and the tip; it deflects away as it is brought even closer to the surface due to the repulsive forces. These deflections are recorded by a laser beam reflected from the flat top of the cantilever beam with a suitable detection system, such as a position-sensitive photo diode. The changes in the deflection provide a 3D map of the topology of the surface. A feedback loop is generally used to maintain the height of the cantilever just above the surface.

In the present work, a specialist High-Speed Atomic Force Microscope (HS-AFM) was used for characterising cavities and carbides in creep deformed specimens. The HS-AFM was developed in-house at the University of Bristol; details of the development can be found in [161]. The microscope is capable of imaging areas of square millimetres in the order of hours of time, thus improving the time limitations of traditional AFM for macro-scale imaging [162]. Figure 3-5 shows a photo and the various working parts of the instrument. The general procedure of specimen preparation for AFM imaging is similar to that of SEM imaging. However, a near pristine specimen surface is required to obtain good quality results using AFM, because any organic residue such as those from the polishing lubricants can affect the

quality of imaging significantly. A specimen preparation guideline for AFM imaging of stainless steel specimen is described in [163] and was followed in this project.

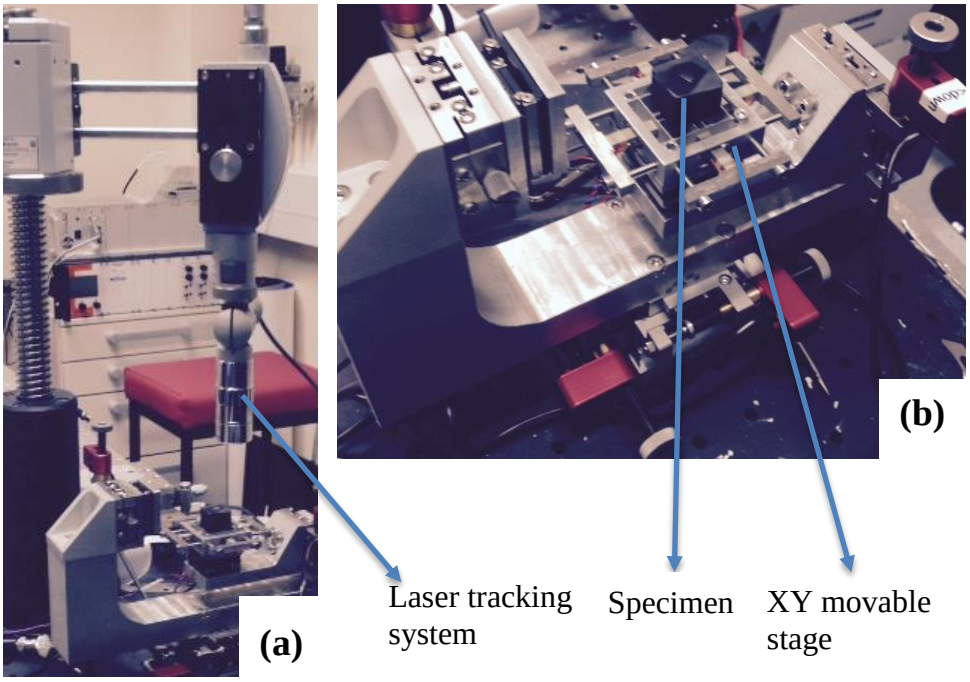

Figure 3-5 Images showing (a) HS-AFM instrument developed at the University of Bristol and (b) mounting of the specimen in a movable stage for the imaging

3.4 Hardness measurement

Hardness measurement refers to the resistance of a particular material to the penetration of another material. Hardness is not an intrinsic property of the material and measurement of it is usually used to provide relative material's properties. Hardness measurement can be conducted at Macro, Micro and Nano length scales; macro hardness testing using Vicker's hardness measuring technique was used in this project. In this technique, a square-base diamond pyramid indenter, with 136° between its opposite facets, is used to create an indent on the specimen surface. A Vicker's hardness value can be calculated by using Equation 3.1.

$$HV = 1.854\ F / D^2 \qquad (3.1)$$

Here, HV = Vickers hardness number

F = Force in kg

D = Average length in mm of the diagonals of the indentation

A Struers Duramin-A300 hardness measuring machine was used to measure hardness in this project. A fixed force of 5 Kg and a lens magnification of 365.72 was used for the measurements. The machine was calibrated using a standard stainless steel calibrator disc. The expected average hardness value of the calibrator is 197.2 for a 5 kg load. At different positions of the disc, a hardness value of 199 ± 5 was observed. Load calibration of the machine was conducted using a sensitive weight measuring machine. The load measurement of 5 kg was found to be 4996 g which is within acceptable experimental error.

The measurement process was controlled by the Duramin software. The indentations were created at selected locations of the specimen surface. The lengths of the two diagonals of the indentation were measured automatically with image detection software. When the lengths of the diagonals were found to vary significantly between each other, the measurement was adjusted manually with careful observation. At least 40 measurements in each specimen were conducted with identical instrument settings to give a good statistical representation. The average hardness of each specimen was determined by linear averaging.

3.5 Techniques for measuring internal stress

A number of techniques are available for measuring internal stress at different length scales as depicted in Figure 3-6. The experimental techniques found suitable for this project are described briefly below.

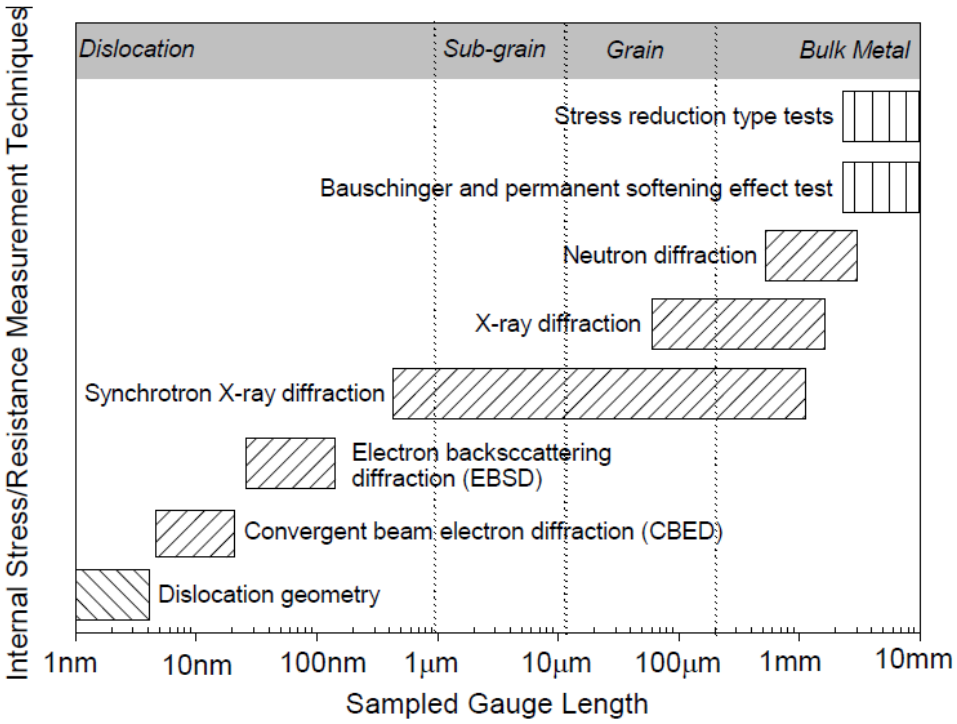

Figure 3-6: Different techniques for measuring internal stress in material at different length scales [164]

3.5.1 Microscope-based techniques

Figure 3-6 shows that microscope based techniques have the highest spatial resolution for measuring internal stress in materials. Using TEM, a measure of the internal stress can be obtained by analysing the geometry of the dislocations. In a deformed specimen, the effective shear stress acting on the dislocation can be calculated from the radius of curvature of the curved (bowed) dislocations [165] [166]. This technique was used in measuring internal stresses in a number of different materials, for example, in crept specimens of an Al-Zn alloy [165, 166] and in type 316H austenitic stainless steel [167]. Convergent beam electron diffraction (CBED) is also reported to achieve high lateral spatial resolution in measuring both type II and type III internal stresses [83] [168]. This technique measures localised lattice parameters with high accuracy by transmission of electrons through the specimen. High Order Laue Zones (HOLZ) present in the transmitted beam of CBED patterns are then analysed to calculate the internal stresses.

A major limitation of the microscope based techniques is that the measurement samples a very small volume, which does not always represent the stress state in the bulk of the material. Moreover, multi-step sample preparation is required for these techniques to be applied, which may cause relaxation and alteration of the internal stress state itself. These techniques are also time-consuming, operator dependent and often prone to large errors. Nevertheless, microscope based techniques are essential for qualitative observation of the microstructures and are complementary to other quantitative internal stress measurement techniques.

3.5.2 Diffraction techniques

Diffraction techniques are widely used for quantitative measurements of internal stress; X-ray diffraction being the most widely known of all such techniques. The principal of diffraction measurement is based on Bragg's law of diffraction. When a beam is an incident upon an arranged array of atoms as in any crystalline material, the scattering happens in all directions. In certain directions, scattered beams mutually reinforce each other and a constructive interference occurs. This constructive interference occurs only when Bragg's law (equation 3.3) is satisfied.

$$\lambda = 2d_{hkl}\mathrm{Sin}\theta_{hkl} \qquad (3.2)$$

Here, λ = wavelength of the incident beam

d_{hkl} = Inter-planar spacing between lattice planes

θ_{hkl} = Incidence angle of the beam (See Figure 3-7)

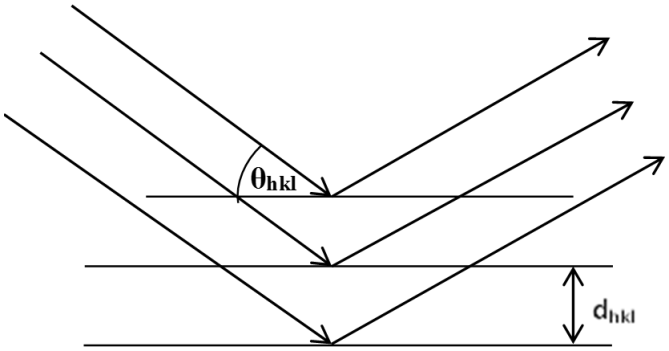

Figure 3-7: Schematic showing Bragg's law of diffraction

Diffraction-based techniques have a number of advantages over microscope based techniques when measuring internal stress. Diffraction measurements can be conducted on a comparatively larger volume of material and usually require very little or no specimen preparation prior to measurement. However, the availability of suitable diffraction instruments is limited.

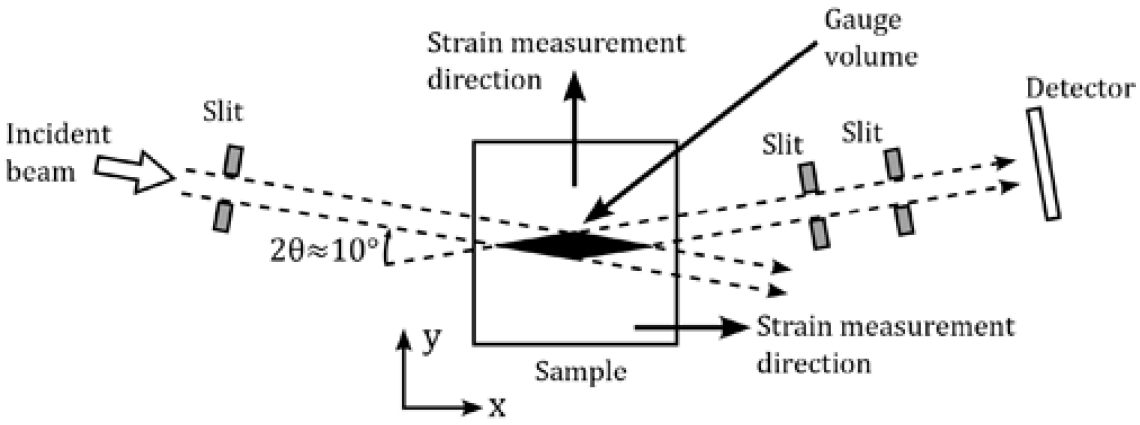

Figure 3-8: Schematic of strain measurement technique using X-ray Synchrotron. Due to a high energy beam the scattering angle gets smaller leading to a diamond shaped gauge volume of measurement.

Laboratory x-ray instruments have a very limited depth of penetration in metals and therefore measure stress and strain close the surface of the specimen. This drawback can be overcome by using high-energy synchrotron X-rays, available at a few central research facilities around the world. Synchrotron sources can be a million times more intense than laboratory sources producing high energy photons which can penetrate thousands of times deeper than laboratory X-rays [83]. Moreover, this method has a much faster data acquisition rate

compared to conventional X-ray measurements. However, due to the high energy of the photons, the scattering angle in this measurement has to be very small. This means that the gauge volume of the measurements has to be an elongated diamond shaped, as shown in Figure 3-8. Therefore, the measurement resolution perpendicular to the scattering vector is very poor using this technique. A typical gauge length lateral to the beam might be as small as 20 μm [83], which is much smaller than the average grain size of the material to be investigated in this project.

3.6 Neutron diffraction and Scattering

The wavelength of neutrons is in the same order as the distance between atoms in crystalline materials, therefore neutrons can penetrate much further into the material than electrons. Due to this unique capability, neutron diffraction has proved to be a very useful tool for studying the structure [169, 170], phase transformation [171], micromechanics [172] and deformation mechanisms [151, 173-175] in the bulk of engineering materials. This technique was used extensively in the present work and is reviewed briefly below. Further information on the technique and its application can be found elsewhere, for example, in [176] [177] and [178].

3.6.1 Fundamentals of neutron scattering

A neutron is neutrally charged and therefore it does not interact with the electron cloud of an atom. A neutron is scattered by a nuclear interaction with the nuclei of atoms [176], that is by the short-range nuclear forces. Therefore, neutrons can penetrate much further into materials than laboratory X-rays. Interaction of a beam of neutrons with matter is an interesting phenomenon where a number of things can happen. The nuclear interaction distance is usually much smaller than the distance between the nuclei of the atoms. Therefore if a beam of neutrons is fired into a material, most neutrons will simply pass by the atoms without scattering. The neutrons which interact with an atom can either scatter or be absorbed. Let us consider a single atom of a material, with which the interaction of a neutron has occurred and the neutron did scatter. If the kinetic energy of the neutron and the nucleus of the atom is preserved, then the scattering is called elastic scattering. On the other hand, if the scattering process causes a transfer of kinetic energy between the neutron and the nucleus

of the atom, then the scattering process is called inelastic scattering [177]. In inelastic scattering, the nucleus of the atom gets in an excitation stage due to the energy of the neutron and at a later stage, the nucleus may emit radiation during de-excitement. Finally, the neutron may get absorbed in the nucleus of the atom by emitting a particle from it depending upon the energy and trajectory of the neutron. When a neutron gets absorbed in a material, beam attenuation occurs. However, in 316H stainless steel, the percentage of absorbed neutrons is usually negligible.

The scattering of neutrons can either be coherent or incoherent depending upon the interaction of the neutrons with the nucleus. In coherent scattering, neutron waves scatter from different nuclei in interference with each other. On the other hand, in incoherent scattering, there is no interference between waves scattered by different nuclei [177]. So, coherent scattering occurs from an array of atoms arranged in order in a lattice of a material and incoherent scattering occurs from individual random atoms, whose position may not be correlated. Both coherent and incoherent scattering can provide useful information, for example, coherent scattering usually gives information about correlations in space and time between all the atoms and incoherent scattering gives information about self-spatial and time correlations of each individual atom [176]. Coherent scattering is reinforced only in specific directions corresponding to the Bragg condition [177].

In this project, the measurements are mostly concerned with elastic coherent scattering, which is usually used in diffraction experiments to measure lattice spacing in the material. In such experiments, incoherent elastic scattering only adds up to the background of the neutron measurement as it is the same in all directions. Incoherent inelastic scattering occurs due to scattering of neutrons from the same atom at different positions and times and is therefore not useful in measuring the change in lattice spacing [177].

3.6.2 Neutron sources

Neutron diffraction facilities can be divided into two main groups depending on the process of generation of neutrons; a reactor source and a spallation source. In reactor sources, neutrons are generated by nuclear fission reactions. The most commonly used fuel is uranium alloy plate enriched in U_{235}. In this process, a uranium atom is hit with a neutron at a high speed that splits the atom into two atoms. A number of neutrons are generated in this

process, essentially making the process a chain reaction. The speed of the generated neutrons in this process is very high; these are made useful for diffraction experiments by passing them through moderators. In a spallation source, neutrons are generated by firing a beam of highly accelerated protons to a heavy metal target (for example, Lead, Tungsten or Tantalum). Upon striking, the high energy protons emit neutrons from the target material in a process called spallation. A number of high energy neutrons are produced from each proton and these are passed through a moderation process to reduce the energy of those to the thermal range. This process is repeated many times a second.

The important parameters for a neutron diffraction experiment are the flux of neutrons, intensity and the speed of neutron generation. In reactor sources, the generation of neutrons is usually continuous and in the spallation sources, it is usually pulsed. The beam of neutrons from a steady-state reactor source is usually monochromatic, and therefore diffraction from just one orientation of the crystal in the material can be captured at a time. However, the beam of neutrons from a pulsed spallation source is usually polychromatic, so diffraction from a full spectrum of the crystal orientations is possible that can be measured simultaneously. However, a continuous flow of neutrons can be converted to a pulsed flow by using suitably configured choppers in the neutron path, for example, the Heinz Maier-Leibnitz (FRM II) facility is a pulsed reactor source. Conversely, generation of neutrons in a spallation source can also be made continuous for example, the Swiss Spallation Neutron Source (SINQ) facility is a steady-state spallation source.

3.6.3 Time of Flight technique

In the time of flight (ToF) technique, the lattice spacing of the crystals can be determined from the flight time of the neutrons. The pulsed beam of neutrons from the moderator reach the sample. Diffracted neutrons are recorded using suitably located detectors. The flight time of the neutrons, t, over a known flight path of, l, is recorded precisely. De Broglie's equation of wave-particle can be used to relate the velocity of the neutron (v) with the wavelength (λ).

$$\lambda = \frac{h}{mv} \qquad (3.3)$$

Here, m is the mass of neutron and h is the Planck's constant.

Substituting this equation in Bragg's law of, $\lambda = 2d\,\mathrm{Sin}\theta$, the following equation can be derived.

$$\frac{h}{mv} = 2d_{hkl}\mathrm{Sin}\theta_{hkl} \qquad (3.4)$$

Now, as the neutron travels over a known length of distance (l), so the equation can be written in terms of flight time of the neutron (t) as in Equation 3.5, from which the lattice spacing d_{hkl} for a particular group of grains can be calculated.

$$\frac{ht}{ml} = 2d_{hkl}\mathrm{Sin}\theta_{hkl} \qquad (3.5)$$

$$\epsilon_{hkl} = \frac{d_{hkl} - d_{0\,hkl}}{d_{0\,hkl}} \qquad (3.6)$$

Lattice strains in the material can be calculated from the relative change of the d_{hkl} spacing from its initial stress-free reference measurement $d_{0\,hkl}$, using Equation 3.6.

3.6.4 Analysing neutron diffraction data

In Engin-X, a software package named GSAS [179] is used to fit the raw data points of the diffraction peak, to determine the position of the peak precisely. Figure 3-9 shows a typical full spectrum of the diffraction peaks for a steel specimen [180]. Using the software, it is possible to fit individual diffraction peaks to obtain the volume averaged strain magnitude of differently oriented grains as well as the full spectrum of the diffraction peaks to obtain an average strain magnitude of all the grains measured.

In the case of single peak fitting, a number of peaks are selected (usually 5-10 peaks with higher intensities) and a peak shape function is fitted to the data using a least squares minimisation procedure. A Pseudo-Voigt function (linear combination of Gaussian and Lorentzian function) is used for this purpose. The output of the fitting procedure is a single value for d-spacing for each individual diffraction peak for each measurement point. Each diffraction peak is constructed from the reflection of grains from similarly oriented grains which satisfy Bragg's law. Therefore, d-spacing for a single peak is an average of the lattice spacing of a group of similarly oriented grains (typically termed a grain family), in a particular direction within the gauge volume of the material. In the case of an in-situ loading

experiment, the first neutron measurement is done without putting any load onto the specimen (or putting a very small load), which provides the stress-free reference d spacing value for each grain family.

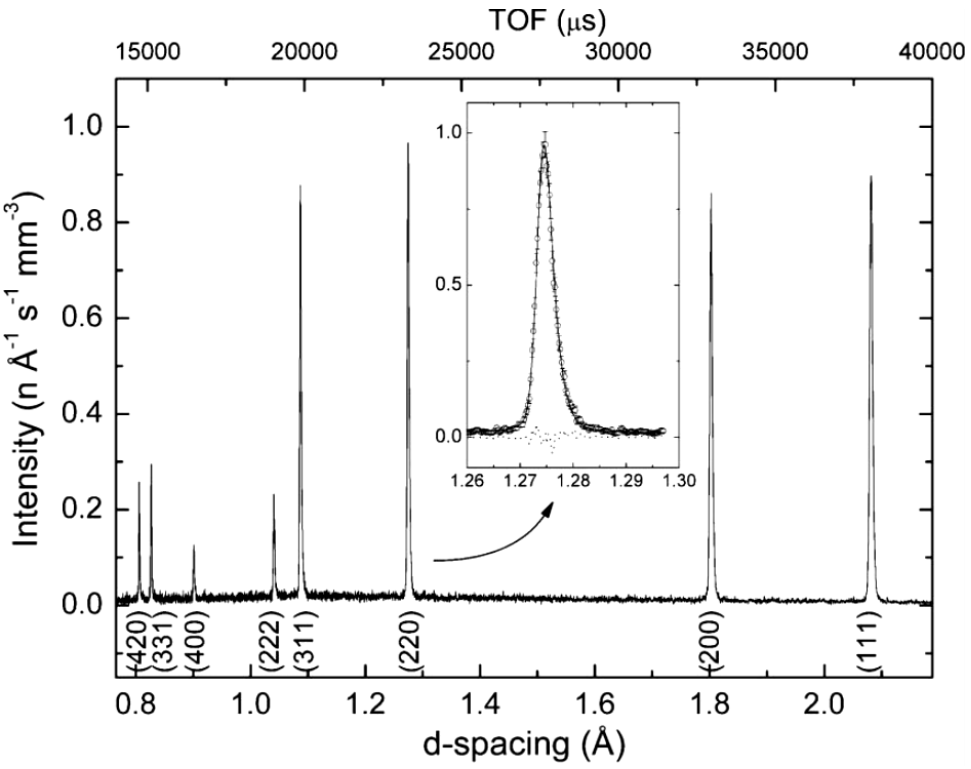

Figure 3-9 Typical diffraction pattern of steel specimen measured at the Engin-X diffractometer [180]

An average measure of the change of lattice parameter of the crystals can be obtained using the Rietveld method [181]. In this process, a number of diffraction profiles are recorded in the fitting software and a theoretical diffraction profile is predicted when a known crystal structure of the material is supplied. The predicted diffraction profile is fitted to the experimental diffraction profile by using a number of fitting parameters such as the lattice parameter, structure factors and peak shape using a least squares minimisation procedure. Further details of the fitting procedure are described in [182].

The Rietveld refinement procedure has many advantages over single peak fitting for measurement of residual stress in bulk material. The average of the full diffraction spectrum provides a more reliable measurement of the macroscopic residual stress in the material, as the measurement is not affected by the anisotropy of the deformation of the grains. Moreover, adding the data points from all diffracted grains increases the statistical reliability of the measurement, eventually reducing the counting time. In this project, single peak fitting

is mostly employed, as the anisotropy of the deformation is the topic of interest here. Nevertheless, the experimental data were also fitted using Rietveld refinement, which provided a guideline to check the reliability of the test data.

3.6.5 Converting lattice strain to stress

The determined lattice strain from neutron measurements is often enough to quantify the deformation of the material and can be directly used in many engineering applications. However, in some cases, it may be required to determine the stress at a point that causes the strain in the material. The measured lattice strain in an individual grain family or the average strain obtained from the Rietveld refinement can be converted to stress with reasonable accuracy. Three orthogonal principal strain components need to be measured to convert the strain to stress. The stress in three dimensions can be calculated using the following equations, assuming the material is an isotropic solid.

$$\sigma_{xx} = \frac{E}{(1+v)(1-2v)}\left[(1-v)\varepsilon_{xx} + v\left(\varepsilon_{yy} + \varepsilon_{zz}\right)\right] \qquad (3.7)$$

$$\sigma_{yy} = \frac{E}{(1+v)(1-2v)}\left[(1-v)\varepsilon_{yy} + v(\varepsilon_{xx} + \varepsilon_{zz})\right] \qquad (3.8)$$

$$\sigma_{zz} = \frac{E}{(1+v)(1-2v)}\left[(1-v)\varepsilon_{zz} + v\left(\varepsilon_{xx} + \varepsilon_{yy}\right)\right] \qquad (3.9)$$

It is important to note that the diffraction technique measures only the elastic strain and cannot measure plastic strain in the material directly. However, due to the elastic and plastic anisotropy of the grains, during plastic deformation, non-linearity is introduced in lattice strain measurement. This non-linearity can be indicative of the onset of plastic deformation in the grains. The non-linearites in the strain must be accounted for when converting strain into stress, otherwise, it will lead to serious miscalculation of stress values [176]. In most parts of this thesis, lattice strain measured from the neutron diffraction has been used directly without converting to stress. Occasional transformation of the lattice strain to stress was undertaken, mostly to emphasise the significance of these strains in the engineering applications.

3.6.6 Engin-X neutron diffractometer

The neutron diffraction experiments of this project were conducted using the Engin-X neutron diffractometer at the Rutherford Appleton Laboratory ISIS Facility. ISIS is a pulsed spallation source of neutrons and Engin-X is a time of flight neutron diffractometer. In this section, the operational procedure of the instrument will be described in brief. Details of the instrument can be found in [180] and [183].

At the ISIS Facility, negative hydrogen ions (H^-) are first generated using an ion source and then accelerated using a Linac accelerator to a speed of about 37% that of light. The ions are then entered in a synchrotron ring of 163m circumference and separated into protons and electrons using an alumina foil. The protons are further accelerated in the synchrotron ring using radio-frequency electric fields to a speed of about 84% that of light. This high energy beam of protons collides with a tungsten target and drives neutrons from the nuclei of the target. Moderators are used to reduce the speed of the neutrons which are then supplied to various neutron instrument situated surrounding the target station.

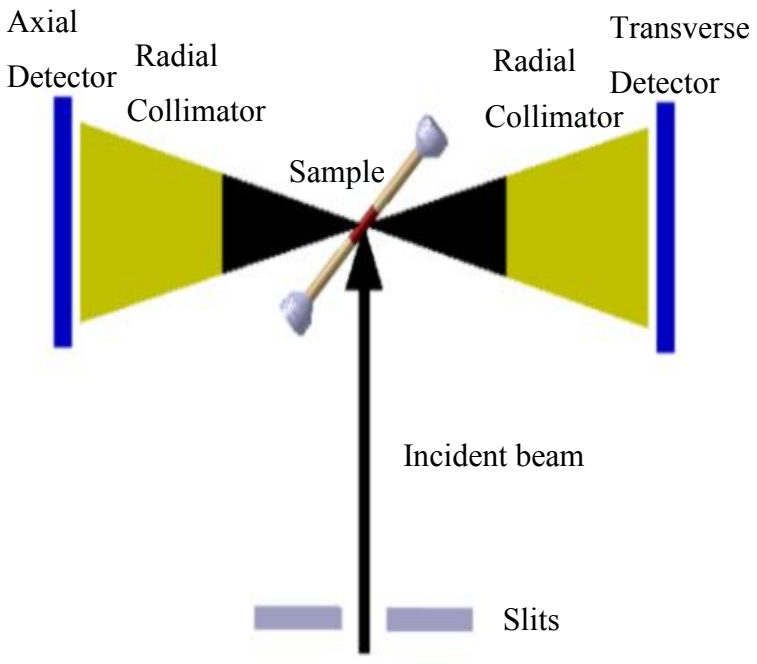

Figure 3-10 Schematic showing the neutron beam path and relative positions of the specimen and the detectors in the Engin-X diffractometer.

Engin-X uses a methane moderator which was chosen because of the narrow pulse width and high flux over the required wavelength (1-3 Å) for the instrument [180]. The distance between the moderator and the sample, known as the primary flight path is ~ 50m. This distance was chosen to minimise the neutron counting time [184]. Neutron guides made of supermirror are used to guide the neutrons from the moderator to the sample.

Figure 3-10 shows a schematic illustrating the neutron diffraction experiment set-up at the Engin-X instrument. The specimen in the loading rig is aligned at a 45° angle to the incident neutron beam. Adjustable horizontal and vertical slits are used to limit the length and breadth of the neutron beam. The depth of the beam is controlled by using different sized radial collimators. The horizontal dimension of the beam could be 0.3 – 10 mm and the vertical dimension of the beam could be 0.3-30 mm. There is a choice of 0.5, 1, 2, 3 and 4 mm sized radial collimators [180]. Using different sized slits and collimators, the gauge volume of measurement can be fixed. The gauge volume essentially means the volume of the specimen in which the measurements are being conducted. In Figure 3-10 the gauge volume is marked in brown colour on the specimen. Two detectors are set perpendicular to the beam which collects neutrons diffracted from lattice planes oriented parallel to the axial and transverse directions of the loading. The component of strain measured with a detector lies along the direction of the neutron scattering vector Q, which lies in the direction of the bisector of the incident and diffracted path of the neutron. The distance of these detectors from the centre of the instrumental gauge volume is ~1.53 m. The detectors cover a range of ±16° in the horizontal plane and ±21° in the vertical plane. Each detector of the instrument consists of 1200 scintillators which detect the diffracted data. The data from each of these scintillators are combined to a single d-spacing value using a process known as time focusing [185]. To get a meaningful statistical representation of the material strain, it is required to measure the strain at the point of loading for a certain duration of time. This counting time is usually in the order of minutes depending on the material properties, the flux of neutrons and gauge volume of the measurement. The bigger the gauge volume, typically the quicker is the measurement in any specific material.

3.6.6.1 In-situ mechanical testing at Engin-X

The Engin-X diffractometer is equipped with a number of sample environments including custom designed mechanical stress rigs, a high-temperature furnace and a cryogenic chamber. In this project, the stress rig and high-temperature furnace were used to conduct in situ tests in the neutron beamline. The Instron servo-hydraulic stress rig has a maximum loading capacity of 100 KN and in the house built radiant furnace [180] can reach up to 1100℃ of temperature. A typical experimental set-up for an in-situ test using the stress rig and the furnace is shown in Figure 3-11.

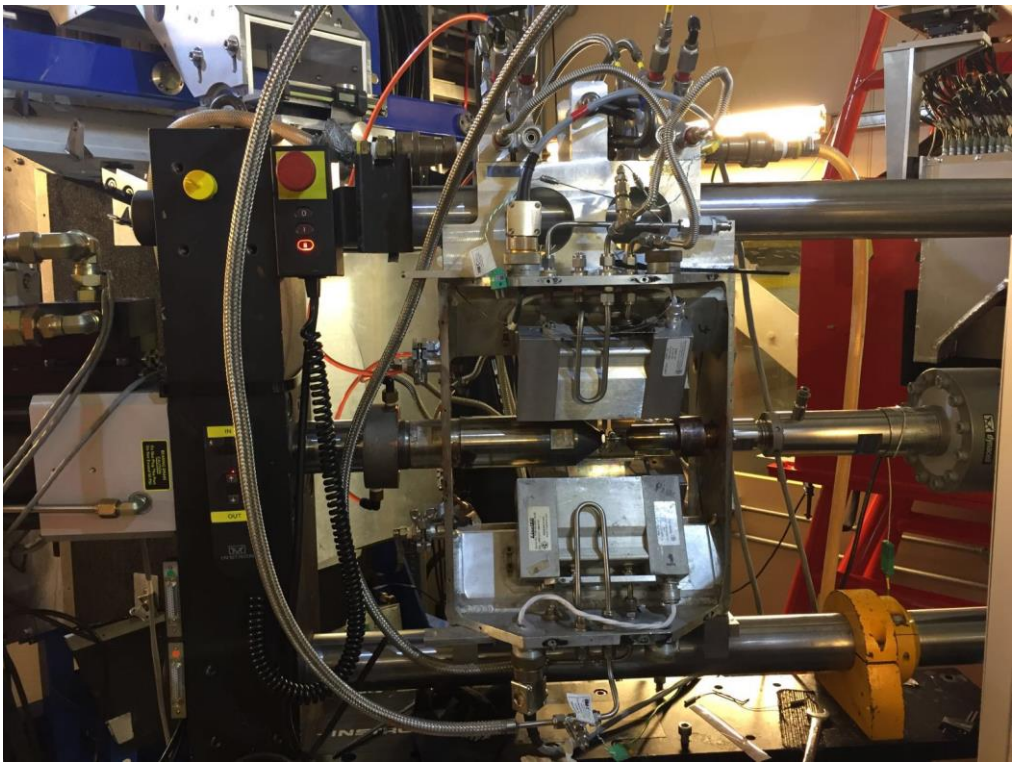

Figure 3-11 Set-up of the in-situ mechanical testing stress rig and furnace at the Engin-x beamline

The specimens used in these experiments were designed according to the dimensions shown in Figure 3-1. The specimen is placed in between the upper and lower jaws of the stress rig using threaded ends. The applied load is measured and controlled using a load cell. Macroscopic strain in the specimen can be measured using an Instron high-temperature extensometer similar to that described in section 3.2. The extensometer is attached directly to the gauge length of the specimen using specialised tension strings. For the high-temperature tests, the temperature of the test specimen is monitored using a K-type

thermocouple either spot welded or clamped using vanadium clip at the centre of the gauge length of the specimen. Only one thermocouple can usually be attached due to the short gauge length of the specimen. A vanadium clip is used due to its transparency to neutrons.

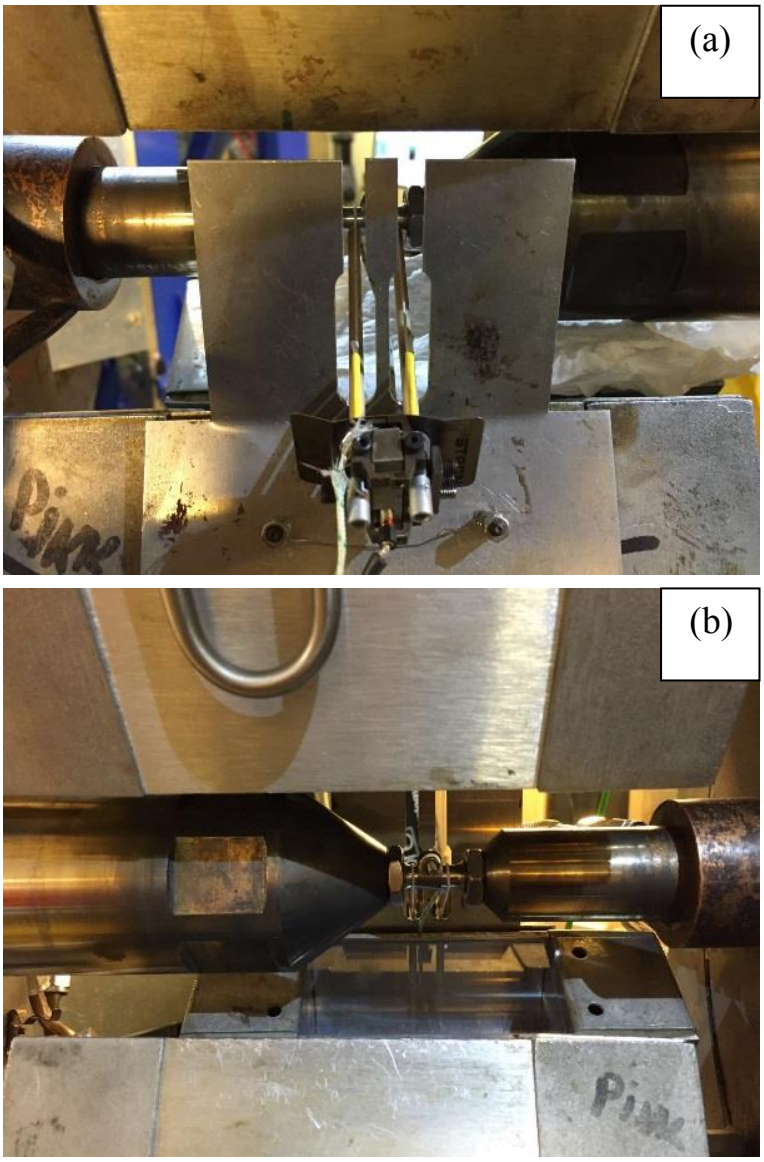

Figure 3-12 (a) Closer view of the attachment of the extensometer on to the gauge length of the specimen (b) attachment of the thermocouple in the specimen with a vanadium clip

Accurate alignment of the grips of the stress rig is crucial for any tension-compression cyclic tests. The stress rig in the Engin-X beamline is placed horizontally, which creates additional challenges of alignment between the grips during high-temperature experiments. This is because, the stress rig has a long pull-rod and due to the large weight of the rods, it puts a small downward torque on the specimen. Upon reaching high temperatures, the rod expands

depending on the coefficient of thermal expansion and creates a small misalignment of the grips. The alignment of the stress rig was therefore checked before each test using an Instron alignpro system. Using a specialised specimen the system can be used to check and fix the concentricity and angularity of the alignment of the grips of a stress rig. The alignpro specimen was not available for all the experiments of the project and an alternative method of alignment was undertaken. In this method, a cylindrical specimen was cut into two halves at mid-length by wire EDM, such that minimal material loss occurred. The split halves of the specimen were inserted into the two grips of the load frame and then brought closer together using the pull rod. A piece of Canon pressure paper was inserted in between the two halves of the specimen and a small compressive load was applied. This created a mark on the pressure paper. By checking the circularity and homogeneity of the mark, the alignment of the grips was adjusted until a complete circular mark with a homogeneous distribution of pressure was achieved.

3.6.7 Small-angle neutron scattering (SANS)

Small-angle neutron scattering (SANS) is capable of measuring (non-destructively) microstructural features across the nanometer to micron size range in small sample volumes (tens of cubic millimetres) in steel. In this technique, neutrons are elastically scattered by a sample and the resulting scattering pattern is analysed. The scattered intensity at any given scattering vector, Q is proportional to the macroscopic scattering cross section of the samples [186], therefore, from the recorded scattering intensity of the neutrons information about the size and volume distribution of the scatterers can be derived mathematically. The mathematical basis for SANS measurements is similar to that of the more widely known technique of Small angle X-ray scattering (SAXS) that can be found in standard textbooks, for example [187].

3.6.7.1 SANS data analysis

For SANS measurements at a pulsed source, the raw neutron scattering cross section data are obtained at different wavelengths. In order to combine these data, the wavelength dependencies are normalised in terms of the incident neutron flux, the sample transmission and the detector efficiencies [188]. A number of calibration measurements are required to

characterise these normalising factors. The detector efficiency can be obtained by measurements of the ratio of the incident beam current, $I_H(\lambda)$ in neutrons s^{-1} with that of the scattering beam detector that is $I_M(\lambda)$ in neutrons s^{-1}. Such measurements are obtained by measuring a direct beam without any sample and beam stopper. Transmission of the sample is obtained by inserting a separate detector immediately after the sample and by reducing the incident beam diameter between the monitor and the sample. Details of the calibration measurements and the data reduction procedures are described in [189]; the same procedure was followed in this project. Data analysis software developed in-house in the ISIS facility, named 'Mantid' [190] was used for data reduction.

The reduced data were fitted to a model using a maximum entropy algorithm MAXE [191] by assuming that the shape of the scatterers (such as carbides and cavities in the microstructure) are spherical in shape. The MAXE routine outputs the volume fraction distribution of the scatterers, V(D), of diameter D. The MAXE routine was developed at Southampton University and Harwell [191]. This routine has recently been re-written in C++ by the Open University.

Scattering from different types of scatterers, for example, that from a carbide and a cavity, cannot be directly differentiated in SANS data. Prior information is required from microscopic images of similar samples that establish the nature of the scatterers in order to define the scattering contrast factor (CF). For example, the CF for carbides and cavities can be calculated from knowledge of the chemical composition of the matrix and carbides [192]. The absolute volume fraction of one type of scatterer can be separated by subtracting a reference measurement for the other type of scatterer using the CF. In this project, measurement of the volume fraction of creep cavities was of interest, while the measured V(D) originated from scattering of both carbides and cavities in the microstructure. The absolute volume fraction of cavities, C(D) was calculated using equation 3.10.

$$C(D) = (V(D) - V(D)_{ref}) / CF \qquad (3.10)$$

Here, CF is the contrast factor and $V(D)_{ref}$ is the measure of V(D) from samples with the same distribution of carbides as that in the creep deformed samples but without any creep cavities.

Specimen-specific reference measurements of $V(D)_{ref}$ were obtained from samples extracted from the grip sections (d5 samples) of the creep specimens. These samples were assumed to be free of creep cavities as the creep deformation in the grips is much smaller compared to that in the gauge length of the specimen. An alternative global reference measurement was also undertaken by measuring two points in an undeformed material extracted from the same ex-serviced header to that of the creep specimens. It was ensured that these measurement locations were in a far-field region away from any creep crack or weld, such that no cavities were present in the samples. In the case of both the sample specific and far-field reference measurements, the distribution of carbides was assumed to be uniform throughout the material.

The fractional distribution of the number of creep cavities, N(D) can be calculated from the obtained C(D) using equation 3.11.

$$N(D) = C(D) / V_{sph}(D) \qquad (3.11)$$

A detailed description of the SANS data analysis procedure has been reported by Hutchings [193].

3.6.7.2 SANS2D instrument

The SANS2D instrument at the ISIS facility was used for the SANS measurements in this project. SANS2D is a time-of-flight instrument situated at the 10Hz pulsed second target station of the ISIS facility. A schematic of the instrument and its various parts is shown in Figure 3-13. The instrument is equipped with two movable position sensitive detectors with an area of ~1 m^2 each. The moderator to sample distance is 17 m and the two detectors can be positioned in between 3.5 m and 12.5 m from the sample. The biggest advantage of the SANS2D instrument, over its predecessor Loq instrument in ISIS TS1, is that a wider Q range can be measured using this instrument without changing the instrument's configurations. Varying the detector to sample distance, a range of Q between 0.002 $Å^{-1}$ to 3$Å^{-1}$ is achievable with this instrument. Further details of the instrument can be found in [188].

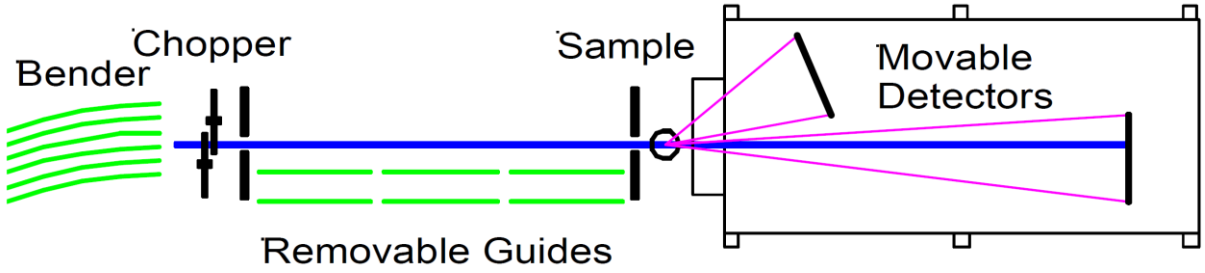

Figure 3-13 Schematic showing the SANS2D instrument of the RAL, ISIS Facility [194].

In this project, SANS measurements were conducted on 1mm thick disc-shaped specimens extracted from the grip and gauge sections of interrupted creep deformed specimens. The specimens were wrapped in vanadium foils (vanadium is highly neutron transparent) and placed in a custom built specimen holder as shown in Figure 3-14. The disc specimens were positioned carefully in the specimen holder such that their centres were aligned with the circular windows. The specimen holder was placed in the beamline and the specimen windows aligned with the centre of the neutron beam (projected using a laser). The recorded co-ordinates for each window were input into the control software and the measurements conducted at those locations by automatic movement of the specimen holder.

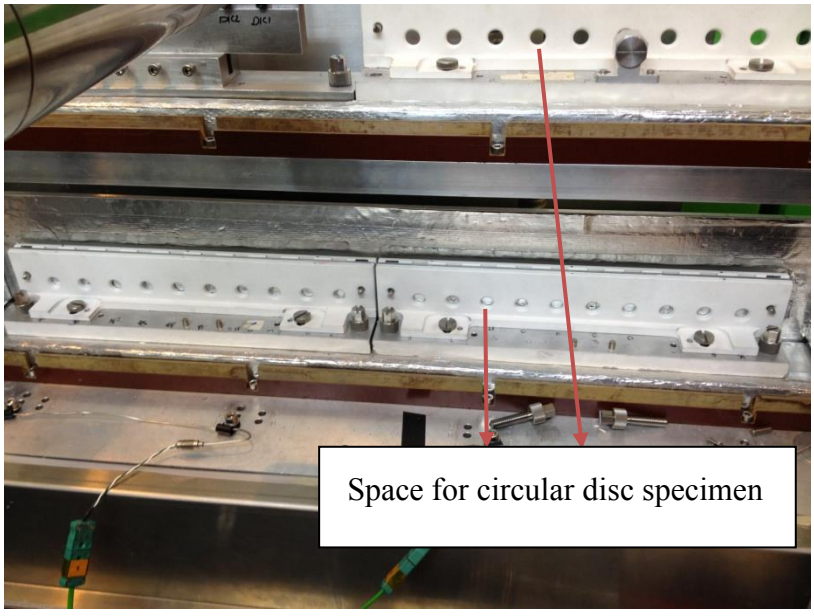

Figure 3-14 Custom built specimen holder used for the SANS measurements of circular disc-shaped specimens in the SANS2D beamline

3.7 Summary

This chapter described the mechanical testing, microscopy and neutron scattering experimental techniques and procedures used to generate results presented in the chapters that follow. The mechanical and microscope based work was conducted at the laboratories of the Open University (except for the AFM measurements which were conducted at the University of Bristol). The neutron scattering and neutron diffraction experiments were conducted at the Rutherford Appleton Laboratory of the ISIS Facility. The experiments were conducted according to relevant testing standards wherever feasible and care taken to minimise random and systematic errors in the measurements.

Chapter 4 Generation and evolution of intergranular strain

4.1 Overview

This chapter presents experimental results, investigating the generation of intergranular strain in AISI type 316H austenitic stainless steel during mechanical deformations. First, results from standard material characterization tests are described, which includes compositional analysis, tensile tests, hardness measurement, grain size measurement and texture analysis. The evolution of intergranular strain is studied by neutron diffraction (see Chapter 3) during uniaxial tension, uniaxial compression and uniaxial cyclic tension-compression tests at room and high temperature. The observed differences in the generation of intergranular strains during these loading sequences is discussed. The results in this chapter form the basis of later investigations about the effect of intergranular strain on creep and cyclic deformation of type 316H austenitic stainless steel, presented in Chapter 5 and Chapter 6 respectively.

4.2 Material characterization

The materials for this project (AISI type 316H stainless steel) were obtained from two different sources. Material A refers to samples extracted from an ex-serviced steam-header supplied by the EDF energy (see details below). Material B refers to bar stock procured from a company named power metal suppliers. Material A was used for pilot tests, because of its availability early in the project. Most of the tests reported in this thesis were carried out using material B.

Material A: Ex-service steam header

A steam header made from AISI type 316H austenitic steel was supplied by EDF energy. The steam header is from the cast number 69431and designated as HRA 2B2/1. It had been in service in EDF's operated power plant for ~90,930 hours at an average temperature of ~525°C under an average internal steam pressure of ~16MPa. The header was retired due to failure following the discovery of extensive reheat cracking near the header- nozzle weld. The internal diameter and thickness of the header are 304.8mm and 63.5mm respectively. Figure 4-1 shows photographs of the steam header and the marked sections in it from where the specimen blanks for this project were extracted.

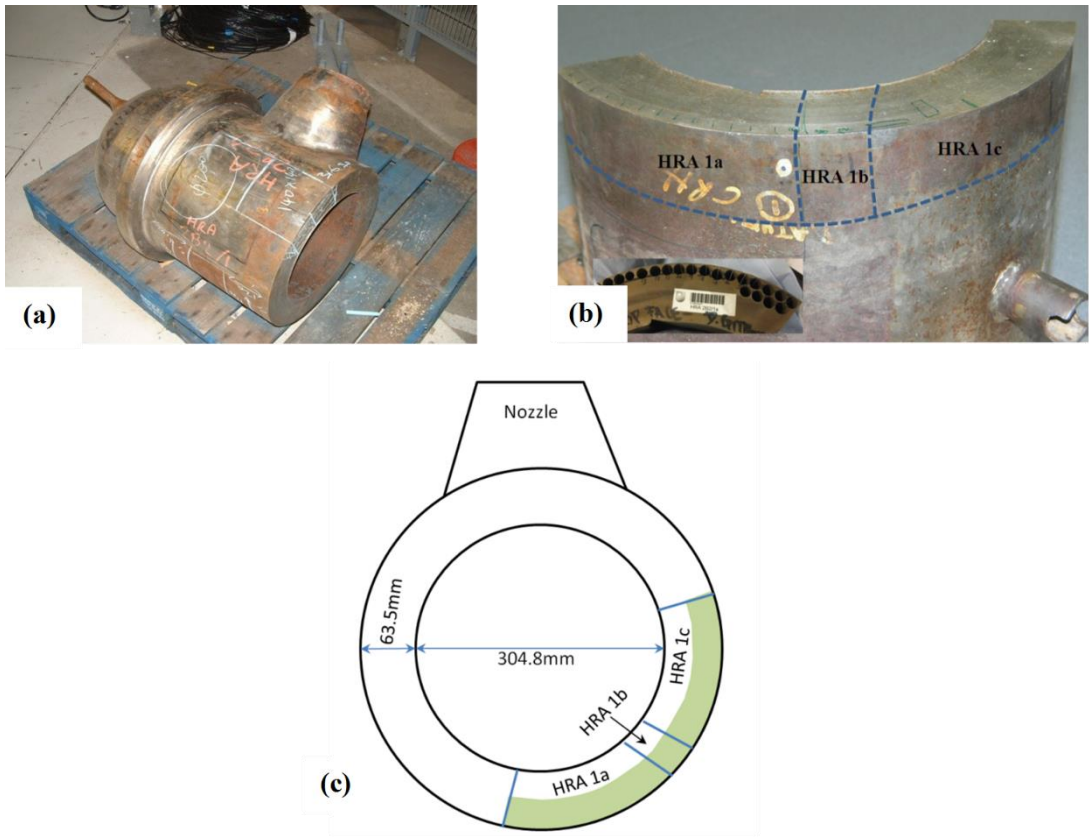

Figure 4-1 (a) The ex-service steam header made of type 316H austenitic stainless steel, supplied by EDF Energy (b) photograph of a section of the header showing the zone HRA 1c, where the specimen blanks were extracted from (c) location of HRA 1c in the supplied steam header [195]

Significant variation in mechanical properties was observed through the wall thickness of this header [195], therefore, care was taken to extract all the specimens from the same region of the header. The specimens were extracted from the outer surface of section HRA 1c of the header, as shown in Figure 4-1(b). That section was in a far field from the welded region

at the nozzle of the header. The test specimen blanks were extracted using an EDM machine available in-house. The blanks of the specimen were re-solution heat treated at 1050℃ for 1 hour followed by water quench to remove any service caused precipitation from the microstructure. The specimens were then machined to specific dimensions as described in chapter 3. Energy dispersive X-ray spectroscopy (EDS) technique was used initially to analyse the elemental composition of the material, however, this technique is found to be insufficiently sensitive to quantify the content of low atomic number elements. Therefore, to confirm the element's wt%, in particular, the carbon content, optical emission spectroscopy (OES) analysis was commissioned. The OES analysis was outsourced to a company called Inspiratech. The results of the elemental analysis for this material and material B are shown and compared in Table 4-1 below.

Table 4-1 Comparison of chemical composition in Wt% between material A (extracted from an ex-service header supplied by the EDF energy) and material B (procured from power metal suppliers). The wt% of the alloying elements was measured using optical emission spectroscopy (OES) technique.

Element	**C**	**Si**	**Mn**	**P**	**S**	**Cr**	**Mo**	**Ni**	**Al**	**Co**
Material A	0.066	0.42	1.00	0.029	0.015	17.82	2.33	11.81	0.003	0.093
Material B	0.063	0.26	0.62	0.036	0.013	16.60	2.02	10.03	.015	.025
Element	**Cu**	**Nb**	**Ti**	**V**	**W**	**Pb**	**Sn**	**N**	**Fe**	
Material A	0.23	0.007	0.004	0.031	0.068	0.003	0.007	0.096	Bal.	
Material B	.116	.008	0.008	0.041	.044	.003	.001	.039	Bal.	

Material B: AISI type 316H bar stock

This batch of material was procured from Power Metal Suppliers in the form of cylindrical bars. The bars were supplied in size of 3 m length and 12.5 mm diameter. The material is graded as 316H stainless steel (UNS S31609). The material has been furnace melted, cold drawn and centreless ground. The material was supplied as heat-treated at 1100°C for 90

minutes followed by water quenching. Table 4-1 shows the comparative elemental wt% of material A and material B obtained from the OES analysis. Only a small variation can be noticed in the Wt% of Mn, Ni and Cr between these 2 batches of materials. Nevertheless, both materials contain min. and max. wt% of elements to be graded as type 316H stainless steel. The carbon content of the 316 stainless steel has to be within .04-.10 % to be termed as 316H stainless steel.

4.2.1 Tensile properties

Type 316H austenitic stainless steel has been widely used in many high-temperature applications and its mechanical properties are well known. Benchmark tensile tests were conducted using both material A and B to obtain the yield properties of the material. Material A was tested only at room temperature; this is because this batch of material was used only for initial pilot tests at room temperature. Material B was tested both at room and high temperatures. All the tests were conducted using Instron 8862 slow strain rate machine following the procedures described in chapter 3.

A set of different strain rates were used to test material A in order to assess the room temperature strain rate sensitivity of type 316H austenitic steel. The main objective of the tests was to justify the use of a specific strain rate for the later neutron diffraction tests at room temperature. During in-situ neutron diffraction loading tests, finite amount of time (usually in the orders of minutes) is required to generate a satisfactorily accurate diffraction peak. During this time of measurement, the loading of the material is stopped either in stress or strain control giving rise to the possibility of creep and stress relaxation respectively to occur in the material. In order to avoid this, neutron measurements can also be obtained during continuous loading, if a very slow strain rate can be used for the test such that no significant changes occur in the material's strain within the duration of neutron measurement. However, if the material is strain rate sensitive, conducting loading at very slow strain rate will not be representative of the deformation occurring at the other strain rates. The strain rates chosen for the tensile tests were 10^{-3}, 10^{-5}, 10^{-6} and 10^{-7} s^{-1}. Figure 4-2 shows the results of the tensile tests; the measured yield stress es obtained from the tests are presented in Table 1. The yield stress for a particular stress-strain curve was determined by

drawing a parallel line to the initial elastic line from a strain offset of 0.2% and then determining the intersection point of this line with the stress-strain curve.

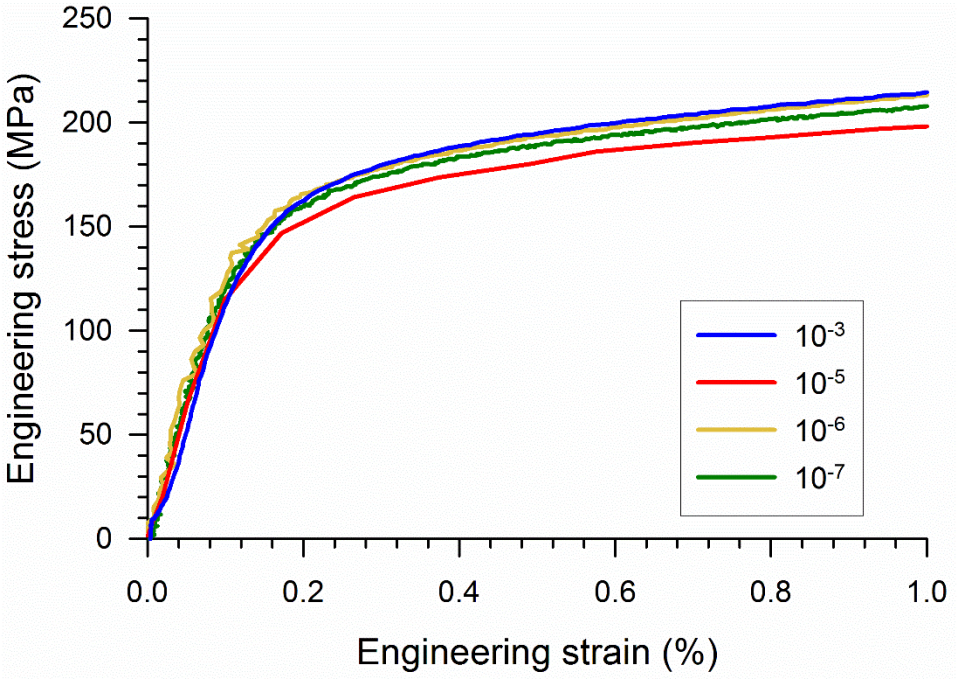

Figure 4-2 Stress-strain curves for material A tested at room temperature under strain control at four different strain rates.

A small variation in the stress-strain curves (within experimental scattering) can be noticed between the tests conducted at different strain rates; only a noticeable variation can be noticed for the tests conducted at 10^{-5} s^{-1} strain rate. The yield stress for the tests at the strain rate of 10^{-3}, 10^{-6} and 10^{-7} s^{-1} was found to be in the range of 181-187 MPa while that for the test at a strain rate of 10^{-5} s^{-1} was found to be 172 MPa (see table Table 4-2). The yield stress found in these tests are much lower compared to yield stress of a conventional undamaged 316H stainless steel reported in the literature, that is 205 MPa [196]. However, no systematic variation of the yield stress was observed in relation to the strain rate of the test.

Material B was tensile tested both at room temperature, at 550℃ and at 650℃. The results of the tests are also presented in Table 4-2 and stress-strain curves are shown in Figure 4-3. All the tests were conducted at a strain rate of 10^{-3} s^{-1}. The yield stress (at 0.2% strain offset) of Material B was found to be 208 MPa at room temperature, which is expected for this material; yield stress for conventional 316H stainless steel reported by the metal suppliers in

205 MPa [196] and the yield stress quoted in the test certificate of this material is 210 MPa. yield stress at 550°C and at 650°C was found to be 112 MPa and 94 MPa respectively.

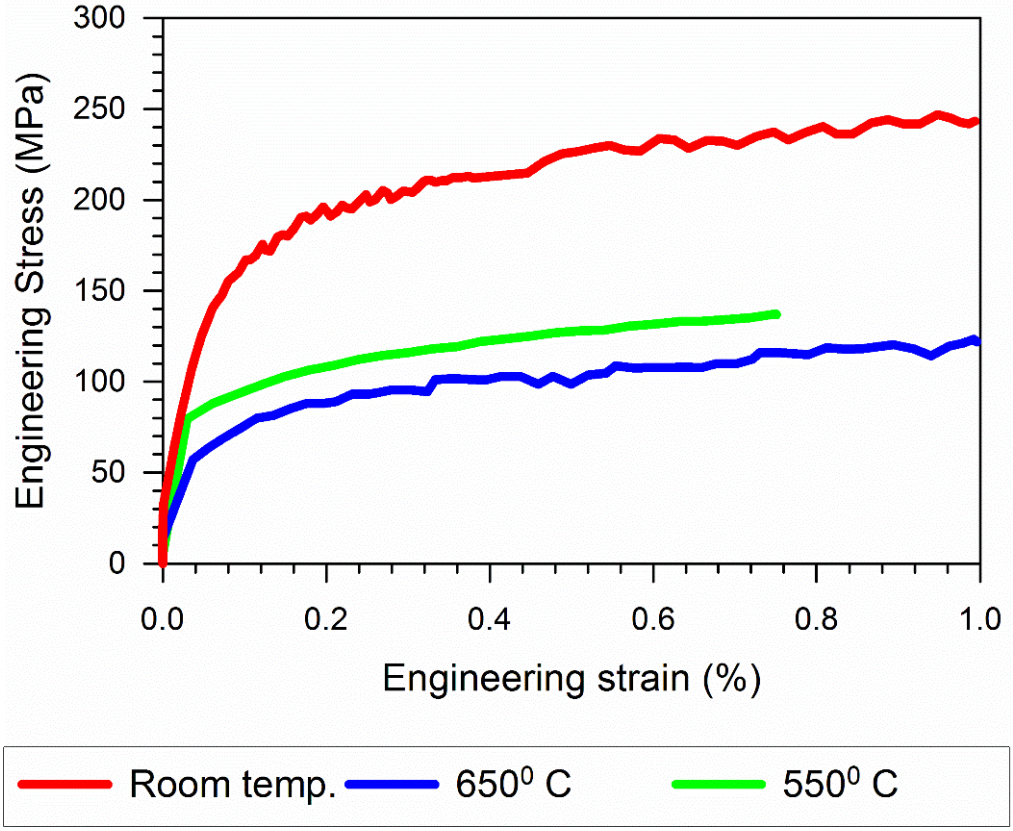

Figure 4-3 Results of tensile test for Material B at room and two different high temperatures conducted at the strain rate of 10^{-3} S^{-1}

Table 4-2 Summary of the tensile tests conducted at various strain rates and temperatures for material A and material B respectively

Material A	Strain rate	10^{-3} s^{-1}	10^{-5} s^{-1}	10^{-6} s^{-1}	10^{-7} s^{-1}
	Yield stress (MPa)	187	172	185	181
Material B	Temperature	Room temp.	550°C	650°C	
	Yield stress (MPa)	208	112	94	

4.2.2 Hardness measurements

The hardness of material B was measured using a Struers Duramin-A300 hardness measuring machine following the procedure described in Chapter 3. The measurements were conducted in accordance with the BS EN ISO 6507-1:2005 standard [197]. Cylindrical specimens similar to that used in the tensile tests were sectioned using Struers cutting machine. Two sections were extracted from the material parallel and perpendicular to the loading direction of the specimen. In both the sections, at least 40 measurements were conducted in a series with a 5 Kg force. The average hardness found for the material in the as-received state is 120 ± 7 HV.

4.2.3 Grain size measurement

Grain size has significant effects on the mechanical properties and deformation rate of type 316H austenitic stainless steel, as described in Chapter 2. In general, the effect of grain size on the mechanical properties of the material can be described using the widely known Hall-Petch relationship [198, 199] which describes that the strength of a material is inversely dependent on the square root of its grain size. Grain size is also an important parameter in diffraction measurements of strains in the material; optimum gauge volume of a diffraction test is determined based on the grain size of the material to be investigated. There are a number of well-established techniques to measure grain size in the material; Mean Linear Intercept (MLI) method [200] was used in this project. An orientation map obtained using EBSD technique was used for the purpose. In EBSD, grains are defined as a group of similarly oriented neighbouring points on the scan grid, which is surrounded by other grains with a misorientations value exceeding certain tolerance value [201].

The grain sizes for material A and material B were measured in samples extracted from orientations parallel and perpendicular to the loading direction of a cylindrical specimen. An image analysis software, ImageJ [202] was used to draw a number of horizontal and vertical straight lines on the orientation maps obtained using EBSD, an example of such drawn vertical lines is shown in Figure 4-4. The straight lines were drawn with spaces such that oversampling of big grains was minimised. The number of intercepts of these lines with grain boundaries in the image was counted from which the mean linear intercept was calculated in horizontal and vertical direction separately using Equation 4.1 [203]. The

intersections of the lines with twin grain boundaries were not counted. The average grain size was calculated by averaging the MLI in the horizontal and vertical direction.

$$L = \frac{R\delta P}{N} \qquad (4.1)$$

Here, L is the mean linear intercept grain size, R is the number of rows scanned, P is the number of pixels, δ is the scan step distance between pixels and N is the number of intercepts.

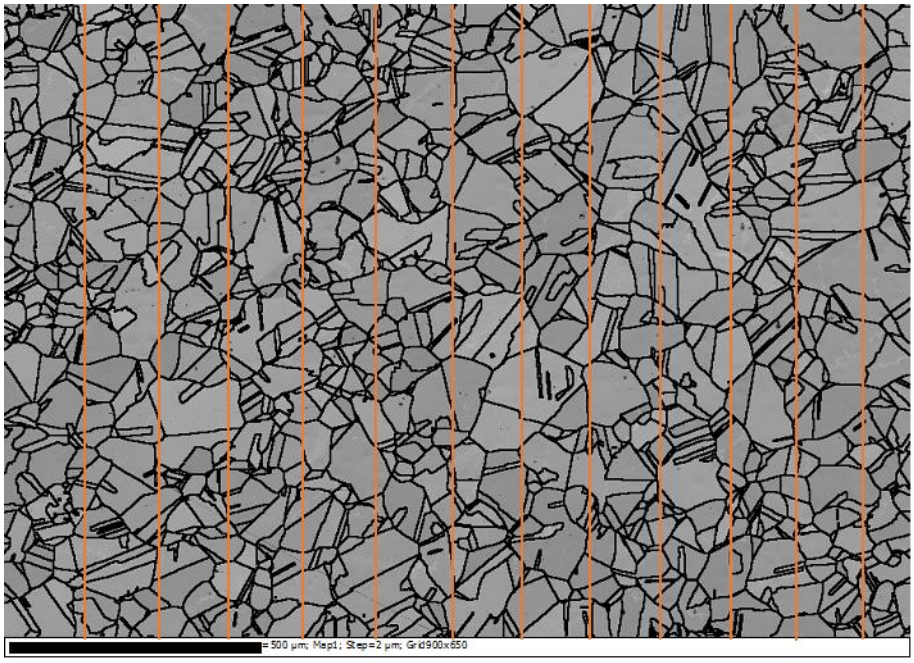

Figure 4-4 Example of SEM image showing the grain structure and application of the linear intercept method for determining the average grain size.

In order to reduce statistical errors, at least 500 grain intercepts were counted using a number of images taken at the same instrument setting. The average grain size of the serviced aged Material A and Material B were found to be 95 ± 5 µm and 71 ± 4 µm respectively. The larger grain size of the service aged material A can be attributed to the grain growth during prolong period of high-temperature deformation in this material.

4.2.4 Texture measurement

Texture can be defined as a non-random distribution of crystallographic orientations of the grains in a material [204] that is if the orientation of all the grains within a polycrystalline

material is random, then the material is said to having no texture. Texture can significantly affect the deformation behaviour of metals; many of the mechanical properties of the polycrystalline material are anisotropic [204]. Intergranular strains in the polycrystalline material are generated due to anisotropic deformation of the grains, therefore, measurement of texture is important in the context of this project.

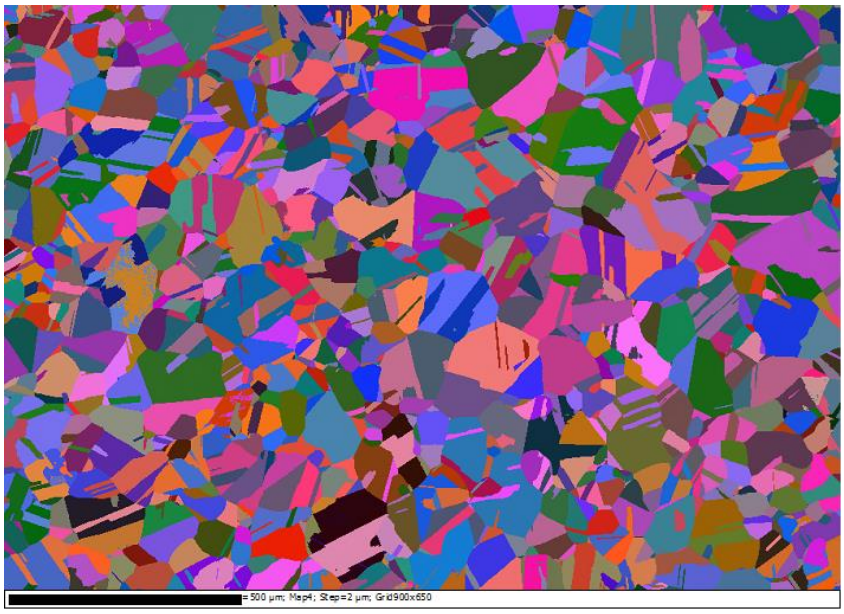

Figure 4-5 Orientation map of an undeformed 316H stainless steel material (material B) obtained using EBSD technique showing the different orientation of grains represented by different colours.

The texture of a material can be assessed by analysing orientation data [205] obtained using EBSD technique. An example of an orientation map obtained for type 316H austenitic stainless steel is shown in Figure 4-5. In this map, different colour represents different orientations of the grains. The density of similar orientation of grains can be quantified and plotted as pole figures to visualise the texture in the material. The pole density in these figures shows the strength of the poles clustering relative to a completely random distribution; the occurrence of poles of specifically oriented grains with respect to the random distribution of grains can be expressed as multiples of uniform density (MUD) [205]. Figure 4-6 shows the pole figure generated from the orientation map of an undeformed type 316H austenitic steel sample (material B). The material shows a week texture, with a maximum MUD of 2.22.

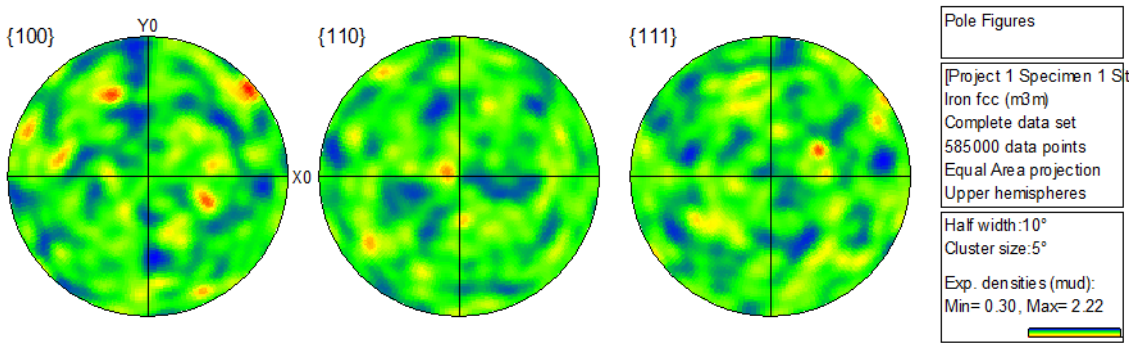

Figure 4-6 Generalized pole figures produced using HKL Channel 5 software, showing crystallographic texture of type 316H austenitic steel (material B) in the undeformed condition. The material is found to exhibit weak texture with a maximum MUD of 2.22.

4.3 Generation of intergranular strain

In this section, experimental results describing the generation of intergranular strain during tensile, compression and cyclic loading at room and high temperature are presented. The stock of virgin 316H stainless steel that is Material B was used for all these testing. Neutron diffraction technique was used to record changes of d-spacing between crystallographic lattice planes during uniaxial and cyclic deformation tests, from which lattice strain and intergranular strain for individual grain families were calculated following the procedure described in Chapter 3. Rietveld refinement [181] was used to determine a theoretical average of strain for the recorded grain families. Daymond [151] shows that considering at least 5 diffraction peaks in the averaging, an accurate estimate of the bulk (macroscopic) strain can be obtained from the Rietveld prediction.

4.3.1 Tensile testing

Figure 4-7 shows the evolution of (a) axial (parallel to the loading direction) and (b) transverse (perpendicular to the loading direction) lattice strains in 4 different grain families during elastic and plastic deformation of type 316H stainless steel at room temperature. In the elastic regime, different grain families deform differently depending upon the elastic stiffness of a specific grain family. At any applied stress, the {200} grain family accumulates more lattice strains than other grain families in both axial and transverse directions while the {220} and the {111} grain families accumulate least. The {311} grain family deforms in a

manner similar to the macroscopic behaviour characterised by Rietveld refinement analysis of the diffraction spectrum. In the transverse direction, it can be noticed that the lattice strains in various grain families are less widely spread than that in the axial direction, particularly at the higher stresses.

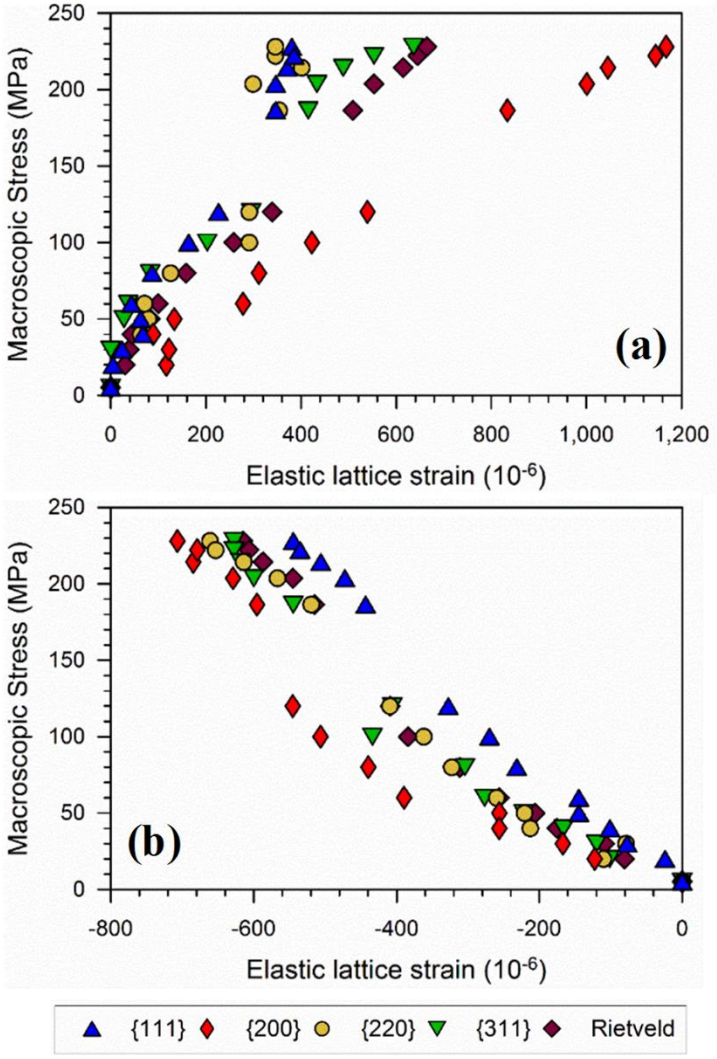

Figure 4-7 Evolution of (a) axial and (b) transverse elastic lattice strain during uniaxial tensile loading of type 316H austenitic stainless steel (material B) at room temperature.

In the elastic-plastic transition regime, lattice strains start to deviate from initial linearity in a number of grain families. This is more apparent in the axial direction than in the transverse direction. The deviations from linearity for different grain families' start at different applied stresses and in different senses. For example in Figure 4-7(a), at about 100 MPa of applied stress, lattice strain of the {220} grain family starts to deviate negatively from linearity,

whereas at a slightly higher applied stress, lattice strains in the {200} grain family start to deviate positively from those respective initial elastic linear behaviour.

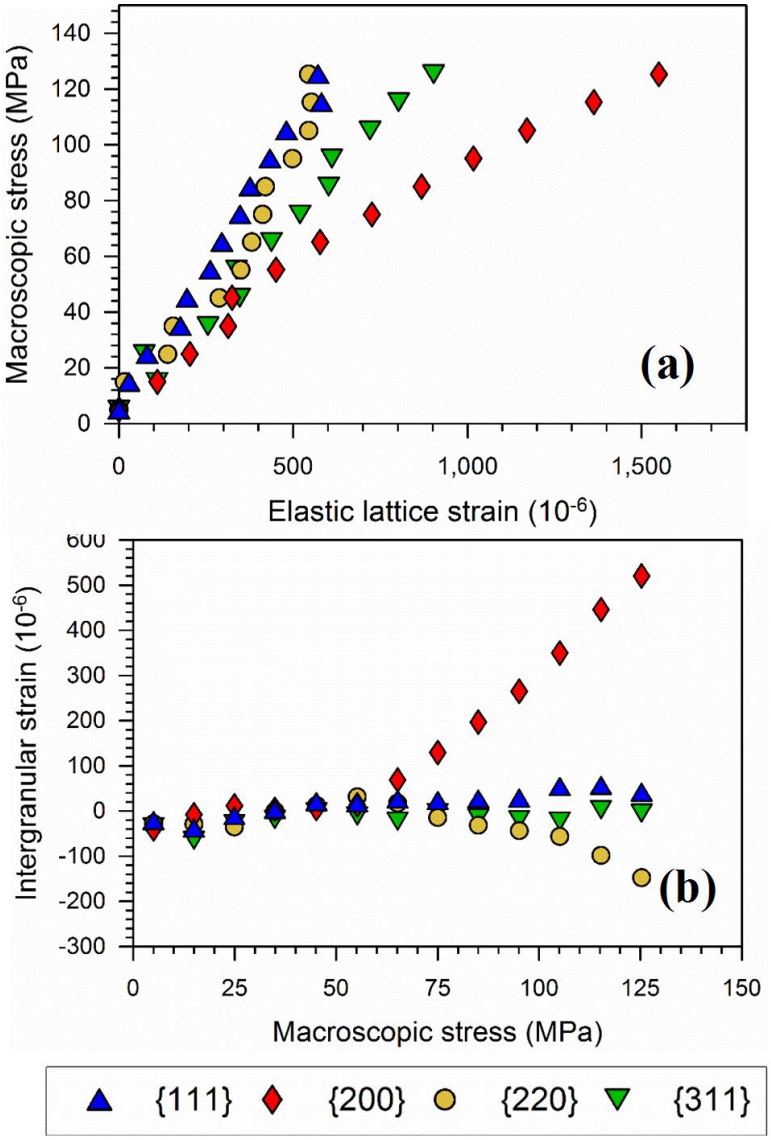

Figure 4-8 (a) Generation of axial lattice strain and (b) evolution of intergranular strains in different grain families during tensile loading of type 316H austenitic stainless steel (material B) at 650℃

When the macroscopic load is applied to a polycrystalline material like type 316H austenitic steel, differently oriented grains elastically deform differently because of the anisotropy in elastic properties of the grains. When the load is increased further, plastic deformation in the material is initiated by slip occurring on a single slip plane of a single grain. The yielding of grains with a particular orientation activates slip in a number of parallel slip planes before it propagates to the next favourably oriented grains [204]. When the sheared region is extended

more, this propagation increases leading to a macroscopic yield of the material. Therefore, during the elastic-plastic transition of deformation, grains which are favourably oriented for slip, start to deform plastically while other grains are still deforming elastically. When a particularly oriented grain family starts yielding, the increment of elastic strains in that grain family with increasing applied stress is relatively smaller. Therefore, the measured elastic lattice strains start to deviate negatively from the earlier slope of elastic lattice strains of that grain family, as can be seen for the {220} grain families. Conversely, elastic strains in other grain families, for example in the {200} grain families, start to deviate positively by bearing a larger share of the applied load.

If only plastic anisotropy of grains is considered, the grains with orientations more favourable for slips to occur can be identified by simply calculating the Schmidt factor of the grain orientations. Based on such calculations, it is expected that the {200} grain family will yield relatively earlier in this material, however, the experimental results show that this grain family is one of the last to yield. This is due to the fact that, the stress that differently oriented grain families experience is itself different due to inherent elastic anisotropy in the material. Therefore, although the critical shear resolved stress required for slips to occur in particular orientation of grains is less, it may not yield first as the stress experienced by these favourably oriented grains can be lower than grains with other orientations. This complex inhomogeneity in deformations due to elastic and plastic anisotropy generates the intergranular strains in the material.

The magnitude of intergranular strain in any individual grain family at any particular applied stress can be measured by quantifying the deviation of elastic lattice strain of that grain family from its initial linear elastic line. Alternatively, if the macroscopic material is elastically unloaded after being plastically deformed (or at least some of the grains being plastically deformed), upon unloading the grains will retain a portion of the elastic strain as residual strain, which again is a measure of the intergranular strain in that grain family at that particular load from which the material has been unloaded. In the following sections, both of these measures for intergranular strains are used to illustrate the generation of intergranular strains during different mechanical deformation.

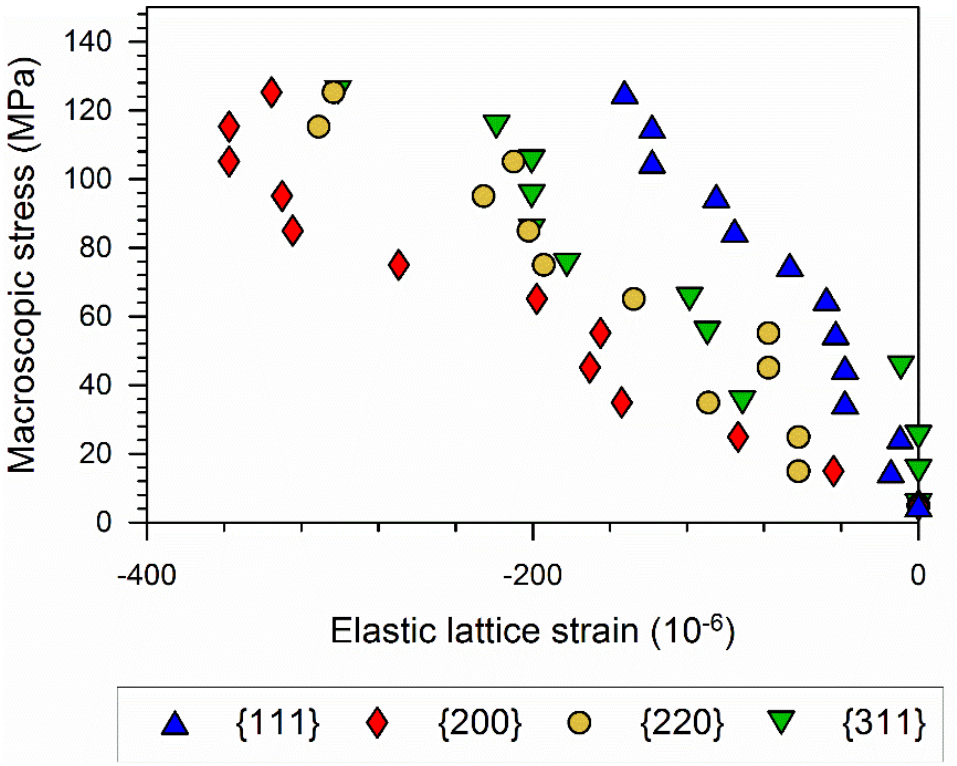

Figure 4-9 Evolution of lattice strain in transverse direction during tensile loading of type 316H austenitic stainless steel at 650℃

Figure 4-8(a) shows the results from a tensile test of type 316H austenitic stainless steel conducted at 650℃. During high-temperature deformation of type 316H austenitic steel, conventional slip is not the sole mechanism of plastic deformation. Other mechanisms such as dislocation glide or glide plus climb could also cause plastic deformation and this will affect how the intergranular strains are generated and how those are balanced between differently oriented grain families. In Figure 4-8(a), it can be observed that the {200} grain family accumulates the maximum lattice strains, while the {220} and the {111} grain families accumulate the minimum. Deviation of stress vs lattice strain from linearity is more prominent in this test than that of the room temperature test, suggesting generation of a higher magnitude of intergranular strains during high-temperature deformation in this material. Figure 4-8(b) shows the evolution of intergranular strain, calculated from the difference between the measured lattice strain and the lattice strain predicted using diffraction elastic constants. Intergranular strains in different grain families start evolving at a slightly different applied stress; first being generated at ~65 MPa in the {200} grain families and then being generated at ~80 MPa in the {220} grain families. From the direction

of deviation of the lattice strains from the linearity, it can be stated that the intergranular strains generated in the {200} grain family are tensile and that in the {220} grain family are compressive. Intergranular strains in the {311} and {111} grain family were found to be almost negligible. In other words, if the material is unloaded from the peak tensile stress elastically to zero applied stress, the grains belonging to the {200} and the {220} grain families will end up in tension and compression respectively, while the grains belonging to the {311} and the {111} grain families will unload to zero strain.

Figure 4-9 shows the evolution of lattice strain in the transverse direction (perpendicular to the loading direction) during a same tensile test at 650℃. The {200} grain families accumulate maximum compressive strains and the {111} grain families the minimum, similar to that in the axial direction but in opposite sense. The lattice strains in various grain families are more scattered in this direction than that in the axial direction. The deviation of the lattice strains in the grain families from its initial linearity is not as clear as in the results of the axial direction. However, there are clear differences between the macroscopic stress vs lattice strain deformation characteristics of the different grain families that are the magnitude of intergranular strains in various grain families. Strain measurement with neutron diffractions in the transverse directions are far less reliable than that in the axial directions [206] [207] [151]due to increasing uncertainty of the exact grain population in this orientation. Even small levels of texture in the material can affect the responses in a transverse direction significantly [206]. In most of the following sections, only results of the axial directions are discussed.

4.3.2 Incremental load-unload tests

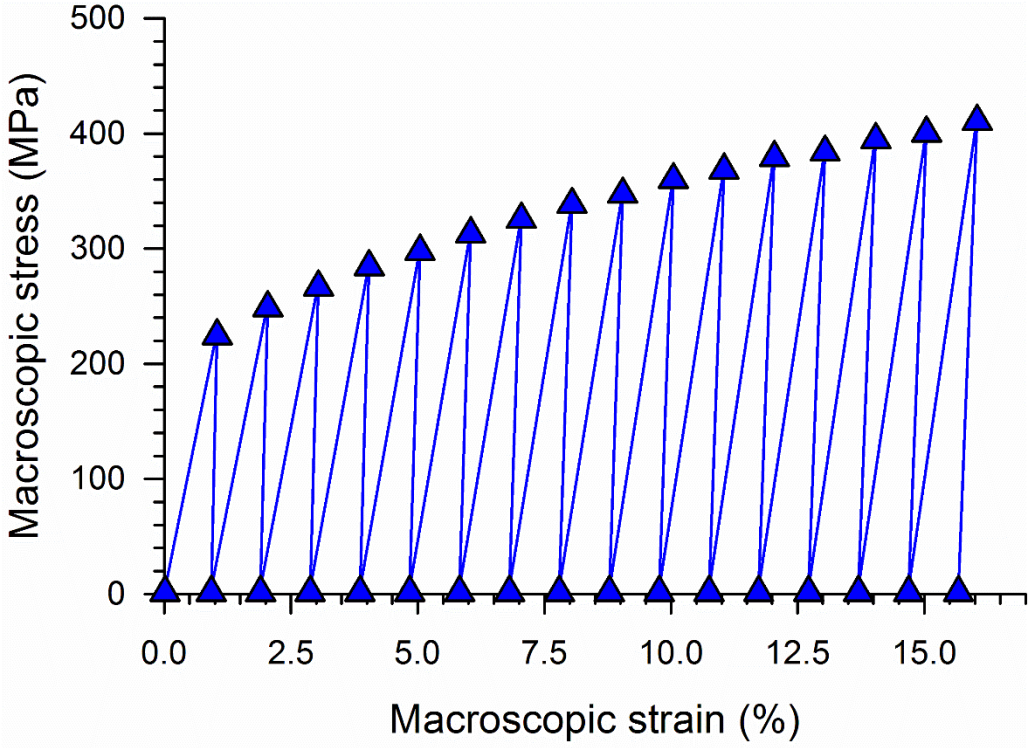

Figure 4-10 Loading sequence of an incremental tensile test conducted at room temperature. Measurements of lattice strain were obtained at the peak strain and at the unloaded state as shown by the triangle markers.

A systematic approach has been employed in studying the evolution of intergranular strain during plastic deformation. In these tests, the specimen was loaded in tension, or compression, up to a known value of macroscopic strain and the lattice strain at that point measured. The specimen was then unloaded to near zero stress (5 MPa) in order to measure the residual lattice strain upon unloading. As described earlier, this measured residual strain in any specific grain family is a measure of the intergranular strain in that family. Following measurement at the 'unloaded' state, the specimen was reloaded to a higher macroscopic strain (usually with an increment of 0.5% or 1% strain) and the procedure repeated. Figure 4-10 shows the loading sequence undertaken for the room temperature incremental tensile test; the blue triangles being the points at which neutron measurements were undertaken. In this test, an increment of 1% strain has been taken after each load-unload cycle.

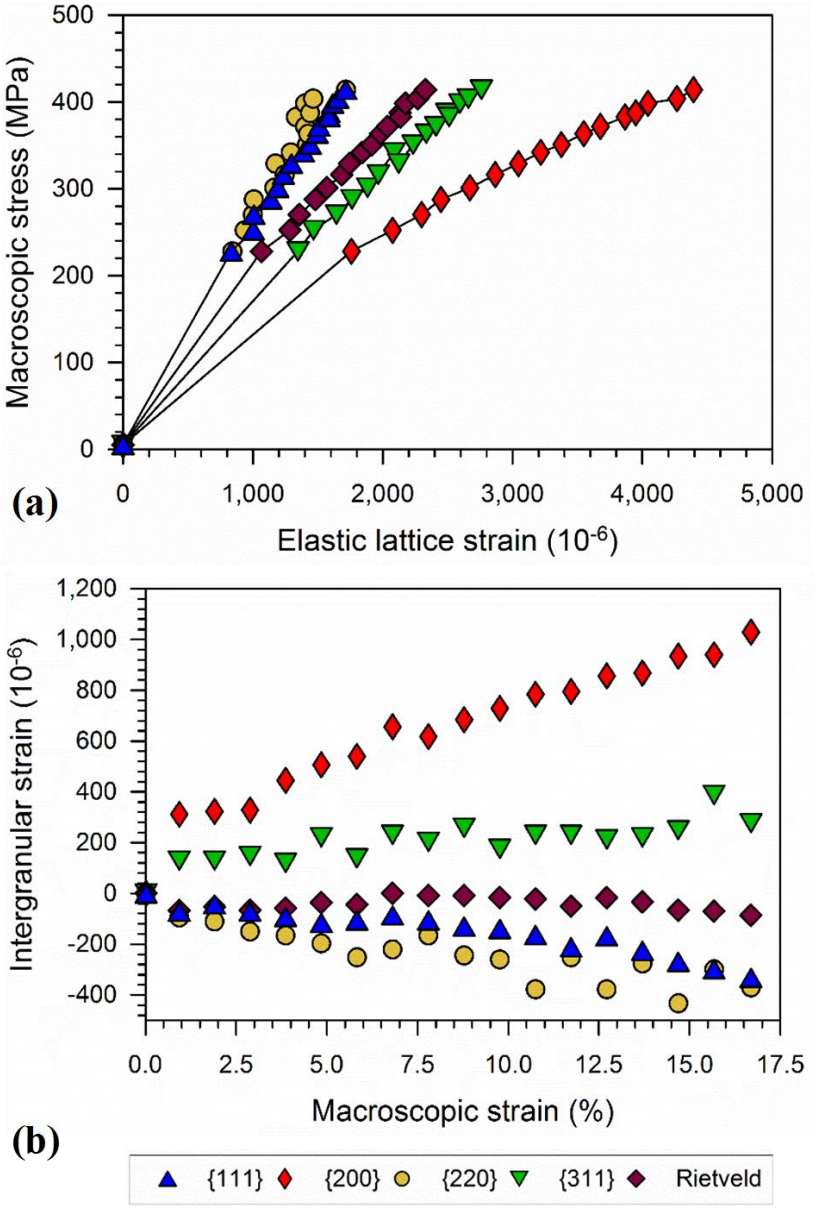

Figure 4-11 Evolution of (a) lattice and (b) intergranular strain in different grain families during an incremental tensile test of type 316H austenitic stainless steel at room temperature. The measurements of (a) lattice strain were collected at peak strain and measurements of (b) intergranular strain were collected after unloading, for each of the incremental loading cycles.

Figure 4-11 shows the evolution of axial lattice and intergranular strain during the incremental tensile test at room temperature. In Figure 4-11(a) the evolution of lattice strain is plotted against macroscopic stress and in Figure 4-11(b) the evolution of intergranular strain is plotted against macroscopic strain in order to illustrate the data more meaningfully. In Figure 4-11(a), the evolution of lattice strain in different grain families shows a similar trend to that in Figure 4-7(a), the {200} grain family accumulating higher tensile lattice strain

than the {220} and {110} grain families. The lattice strains increase with increasing applied stress, however, after the material reaches to a certain magnitude of plastic deformation (at about 350 MPa), the elastic lattice strains in the {220} grain family stop increasing with increasing applied stresses. This saturation behaviour implies that grains belonging to this family are yielded at this macroscopic stress.

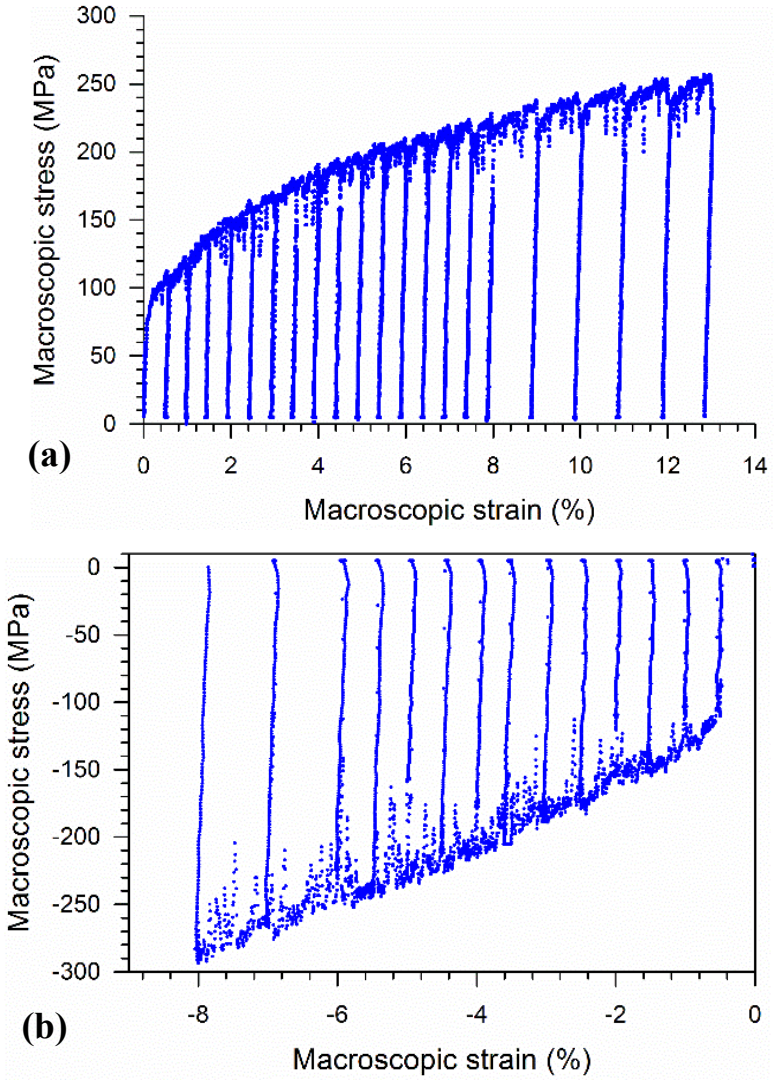

Figure 4-12 Experimental programme and macroscopic deformation curve of incremental (a) tension and (b) compression test of 316H austenitic steel at 650℃.

Figure 4-11(b) shows the changes in intergranular strain in different grain families with increasing strain. The increase of intergranular strains in the {200} grain family is greatest and almost a linear function of the macroscopic strain. Only a small increment of compressive intergranular strains can be noticed in the {220} and {111} grain families. The

magnitude of intergranular strain in the {311} grain family is slightly tensile and remains almost unchanged with respect to increasing macroscopic strain.

Figure 4-12 shows the experimental programme and macroscopic stress-strain curve for incremental tensile and compressive tests at 650℃. The test programme was essentially similar to the room temperature test except that a finer increment of strain (0.5% strain) was used for the first part of these tests. The macroscopic curve for the compression test is almost a mirror image of the tensile test, both in terms of magnitude and shape. Unlike the room temperature test, upon unloading from a tensile or compressive peak strain, a very small amount of strain was recovered. This recovery was time dependent and occurred during the holding time, in load control, while the neutron measurement was made in the unloaded state. This strain recovery phenomenon is known as anelasticity. Intergranular strains are believed to play a strong role in causing this anelastic recovery in this material at high temperature [81].

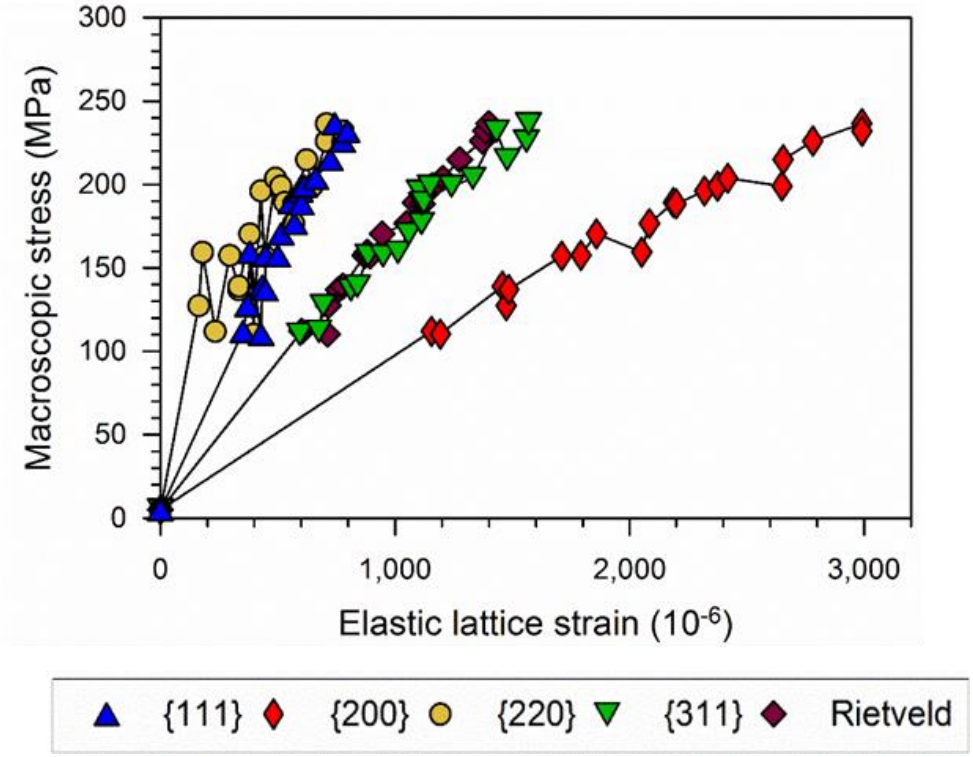

Figure 4-13 Evolution of axial lattice strain during incremental tensile testing of 316H austenitic steel conducted at 650℃

A change in experimental plan for the high-temperature test was made in order to observe the changes in intergranular strains during anelastic recovery of strains and to look for any

correlation between the that and the macroscopic strain recovery. In order to do so, two neutron measurements were collected upon unloading from each tensile and compressive peak load, instead of one. In type 316H austenitic steel, the largest anelastic recovery has been observed in first few minutes after unloading at this temperature [173]. To capture the differences, the first measurement was shortened in time to 3 minutes and then a second measurement is taken immediately after. However, the changes in intergranular strains were too small to resolve any conclusion from the data (not presented here). Anelasticity and its relationship with intergranular strains are discussed further in Chapter 5 and Chapter 6.

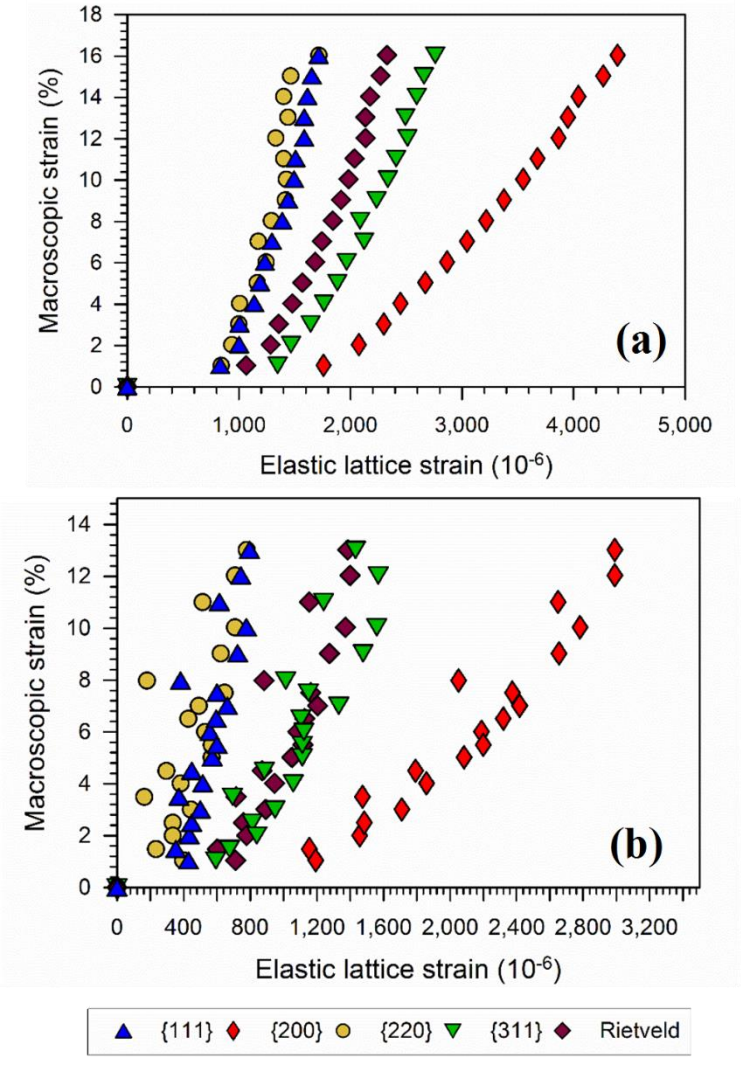

Figure 4-14 Comparison of the evolution of lattice strains during incremental tensile deformation at (a) room temperature and (b) at 650℃

Figure 4-13 shows the evolution of axial lattice strain during an incremental tensile test at 650℃. Compared to the room temperature test, a significant increase in the scatter of the data can be noticed, this is expected as coherent neutron scattering is attenuated at high temperature due to the Debye-Waller factor. Similar to that of room temperature test, the {200} grain family accumulates the maximum lattice strain while the {220} grain family accumulates the minimum, at any given macroscopic stress.

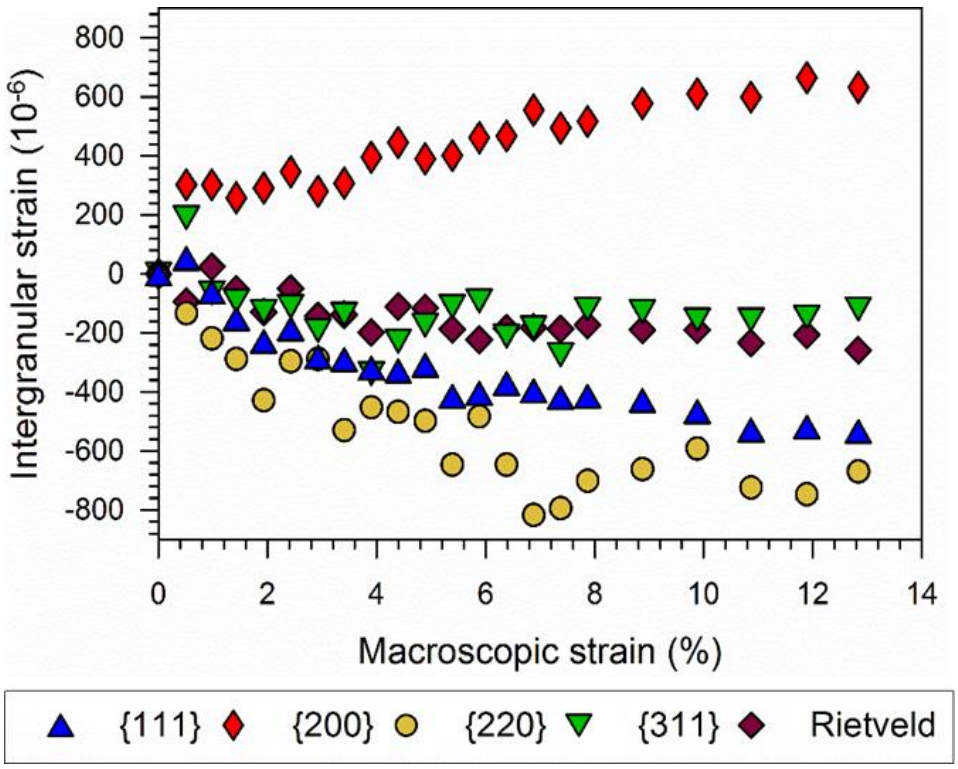

Figure 4-15 Evolution of intergranular strains during incremental tensile loading of 316H austenitic steel at 650℃

Only elastic strains are measured using the neutron diffraction technique, however, by investigating the trend of the elastic lattice strain vs macroscopic strain behaviour gives an insight into the onset of plastic deformation in any specific grain family. Generally speaking, if the elastic lattice strains in a particular grain family stop increasing with increasing applied stress, that means, grains belonging to that family can no longer accommodate any further elastic loading, that all grains belonging to that family have started to deform plastically. Thus the onset of plastic deformation in grains with a specific orientation can also be qualitatively estimated. An example is shown in

Figure 4-14, in which elastic lattice strains have been plotted against macroscopic strain for the (a) room temperature and (b) high-temperature test. It can be observed that after about 8% macroscopic strain in room temperature test and at about 4% strain in high-temperature test, the elastic lattice strains in the {220} and the {111} grain families have almost stopped increasing with increasing applied stress. This suggests that the grains belonging to these grain families have already yielded, while grains of other families, for example, those belonging to the {200} grain families are still deforming elastically.

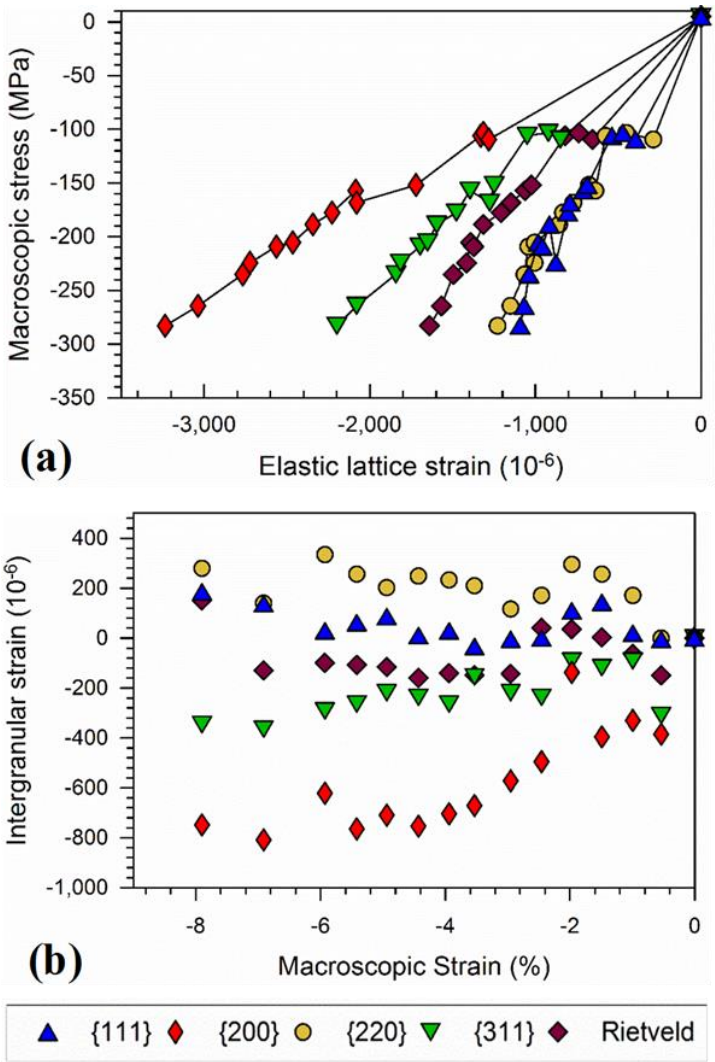

Figure 4-16 Evolution of axial (a) lattice and (b) intergranular strain during incremental compression test of type 316H austenitic stainless steel at 650℃.

Figure 4-15 shows the evolution of intergranular strain during the incremental test at high temperature. Compared to the room temperature test, the tensile intergranular strain in the {200} grain family is more evenly balanced by the compressive intergranular strain in the

{220} grain family. Unlike the room temperature test, compressive intergranular strains in both the {220} and {111} grain families to increase in a mirror sense to the tensile intergranular strains in the {200} grain family. The intergranular strain in the {311} grain family is negligible and resembles closely the bulk Rietveld response.

Figure 4-16(a) shows the evolution of axial lattice strain and Figure 4-16(b) shows the axial intergranular strain during incremental compression test of type 316H austenitic steel at 650°C. All grain families presented here accumulate increasing compressive lattice strains with increasing macroscopic strain. The deviation from initial elastic linearity is in an opposite sense to that of the tensile test as can be seen in Figure 4-16(b), that is with increasing strain, the {200} grain family accumulates compressive intergranular strain and the {220} grain family accumulates tensile intergranular strain. The magnitude of intergranular strain in the {200} grain family is much higher than the magnitudes in other families.

4.3.3 Tension-compression cyclic loading

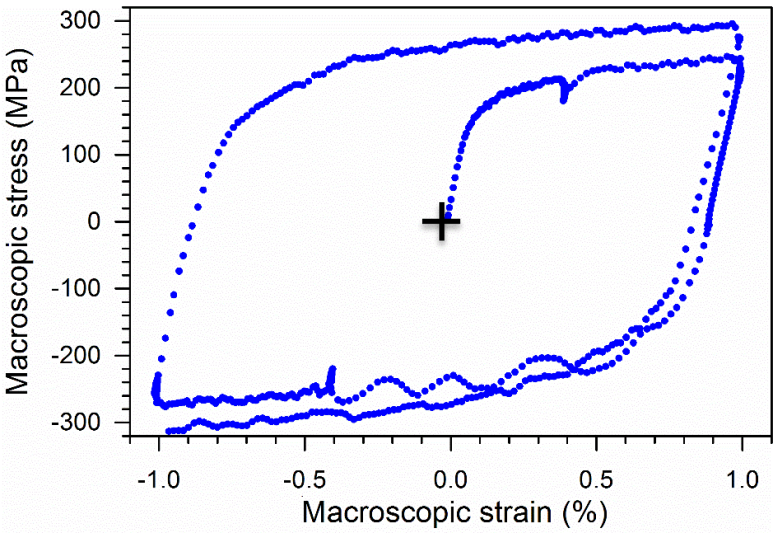

Figure 4-17 Macroscopic stress-strain curve during tension-compression cyclic loading of 316H stainless steel at room temperature. During the elastic regime the neutron measurements were conducted in stress control and during plastic regime, the measurements were conducted in strain control.

Generation of intergranular strain was investigated during room and high temperature tension-compression cyclic loading, in which specimens were cyclically loaded in strain control within a fixed tension-compression ±1% strain range. Lattice strains were measured

at selected points by stopping in stress control during elastic loading and in strain control during plastic loading. This was to avoid creep occurring in the material under higher stresses during the neutron measurements. Figure 4-17 shows the experimental programme for room temperature cyclic loading, the neutron measurements were collected only in few points on the loading path, due to the limitation of the neutron beam time.

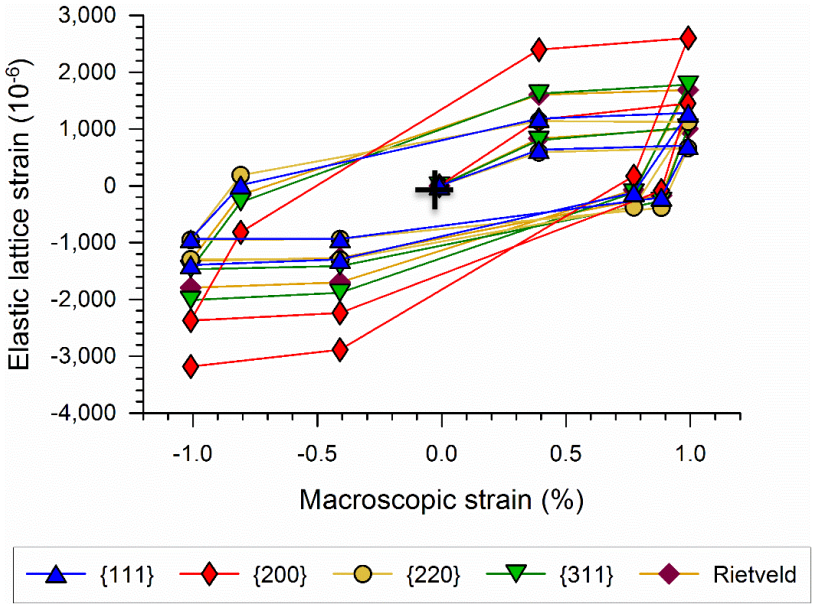

Figure 4-18 Evolution of lattice strains in different grain families during tension-compression cyclic loading of 316H austenitic steel at room temperature

Figure 4-18 shows the evolution of axial lattice strain in different grain families during tension compression cyclic loading of 316H austenitic steel at room temperature. Elastic lattice strains in various grain families' were found to increase with repeated cycling; the increase being more significant in some grain families than the other. The increase of the elastic lattice strains is associated with the increase of macroscopic stress due to strain hardening occurring in the material. The {200} grain family was found to be most responsive to the changes of macroscopic load. The grain families sustaining higher tensile and compressive lattice strains in the tensile half cycle also sustain higher compressive and tensile lattice strain respectively in the compression half cycle. Upon reversal of load from tensile to compressive, the lattice strains of the grain families do not change directions instantly. This means, a change of direction of lattice strains do not take place at zero macroscopic strain rather at a positive macroscopic strain during unloading and a negative macroscopic strain during reloading.

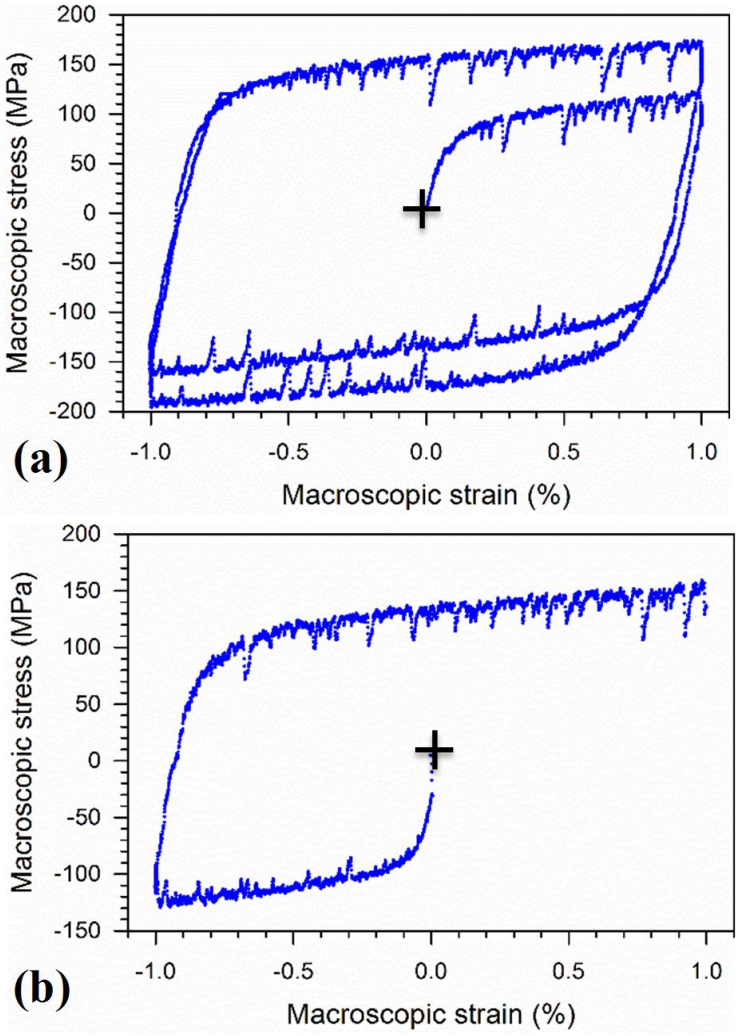

Figure 4-19 Macroscopic stress-strain curve of displacement controlled (a) tension-compression and (b) compression-tension tests of 316H austenitic steel conducted at 650℃. Stress relaxation is observed at various points in the curve due to neutron measurement at those points in strain control.

A high-temperature tension-compression test, similar to that at room temperature, was conducted. An additional compression-tension test was also conducted at high temperature, in which the loading was applied in compression first instead of tension. Figure 4-19(a) shows the macroscopic deformation curves for tension-compression and Figure 4-19(b) for compression-tension test. Compared to the room temperature test, a greater number of measurements were collected during the tests, in order to capture a more detailed variation of lattice / intergranular strains with macroscopic loading.

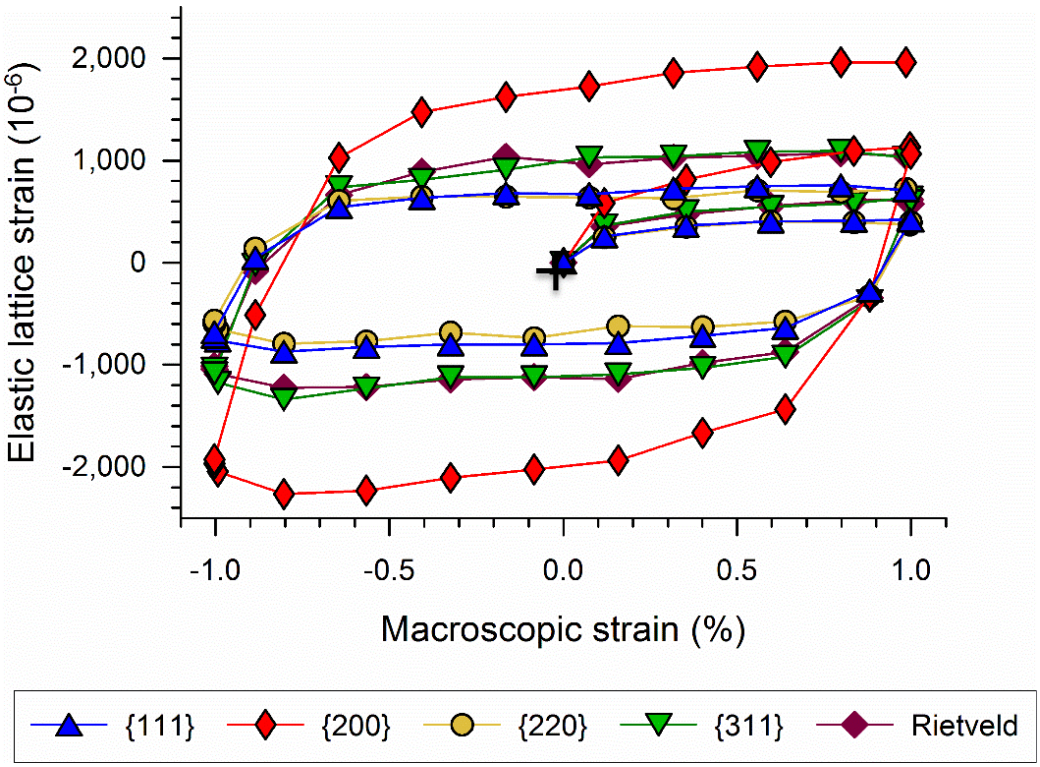

Figure 4-20 Evolution of lattice strains during tension compression cyclic loading of 316H austenitic steel at 650℃

Figure 4-20 shows the evolution of lattice strain during tension-compression cyclic loading at 650℃. Compared to the room temperature test, the magnitudes of lattice strains at this temperature are much lower both in peak tension and compression. The lattice strains in all the grain families increase with repeated cycling, more in the {200} grain family than the others. Figure 4-21 shows the evolution of lattice strain of the {200} and the {111} grain families during the test, to give an example of how differently oriented grain families are deforming during cyclic loading. It can be clearly seen that the lattice strains in the {111} grain family evolve almost linearly while that of the {200} grain families deviate from linearity more and more with repeated cycling. At zero macroscopic stress, the lattice strain in the {200} grain family is positive (tensile) during unloading from a tensile peak strain and negative (compressive) during reloading from compressive peak strain. This shows that residual lattice strain (that is intergranular strain) in this grain family is increasing with repeated cycling. On the other hand, at zero macroscopic stress, lattice strain in the {111} grain family is very close to zero, and may only be slightly tensile and compressive during unloading and reloading respectively. Therefore, intergranular strain remains insignificantly

changed for the {111} grain family although the lattice strain is increased with repeated cycling.

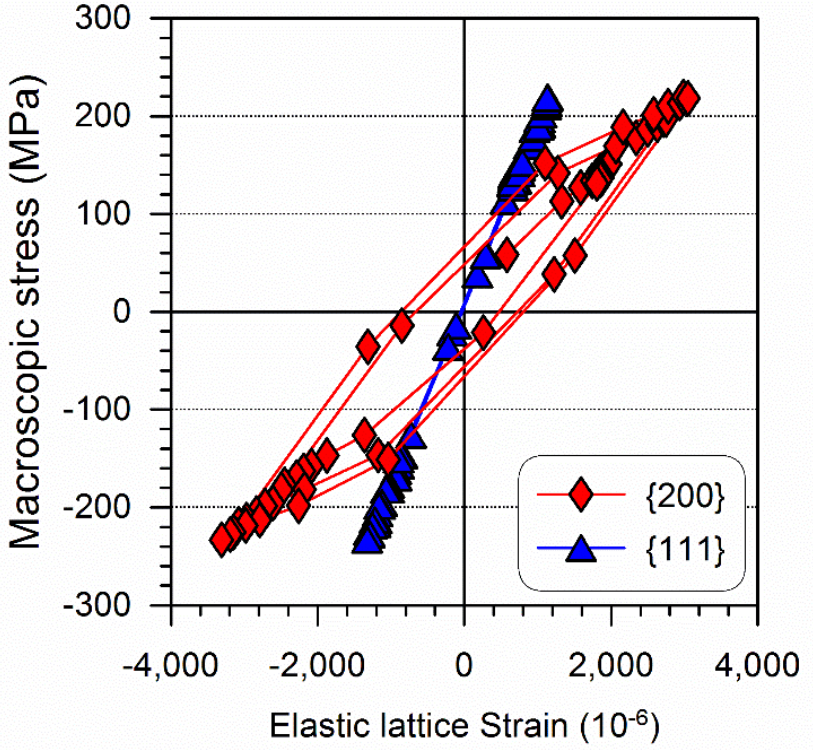

Figure 4-21 Comparison of lattice strain evolution between {111} and {200} grain families during cyclic loading of 316H austenitic stainless steel at 650℃

Figure 4-22 shows the evolution of intergranular strain in the {200} and {220} grain families during cyclic loading in which a number of features can be noticed. After the first half tensile cycle of loading, the magnitude of intergranular strains in the {200} and the {220} grain families is almost similar but tensile in the {200} grain families and compressive in the {220} grain families. With repeated cycling, the intergranular strains in the {200} grain family increase significantly more than these in the {220} grain family. Compared to the macroscopic curve, it can also be noticed that the magnitude of intergranular strain is neither a function of the macroscopic stress nor the strain. It varies significantly depending upon the position in the loading cycle and loading path history, for example, at an applied stress of 100 MPa, intergranular strains in the {200} grain family at the first half cycle is ~ 30 με while at the 2nd cycle during reloading from compression peak strain is ~ -400 με.

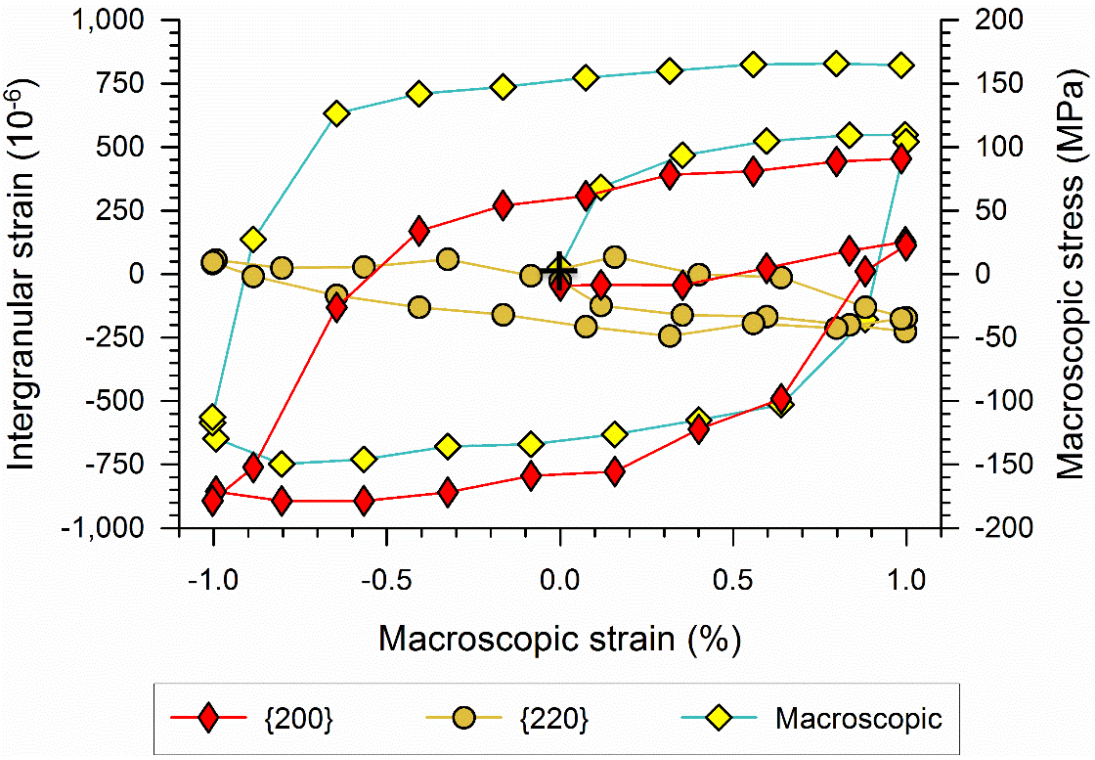

Figure 4-22 Evolution of intergranular strains during tension-compression cyclic loading of 316H austenitic steel at 650℃

Figure 4-23 shows the evolution of lattice strains during the compression-tension test. The distribution of lattice strain between grain families is similar to that of the tension-compression test but in opposite sense, no fundamental difference can be noticed in the evolution of lattice strain for this test in comparison to that of the tension-compression test, therefore the test was stopped halfway. Figure 4-24 shows the evolution of intergranular strains during the compression-tension test. In first half compression cycle, the magnitude of intergranular strains in the {200} grain family is found to be much higher than that of the {220} grain family. However, on reaching 1% tensile strain in the next half cycle, the magnitudes become almost similar in these two grain families but tensile in the {200} grain families and compressive in the {220} grain families. Intergranular strain in the {311} grain family is negligible during first half compression cycle but it increases significantly in compression during the reverse tensile cycle.

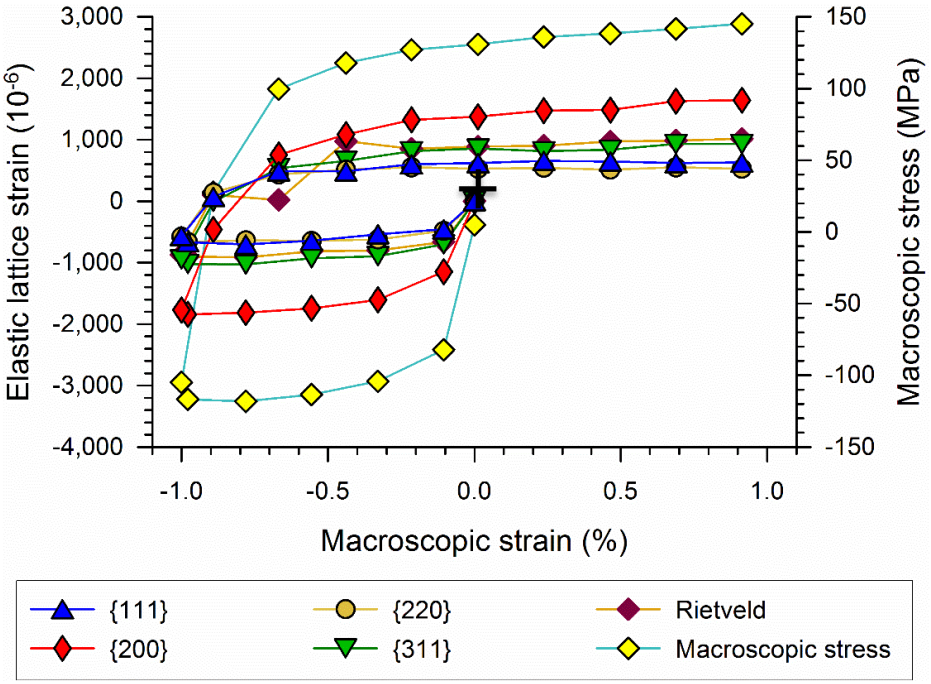

Figure 4-23 Evolution of elastic lattice strain during compression-tension cyclic loading of 316H austenitic steel at 650℃

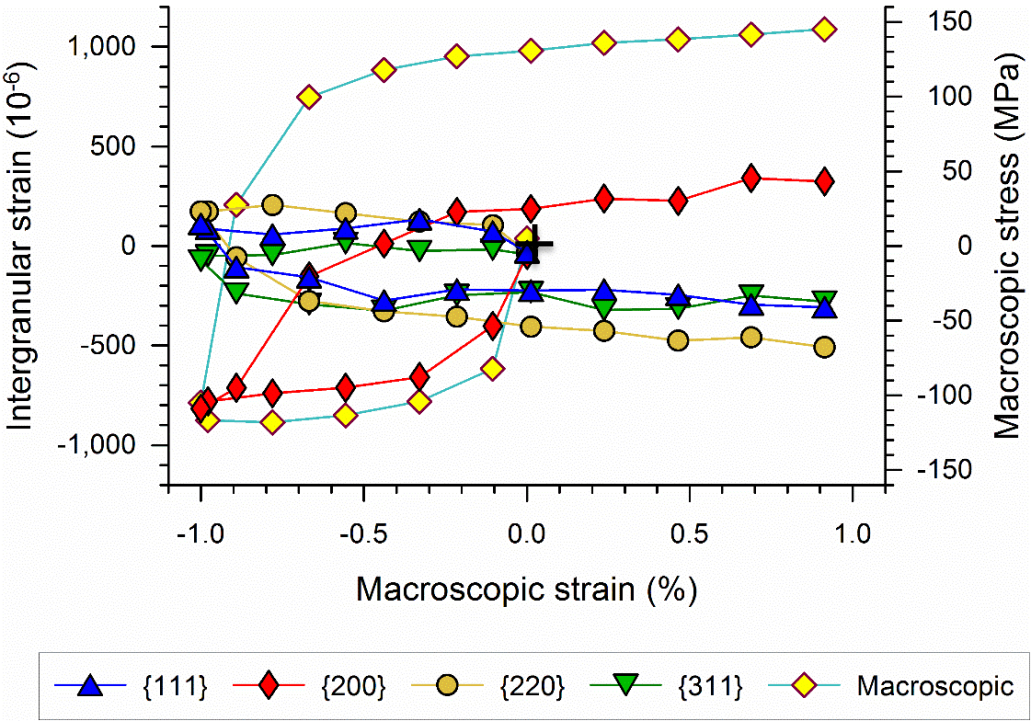

Figure 4-24 Evolution of intergranular strains during tension-compression cyclic loading of 316H austenitic steel at 650℃

4.4 Summary

This chapter has been presented in two distinct parts. In the first part, materials used in the project have been described and results of relevant material characterisation have been presented. In the second part, generation of intergranular strains during various mechanical deformation relevant to real life engineering applications have been described. The main findings from both parts of the work are summarised below.

Material characterisation

Two different batches of material have been used in this project, one batch (material A) extracted from an ex-service header supplied by EDF energy and the other batch (material B) extracted from outsourced virgin material in the shape of the cylindrical bar. OES analysis has been conducted for both sets of material and only small differences in weight percentage of alloying elements has been noticed. Material A has been used for the pilot studies due to its earlier availability and material B has been used for the rest of the tests.

Tensile testing at room and high temperatures of both batches of material have been conducted. Material A was tensile tested at a number of different strain rates and no significant strain rate sensitivity was found for this material at the room temperature. The yield stress of material B at room and the high temperature was determined; the yield stress at room temperature closely matched the value provided by the supplier in the material test certificate and the value reported in the literature for conventional type 316H stainless steel. Other characterizations conducted on this material include hardness measurement, grain size measurement and texture measurement. In the as-received condition, the average hardness of the material was found to be 120 ± 7 HV and average grain size was found to be 71 ± 4 μm. The material was found to have a weak texture with a maximum MUD of 2.22.

Intergranular strain generation

Generation of intergranular strains has been studied during room and high-temperature tensile, load-unload and cyclic deformation using in-situ neutron diffraction. During elastic deformation, differently oriented grain families were found to deform differently depending upon their specific crystallographic elastic stiffness. Significant intergranular strains start to

generate during elastic-plastic deformation of the material due to a combination of elastic and plastic anisotropy.

In almost all loading sequences, the {200} grain family was found to accumulate maximum lattice strains and the {220} and the {111} grain families were found to accumulate minimum lattice strains. The lattice strains of the {311} grain family was found to resemble the average response captured by Rietveld refinement; with closer correlations at room temperature than at high temperatures. The intergranular strains in the grain families increase with macroscopic plastic strain, the increase being significant only in the {200} and {220} grain families. During cyclic deformation at room and high temperatures, intergranular strains were found to increase with repeated cycling, again, the increase being significant only in the {200} and the {220} grain families. It has been found that the direction of intergranular strains in a grain family does not change instantly with the change of direction of macroscopic loading, rather, it starts changing when the macroscopic material starts to plastically deform in the reverse direction. The {200} grain family has found to be the most responsive of the grain families of these changes, accumulating maximum tensile intergranular strain at macroscopic tensile peak strain and maximum compressive intergranular strain at macroscopic compressive peak strain. It has also been shown that the magnitude of intergranular strain is not a function of total strain/stress in the material, that is, at an identical stress/strain, the magnitude of intergranular strains in a grain family could be very different depending upon the loading path history.

Chapter 5 The role of intergranular strains in the Bauschinger effect

5.1 Overview

Kinematic hardening of steel during tension compression cyclic loading was first described by Bauschinger [82] in 1886. In his paper he established the following two laws [87]:

- If a bar is loaded beyond its elastic limit, this increases the elastic limit of the bar for a subsequent load
- Plastically deforming a bar in tension or compression reduces the elastic limit of the bar for a subsequent compression or tension loading respectively. The more the bar has deformed plastically the greater the reduction in reverse loading elastic limit.

Bauschinger effect can significantly affect the deformation response of materials and structures which experience tension-compression cyclic loading, by altering the material's elastic limit during the reverse cycle. This can be important for the life assessment of power plant components as many components go through cyclic loading in plant operation due to cyclic thermal stresses generated during start-up, shutdown, fault, or repair of the plant. Moreover, there is a growing need for large power plants to operate in 'load-follow' mode to fill the gaps created by low carbon power generation (for example solar and the wind) which can be intermittent in nature. The components in this type of plant will experience frequent load cycles. Inelastic constitutive models (for example [208]), are usually used to predict the evolution of stress-strain during such cyclic loading in which Bauschinger tests are often used as a sensitive probe for comparing against the physical understanding of work hardening in the material. Therefore, to develop an accurate inelastic constitutive model for a material it is critical to understand the sources/mechanisms of origin of the Bauschinger effect in that material.

The Bauschinger effect has been observed in many single crystals and polycrystalline metallic materials including aluminium [209], nickel [210], steel [119, 211], copper and brass [212]. Many investigations have been conducted exploring the origin of the observed Bauschinger effect in various metals and a number of theories have been proposed [86]. The most notable of those explanations are given by Orowan [93] and Sleeswyk [94] which describe the mechanism by proposing easy reversibility of dislocation motions upon load reversal. Mughrabi [31] proposed the role of intragranular stresses (originating from inhomogeneous distributions of dislocations cell type structures) as a potential source of back stress causing the Bauschinger effect.

In this chapter, results of a set of experimental works exploring the role of Intergranular (IR) strains on causing the Bauschinger effect in type 316H stainless steel at room and high temperatures are presented. The main aim of the experimental works was to investigate whether IR strains is a dominant contributor to the observed Bauschinger effect in type 316H stainless steel at room and high temperatures.

5.2 Experimental

A similar experimental approach was undertaken for the room and high temperature tests. In this section, the generic approach of the experiments is described, the details of the experimental plan for room temperature and high temperature tests are described separately in those respective sections.

The macroscopic loading sequence of the specimen followed the work done by Skelton [87]. AISI type 316H austenitic stainless steel specimens were subjected to tension-compression cyclic loading with a strain rate of 7×10^{-6} s^{-1} over a total strain range of ±1% up to the point of saturation of isotropic work hardening in the material. The loading was always started in tension. Figure 5-1 shows an example of such tension-compression loading sequence conducted at 650℃. The work hardening in the material with repeated cycling is most prominently observed in the first 5-6 cycles, after which it starts to saturate. The specimen's hardening was considered saturated when the difference in the stress required to reach to the peak strain (both tensile and compressive) in 2 subsequent cycles was less than ±1 MPa. Figure 5-2 shows an example of a stress-time curve of type 316H stainless steel at 650°C

used to determine the saturation of strain hardening. Care was taken such that the steady state cycles were not close to the fatigue endurance of the material.

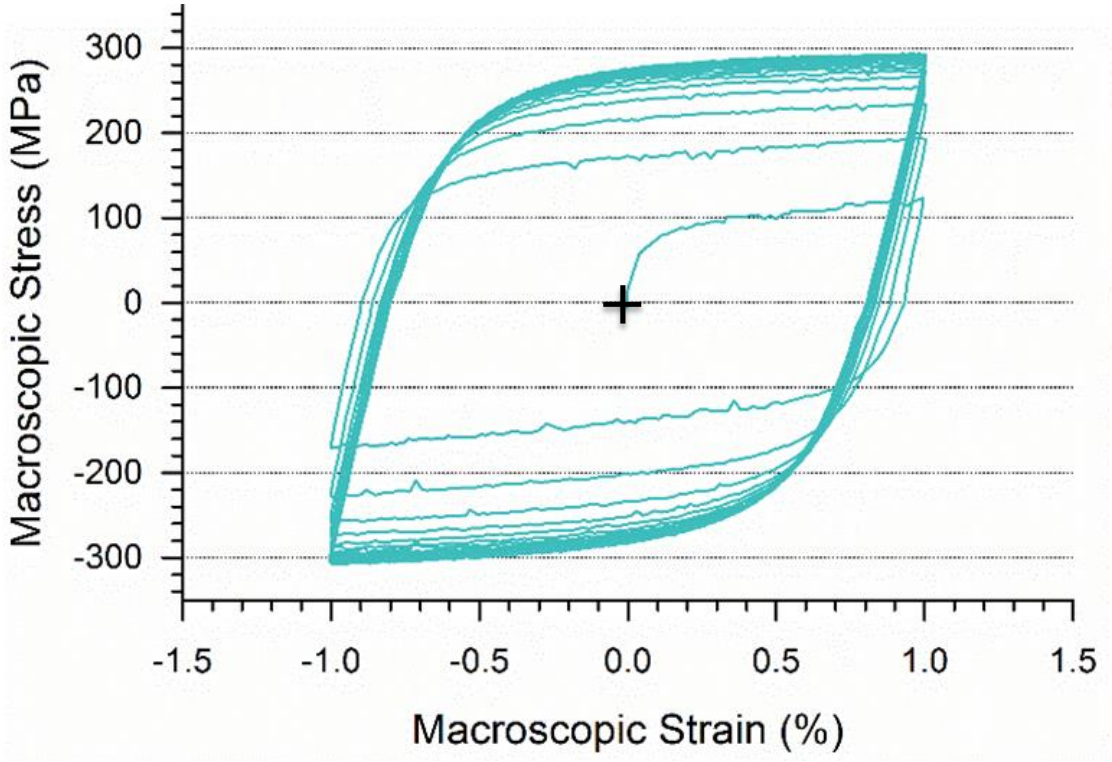

Figure 5-1 Evolution of stress-strain during tension-compression cyclic loading (in ±1% strain range) of type 316H stainless steel conducted at 650 °C. Large work hardening can be noticed in the material in the first 5-6 cycles after which the hardening starts to saturate with further repeated cycling.

The work hardening overserved in tension and compression is almost symmetrical, although, slightly higher compressive stresses can be observed reaching to 1% compression than that to reach to the 1% tension. Upon reaching an isotopically saturated work hardened stage, the loadings of the specimen were interrupted at various tensile and compressive strains, such that, a pronounced Bauschinger effect is observed in the material's yielding behaviour during reloading cycles. In between each interrupted cycle, at least 2 full cycles were performed to return the specimen to the saturated hardened state. Lattice strains in at least five grain families were measured in-situ during the interrupted loading cycles. The relative changes of elastic limits of the material with respect to the interruption strains and the evolution of IR strains during those are compared in order to capture the effect of the later on the former.

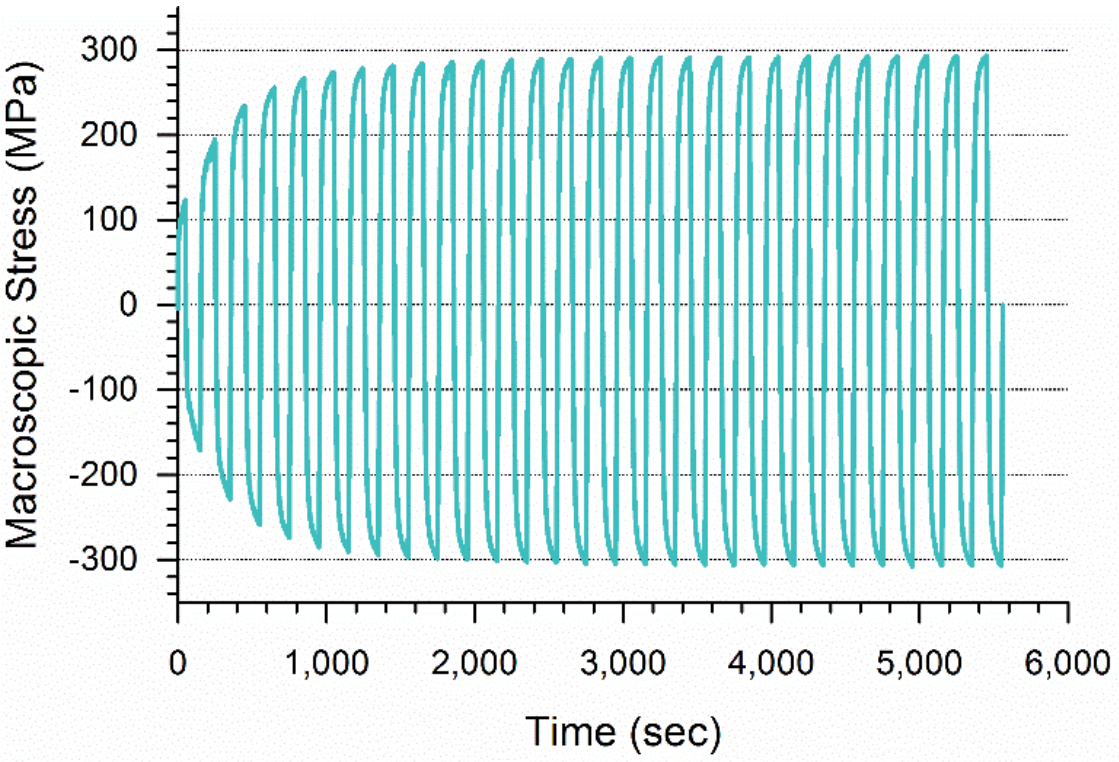

Figure 5-2 Evolution of work hardening in type 316H stainless steel during tension-compression cyclic loading conducted at 650°C with strain range of ± 1%. The isotropic work hardening was found to saturate after ~20 cycles determined by the criterion that the difference in the stress required to reach to the peak strain (both tensile and compressive) in 2 subsequent cycles was less than ±1 MPa.

5.3 Room Temperature Tests

5.3.1 Approach

The specimens used in the experiments were identical to that shown in Figure 3.5 in chapter 3. The specimens were extracted from AISI type 316H stainless steel bar (material B as referred in chapter 4) and heat-treated at 1050° C for 1 hour followed by a water quench. The cylindrical test specimen had a diameter of 8 mm and a gauge length of 14 mm. The Instron 100 KN stress rig available at the Engin-X diffraction beamline was used for the tests. Macroscopic strain was measured using an Instron high-temperature extensometer throughout the test.

Initial d spacing values (lattice spacing between 2 crystallographic planes) of variously oriented grain families were measured at the beginning of each test and used as the d_0 value

for the calculation of lattice strains throughout the test. This d_0 value was measured after applying a very small stress of 5 MPa in order to remove any slack in the load train of the stress rig. A neutron gauge volume of 4 × 6 × 4 mm^3 was used with an average neutron counting time of ~300 seconds per measurement point. Details of the neutron measurement technique and set-up of the experiments are provided in section 3.6 in chapter 3.

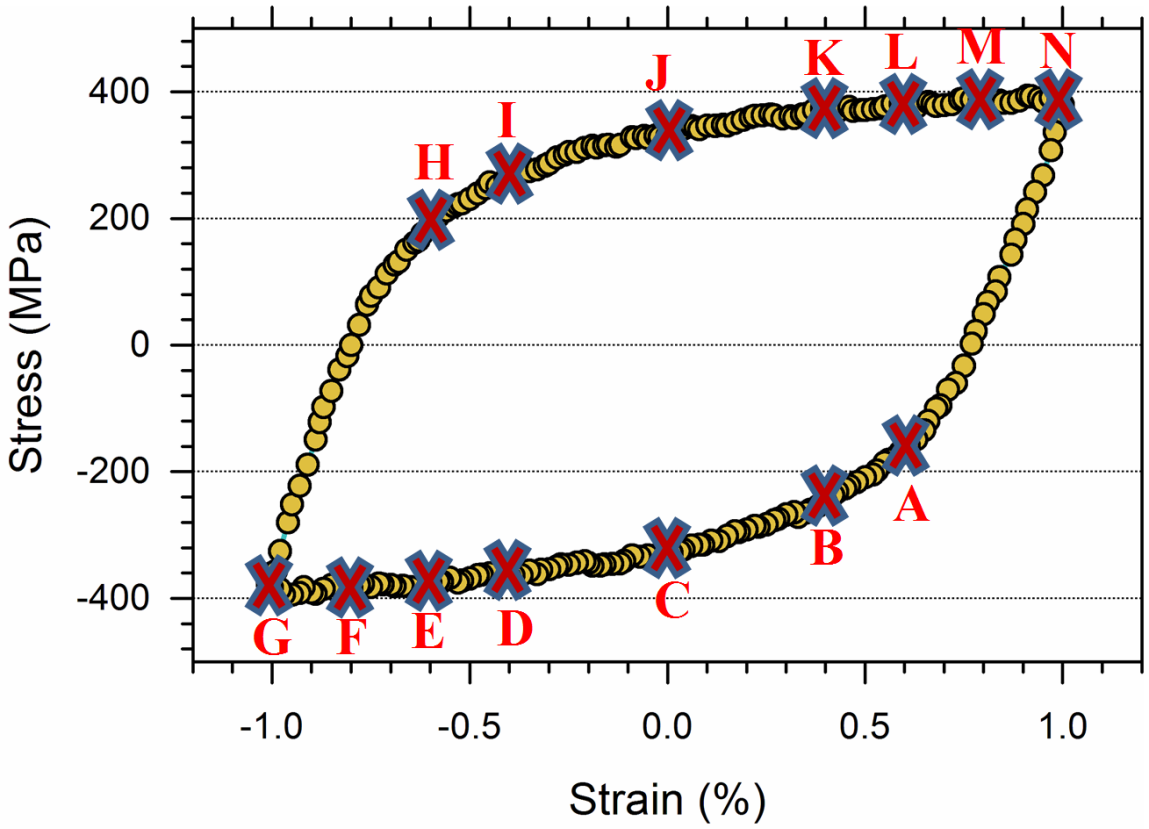

Figure 5-3 Interruption points for tension yield test shown in a typical stress-strain curve of 316H stainless steel after hardening saturation. Points A-G were interrupted while going into compression from a tensile peak strain of 1%. The specimen was reloaded to tensile peak strain after each of the interruptions. Points H-N were interrupted while going into tension from a compressive peak strain of -1%. The specimen was unloaded to near zero stress (~5 MPa) and reloaded back to tensile peak strain of 1% after each interruption.

Two tests were performed at room temperature using two identical specimens. The first specimen was tested to look at the changes in tension yield stress with respect to interruption at various points in tension and compression, hence the test is named ‘tension yield test’. The second specimen was tested to look at the changes in compressive yield stress es again with respect to interruption at various points in tension and compression, hence the test is named ‘compression yield test’. Upon reaching the saturated hardening stage (after ~20

cycles), the specimen's loading was interrupted at various points in the loading curves systematically. The interruption points of the tension yield test and compression yield test are shown in Figure 5-3 and Figure 5-4 respectively.

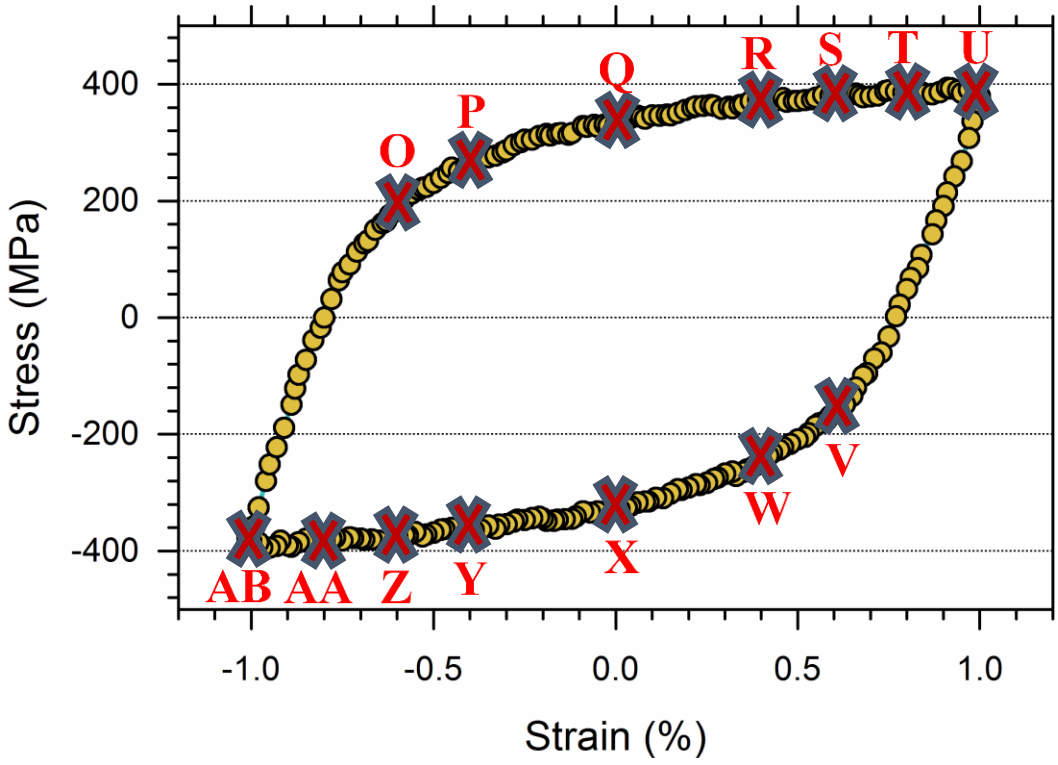

Figure 5-4 Interruption points for compression yield test shown in a typical stress-strain curve of 316H stainless steel after hardening saturation. Points N-T were interrupted while going into tension from a compressive peak strain of -1%. The specimen was unloaded to compressive peak strain after each of the interruptions. Points U-Z were interrupted while going into compression from a tensile peak strain of 1%. The specimen was unloaded to near zero stress (~5 MPa) and reloaded to compressive peak strain of -1% after each interruption.

In the tension yield test, the loading was first interrupted systematically at various points under compressive loads and reloaded back to the tensile peak strain of 1%. Loading of the same specimen was then interrupted at various points under tensile load followed by unloading to a near zero load (to 5 MPa) and reloading back to the tensile peak strain of 1%. The compression yield test is simply a mirror image test of the tension yield test. Thereby, the load was first interrupted systematically in tension and reloaded to the peak compressive strain of -1%. The load was then interrupted in compression, unloaded to 5 MPa and reloaded to -1% compressive strain. The interruption strains were chosen systematically at an interval of 0.2% strain, starting from 0.6% strain to -1% strain. A few interruption points (for

example 0.2% and -0.2%) were skipped because of the limited neutron experiment beam time availability.

Lattice strains were not measured directly at the point of interruption, because, the finite time required to make the neutron measurement would have allowed the macroscopic stress-strain state to change at the interruption points by creep (under stress control) or by stress relaxation (under strain control) [213]. Therefore, the lattice strains were measured in stress control upon unloading to 5 MPa after each interruption. This allowed the measurement of residual lattice strains in various grain families corresponding to different compressive and tensile interruption strains. After this measurement at 5 MPa, the specimen was loaded to 1% and -1% strain in the tension and compression yield test respectively. The lattice strains were also measured by stopping at various strains (at an interval of 0.2% strain) during each reloading cycle. The measurements were conducted keeping the specimen in strain control, therefore, macroscopic stresses relaxed during the measurement's duration. IR strains at each of these measured points were derived from the lattice strains using the procedure described in chapter 4.

The yield stress of a material can be defined by arbitrarily specifying a corresponding yield strain. In most engineering applications, the yield of the material is calculated at an offset of 0.002 strain. In this work, the yield stress has been determined at a strain offset of 0.05% and the same criteria has been used throughout the chapter. This smaller offset of strain has been chosen to measure the effect of the IR strain on the initiation of the macroscopic yielding more precisely. Use of such a yield strain is justified in published work, for example, in [87]. If the yielding of the material is sharp enough, the choice of the offset strain will not make any significant difference. In this thesis, the term 'yield stress' has been used referring to this measured yield stress at 0.005% strain offset.

The yield stress at this strain offset was calculated manually using Microsoft excel. In this process, a straight line parallel to the initial elastic stress-strain part of an unloading or reloading curve was drawn originating at a strain offset of 0.0005. The intersection of this line with the curve was taken as the yield stress for that corresponding curve. An example of determination of yield stress using this method is illustrated in Figure 5-5.

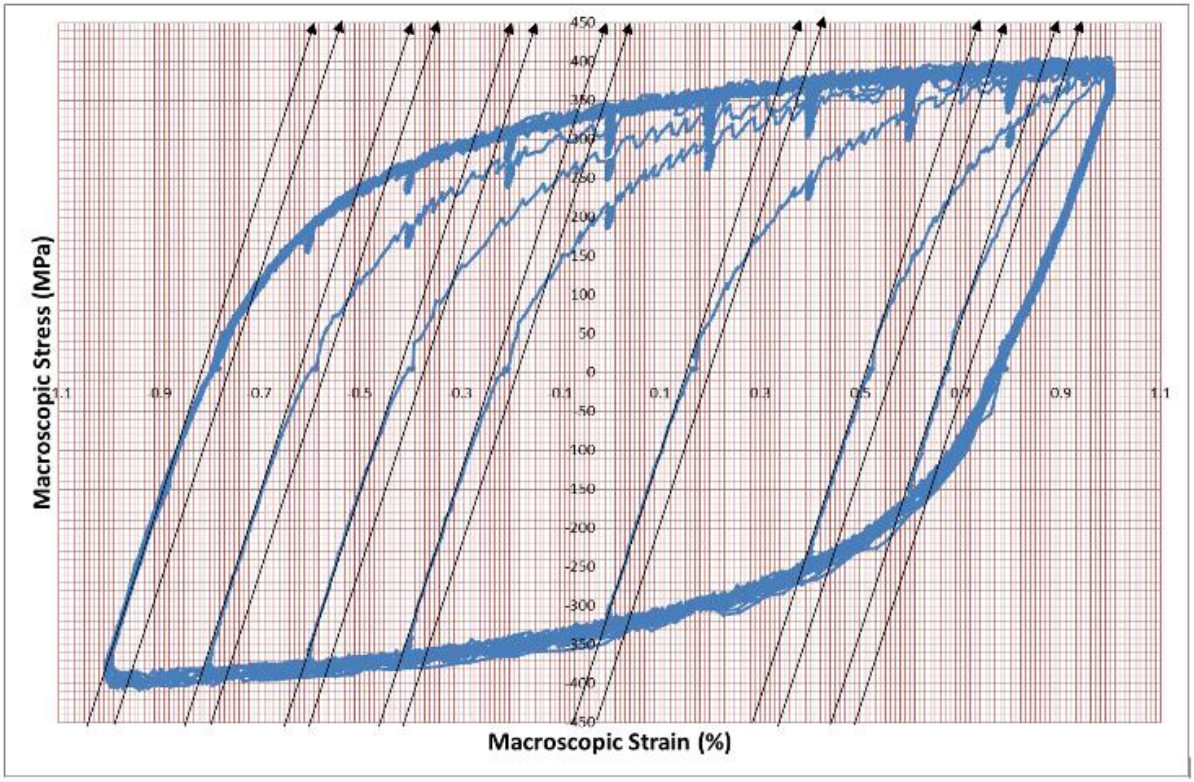

Figure 5-5 Illustrations of the determination of the Yield stress in the tensile reloading cycle after the interruption at various points in compression. Lines Parallel to the elastic reloading line from the peak compressive strain were drawn at an offset of 0.0005 strain. The intersection point of the line and the loading curve is taken as the Yield stress

5.4 Results and Discussion

5.4.1 Tension yield test

Figure 5-6 and Figure 5-7 show the macroscopic deformation curves during tension-compression cyclic loading with interruptions at various strains during compressive and tensile loading respectively. In Figure 5-6, the tensile yield stress in the reloading cycle was found to systematically decrease with the increase of interruption strain in compression. Conversely, in Figure 5-7 the tensile yield stress was found to systematically increase with the increase of interruption strain in tension. In other words, the results show that the further the elastic limit is exceeded in the compression going direction, the lower the yield stress in the subsequent tension reloading cycle, and the further the elastic limit is exceeded in the tension going direction, the higher the yield stress in the subsequent tension reloading cycle.

The measured tensile yield stresses with respect to various compression and tension interruption strains are shown in Table 5-1 and presented in Figure 5-8.

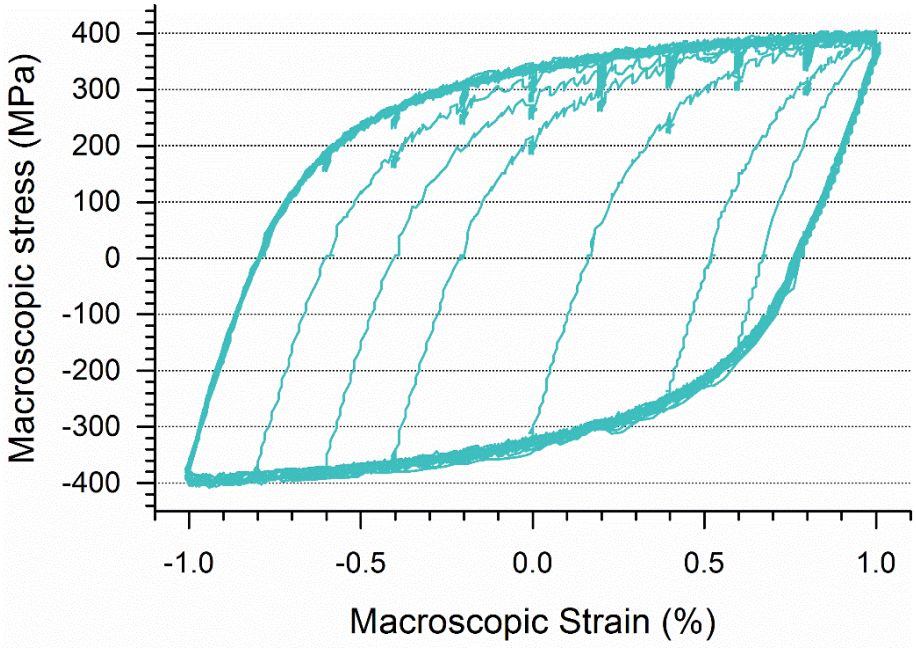

Figure 5-6 Variation of yield stress on reloading due to interruption at various compressive loads. After each interruption, the load was reduced to 5 MPa and then increased to the peak 1% tensile strain

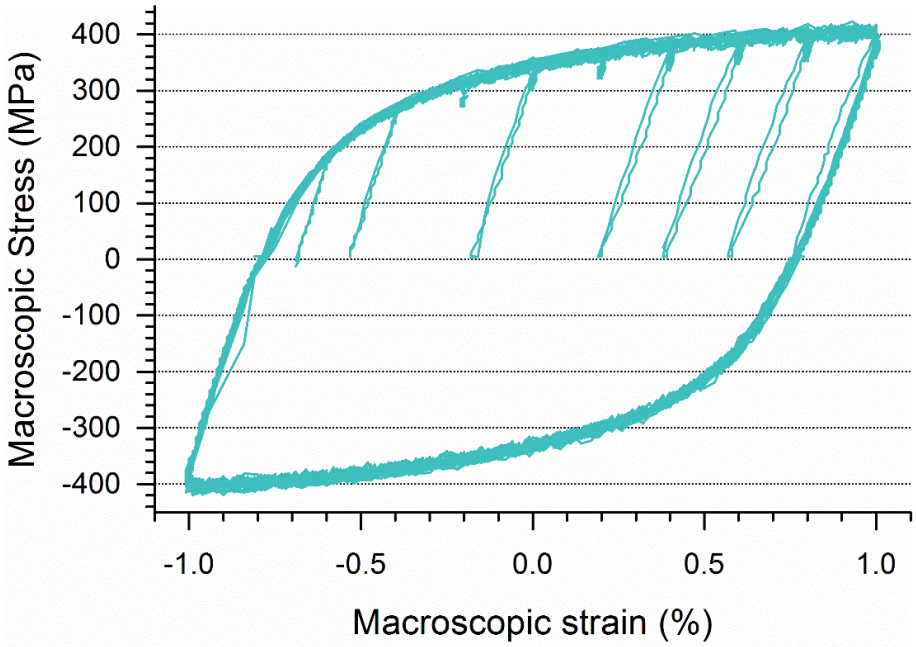

Figure 5-7 Variation of the yield stress on reloading due to interruption at various tensile loads. After interruption, the load was reduced to 5 MPa and then increased back to the peak 1% tensile strain

Table 5-1 Measured yield stress at 0.05% strain offset in the reloading cycle after load interruption at various points in compression and tension loading. The points of interruption are referred to in Figure 5-3

Compression Interruption	**A**	**B**	**C**	**D**	**E**	**F**	**G**
Interruption strain (%)	0.60	0.40	0.0	-0.40	-0.60	-0.80	-1.0
Yield stress at 0.05% strain offset	282	225	155	118	110	100	88
Tension Interruption	**H**	**I**	**J**	**K**	**L**	**M**	**N**
Interruption strain (%)	-0.60	-0.40	0.0	0.40	0.60	0.80	1.0
Yield stress at 0.05% strain offset	210	275	338	372	384	392	398

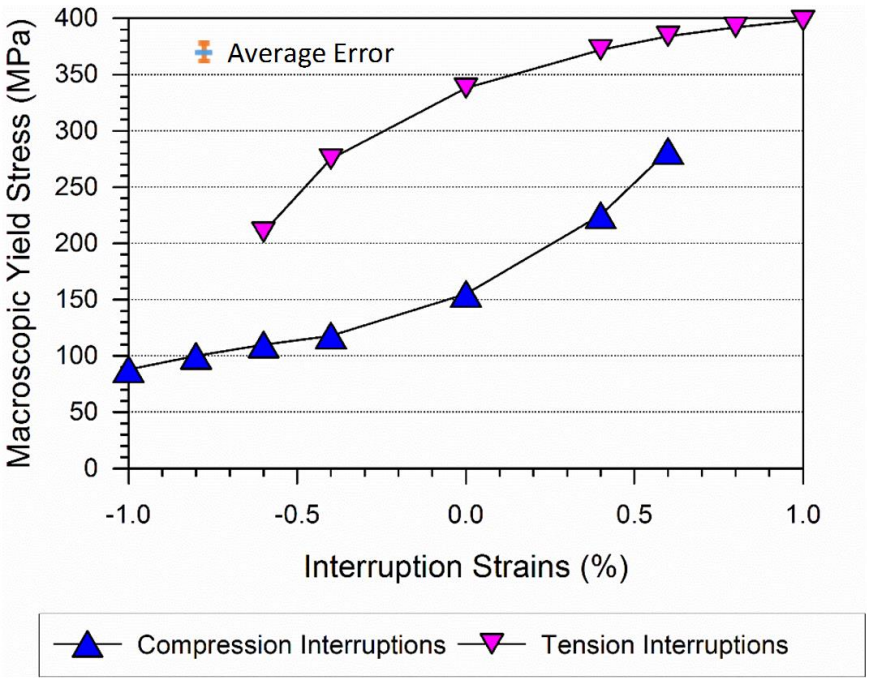

Figure 5-8 Corresponding changes of the tensile yield stress at 0.05% strain offset in the reloading cycle subsequent to various tensile and compressive load interruption. The yield stresses decrease with the increasing interruption in compressive load and increase with the increasing interruption in tensile load

The yield stresses show a large variation with respect to various interruption strains. The range of the variations in the yield stress is similar for tension and compression interruptions.

As reported in chapter 4, yield stress of the undeformed type 316H stainless steel at .05% strain offset was found to be 179 MPa. In case of the tension interruptions, the macroscopic yield stress is always higher than the yield stress found for the undeformed type 316H stainless steel and in case of the compressive interruptions, the yield stress is below that of an undeformed material upon an excursion of small compressive deformation and above upon excursion of larger compressive loads. The macroscopic stress-strain curves in Figure 5-6 and Figure 5-7 also show a distinct difference in the 'elastic to plastic transition' after the compression and tension interruptions. The elastic to plastic transition after compression interruptions occurs gradually over a range of the applied stress while that after the tension interruptions occurs sharply. This observed difference in the macroscopic yielding behaviour is discussed in details later.

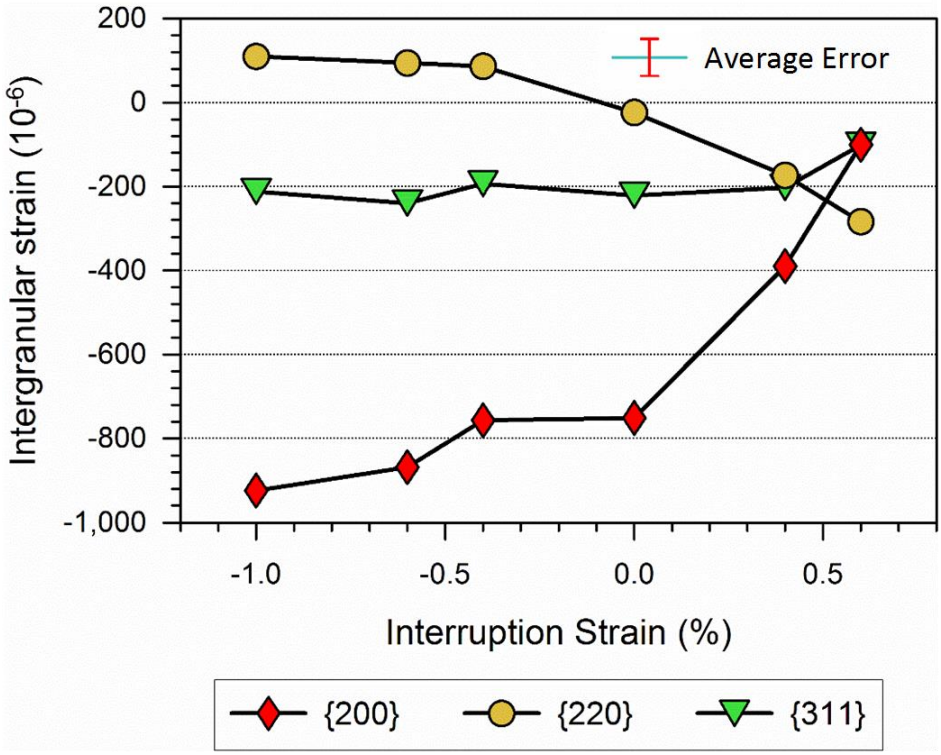

Figure 5-9 IR strains at 5 MPa after interruption at various strains during compressive loading (points A-G in Figure 5-3)

Axial and transverse lattice strains of at least five grain families were recorded during the interruption loadings. Investigating the lattice strains of the few grain families covering the full spectrum of anisotropy is sufficient to provide a complete insight of the microscopic deformation mechanisms [151]. Therefore, for simplicity of the discussion, only three grain

families were chosen as examples to demonstrate how plastically strong, weak and average grain families deform during the interrupted cyclic loadings. During uniaxial tensile/compressive deformation of an undeformed type 316H stainless steel, the {220} grain family usually yields first, the {200} grain family last and the {311} grain family usually exhibits grain average behaviour. These three grain families were chosen.

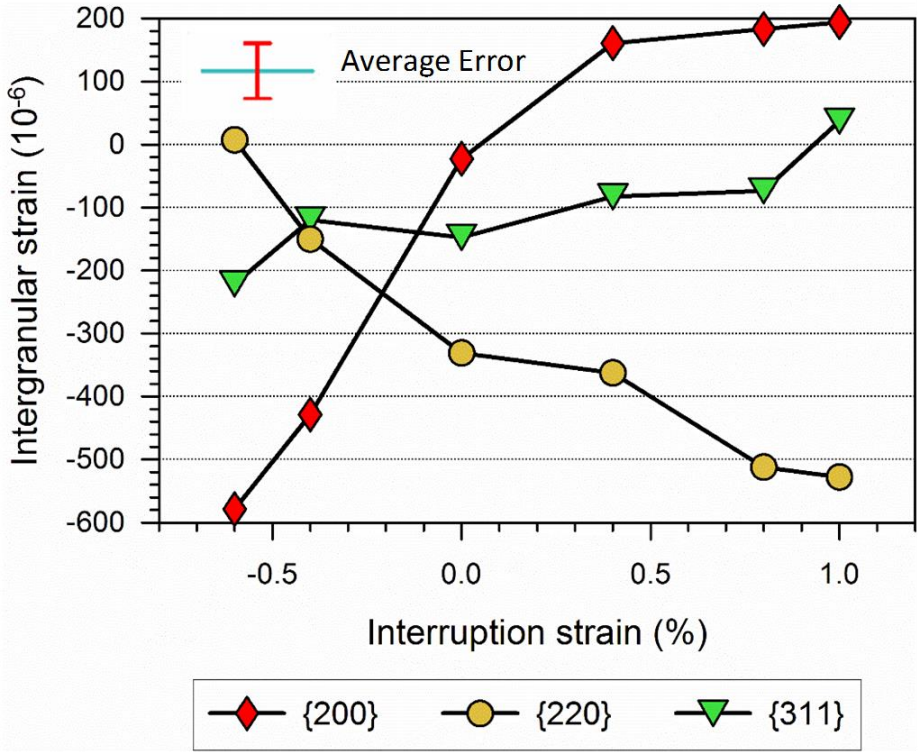

Figure 5-10: IR strains at 5 MPa after interruption at various strains during tensile loading (Point H-N in Figure 5-3)

Figure 5-9 shows the axial IR strains measured at the unloaded state (at 5 MPa) after the interruption at various strains under compression. After unloading from a small excursion of the compressive load at 0.6% strain, all three grain families show negligible IR strains. The IR strains in the {200} and {220} grain families show a systematic increase in compressive and tensile directions respectively, with an increase of interruption strains. The IR strains in the {311} grain family remain nearly unchanged irrespective of the interruption strain. Figure 5-10 shows the axial IR strains in the same three grain families with respect to various tensile interruption strains. In an opposite sense to the compression interruption points, the IR strains in the {200} and {220} grain families show a systematic increase in tensile and compressive directions respectively, with an increase of interruption strain. The IR strains

in the {311} grain family remain nearly unchanged in most of the interruption strains, apart from a couple of points.

Yielding of macroscopic polycrystalline material initiates by slip occurring in the grains which are favourably oriented, rather than slip occurring in all the grains simultaneously. For example, in a tensile test of an undeformed 316H specimen, the slip will occur in the {220} and {111} grain families much earlier than in {200} grain families. If the macroscopic material is deformed plastically sufficiently severely in tension and unloaded to zero stress, the plastically weak grain families end up in compressive residual strain while the plastic strong grains will be in tension. Conversely, if the macroscopic material is compressively deformed, upon unloading to zero stress, the plastically weak grains end up in tensile residual strain while the plastically strong grains will be in compression. These residual strains either assist or oppose the macroscopic deformation in the subsequent loading depending upon the direction of the loading.

In the case of the compression interruption, if the subsequent loading is in tension, the tensile residual strains in the weaker grain families will assist yielding to occur in those grains. Therefore, the higher the compressive interruption strain, the lower is the stress required for the weaker grains to deform plastically during the reverse tensile loading. As the plastic deformation in the weaker grains initiates macroscopic yielding, with an increase in interruption strain in compression, the macroscopic yield stress of the material is reduced. For example, in Figure 5-9, after unloading from interruption at 0.6% strain and at -0.6% strain, the {220} grain family possesses a compressive residual strain of ~ 300 με and tensile residual strain of ~100 με respectively. When a further load is applied in tension at these two points, the load after 0.6% interruption strain overcomes an extra compressive residual strains of ~400 με in the {220} grain families compared with the to -0.6% interruption strain, before these grains start deforming plastically. As a result, the macroscopic yielding started at a higher applied stress after the interruption at 0.6% strain than at -0.6% strain.

Conversely, in the case of tension interruption, the compressive residual strains in the weaker grain families oppose the yielding to occur in those grains. For example, in Figure 5-10, upon unloading after the interruption at 0.8% strain, the {220} grain families possess compressive residual strains of ~500 με compared to negligible residual strains upon interruption at -0.6% strain. When the further load is applied in tension at these two points,

less stress was required to deform the {220} grain families plastically after -0.6% strain interruption than the 0.8% strain interruption. Therefore, the macroscopic yielding has started at a higher applied stress after the interruption at 0.8% strain compared to -0.6% strain.

On the other hand, the stronger grains, for example, the {200} grain family possess increasing tensile and compressive residual strains with an increase in tension and compression interruption strain respectively. In the reloading tension cycle, the tensile residual strains assisted plastic deformation while compressive residual strains opposed plastic deformation in the {200} grain family. If only the compression interrupted points are considered, it can be reported with confidence that, during the tension reloading cycle, the {200} grain family has always deformed plastically last among the 3 grain families reported here. This is because, the {200} grain family is already the strongest grain family to yield in an undeformed material; in the compression interrupted points, the {200} grain family possess compressive residual strains which oppose further plastic deformation in tension. Experimental evidence of this hypothesis is presented in Figure 5-11 which shows the evolution of lattice strains during the tensile reloading cycle after compression interruption at (a) -0.6% strain and (b) 0.0% strain.

Neutron diffraction measures the strain in the material by measuring the changes in the lattice spacing between crystallographic planes, therefore, it only measures the 'elastic' lattice strains. When a particular grain family start to deform plastically, the distances between crystallographic planes do not change, therefore, elastic lattice strains of that particular grain family remain unchanged with the increasing load. Figure 5-11 (a) shows, during the tension reloading, after the interruption at -0.6% strain, the {220} grain families are already plastically deformed at about -0.2% strain (at 270 MPa), evidenced by the near constant elastic strains in that grain family with the increasing load. The other two grain families are still deforming elastically at that point of loading. The {311} grain families start deforming plastically next at about 0.4% strain (at 350 MPa). The {200} grain families do not show any clear sign of plastic deformation up to the peak tensile strain of 1%. Figure 5-11 (b) shows the evolution of lattice strains during reloading after 0.0% strain interruption in tensile load. After unloading from interruption at 0.0%, the {200} grain families and {220} grain families have more tensile and compressive residual strains respectively,

compared to that after unloading from interruption at -0.6% strain. Therefore, the {200} grain families are expected to yield at a lower macroscopic applied stress and {220} grain families are expected to yield at a higher macroscopic applied stress.

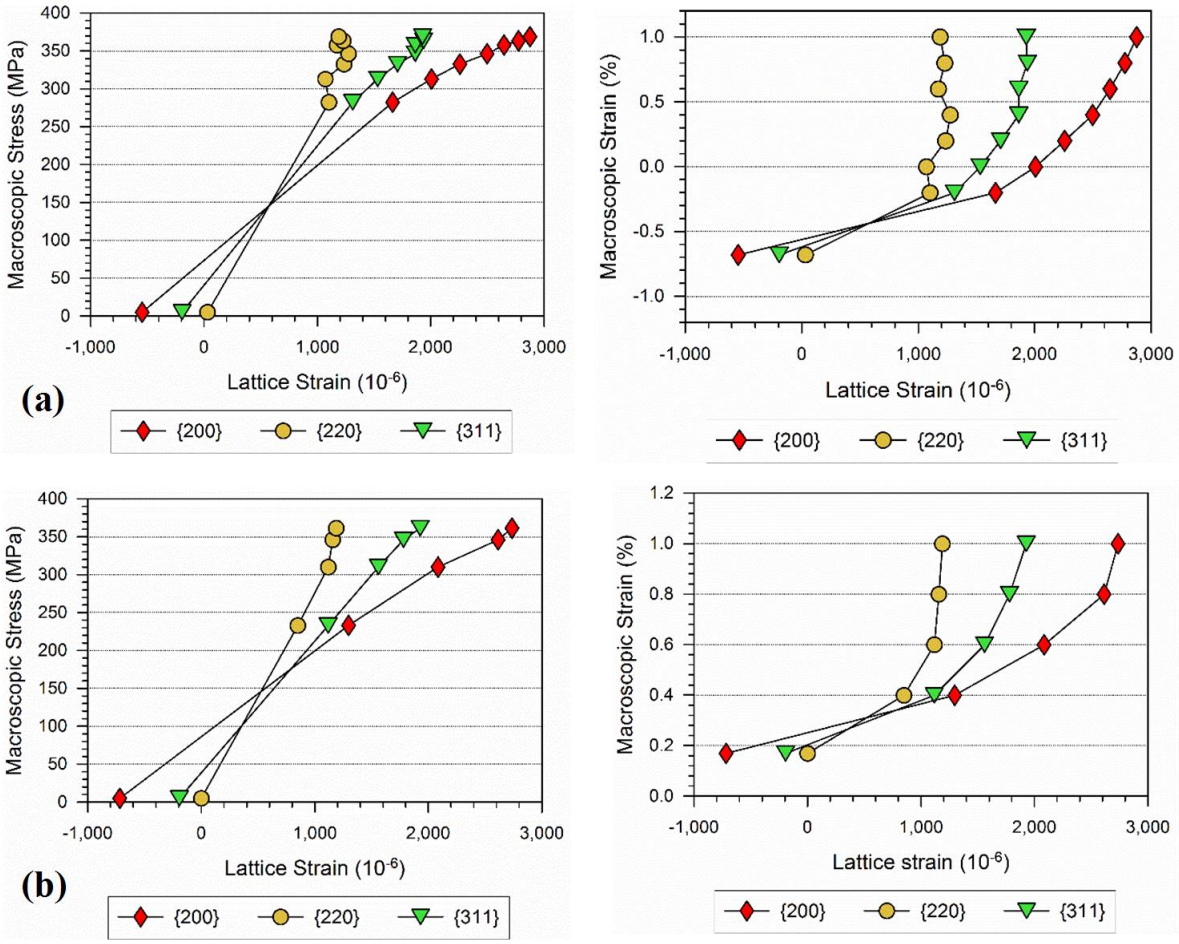

Figure 5-11 Evolution of elastic lattice strains during reload after interruption at (a) -0.6% strain and (b) 0.0% strain both in compressive load

Figure 5-11 (b) shows the yielding of the {220} grain families at ~300 MPa and yielding of {200} grain families at ~350 MPa. Out of these observations, it can be deduced that, in the case of the compression interruption, the initial plastic weaker grains always deformed plastically first and therefore, the initiation of the macroscopic yield stress is negatively correlated with the magnitude of the residual strains in these grain families.

In the case of tension load interruption, a similar assumption of the initial weaker grains always deforming plastically first, cannot be made. This is because, upon unloading from tension interruption (when a severe enough excursion of tensile deformation is made), the

plastic stronger grains possess tensile residual strains while the plastic weaker grains possess compressive residual strains. When the further load is applied in tension, the plastic deformation in the stronger grains is assisted while plastic deformation in the weaker grains is opposed by these residual strains. So, it is possible for the stronger grain families to yield prior to the weaker grain families if the difference in residual stress is positive and larger than the difference in the yield stress of these grain families in an undeformed material.

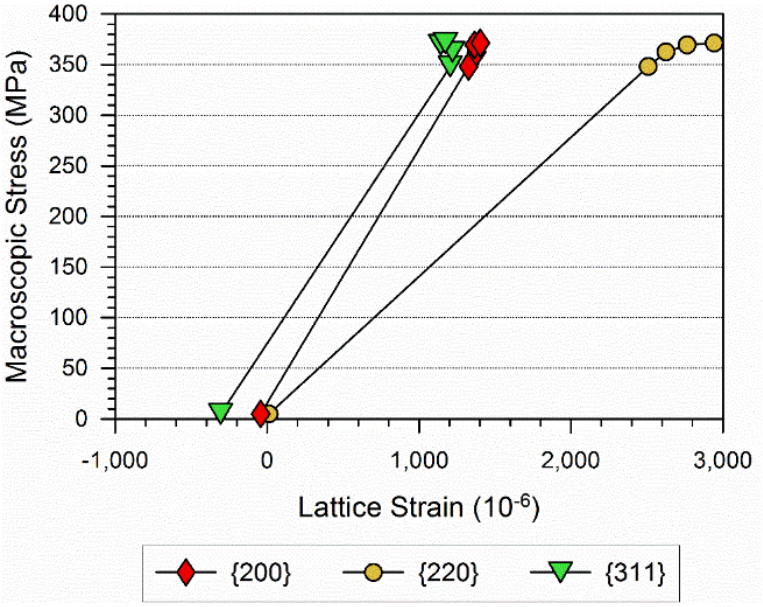

Figure 5-12 Evolution of elastic lattice strain after interruption at 0.0% in tensile load

In that case, linking the change of macroscopic yield stress with the change of residual strains just in the weaker grain families is not always possible. Nevertheless, Figure 5-12 shows after a small magnitude tensile strain excursion, despite possessing compressive residual strain, the plastic weaker {220} grain family still plastically deformed before the {311} and the {200} grain families. Upon unloading after a higher excursion of the tensile load, the plastically strong {200} grain family possesses large tensile IR strains and the plastically weak {220} grain family possesses large compressive IR strains. So, it's possible for the {200} grain family to yield prior to the {220} grain family. However, in that case, for the difference in the residual stress between the {200} and the {220} grain family to be larger than the difference in the yield stress of these grain families in an undeformed material, the compressive residual strains in the {220} grain family has to be even more. Therefore, the negative correlation between the IR strains in the weaker grain families with the macroscopic yield stress will still remain valid.

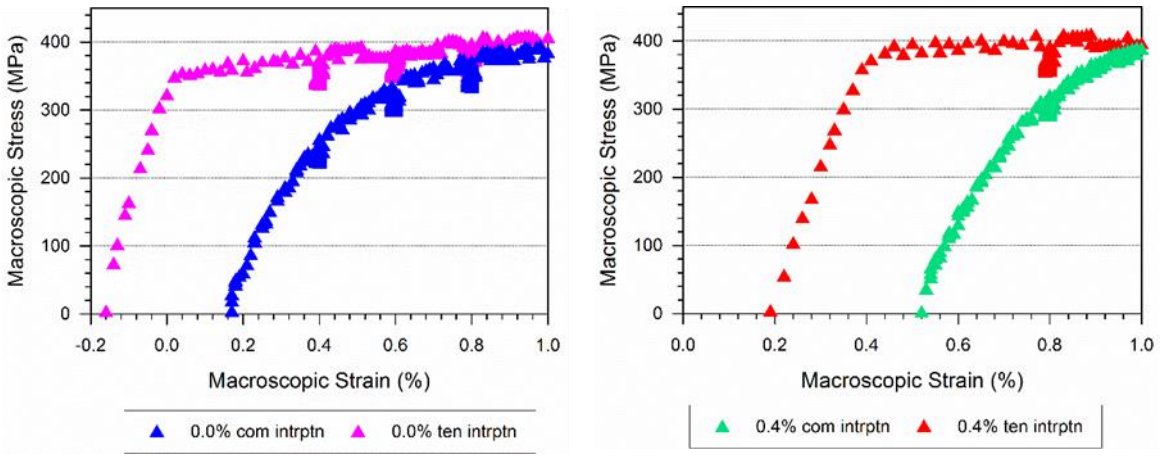

Figure 5-13 Comparison of the macroscopic yielding after the interruption at the same strain (a) in 0.0% strain and (b) in 0.4% strain in tension and compression.

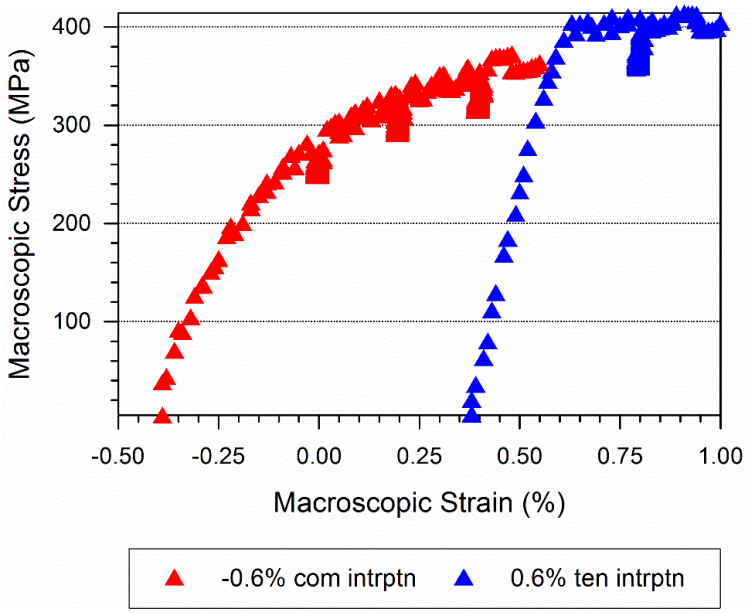

Figure 5-14 Comparison of the macroscopic yielding of the material after -0.6% strain interruption in compression and after 0.6% tension interruption in tension

The observation of the difference in the elastic to plastic transition after compression interruption (in Figure 5-6) and after tension interruption (in Figure 5-7) can also be discussed in the context of the relative yielding of the variously oriented grains. Figure 5-13 shows the comparison of the macroscopic yielding after tension and compression interruption at (a) 0.0% strain and (b) 0.4% strain as examples. In both cases, it can be clearly seen that after the tension interruption, there is a sharp transition from elastic to plastic deformation whereas, after compression interruption, the transition is smooth. Figure 5-14

shows the difference of the shape of the yielding even more clearly after larger strain tension and compression interruption. After increasing interruption in tension the {200} and the {220} grain family possess increasing tensile and compressive residual strains respectively and vice versa after increasing compression interruption. Therefore, during the reloading in tension, the difference in the macroscopic stress at which the {200} and the {220} grain family start to deform plastically, decreases with increasing tension interruption and increases with increasing compression interruption. As a result, at the higher tensile interruption, the differently oriented grains deform within a short span of the stress increase.

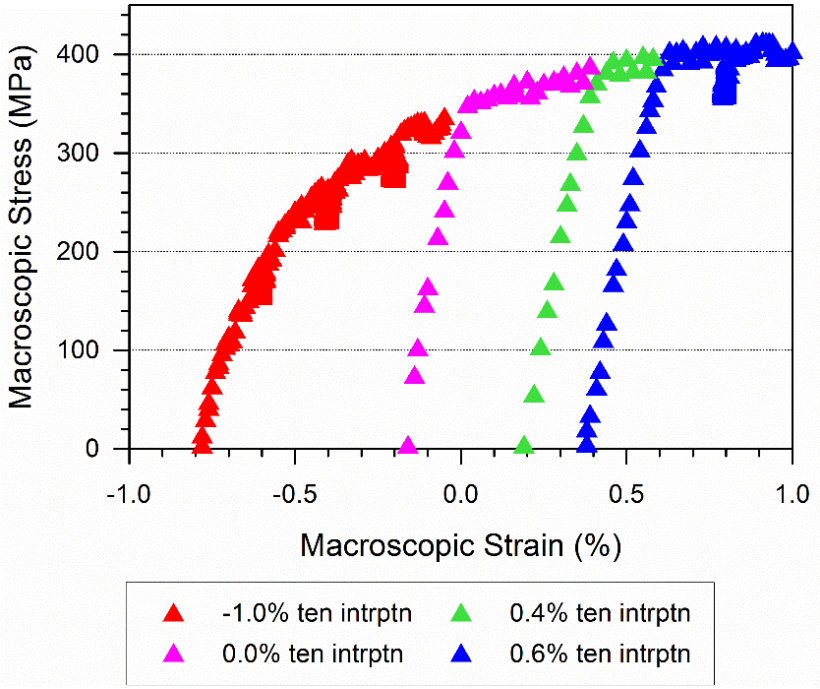

Figure 5-15 Macroscopic yielding after an interruption in various strains under tension. The 'elastic to plastic transition zone' gets sharper with increasing tensile strain interruption.

On the other hand, after the compression interruption, differently oriented grains deform at significantly different applied stress due to the large difference in the yield stress between them. The difference in the yield stress of the variously oriented grains increases and decreases with the increase of the interruption strains in compression and tension respectively and so does the sharpness of the elastic to plastic transition during macroscopic yielding. Figure 5-15 shows, as an example, the macroscopic yielding during reloading upon various tension interruption. The difference in the yield stress of various grain families reduces with the increasing tension interruption strains, and therefore, the yielding becomes sharper.

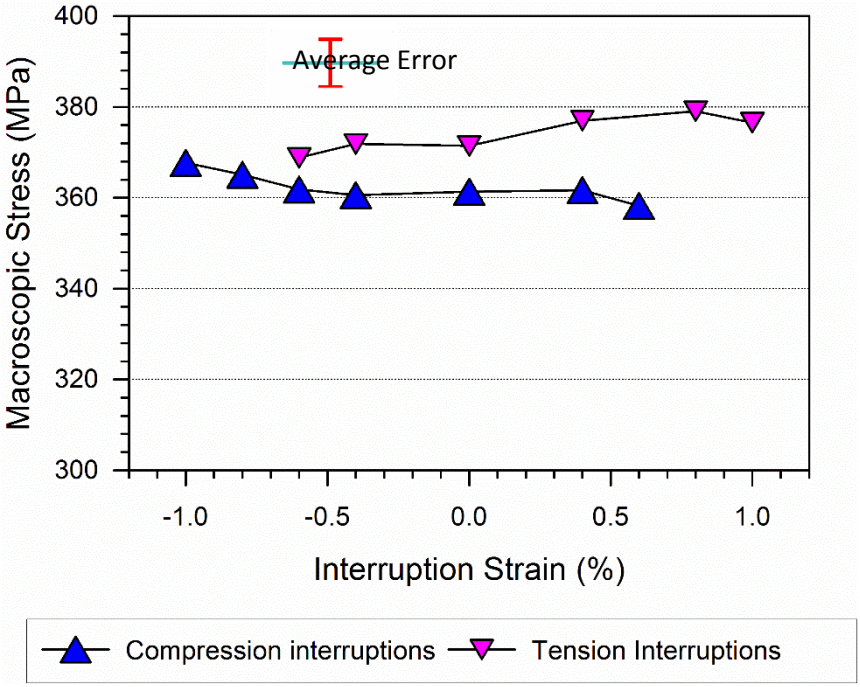

Figure 5-16 Macroscopic stress required to reach to the peak 1% tensile strain after interruption at various compression and tensile loads. The set of macroscopic stress value for both tension and compression interruptions show only small difference (within experimental error) with respect to various interruption strains, implying a zero permanent softening in this material during reverse loading.

The discussion has so far has been limited to the effect of the IR residual strains on macroscopic yielding. An insight of the evolution of the IR strains during the plastic loading can be gained by investigating the changes in the macroscopic stress and the corresponding IR strains at the peak macroscopic strains with respect to various interruption strains. Figure 5-16 shows the macroscopic stress at the peak tensile strain of 1% after the interruption at various strains in tensile and compressive loads. No significant difference in the macroscopic stress required to reach to the peak strains can be observed irrespective of the interruption strains. There is a distinct difference between the macroscopic stresses after compression and tension interruption. The small difference is due to the fact that the tension interruptions were performed after the compression interruptions in the test, while the specimen has been cyclically hardened slightly more.

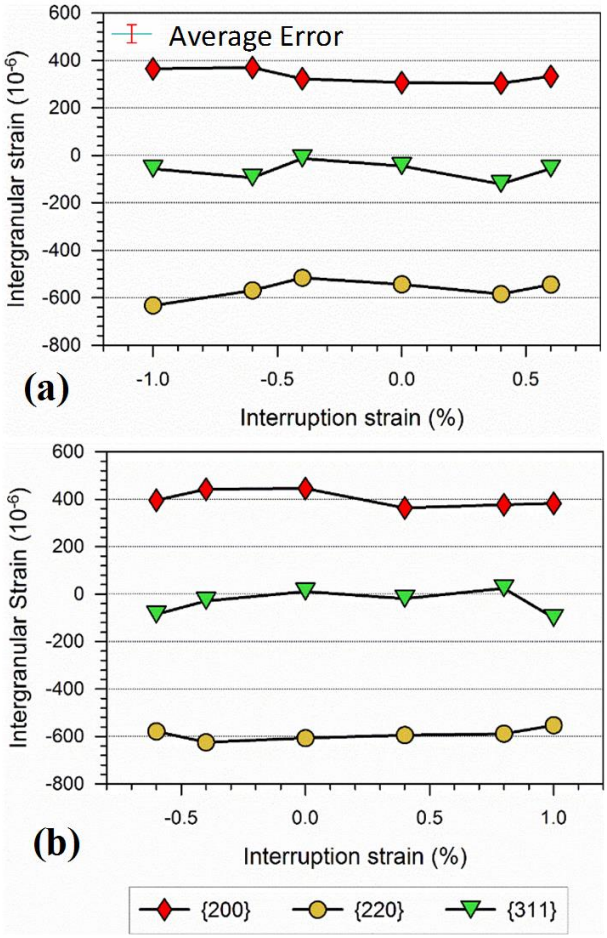

Figure 5-17 Variation of axial IR strains reaching to peak strain after interruption at (a) compressive and (b) tensile loads

Interestingly, in Figure 5-17, it can be noticed that IR strains in individual grain families also remain nearly unchanged irrespective of the interruption strains, that is, whether the IR strain in a grain family is compressive or tensile in the unloaded state, upon reaching the peak macroscopic tensile strain it has reached the same magnitude. For example, as shown in Figure 5-9 and Figure 5-10 , at the unloaded state after the interruption at 0.0% strain in compression and at 0.0% strain in tension the approximate IR strains in the {200} grain families are -800 με and 0 με respectively. When the specimen was reloaded macroscopically from these 2 points to the tensile peak strain, the IR strains in the {200} grain family in both cases reached ~400 με. After the macroscopic material is completely deformed plastically, the magnitude of the IR strains in each grain family reached a saturated magnitude and is not affected by the variation in the interruption strains. Figure 5-17 also shows that the magnitude of the IR strains in any specific grain family is of the same

magnitude in the case of both tensile and compressive interruption. This provides added confidence in the precision of the collected data and in the consistency of the tests.

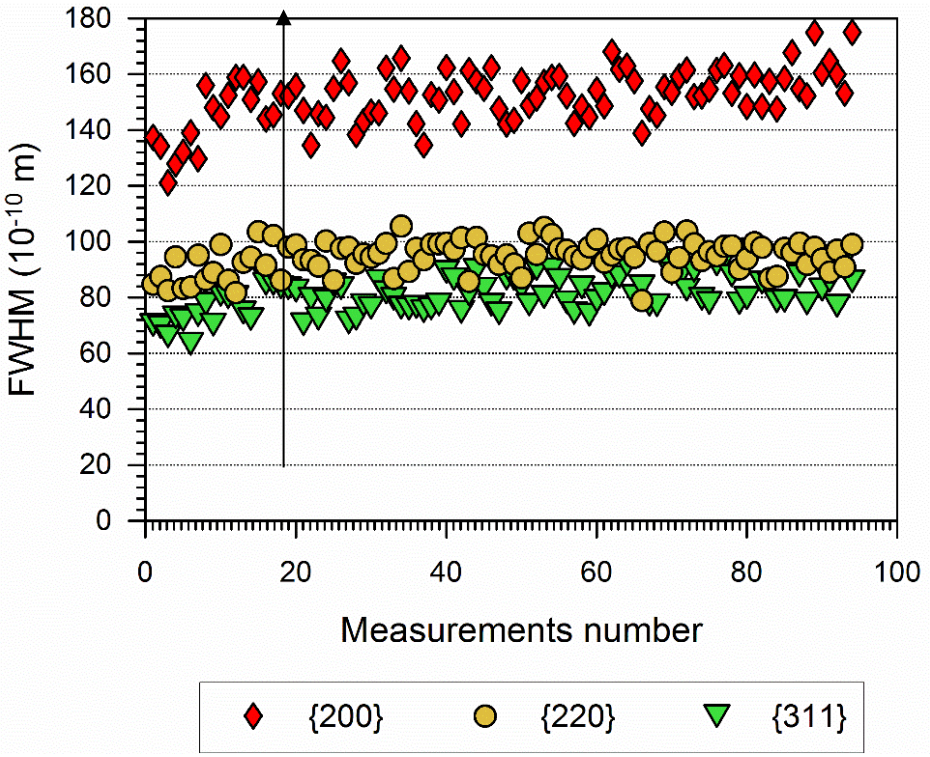

Figure 5-18 Evolution of the diffraction width at the half maximum of the diffraction peaks. The black arrow line separates the measurements before and after 20 tension-compression cycles

An anomaly in the data can be observed in Figure 5-9 and Figure 5-10 (at the unloaded state) where the IR strain in the {311} grain families is slightly compressive. On the other hand, the IR strains in the {311} grain families in Figure 5-17 (at the peak tensile strains) is near zero. The {311} grain families usually represent the average yield strength behaviour of the variously oriented grains in the 316H stainless steel, and therefore, these grain families are expected to generate insignificant IR strains in the unloaded state, as explained in Chapter 4. Even if the {311} grain families generate IR strains at the unloaded state due to continuous cyclic loading at the beginning of the experiment, those strains should be tensile after an interruption from the tensile stress and compressive after an interruption from the compressive stress. Moreover, if the magnitude of the IR strains at the unloaded state is expected to be zero, it should be slightly tensile at the peak tensile strain. So, the magnitude of the IR strains in the {311} grain family is implying a negative shift in the values of the IR

strains. This shift in the magnitude of the IR strains is also true for the other 2 grain families plotted here.

This shift in the magnitude of the IR strains can be attributed to the variation in d space measurements due to peak shape broadening. The initial d spacing measured at the beginning of the test was used as the stress free lattice spacing in the analysis of the test data. However, during the 20 tension-compression loading cycles, the shape of the peak broadened compared to the shape of the peak of the initial measurement of the d spacing. Figure 5-18 shows the evolution of the Full Width at the Half Maximum (FWHM) of the diffraction peaks during the tensile yield test. The black arrow line in the figure separates the measurement points before and after the 20 cyclic loadings. The first 13 points measured before the cyclic loading have a lower FWHM compared with the rest of the measurement points which were collected after. When calculating the lattice strains, these d spacing value measured afterwards were compared with the d_0 spacing measured beforehand, essentially introducing an error in the analysed data due to peak broadening. This error may have caused the small shift in the magnitude of the lattice strains. However, in the measurements after cyclic loading, when hardening of the material was already saturated, the width of the peak shape remained within the experimental error. Therefore, these shifts of the IR strain magnitude due to diffraction peak broadening do not affect the relative changes of the IR strains with respect to various interruption points.

5.4.2 Compression yield test:

In this test, yielding in compression was investigated instead of tension. The sequence of the load interruption for the test is described in 5.3.1 and the interruption points are presented in Figure 5-4. Figure 5-19 and Figure 5-20 show the macroscopic stress-strain curves of the material yielding in compression after the interruption at various points in tension and compression respectively. The macroscopic compressive yield stress decreases with the increase of the excursion of tensile deformation before the interruption and increases with the increase of the excursion of compressive deformation before the interruption. Therefore, the macroscopic findings of the test are similar to those of the tensile yield test. The yield stresses in various reloading cycles were measured following the procedure described in

5.3.1. The measured values of the compressive yield stress as a function of the tension and compression interruption strains are listed in Table 5-2 and presented in Figure 5-21.

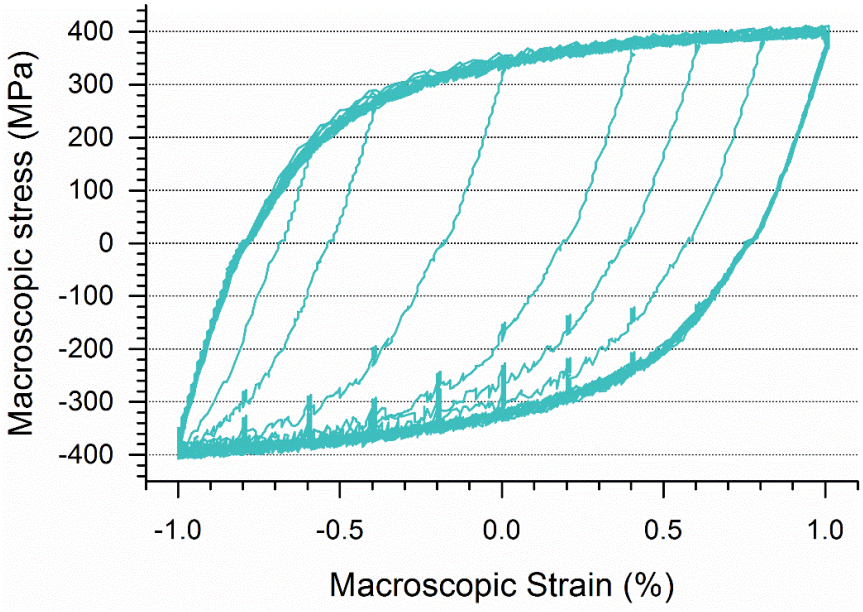

Figure 5-19 Variation of the yield stress in the reloading cycles due to interruption at various tensile loads. After interruption, the specimen was reloaded back to the peak -1% compressive strain

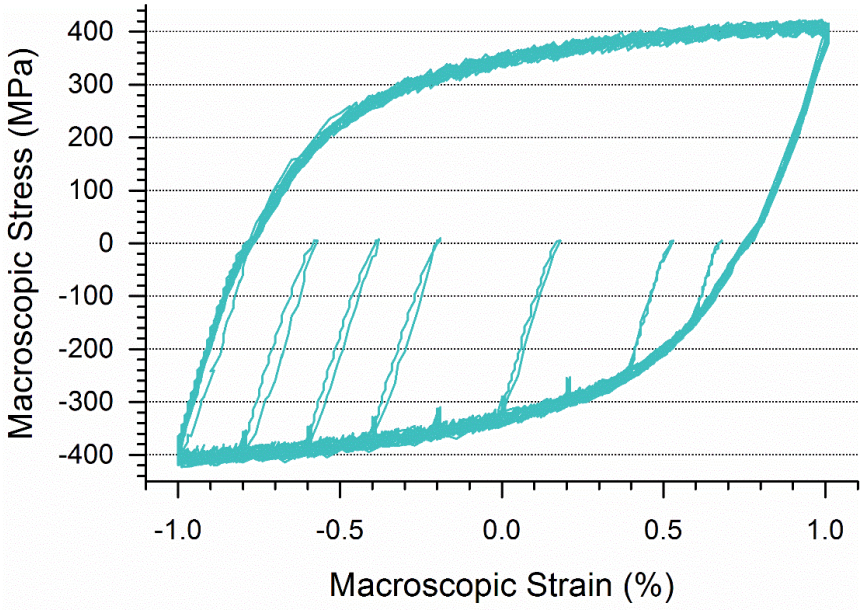

Figure 5-20 Variation of yield stress on reloading due to interruption at compressive loads. After interruption, the specimen was unloaded to 5 MPa and then reloaded back to the peak -1% compressive strain

Table 5-2 Measured yield stress at 0.0005 strain offset in the reloading cycle after load interruption at various points in compression and tension loading. The points of the interruption are referred to in Figure 5-4

Tension Interruption	**O**	**P**	**Q**	**R**	**S**	**T**	**U**
Interruption strain (%)	-0.60	-0.40	0.0	0.4	0.6	0.8	1.0
Yield stress at 0.05% strain offset (MPa)	-313	-209	-90	-58	-35	-20	-12
Compression Interruption	**V**	**W**	**X**	**Y**	**Z**	**AA**	**AB**
Interruption strain (%)	0.6	0.4	0.0	-0.4	-0.6	-0.8	-1.0
Yield stress at 0.05% strain offset (MPa)	-182	-265	-322	-365	-378	-385	-405

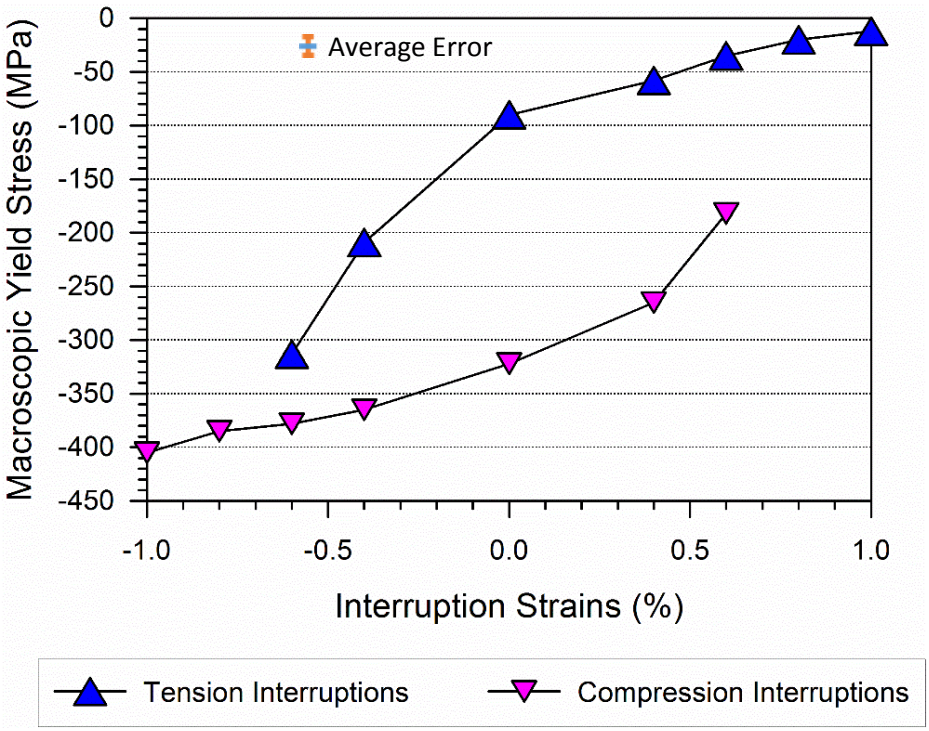

Figure 5-21 Corresponding changes of compressive yield stress at 0.05% strain offset in subsequent reloading cycles with respect to various tensile and compressive load interruption. The yield stresses decrease with increasing interruption in tension and increase with the increasing interruption in compression

Similar to the tensile yield test, the magnitude of the yield stress shows a large variation with respect to the interruption strains. After the tensile load interruptions, the compressive yield

stress was found to be either higher or lower than the compressive yield stress of an undeformed 316H stainless steel, depending upon the interruption strain. However, after the compressive load interruptions, the yield stress was found to be higher, upon any interruption strain. A distinct difference in the macroscopic yielding after tensile and compressive load interruptions can also be noticed in Figure 5-19 and Figure 5-20. The macroscopic yielding is comparatively sharper (change from elastic to plastic strain changing quickly) after the interruptions in compression and smoother after the interruptions in tension.

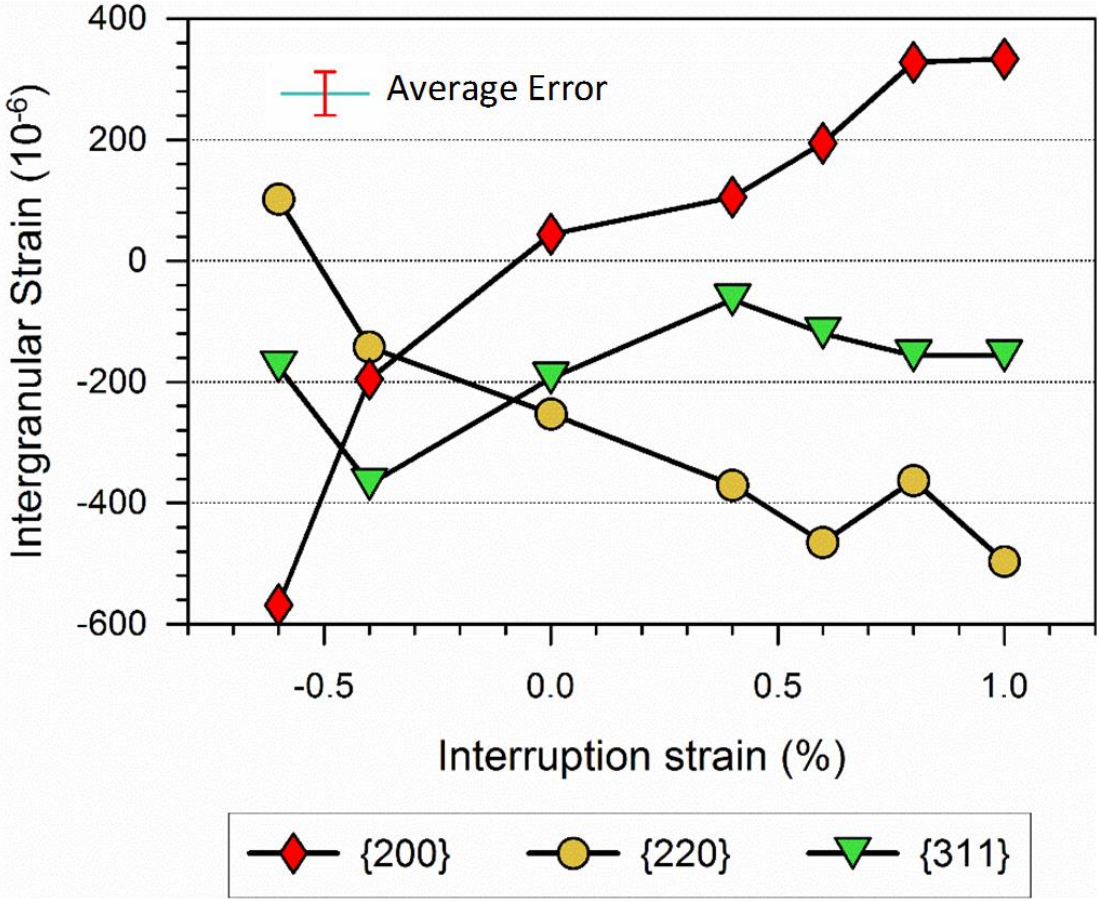

Figure 5-22 IR strains at 5 MPa after interruption at various strains in compressive loading (points N-T in Figure 5-4)

Figure 5-22 shows the axial residual strains in the 3 grain families at 5 MPa after being interrupted at various tensile stresses. The compressive IR strain in the plastic weaker {220} grain family and the tensile IR strain in the plastic stronger {200} grain families increase with the increase of interruption strains under tensile stresses. If the compressive load is applied to undeformed 316H material, the slip will occur first in the {220} grain family,

eventually, initiating the macroscopic yielding. Thus, if the {220} grain family possesses compressive IR strains upon unloading from a tensile stress, it will be easier for these grains to deform plastically. So, a macroscopic material with {220} grain families possessing compressive IR strain at the unloaded state will start deforming plastically at a lower magnitude macroscopic applied compression load than an undeformed material. Therefore, the higher the magnitude of compressive IR strains in the plastic weaker grain families (as shown for the {220} grain families here), the lower is the magnitude of compressive yield stress in the macroscopic material.

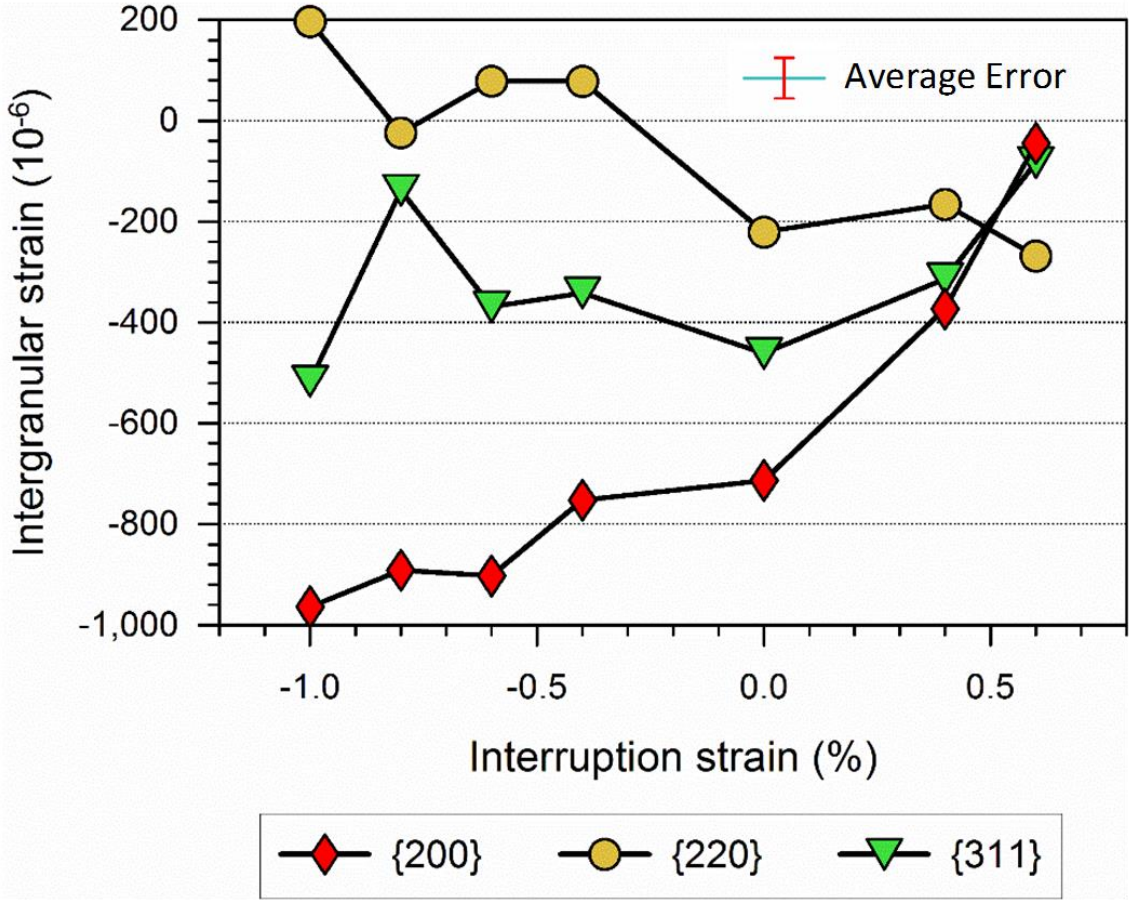

Figure 5-23 IR strains at 5 MPa after at various interruptions in compressive loading (points U-Z in Figure 5-4)

Figure 5-23 shows the variation of IR strains in the grain families after the interruption at various compressive stresses. The tensile IR strains in the {220} grain families and the compressive IR strains in the {200} grain families increase with the increase of interruption strains in the compressive loads. Opposite to the tensile interruption points, the applied stress

has to overcome the tensile IR strains in the plastic weaker grain families, to initiate plastic deformation in the material. As a result, the macroscopic yield stress will be higher after the interruption at a higher compressive stress.

In both cases of tension and compression interruptions, the correlation between the IR strains in the {220} grain families and the macroscopic interruption strains is not as good as it is in the tensile yield test. Moreover, the IR strains in the {311} grain families, show non-systematic variations/fluctuations at a few points. This deterioration in correlation is because this test was conducted after a tensile yield test using the same specimen. During the continuous cycling of the macroscopic material, more grains have been plastically deformed and therefore, correlations in some of the grain families were worsen. However, the IR strains in the {200} grain families still show a strong correlation with the macroscopic interruption strains.

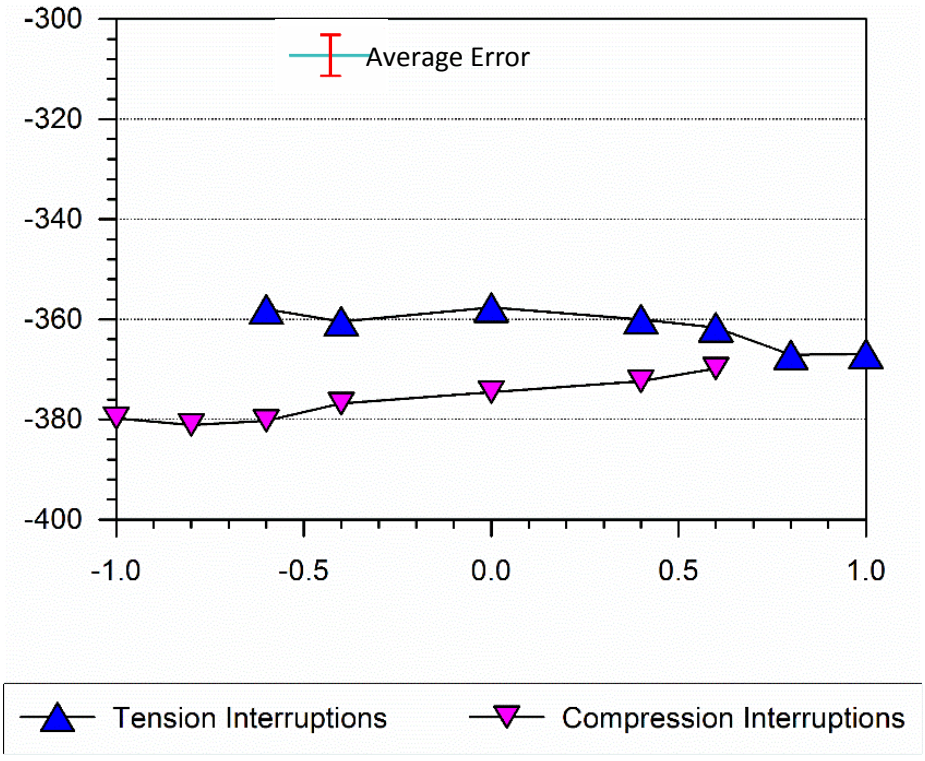

Figure 5-24 Macroscopic stress required to reach to peak compressive strain of -1% after various interruption

Figure 5-24 shows the macroscopic stress associated with reaching a peak compressive strain of -1% after the interruption at various tensile and compressive loads. The macroscopic stress shows a maximum variation of ±10 MPa, which is within the experimental error.

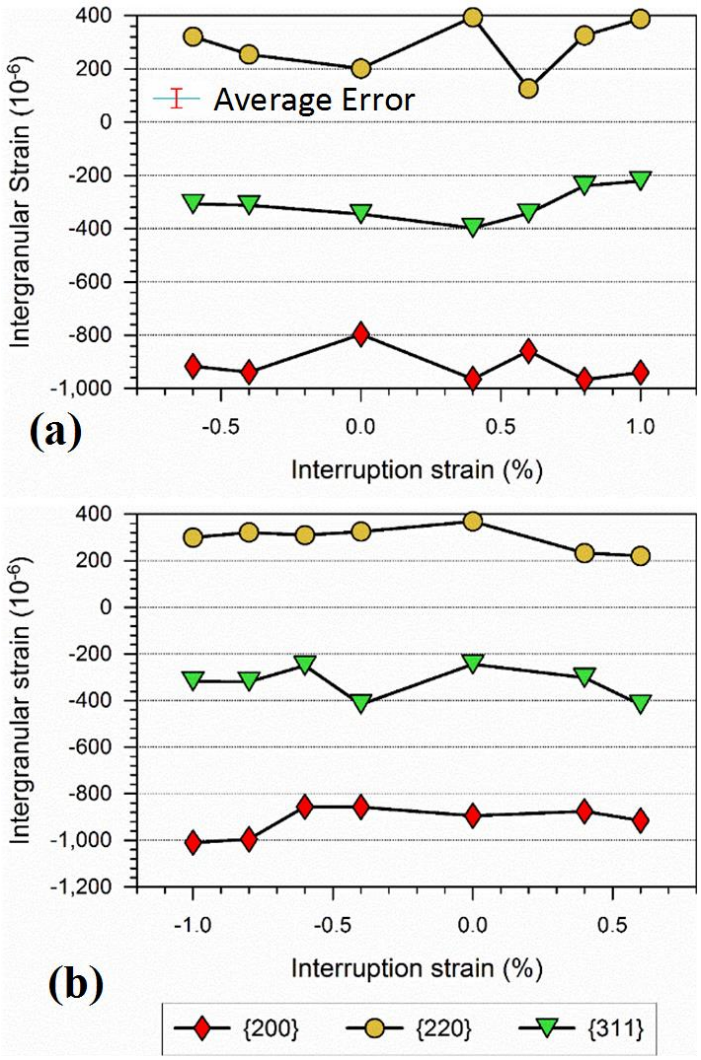

Figure 5-25 Variation of axial IR strains at the compressive strain peak of the cycle after interruption in (a) compressive and (b) tensile loading

Figure 5-25 shows the variation of IR strains at the peak compressive strain tip of the cycle. The magnitude of IR strains remains nearly unchanged irrespective of tensile or compressive interruption strains except in a few arbitrary points showing fluctuations. Unlike the tensile yield test, the peak IR strains in the {311} grain families are not close to zero, rather have a magnitude of 200-400 compressive micro strain after both tensile and compressive interruptions.

5.5 High-temperature tests

5.5.1 Approach

High temperature tests were conducted at 650 ℃ with ±1% strain range following the similar experimental procedures, as above. Based on earlier observations of the room temperature tests, it can be reasonably inferred that the findings of tensile yield tests can be read across to compression yield tests. Therefore, only tensile yield tests were conducted at high temperature to avoid unwanted repetitions.

In the in-situ tests, the specimen was heated to 650° C using an infrared furnace available at the Engin-X facility. The specimen temperature was monitored using a K-type thermocouple attached to the specimen with a vanadium clamp. Vanadium was chosen because of its transparency to neutrons. After reaching the desired temperature of 650° C, the specimen was cyclically loaded to a saturated hardening stage. Saturation of the hardening was determined following the similar procedure described for the room temperature test. The interruption points were chosen more carefully based on the experience gained from the room temperature tests; the points are shown in Figure 5-26. Two complete cycles were inserted between each interrupted cycle to maintain the consistency of hardening in the material.

The yield stress in the subsequent cycles of various tensile and compressive interruption strains was measured by a procedure similar to that described in 5.3.1. However, in the unloaded points where significant anelastic strain (discussed below in 5.5.2) has been observed, the yield stresses were calculated taking those into account. For compressive interruption points, the anelastic strains were added to the strain offsets and for tensile interruption points, the anelastic strains were subtracted from the strain offsets.

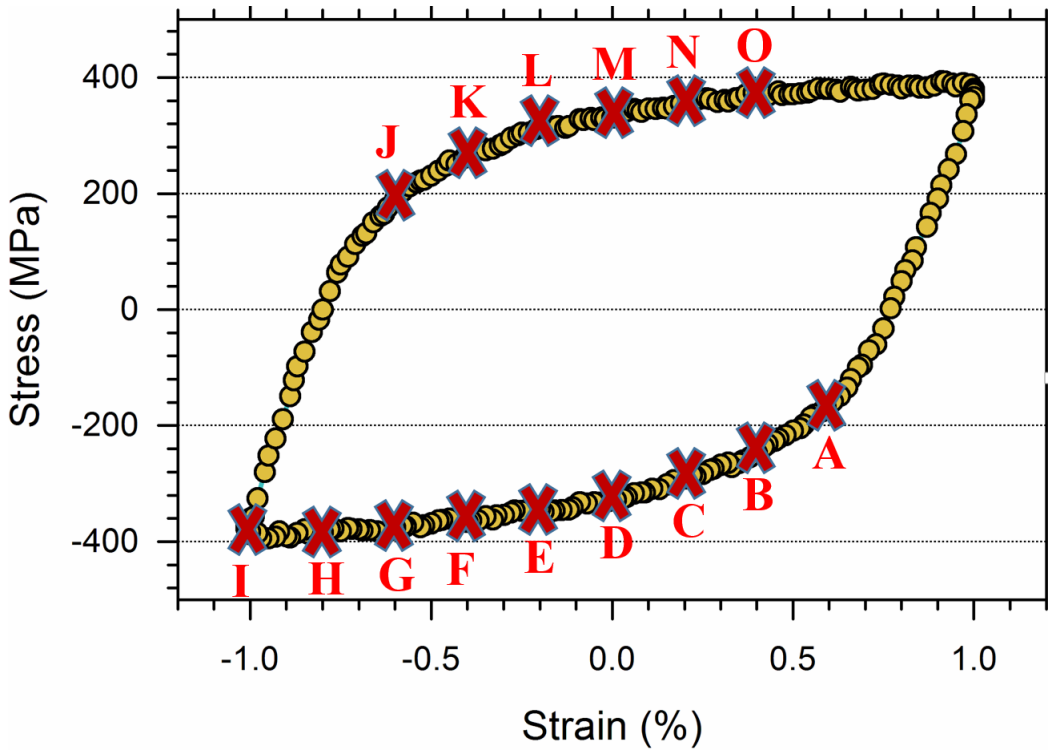

Figure 5-26 Interruption points for the high-temperature tensile yield test are shown on a typical stress-strain curve of 316H stainless steel at 650° C. Points A-I was interrupted during compression loading and Points J-O were interrupted during tension loading. In the case of compression loading interruptions the specimen was reloaded to the tensile peak strain and in the case of tension loading interruptions, the specimen was first unloaded to 5 MPa and then reloaded to the tensile peak strain.

5.5.2 Results and Discussion

Figure 5-27 shows the macroscopic stress-strain curve of 316H stainless steel at 650°C with interruptions at various points in compression. Compared to the room temperature tests, both the yield stress and the stress required to reach to the peak strain are much lower. The yield stress of the subsequent cycles show a negative correlation with the compression interruption strains, that is, the higher the excursion of the load in compression before the interruption, the lower is the yield stress in the subsequent tensile reloading.

During the reloading cycle, upon reaching 5 MPa, lattice strains were measured using neutron diffraction by maintaining the material's load constant for ~6 minutes. It is interesting to note in Figure 5-27, during this holding period, the macroscopic strain in the material increased by a small magnitude. Creep deformation is not significant under 5 MPa at 650° C in undeformed 316H stainless steel, therefore, it is not expected to show any

appreciable increase in strain. However, as back stress is generated in the material during the cyclic loading, this causes the material to increase in strain. Such strain is known as ‘anelastic’ strain.

Anelastic strain can be defined as a recoverable plastic strain. Various mechanisms have been postulated to explain ‘anelasticity’ in metal, for example, unbowing of bowed and immobile dislocations upon removal of load [214], development of heterogeneous dislocation substructures [215], dislocations sub-boundary dissolution and migration [120], unzipping of dislocation network modes [132] etc. The relaxation of compressive IR strains upon unloading from a forward creep load has also been proposed as a potential mechanism for anelasticity in 316H stainless steel [216].

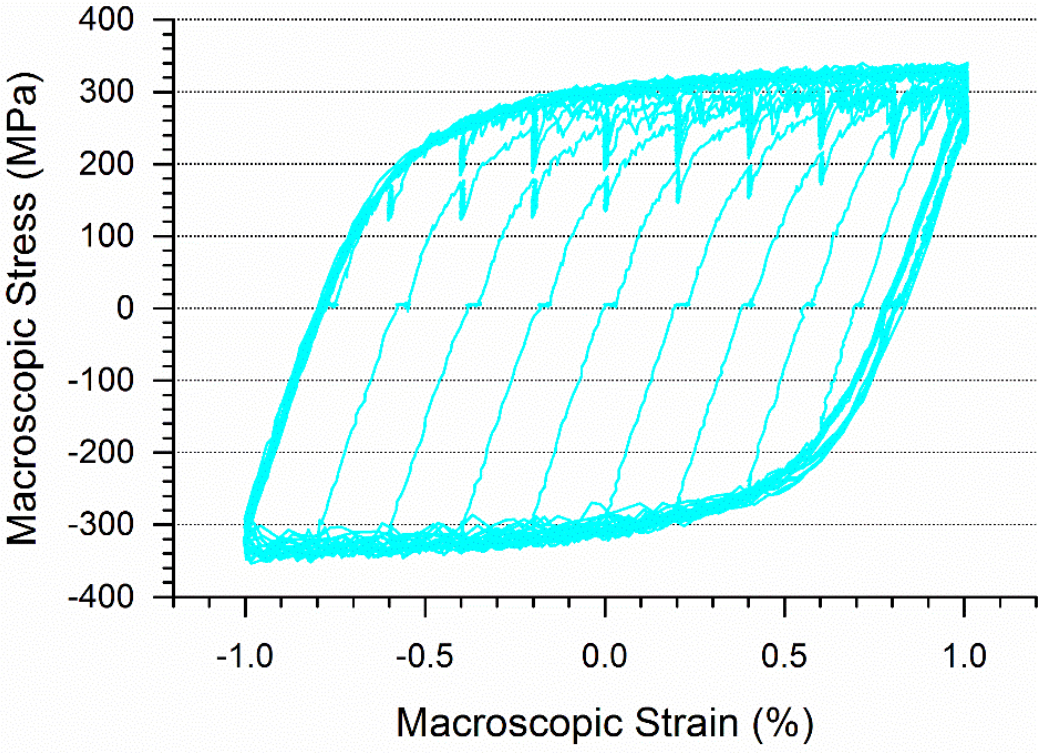

Figure 5-27 Reloading after various interruptions in compressive load during tension-compression cyclic loading of 316H stainless steel at 650° C. During the reloading cycles, neutron measurements were recorded stopping at various points.

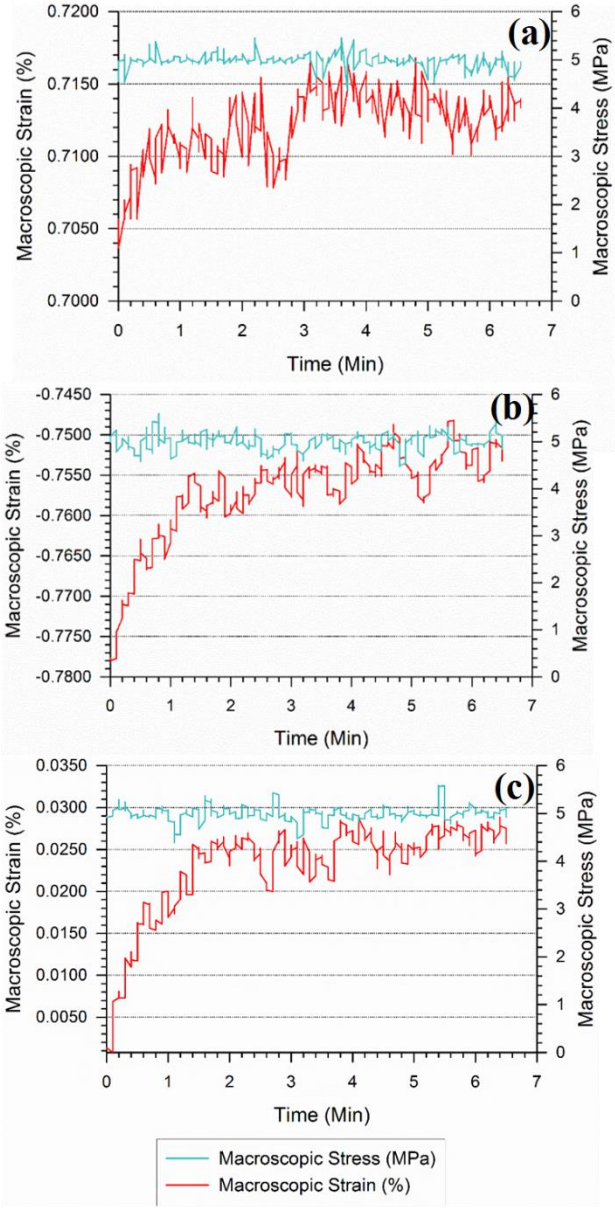

Figure 5-28 Evolution of the anelastic strain during 6 mins holding time for neutron measurements at the unloaded state from (a) 0.6% strain (b) 0.0 % strain and (c) -1.0 % strain in compressive loads

Figure 5-28 shows examples of anelastic strain recovery during the holding time at 5MPa after interruption from (a) 0.6% strain (b) 0.0% strain and (c) -1.0% strain, under the compressive loads. In all the cases, the strain increases sharply in first 2 minutes and then the increase gradually slows down. It is speculative to conclude from this very short holding time, that the magnitude of the anelastic strain increases with the increasing depth of the interruption points in compression. However, the anelastic strain after the interruption at higher compressive load is significantly greater than the anelastic strain after the interruption at lower compressive loads, for example it can be evidenced by comparing the magnitude of

anelastic strains after interruption from 0.6% strain in Figure 5-28(a) with interruption from 0.0% strain in Figure 5-28(b)Figure 5-29. This larger recovery of strain shows that the magnitude of back stress is higher in the material after being unloaded from a higher compressive load.

Figure 5-29 shows the macroscopic loading of 316H stainless steel at 650° C with interruptions at the various strains under tensile load. The specimen was unloaded to 5 MPa after each interruption and reloaded to the tensile peak strain instantly. The yield stress during each reloading cycle was measured. The tensile yield stress on reloading shows a positive correlation with the increase in interruption strain, that is, the higher the interruption strains in tension, the higher is the yield stress in the subsequent reloading cycle.

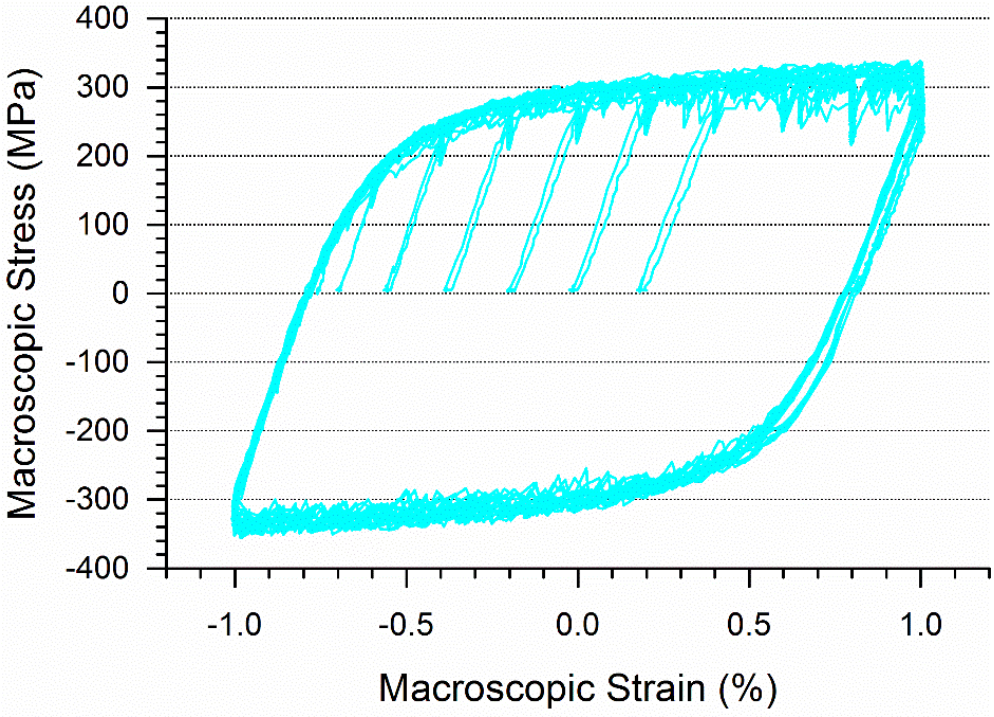

Figure 5-29 Reloading after various interruptions in tensile load during tension-compression cyclic loading of 316H stainless steel at 650° C. After the interruption, the specimen was first unloaded to 5 MPa then reloaded back to the peak tensile strain. Neutron measurements were recorded stopping at various points, during the reloading cycles

Upon unloading to 5 MPa from various interruption strains, the recovery of plastic strain (anelastic strain) can also be noticed in Figure 5-29. As expected, the strain after unloading reduces in this case, conversely to the compression interruption. The magnitude of the back stress in the material is compressive upon an interruption in tensile load, therefore it acts in

opposition to the tensile deformation. When the macroscopic applied load is taken off, this reverse acting back stress causes the macroscopic strain to reduce. Figure 5-30 shows an example of the anelastic recovery upon unloading from the strain of 0.4% under tensile load. The strain recovers quickly in first ~2 minutes and then the recovery slows down gradually.

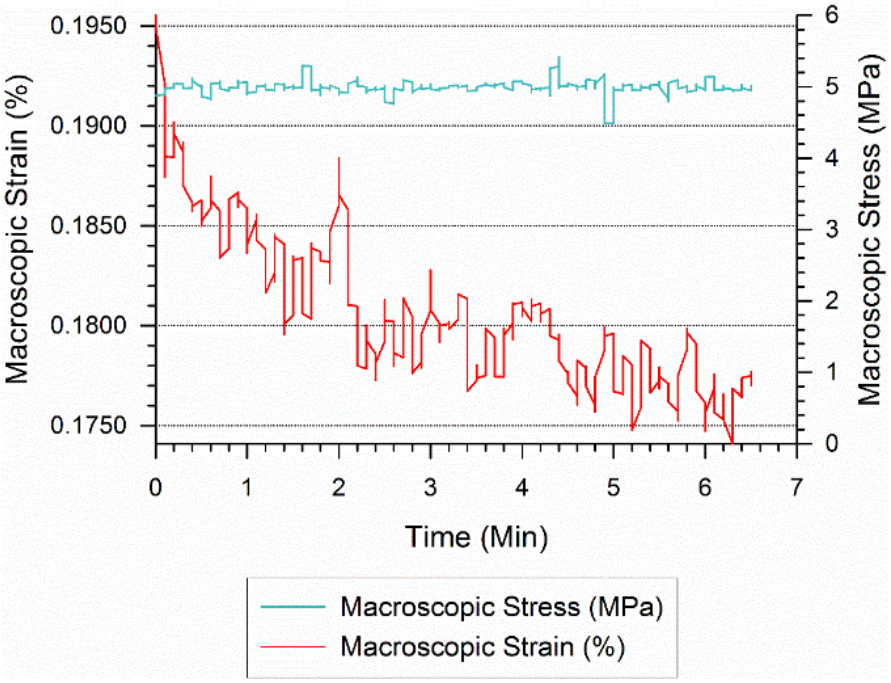

Figure 5-30 Evolution of anelastic strain during 6 mins holding time for neutron measurements at the unloaded state from 0.4% strain under tensile load

Table 5-3 Yield stress at 0.005% strain offset of the subsequent tensile loading cycle after interruption at various points during compressive and tensile loading

Ten. Interruption pts.	**A**	**B**	**C**	**D**	**E**	**F**	**G**	**H**	**I**
Interruption strain (%)	0.6	0.4	0.2	0.0	-0.2	-0.4	-0.6	-0.8	-1.0
Yield stress at 0.05% strain offset (MPa)	181	186	192	199	206	210	223	248	295
Com. Interruption pts.	**J**	**K**	**L**	**M**	**N**	**O**			
Interruption strain (%)	-0.6	-0.4	-0.2	0.0	0.2	0.4			
Yield stress at 0.05% strain offset (MPa)	178	235	257	262	287	292			

Table 5-3 and Figure 5-31 show the change of tensile yield stress with regards to various interruption strains under tensile and compressive loading. Similar to the room temperature tests, the yield stress of the reloading cycle shows a good negative correlation with the compression interruption strains and a positive correlation with the tension interruption strains. The magnitude of yield stresses in the high-temperature tests is smaller than that in the room temperature tests, therefore, the variation in the yield stress is also smaller. The correlation of yield stress with the interruption strains is more evident in the compression interruptions, owing to the availability of more data points. The change in yield stress with respect to the interruption strain is smaller in the strain range from 0.0% to -1% strain and larger from 0.2% to 0.6% strain. The specimen is in the plastic deformation zone during compressive interruptions in the range of 0.0 % to -1% strain such that the variations in macroscopic load from one interruption to the next is small, thus giving a small variation in yield stress in the subsequent cycle. On the other hand, the specimen is in the elastic-plastic transition zone during interruptions in the range 0.6% to 0.2% strain, where the macroscopic load change is higher giving a larger variation in yield stress.

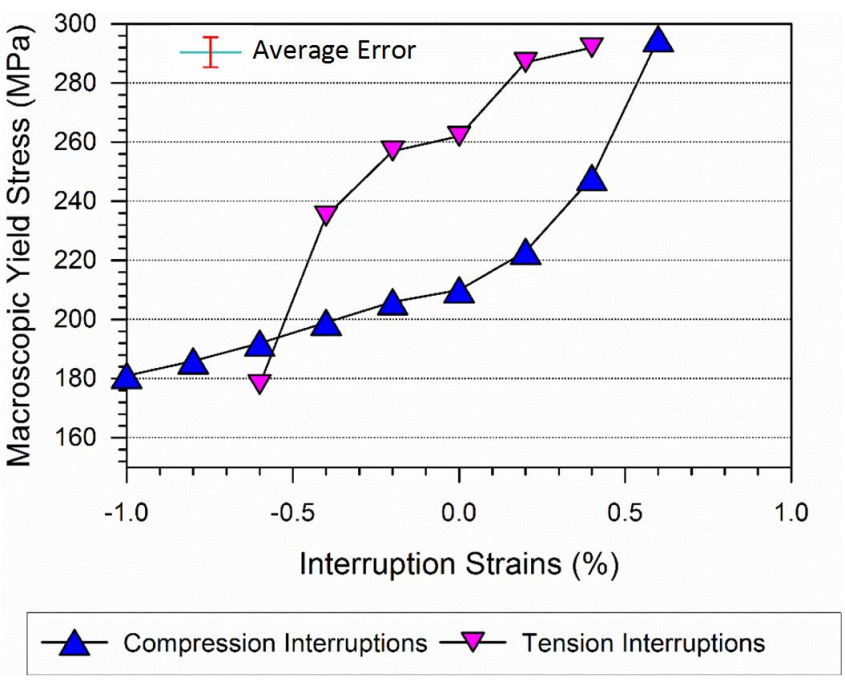

Figure 5-31 Corresponding changes in tensile yield stress at 0.05% strain offset in the subsequent reloading cycle with respect to various tensile and compressive load interruption. The yield stress decreases with increasing interruption strain in tension and increases with the increasing interruption strain in compression

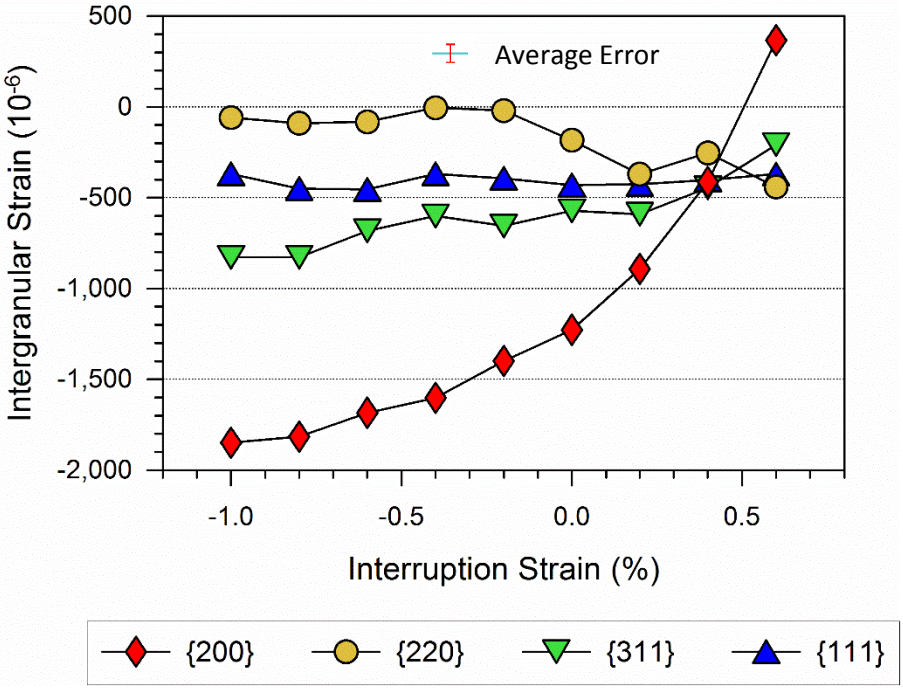

Figure 5-32 IR strains at 5 MPa after interruption at various strains at compressive loads in tensile-compression cyclic loading at 650° C (points A-I in Figure 5-26)

Figure 5-32 shows the IR strains at 5 MPa after various load interruption in compression. Similar to the room temperature tests, the IR strains in the plastic strong {200} grain families show a strong negative correlation with increasing interruption strain in compression. The magnitude of the IR strains in the grain families is larger in magnitude compared to the room temperature tests (shown in Figure 1.23) despite this test being at a lower applied stress. The IR strains in the {311} grain family also show a negative correlation with increasing interruption strain while IR strains in the {111} grain family remain almost unchanged. The IR strains in the plastic weaker {220} grain families don't show any clear correlation, with interruption strain between -0.4% to -1% strain. Therefore, the hypothesis established for the room temperature tests that the 'variation in macroscopic yield stress is due to the variation in yielding of the plastic weaker grain families' established for the room temperature tests cannot be exclusively observed at the high temperature (650° C). Nevertheless, the IR strains in the {220} grain families become more tensile with increasing interruption strain in the range 0.6% to -0.2%. The behaviour of the family at higher compressive interruption strain may be because IR strains have relaxed by anelastic strain recovery during the holding period for neutron measurement. Experimental evidence of such a change in IR strain in this grain family caused by anelastic strain has been reported in published work [216]. Nevertheless,

the strong negative correlation between IR strains in the {200} grain family with interruption strain confirms the strong contribution of the IR strain to the Bauschinger effect in this material at this temperature and loading rate.

It can be observed in Figure 5-32 that the magnitude of IR strains in all the reported grain families shows a shift towards compression. Moreover, the distribution of IR strains in various grain families is different compared to the room temperature test. For example, the IR strains in the {311} grain families are compressive and increase in compression with increasing interruption strain. If the shift of the IR strains towards compression in all the grain families is a true representation of the IR strains in the material, this will lead to incompatibility and non-equilibrium conditions. However, at this operating temperature and loading rate, these experimental data are not surprising as such redistribution of IR strains between grain families and the shift of the IR strains towards tension has been reported for a tensile test of 316H at 650° C [151]. The conventional slip based deformation mechanism is no longer dominant anymore at this temperature (above 0.4 T_m) and other mechanisms, for example, dislocation glide or glide plus climb processes are expected to affect the plastic deformation process [217]. Daymond et el. [151] therefore, postulated that such variations and shift in IR strains can be attributed to the relaxation of the grain boundaries which are too distorted to contribute to the diffraction patterns. As a result of this non-diffracting grain boundaries, the equilibrium condition is not captured in the diffraction data. Moreover, the four diffracted grain families presented here represent about 15-20% of the total grain constitutes [151]. It is possible that the other non-diffracting grains are in tensile IR strains, although, it is unlikely, that the non-diffracting grains will deform very differently from these sampled, as the full spectrum of elastic anisotropy has been considered [151]. This shift may also be partially attributed to the diffraction peak shape broadening during the initial 20 tension-compression cycles, as discussed in the case of room temperature tests. The d_0 value used to calculate lattice strain was measured during the first few measurements before the tension-compression cycles, however, the FWHM of the peaks have changed later due to the cyclic loading, which caused a small erroneous shift in the data. Figure 5-33 shows the measured FWHM for the four grain families reported here, the first 2 measurements were conducted before the 20 tension-compression cycles and the later ones after. The figure shows a significant increase in the FWHM in all four grain families after the 20 tension-compression cycles.

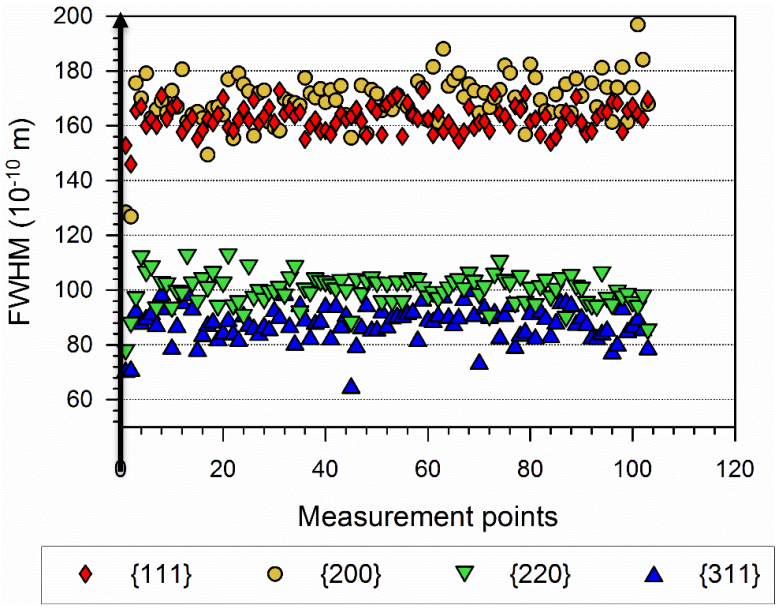

Figure 5-33 Evolution of the full width at the half maximum (FWHM) of the diffraction peaks of various grain families during the cyclic tensile yield test at 650° C. The black arrow line separates the measurements before and after the 20 tension-compression cycles

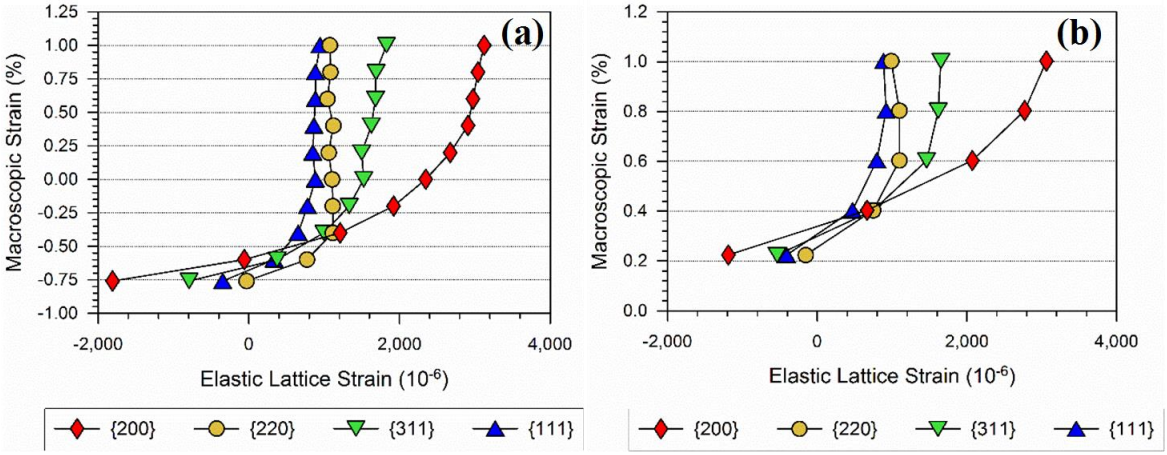

Figure 5-34 Evolution of elastic lattice strain during reload after interruption at (a) -1% and (b) 0.0% strains in compressive loading at 650° C

Figure 5-34 shows the evolution of the elastic lattice strains during reloading after interruptions at (a) -1% strain and (b) 0.0% strain at 650℃. The sequence of the yielding in the grain families at high temperature is consistent with that of the room temperature tests, in both cases, the {220} grain family seem to deform plastically first and the {200} grain family last.

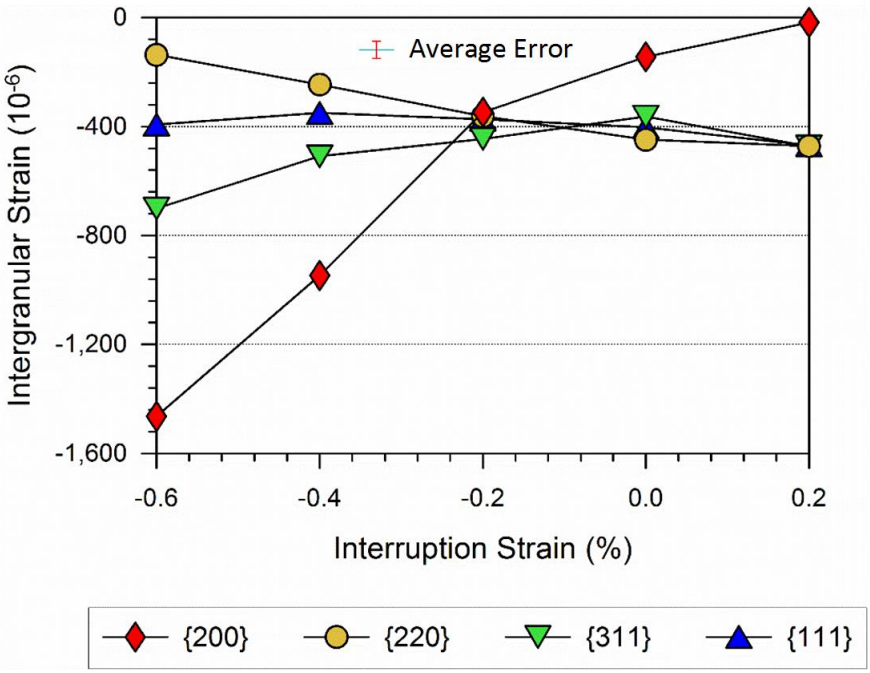

Figure 5-35 IR strains at 5 MPa after interruption at various strains during tensile loading in the tension-compression cyclic test at 650° C (points J-O in Figure 5-26)

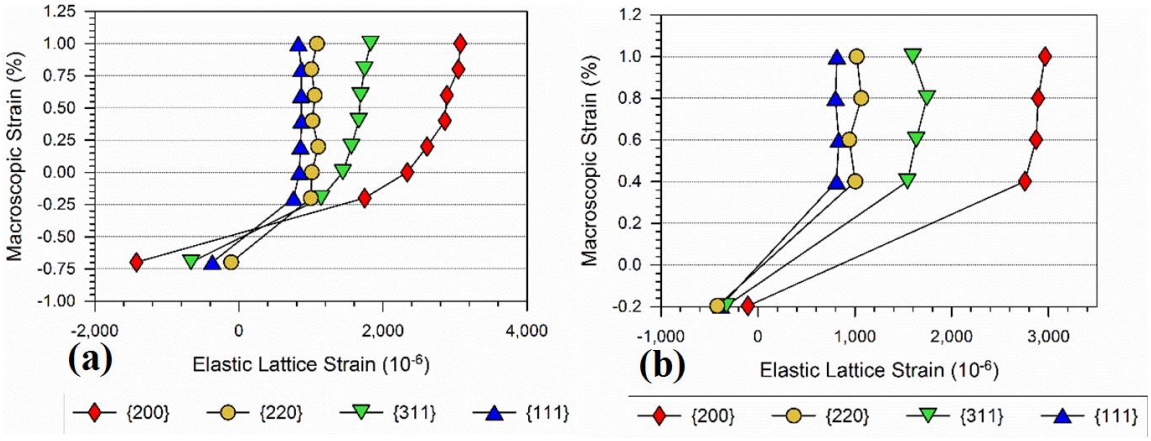

Figure 5-36 Evolution of elastic lattice strains during reload after interruption at (a) -0.6% strain and (b) 0.0% strain in compressive loading

Figure 5-35 shows the IR strains at 5 MPa with respect to various interruption strains in tension. The IR strains in the {200} grain family increase towards tension and the IR strains in the {220} grain family become more compressive with an increase in interruption strain. During reloading of the specimen to the peak tensile strain, the applied stress has to overcome compressive strains in the plastically weaker {220} grain families to initiate

macroscopic plastic deformation. Therefore, increasing compressive residual strains in the {220} grain family with associated with increasing tensile interruption strains, results in increasing yield stress in the subsequent cycle. Figure 5-36 shows the evolution of the lattice strains during the reloading cycle after an interruption from two different strains in tension. The different magnitude of strain at which differently oriented grain families start to deform plastically, confirms the macroscopic yielding of 316H is a phenomenon of plastic deformation occurring systematically from the comparatively weaker grain families to the stronger grain families.

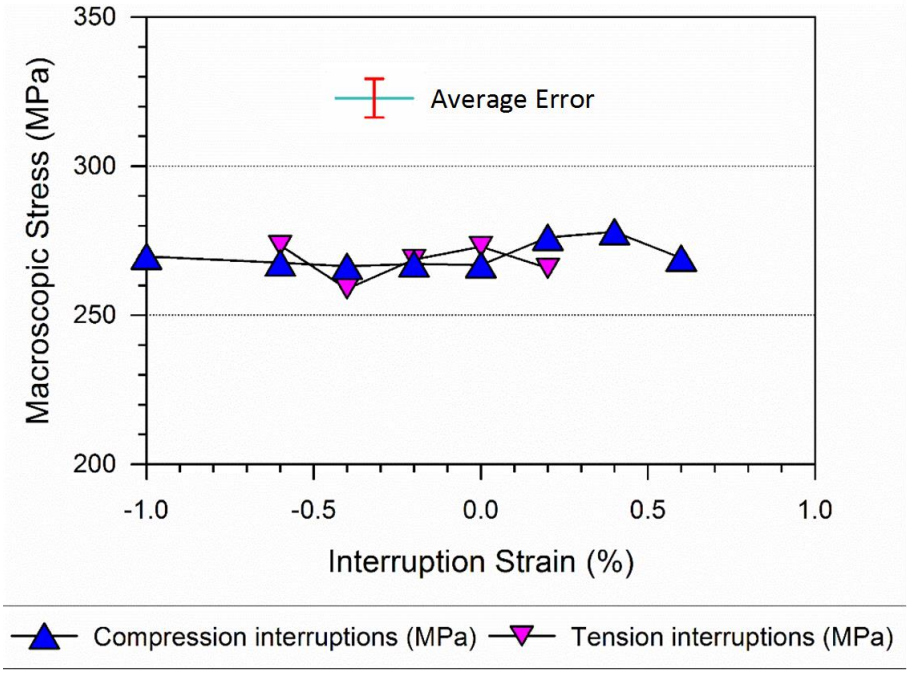

Figure 5-37 Macroscopic stress required reaching to peak tensile macroscopic strain of 1% after various interruption in compression and tension

Similar to the room temperature tests, the IR strains at the peak strain tip of the cycle have been investigated. Figure 5-37 shows that there is no appreciable difference in the macroscopic stress reached at the peak tensile strain of 1% after being interrupted in various tensile and compressive strains. This observation can be coupled with the observation in Figure 5-38 that IR strains in all the grain families of the peak strain point of the cycle are also essentially unchanged irrespective of the interruption strain. At the peak macroscopic strain, the macroscopic material is completely plastically deformed and the IR strains in each of the grain families have reached a saturated magnitude. Thus the macroscopic stress-strain behaviour of the extreme points of the cyclic loading is unaffected by cycle interruptions.

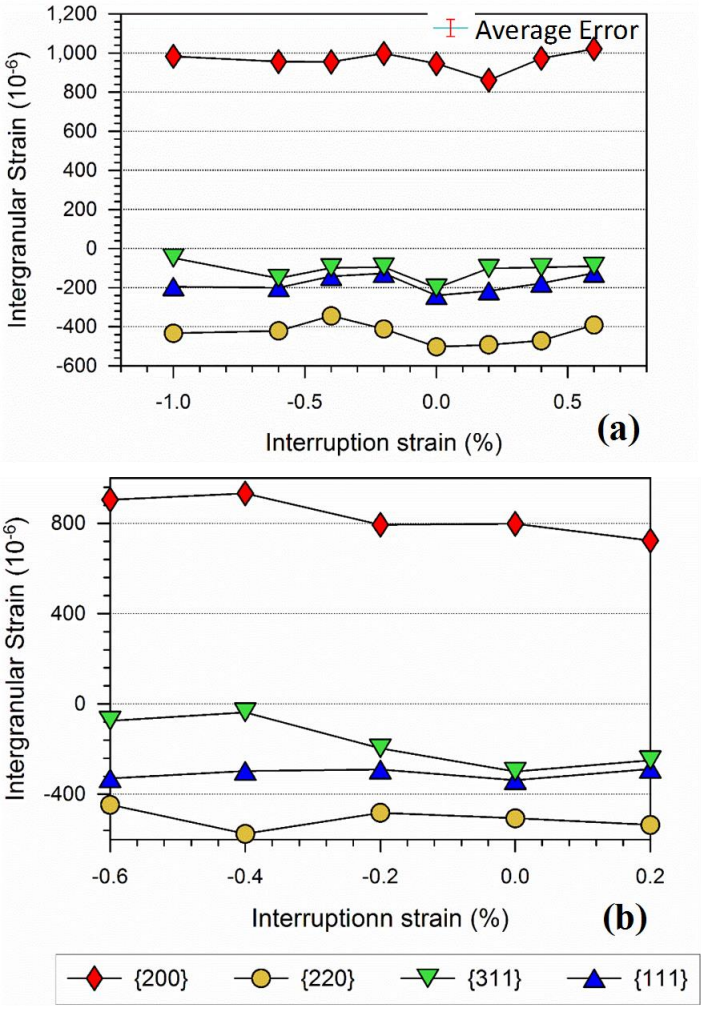

Figure 5-38 IR strains at the peak tensile strain of 1% with respect to various interruption strains in the (a) compressive and (b) tensile loads

5.6 Summary

In both room and high temperature Bauschinger tests, a strong correlation was observed between the intergranular strains and the change of macroscopic yield and peak stresses. This implies that intergranular stress is the primary source of the origin of Bauschinger effect in type 316H austenitic steel. The other findings from the study are detailed below.

5.6.1 Room temperature tests

- During tension-compression cyclic loading of AISI type 316H austenitic steel, only transient softening and no permanent softening was observed in the reverse loading.

- The tensile yield stress of 316H stainless steel decreased with an increase in compressive interruption strain and increased with an increase in tensile interruption strain. Compressive yield behaviour showed similar history dependence in the opposite sense that is, it increased with an increase in compressive interruption strain and decreased with an increase in tensile interruption strain.
- The magnitude of IR strains in the plastically weaker, stronger and average grain families showed a strong correlation with the observed variation of the yield stress during the reloading. Moreover, the IR strains at the peak macroscopic tensile and compressive strains (±1%) reach to a saturated magnitude irrespective of the interruption strains. This observation of near constant IR strain is consistent with the observation of zero permanent softening in the material at the peak strain irrespective of the interruption strains. These strong correlations imply that the IR strains generated due to the anisotropic deformation of the grains play a major role causing the Bauschinger effect in this material.
- It was experimentally inferred that initiation of macroscopic yielding in 316H stainless steel occurs by the yielding of the plastically weaker (for example the {220}) grain families. In the case of tension-compression cyclic loading the magnitude and sign of IR strains in these weaker grain families determine the macroscopic yield stress of the material in the subsequent loading.
- During tension reloading, after tension interruptions, the macroscopic yielding occurred sharply and after compression interruptions, it occurred smoothly. Sharp yielding occurred, when the difference of the yield stress of various grain families are reduced due to the plastically weaker grain families possessing compressive IR strains and plastically stronger grain families possessing tensile IR strains. Smooth yielding occurs when the difference of yield stress of different grain families increases due to possessing of IR strains of opposite sense. A similar observation in opposite sense was made during compression reloading.

5.6.2 High-Temperature tests

- Kinematic hardening of 316H stainless steel was also observed during tension-compression cyclic loading at a high temperature of 650° C. Similar to the room

temperature tests, there was only transient softening observed during reloading and no permanent softening.

- The tensile yield stress found to decrease with an increase in compressive interruption strains and found to increase with an increase in tension interruption strains.
- Anelastic deformation was noticed during the dwell time for neutron measurements in the unloaded state after various interruption strains. The anelastic strain after compression interruption was positive and after tensile interruption was negative. The magnitude of the anelastic strains varied depending upon the degree of compressive or tensile plastic deformation before unloading.
- At the high-temperature tests, similar correlation of the IR strains with the interruption strains can also be observed both during the yielding and at the peak strain. The correlation is worsen compared to the correlation of the room temperature tests which can be attributed to anelastic strain, activation of different deformation mechanisms and peak shape broadening.
- Compared to the room temperature tests, the IR strains in various grain families are found to be more evenly distributed among differently oriented grain families at high temperature. This difference in the distribution of the IR strains is again due to the difference in the deformation mechanisms during room and high temperature.

Chapter 6 Effect of back stress on creep deformation

6.1 Overview

AISI type 316H austenitic stainless steel is widely used in power generation plants because of its high-temperature strength, corrosion and oxidation resistance [216]. Predicting the creep life of this material in power plant components under operation conditions is crucial, to avoid either a disastrous failure, costly repair or premature shut down of the plant. However, estimation of creep life under plant operating condition is challenging because the material not only experiences creep dwell at a constant load or displacement but also complex time-dependent loading cycles where creep dwells can occur at intermediate loads. For example owing to thermal stress generated during plant start-up/shut down or to variations in demand.

Consider the boiler within a steam generating power plant as an example to demonstrate how these cyclic thermal stresses are generated during plant operation. The boiler system can comprise of many thick walled components such as headers, pipes, fittings etc. During start-up of the plant, high magnitude thermal stresses are introduced on these components due to constrained thermal expansion. These stresses could be either tensile or compressive depending upon the geometry of the specific component and how it's restrained. Let's consider a thick walled steam pipe as shown in Figure 6-1.

During the start-up of the plant the inner wall of the pipe gets hot as soon as high-temperature steam passes through the pipe. The inner wall tends to expand but the outer wall constrains the expansion as the temperature in outer wall is still low. Therefore, the inner wall of the pipe experiences compressive loading and drives the outer wall into tensile loading. The temperature distribution from the inner wall to the outer wall of the pipe reaches to steady

state conditions with time. When the plant is shut down either for a routine maintenance check or a repair, the outer wall of the thick pipe cools down much quicker than the inside. Therefore, tensile thermal stresses are again generated towards the outer wall of the pipe and drive the inner wall into compression. This type of start-up or shutdown of the plant gives rise to low-frequency cyclic loading in thick walled components. Such loading can affect the overall creep life of components by altering the microstructure and plastic strain state of the material. Furthermore, due to variation in electricity demand, the steam pressure under which these components operate also varies. This means, the load at which the components of the power plants deform in creep during operation is variable.

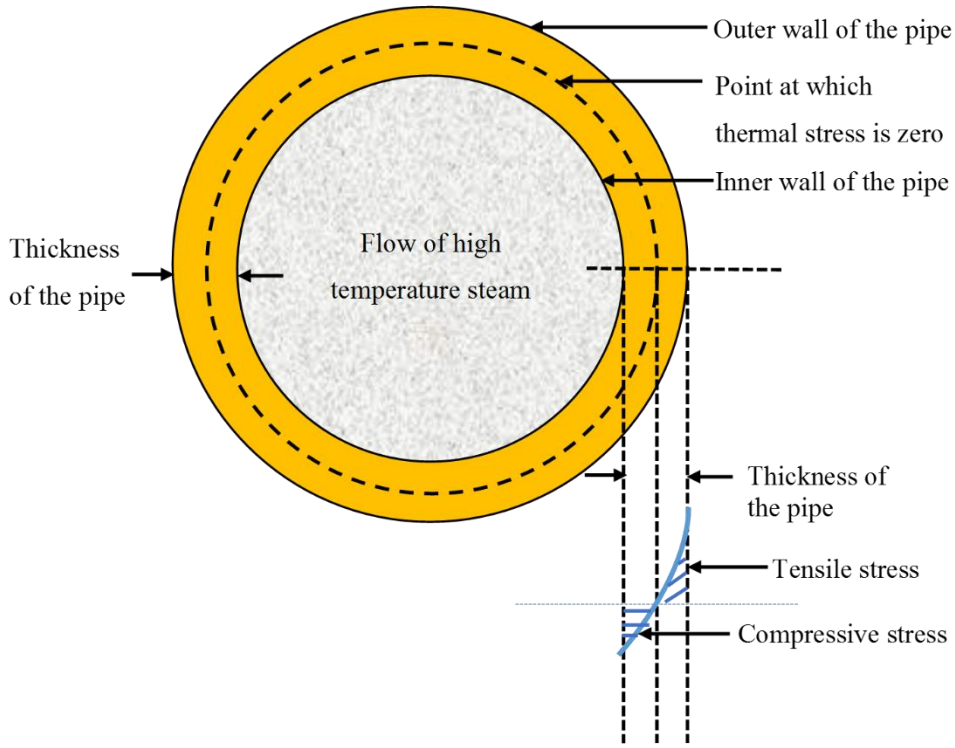

Figure 6-1 Schematic of the generation of tensile and compressive stresses in a thick walled pipe during power plant start-up.

In the previous chapter, the generation and evolution of intergranular strains during cycling loading has been discussed in detail. It has been shown that during cyclic-creep loading, depending upon the point where the creep dwell is being introduced, the actual load experienced by the material at the grain scale can be much higher or lower than the nominal macro stress. Therefore, a simple extrapolation of short-term creep test data accounting for the applied stress, temperature and materials parameters, as used in conventional approaches,

does not necessarily provide an accurate estimate of the overall creep life during creep-fatigue loading under plant conditions.

The term ‘back stress’ is often used in analytical [218-220] and FE creep models [218, 221] to fit experimental creep data better, essentially by reducing the external applied stress. Back stress is also used in constitutive equations to explain the creep rate changes during transient creep processes [5]. So, the argument of creep deformation rate being dictated by an effective stress rather than the applied stress is well established. However, it is still not fully understood how back stresses generated at different length scales correspond to each other and affect the macroscopic creep deformation as a whole, which is essential for creep constitutive models. Back stresses in type 316H austenitic steel are generated from two distinctive sources that are Intergranular stress and Intragranular stress, as explained in details in chapter 2. In this chapter, experimental results are presented showing the effect of this two components of back stress on the creep deformation rate of type 316H austenitic stainless steel. In-situ neutron diffraction was used to measure intergranular strains quantitatively and transmission electron microscopy (TEM) was used to investigate the changes in dislocation structures qualitatively at the start of the load controlled creep dwells. Moreover, the evolution of intergranular strains and dislocation structures during the dwells were also recorded.

In plant operations, many components that operate in the creep regime also undergo displacement controlled creep deformation. One example of such creep deformation is the observed reheat cracks in as-welded austenitic steel components in the UK AGRs [222]. It has been reported that the relaxation of tensile residual stresses due to the conversion of elastic strain to creep strain have resulted in the creep cavitation damage and eventually lead to reheat cracking in these components [76]. Results of in-situ neutron diffraction tests of the displacement controlled creep dwells following cyclic loading is also presented in this chapter.

6.2 Load controlled creep

The results from chapter 4 and chapter 5 show how IR strains are generated and evolve during high-temperature cyclic loading of AISI type 316H stainless steel. It can be observed

that during tension-compression cyclic loading, when the macroscopic loading direction is reversed, the magnitude of IR strains do not change significantly until the material deforms plastically on the reverse loading. It can also be observed that the magnitude of IR strains increase with repeated cycling, that is the magnitude and sign of IR strains at a specific stress could be very different depending upon the loading path history of the specimen.

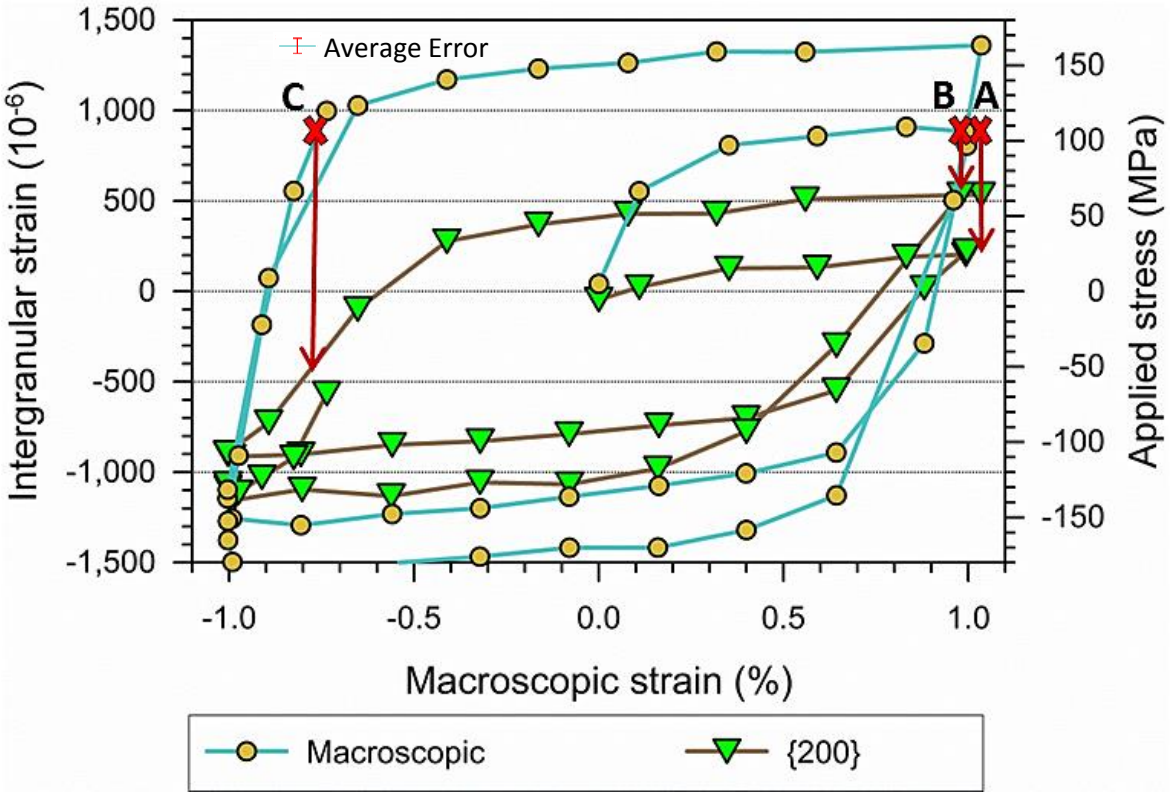

Figure 6-2: Variation of axial intergranular strains in the {200} grain family during cyclic loading of type 316H stainless steel at 650 °C. Points A, B and C marked by cross mark show 3 positions in the cyclic loading curve where the applied stress is same but the IR strain is different. At Point A, the specimen is loaded to 1% tension peak strain, at point B, the specimen is unloaded to the same stress of point A after second loading cycle and at point C the specimen is reloaded to the same applied stress of point A and B from the compressive peak strain in the 3rd loading cycle. The arrow lines from these points show the corresponding magnitude of the IR strains in the {200} grain family at these points.

To give an example, in Figure 6-2 the variation of IR strain in the {200} grain family with macroscopic cyclic loading at 650 °C has been plotted. The {200} grain family has been chosen for this because it is the most responsive grain family to externally applied stress. Three points A, B and C have been marked in the figure which are all exposed to the same external stress of 120 MPa however, the magnitude of IR strains at each of these points is

very different in magnitude and sign (tensile or compressive) as shown by the arrows. At point A, the material has deformed plastically by tensile loading only to reach to 1% macroscopic strain, the magnitude of IR strain is lowest at this point among all three points. Point B is at the same stress as point A, but to reach to that point the material was cyclically deformed. At the peak strain of 1% in the 2nd cycle, the magnitude of IR strain is much higher than that of the peak strain in the 1st cycle. Upon elastic unloading from the peak stress to 120 MPa at point B, the magnitude of IR strain remains almost unchanged to that of the peak strain. Lastly, point C is marked during the elastic reloading from the compressive peak stress in the 3rd cyclic loading cycle. As the material has started to deform plastically at this stress, the magnitude of negative IR strain in the {200} grain family started to change from compression to tension.

The observed differences in the IR strain state at various points under identically applied stress was utilized to quantify the effect of IR strains on creep deformation rates. Three loads controlled creep dwells at points A, B and C were introduced and the creep rate of these dwells was correlated with the magnitude of IR strains at the beginning of the dwells measured using neutron diffraction. Moreover, the evolution of macroscopic strains and IR strains during the creep dwells was also investigated. The magnitude of the range of IR strains between the grain families with highest tensile and highest compressive IR strains was assumed to be representative of the relative magnitudes of IR strains in the material at any points of the cyclic loading. This assumption is based on the fact that magnitude of total IR stress in the material must integrate to zero over the material cross section. So, if the tensile IR strains corresponding to the IR strains increase in some grains, there must be an increase in compressive IR strains in other grains.

Specimens identical to those described in section 3.2.1 for tension-compression cyclic tests were used for this experiment. The specimen was first heated to 650 °C and loaded in strain control at a strain rate of 7 x 10^{-6} s^{-1}. The load was always started in tension. The load was interrupted at various points A, B and C during cyclic loading for the separate specimen and a load controlled creep dwell at 120 MPa was introduced. The changes in macroscopic creep strain during the creep dwell were monitored using a high-temperature extensometer and the corresponding changes in lattice spacing were recorded using neutron diffraction. The IR

strains for at least five grain families were calculated from the recorded neutron data according to the procedures described in Section 3.5.7.

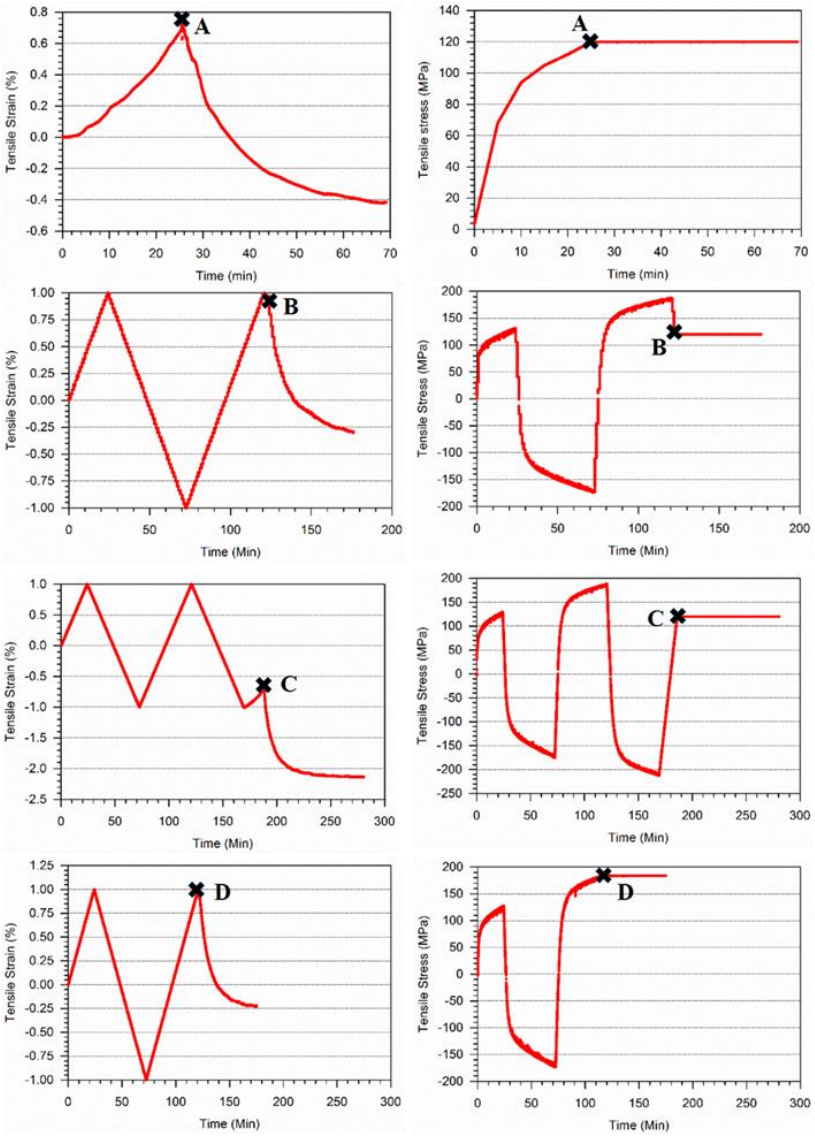

Figure 6-3 Macroscopic stress and strain states of specimen A, B, C and D. Specimens A, B and C correspond to the interrupted loading conditions at points A, B and C respectively of Figure 6-2. Specimen D corresponds to the unloaded state of point B that is load being interrupted at 1% tensile strain in 2nd cycle before unloading of the cyclic loading curve as shown in Figure 6-2. The thermal strain in the samples were balanced to zero after reaching to the intended temperature of 650 ^{o}C. Therefore, the strains in the above figures are only relative strains equalling to absolute strain minus the thermal strain reaching at 650 ^{o}C.

The work hardening state of the specimens at the beginning of the creep dwells that is at points A, B and C were different, therefore the hardness and dislocation structures of the specimens at these points were measured. These measurements were conducted by

deforming another set of identical specimens to those used for the in-situ neutron diffraction tests in the laboratory ex-situ. Four identical specimens were used for this purpose. The specimens were loaded at 650 °C with the same strain rate of 7 x 10^{-6} s^{-1} and the loadings were interrupted at points A, B and C and D. Points A, B and C correspond to the same point of load interruptions as shown in Figure 6-2 and the specimen D correspond to the point of tensile peak strain in the 2^{nd} cycle that is the point before being unloaded to point B. The analysis in the additional specimen D was conducted due to observation of interesting dislocation structures in specimen B.

For clarity, the stress and strain state of the specimens A, B, C and D are shown in Figure 6-3. After load interruptions, the specimens were cooled down quickly using two air blowers while keeping those under load. Upon cooling to room temperature the specimens were unloaded. The deformed interrupted specimens were then cut in half in transverse to the loading direction. Half of the specimens were utilized for hardness measurements and another half for the TEM investigations. The specimens for TEM and Hardness investigations were extracted and prepared following the procedures described in Section 3.3.3.1 and Section 3.3.2.1 respectively.

6.2.1 Creep deformation rate

Figure 6-4 shows the three creep deformation curves associated with load controlled dwells introduced at points A, B and C as illustrated in Figure 6-2. The difference in the shapes of the creep deformation curves and the creep deformation rates can be clearly seen in this figure. The large difference in the total creep strain accumulation arises from the difference in strain accumulation during primary creep regime. In fact, the dwells at point A and C show distinct primary creep but the dwell at point B hardly shows any. The reasons for this difference in the shape of the creep curves is discussed later in this chapter.

The secondary creep regime is often the longest fraction of creep life of type 316H stainless steel [223] and as such is usually of more importance for engineering applications. Therefore, the effect of IR strains on minimum creep rate has been considered here rather than the total creep strain. The blue dashed line in Figure 6-4 shows the time after which the minimum creep deformation rate was calculated from. The comparison of the minimum creep rate of the three dwells is plotted in Figure 6-5. It is to note that the tensile creep dwell

at point C was started at a negative macroscopic strain that is when the specimen was under compressive strain .The creep curve for this dwell is generalized to positive strain in Figure 6-4 and in Figure 6-5, in order to visually compare the changes of creep strain with that in the other two dwells started at positive strain.

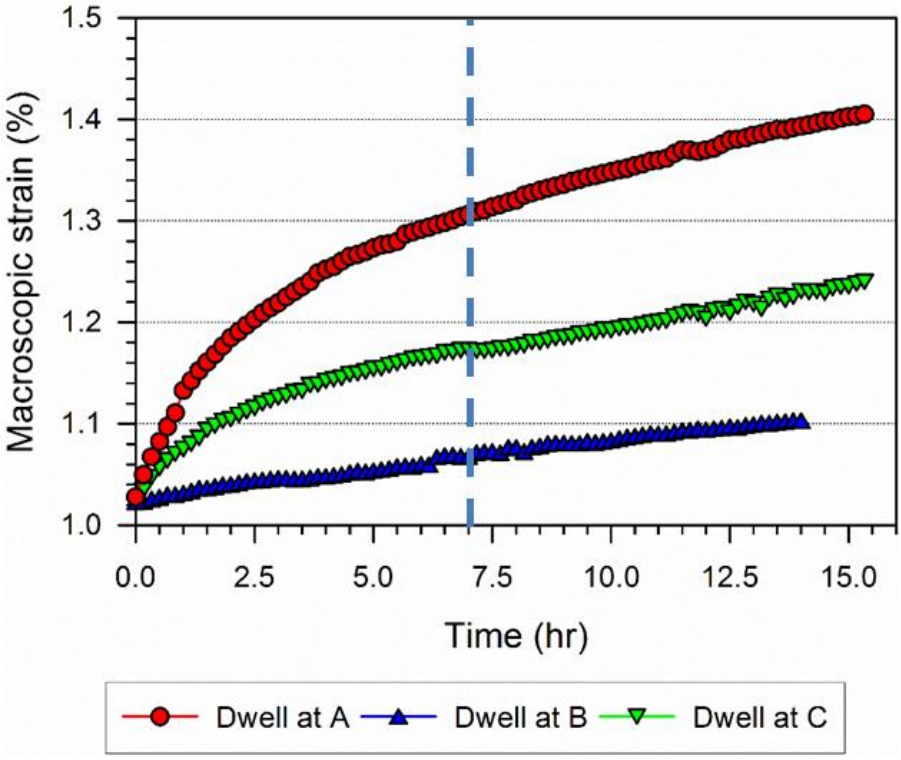

Figure 6-4: Creep curves introduced at the points A, B and C of the tension-compression cyclic loading at ±1% strain range of type 316H austenitic steel at 650℃, as shown in Figure 6-2. The dotted line shows the time after which the minimum creep rate was calculated from. The strain at the start of the dwell from point C was negative in absolute value and generalized to positive strain in order to visually compare the increase of creep strain with that in the other two dwells started at positive strain.

In Table 6-1 the minimum creep rate has been tabulated along with the magnitude of IR strains at the beginning of each of these 3 dwells. The minimum creep rate of the dwells, all under an applied stress of 120 MPa at 650° C but starting at different points in the cyclic loading, are significantly different. The higher the magnitude of IR strains, the slower is the creep deformation rate. The minimum creep deformation rate of the dwell started at point A (with lowest IR strain) is almost twice the rate of the dwell started at point B (with highest IR strain), both being at the same applied stress. This observed difference in the creep deformation rates can be attributed to the difference in the 'effective stresses' in the material which is controlling the creep deformation rate. An increase in the IR strains will increase

the back stress in the material, thus reducing the creep deformation rate. IR strains implies that the inhomogeneity of the strain partition between differently oriented grains has increased. This means that, at point A in Figure 6-2, the strains are much more homogenously distributed among the differently oriented grains compared to at the points B or C that is the magnitude of internally generated stress is much higher at point B than at A, for example.

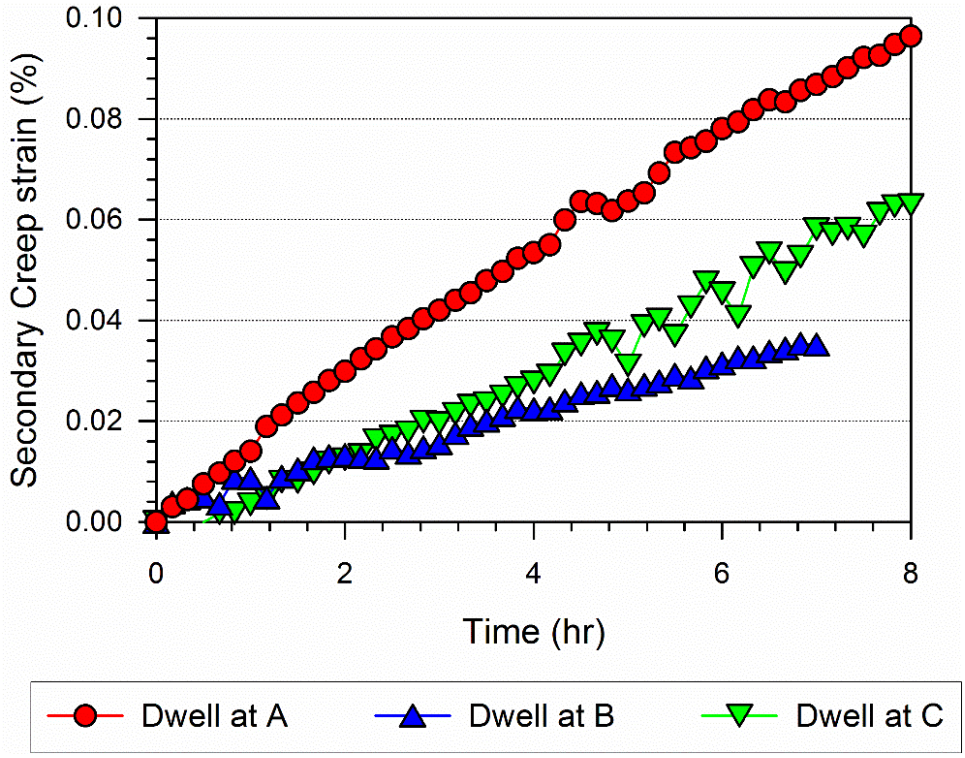

Figure 6-5: Comparison of the minimum creep deformation regimes of the creep dwells started at points A, B and C of Figure 6-2. The calculation of the minimum creep rate was started from a point after 7 hours of the initiation of the dwells. The strain at the start of the dwell from point C was negative in absolute value and generalized to positive strain in order to visually compare the increase of creep strain with that in the other two dwells started at positive strain.

The findings regarding the IR strains can also be explained by imagining elastic unloading of stresses following Hooke's law, during macroscopic elastic unloading, the unloading of the elastic lattice strains in each grain family will follow a straight line with a slope the elastic strength of that particular grain family. Upon elastic unloading to 0 applied stress, there will remain non-zero elastic strain trapped as residual strain in some of the grain families. The bigger the IR strains at the unloading point, the higher the trapped residual strains upon unloading. For example, in the experiments presented here, the specimen will have higher residual strains in all the grain families if the specimen is unloaded from point B than it were

from point A. Now, if an external load is applied for example in a creep test, it has to overcome the compressive residual strain in the creep weaker grain families first before further creep deformation in the material. Therefore, the larger the IR strains in a material, the smaller the effective stress will be, driving the creep deformation at any specific applied stress.

Table 6-1: Comparison of the IR strains and subsequent minimum rate of the creep dwells under 120 MPa started at point A, B and C (as shown in Figure 6-2) of the tension-compression cyclic loading at ±1% strain range of type 316H austenitic steel at 650°C.

Specimen & Dwell Start Point	**Applied stress (MPa)**	**Strain at the start of creep dwell (%)**	**IR strain range at start of creep dwell (10^{-6})**	**Min. creep rate (h^{-1})**
A	120	1.028	385	1.06E-04
B	120	1.022	719	4.58E-05
C	120	-0.718	535	8.90E-05

However, in this case, IR strain is not the only factor contributing to the difference in the minimum creep rates as because the macroscopic strain hardening state is also different at these three points. Moreover, the intragranular stress originating from inhomogeneous distribution of dislocations may also contribute to the changing creep rate. In order to understand the role of these changes in microstructure in affecting the creep rate, the hardness of the specimens were measured and the dislocation structures at each of the start of the creep dwell points were investigated.

6.2.2 Hardness measurements

Hardness measurement technique has been reported to characterise dislocation densities [224], plastic strain [225] and creep strain [226] in steel, however, the reliability and sensitivity of this technique for such characterisation is limited. Large scatter in macro hardness data can arise from the inhomogeneity of local microstructure. Hardness measurement of the specimens A, B, C and D were conducted following the procedures

described in Section 3.4. The results of the hardness measurements is presented in Figure 6-6. A distinct difference in the hardness can be observed between the specimen A and the other 3 specimens. This is expected, as because, at point A, the specimen is only been tensile deformed while in other points the specimen has been work hardened during tension-compression cyclic deformation. The difference in the hardness magnitude between the specimens B, C and D are very small and within the experimental error of measurements.

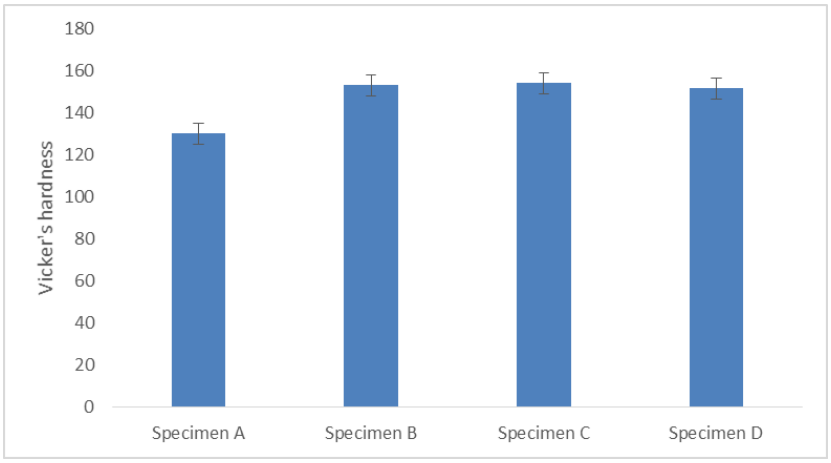

Figure 6-6 Measured Vicker's hardness in the specimens A, B, C and D

6.2.3 Investigations of dislocation structures

A qualitative analysis of the dislocation structures has been conducted to gain insight into the varying state of deformations in specimens A, B, C and D. The main objective of this analysis was to investigate the formation of dislocation cell type structure and hence the, possible contribution of intragranular stresses to the total back stress in the material. Moreover, analysis of the dislocation structures can provide important insight in explaining the observed difference in shapes of the creep deformation curves. It is important to mention that depending on the orientation of the sample, dislocations from only a particular crystallographic plane is observed at a time in the TEM. As mentioned in section 3.3.3, a double tilt specimen holder was used for obtaining the TEM images in this study to overcome this limitation.

6.2.3.1 Specimen A

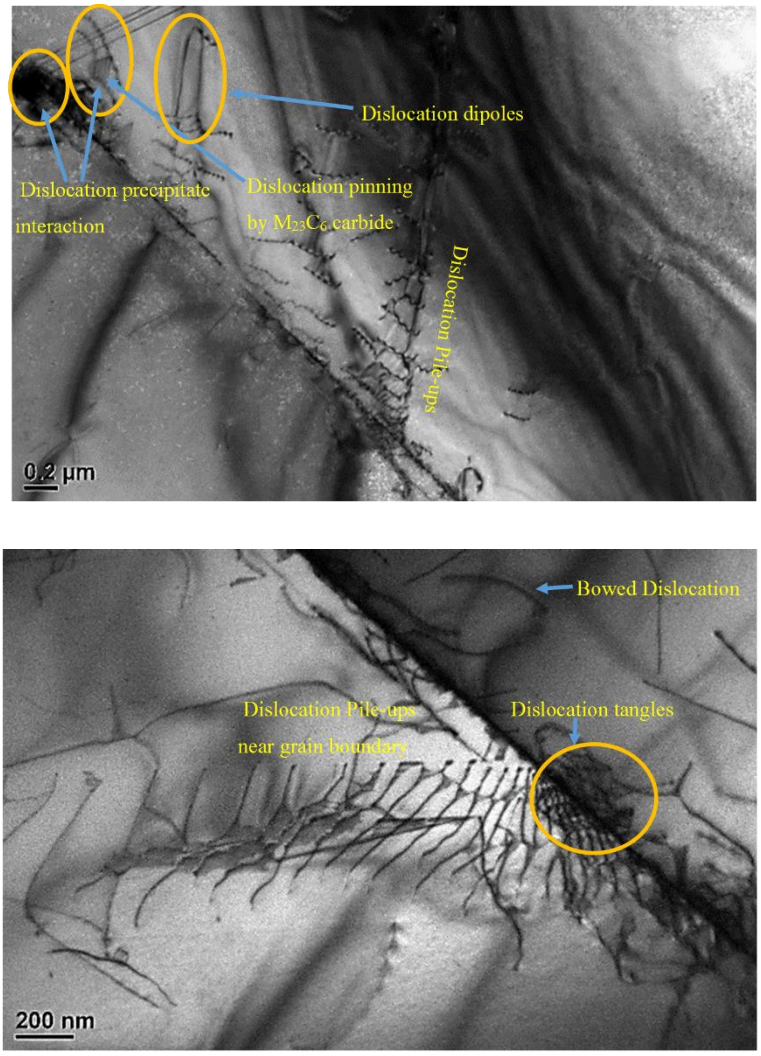

Figure 6-7 BF TEM micrographs of specimen A showing presence of various inhomogeneous dislocation structures.

Figure 6-7 shows the typical BF TEM micrographs obtained from specimen A. The images show typical dislocation structures of a tensile deformed specimen. Dislocations pile ups are visible suggesting predominant single slip in the specimen. Dislocations Pile-ups are a source of internal stresses in the material, particularly near grain boundaries. There is evidence of dislocations bowing, pinning and tangling. Dislocation interactions with other dislocations and precipitates can also be seen. The precipitate was identified as $M_{23}C_6$ carbide by its characteristic moiré fringes. There also appears to be dislocation dipoles present.

6.2.3.2 Specimen B

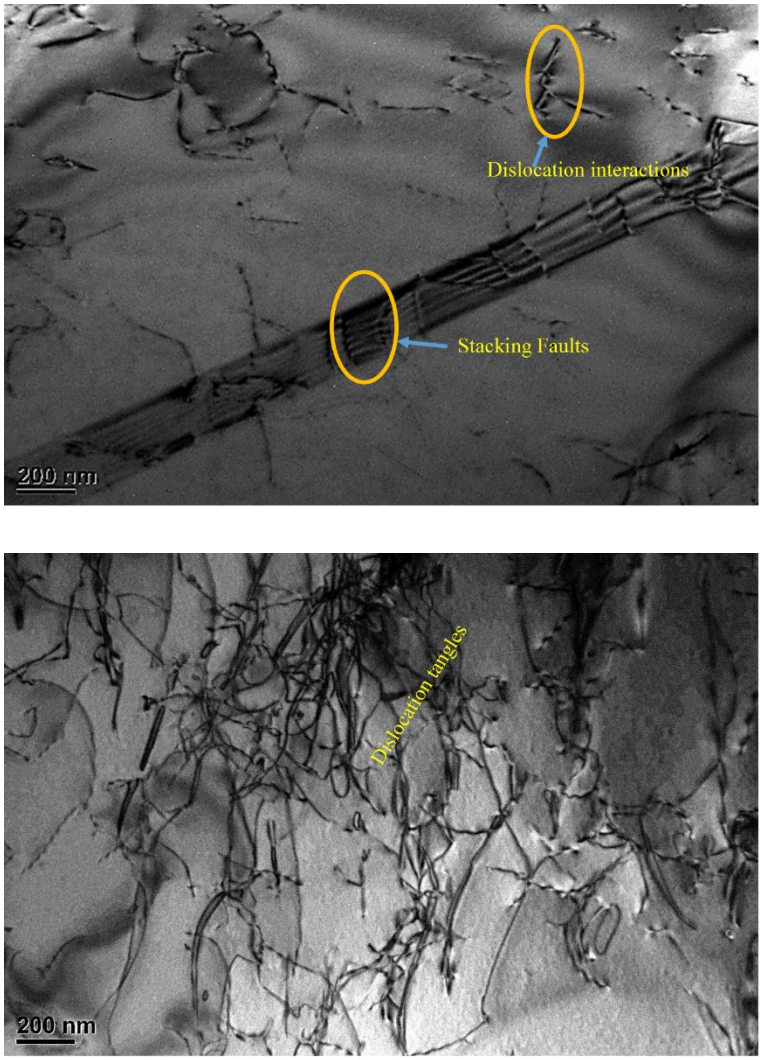

Figure 6-8 BF TEM micrographs of specimen B showing heavy dislocation tangling and stacking faults

The TEM BF micrographs of specimen B shows interesting dislocation features which can explain the loss of primary creep regime during the creep dwell started from this point. Primary creep in in this material occurs due to the increasing strain hardening from the finite number of dislocations introduced on loading. In this specimen, a finite number of mobile dislocations were created during the cyclic plastic loading, however on unloading from the peak strain to 120 MPa, some of the dislocations reversed their direction of motion and tangled with other dislocations, which eventually decreased the number of available mobile dislocations necessary for primary creep. Such heavy tangling of dislocations are formed

due to thermally activated process such as cross slips and multiple slips. Fringes of stacking faults are also visible near the grain boundaries.

6.2.3.3 Specimen D

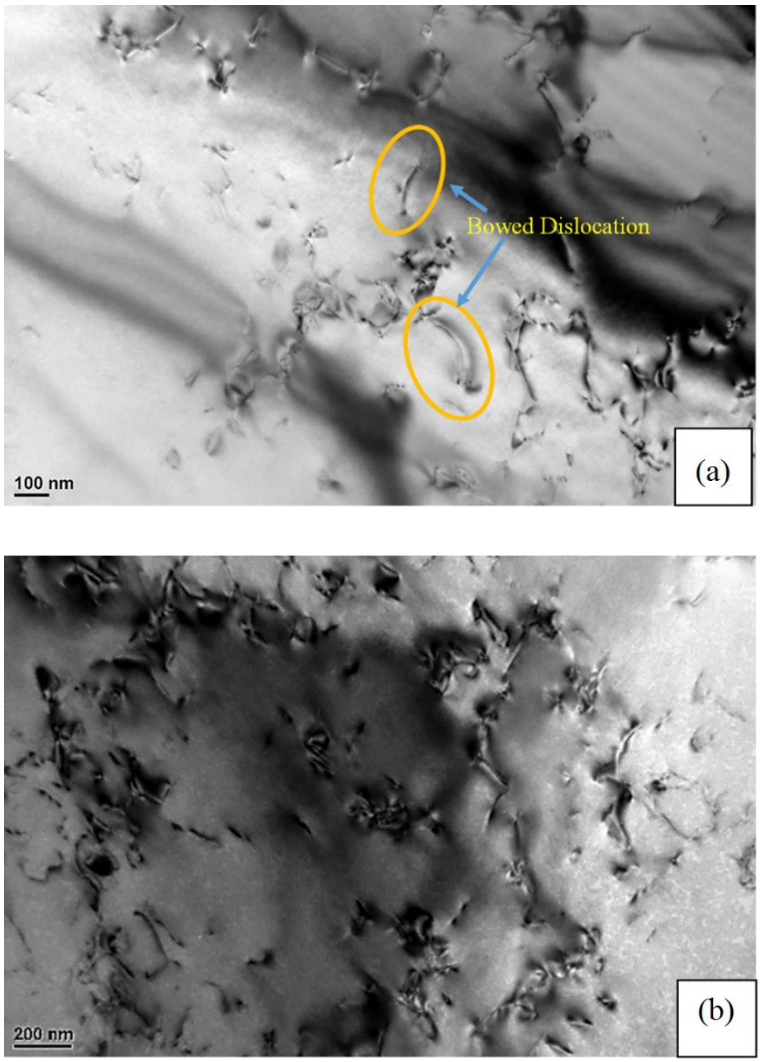

Figure 6-9 BF TEM micrograph of specimen D showing random distribution of mobile dislocations and small degrees of dislocation tangling

TEM BF micrographs of specimen D shows scattered distribution of dislocations in the matrix. Dislocation pile-ups have disappeared suggesting activation of multiple slip systems in the material. During tension-compression cyclic loading of materials, dislocations of opposite signs are annihilated when those meet each other on the same plane. Dislocation tangling and bowed dislocations can be noticed indicating interaction of dislocations with both dislocations and precipitates, causing strain hardening. Interestingly in Figure 6-9 (b),

areas of microstructures can be noticed with very few number of dislocations (similar to cell interior), having surrounded by high dislocation densities (similar to cell wall), typical to formation of dislocation sub-structure.

6.2.3.4 Specimen C

The TEM BF micrographs of specimen C shows stacking faults scattered within the grains. The dislocations tangles have started to reduce in quantity and many single dislocations can be noticed in the micrograph. Dislocations Pile-ups and interaction of dislocations with other dislocations and precipitates can also be noticed.

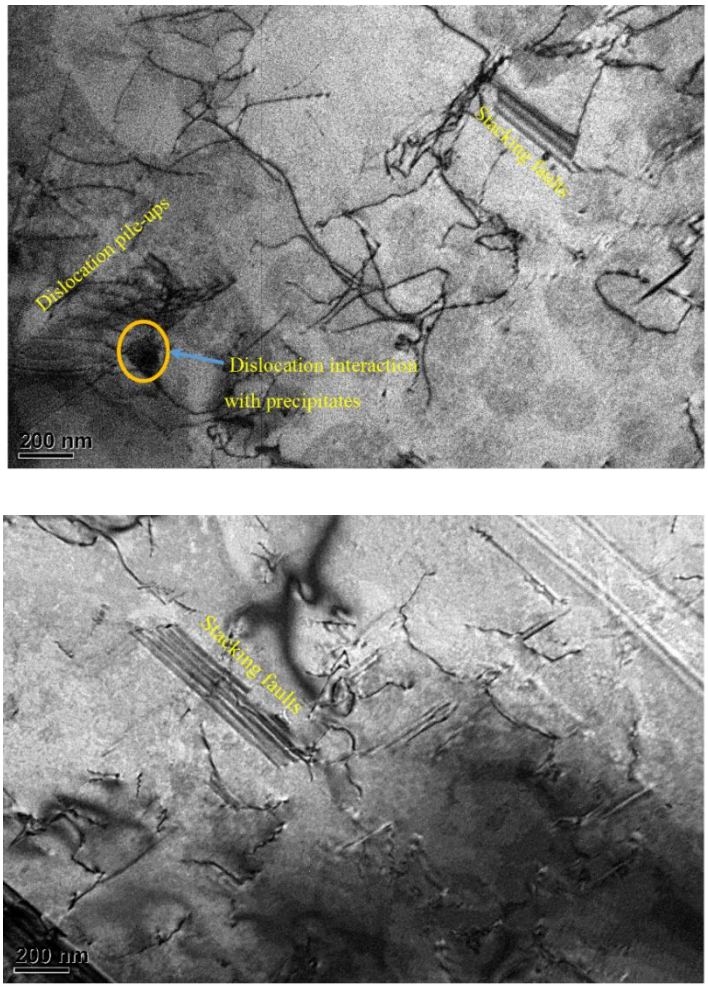

Figure 6-10 BF TEM micrograph of specimen C showing scattered distribution of dislocations, dislocation tangling and stacking fault

In summary, the difference in creep deformation rate observed for the three load controlled creep dwells, under the same applied stress, can be attributed to a combination of the material

hardening state and the intergranular stress. Hardness measurement has shown that there is a significant difference in the hardening state of the material at point A than the other two points. It has been reported [227] that increasing strain hardening reduces the minimum creep rate in this material due to increasing barriers of the dislocation movement owing to the increased dislocation density in the material. The hardening state of the point B and C were found to be almost similar. Difference in the dislocation structures in the specimens were observed in terms of the features such as, dislocation tangling, pile-ups, stacking faults etc. Variations in dislocation structures also affect the creep deformation process in the material, however, it's difficult to quantify the effects of these type of dislocation structures individually. Macroscopic measure of the material's resistance to deformation can be undertaken (for example in terms of tensile strength or hardness) in order to obtain an overall quantification of the effects. Such measurements of internal resistance in the material and those effects on the subsequent creep deformation rate are well studied, for example, in the context of the effect of various types of pre-straining on the creep deformation of this material [228] [227] [229] [230] [231]. However, the subsequent effect of intergranular stresses are usually ignored in this discussions, which the above described results show to be significant. There has been an attempt [136] in separating the effect of internal stresses and internal resistance on the creep deformation of type 316H austenitic steel using in-situ neutron diffraction measurements, however, the measure of the 'internal resistance' in this approach is questionable.

6.2.4 Evolution of IR strains during creep dwells

Evolution of IR strains during the creep dwells was studied to investigate the effect of various microstructural changes occurring during creep process on the IR strains. Lattice strains were recorded in situ during the creep dwells and intergranular strains were calculated from those following the procedure described in 3.6.4.

6.2.4.1 Dwell started at A

In the dwell started at point A, the macroscopic creep curve shows a distinct primary regime followed by secondary regime. The corresponding changes of axial IR strains in the {200}, {220} and {311} grain families during the creep dwell is plotted in Figure 6-11. The {200}

grain family develop the highest tensile IR strains, while the {220} grain family develop the highest compressive IR strains. The {311} grain family develop almost negligible IR strains. The magnitude of the intergranular strains remain almost constant during the creep dwell, only a slight increase in IR strain in the grain families (particularly in the {200} grain family) during the primary stage of creep can be noticed.

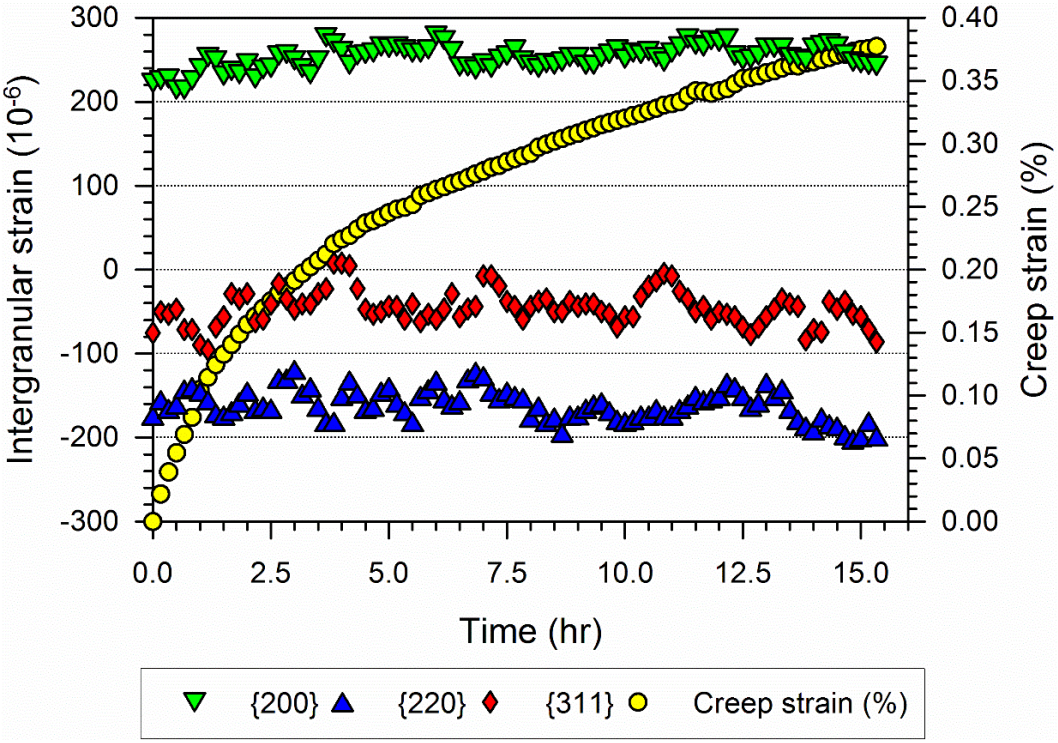

Figure 6-11 Evolution of Axial IR strains during creep dwells of 316H stainless steel at 120 MPa and 650°C started at point A

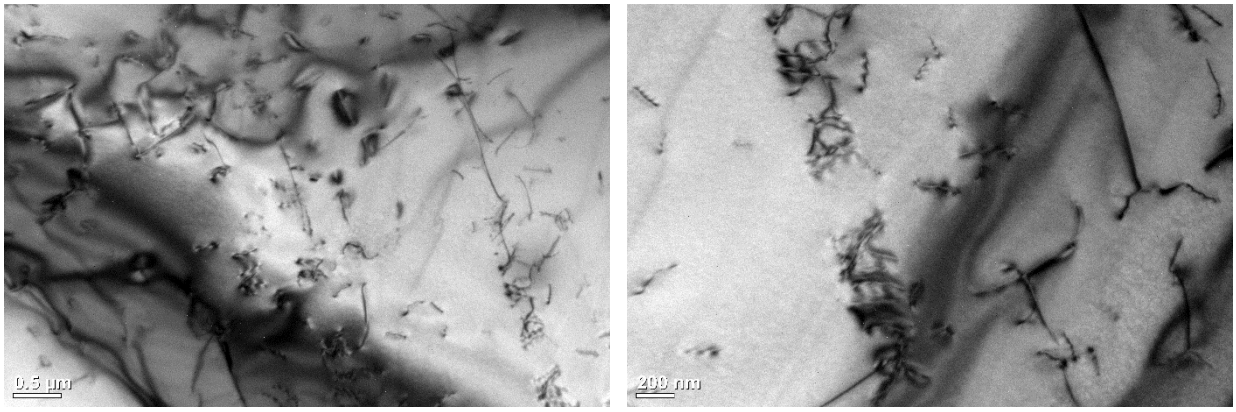

Figure 6-12 Representative BF TEM micrographs of the specimen A, after 7hrs of creep deformation

BF TEM micrographs were also recorded after 7 hrs of creep dwell (the point roughly at which the start of the minimum creep rate has been calculated from) started at this point. Representative micrograph at this point is shown in Figure 6-12. The dislocation pile-ups noticed at the start of the dwell (shown in Figure 6-7) can be seen in these micrographs. Dislocations interaction with other dislocations and precipitates can be observed, which reduced the number of mobile dislocations and as such resulted the start of the secondary creep regime. However, no sign of cell type dislocation substructures can be noticed in the micrographs.

6.2.4.2 Dwell started at B

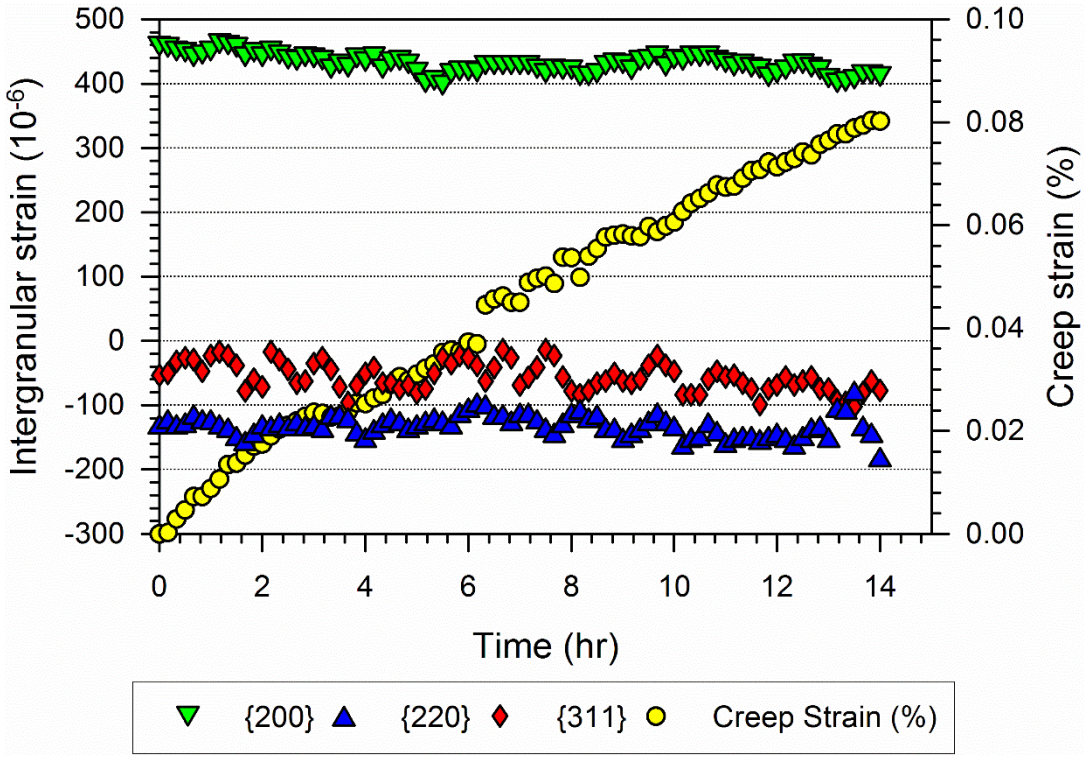

Figure 6-13 Evolution of Axial IR strains during creep dwells of 316H stainless steel at 120 MPa and 650°C started at point B

The macroscopic creep dwell started at point B does not show any distinct primary creep stage. The IR strains in the {200} grain family show a small relaxation of IR strains in the first few hours of the dwell, apart from which, the IR strains in all the grain families remain nearly unchanged during the creep dwell, as presented in Figure 6-13. The magnitude of IR

strains is much higher in the {200} grain family than that observed for the dwell started at A, however in the other two grain families it is in the similar range.

Figure 6-14 shows few BF TEM micrographs acquired from a specimen after 7hrs of creep dwell started at point B. Similar to the initial condition of this specimen (as shown in Figure 6-8) highly tangled dislocations can be observed in this specimen as well. Unlike specimen A, dislocations are not piled-up at the grain boundary, rather distributed inside the grains and at the grain boundaries. In Figure 6-14 (b), the initiation of the formation of cell type structure in can be observed as shown by the points X, Y and Z.

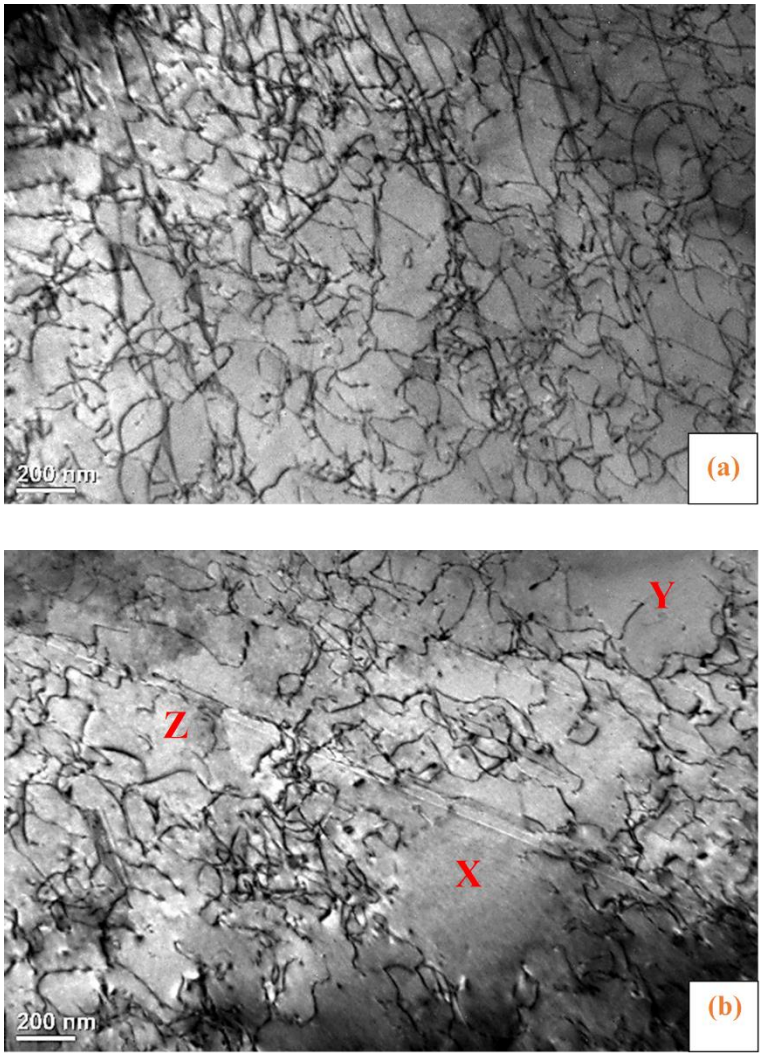

Figure 6-14 BF TEM micrographs after 7hrs of creep deformation of the dwell started at point B. The figure in (a) is showing heavily tangled dislocation structures and the figure in (b) is showing a sign of formation of cell type dislocation structures at locations X, Y and Z

6.2.4.3 Dwell started at C

The creep dwell started at point C shows interesting variation of the axial IR strains. During the primary stage of creep deformation, the IR strains increase and decrease rapidly in the {200} and the {220} grain family respectively. It is to note that the specimen was negatively strained at the beginning of the dwell at this point, so unlike the other two dwells, the IR strains in the {200} grain family were compressive and in the {220} grain family were tensile. During the onset of secondary creep, the changes of IR strains in {200} and {220} grain family seem to reach to a saturation. The IR strains in the {311} grain family remain constant and slightly negative throughout the dwell.

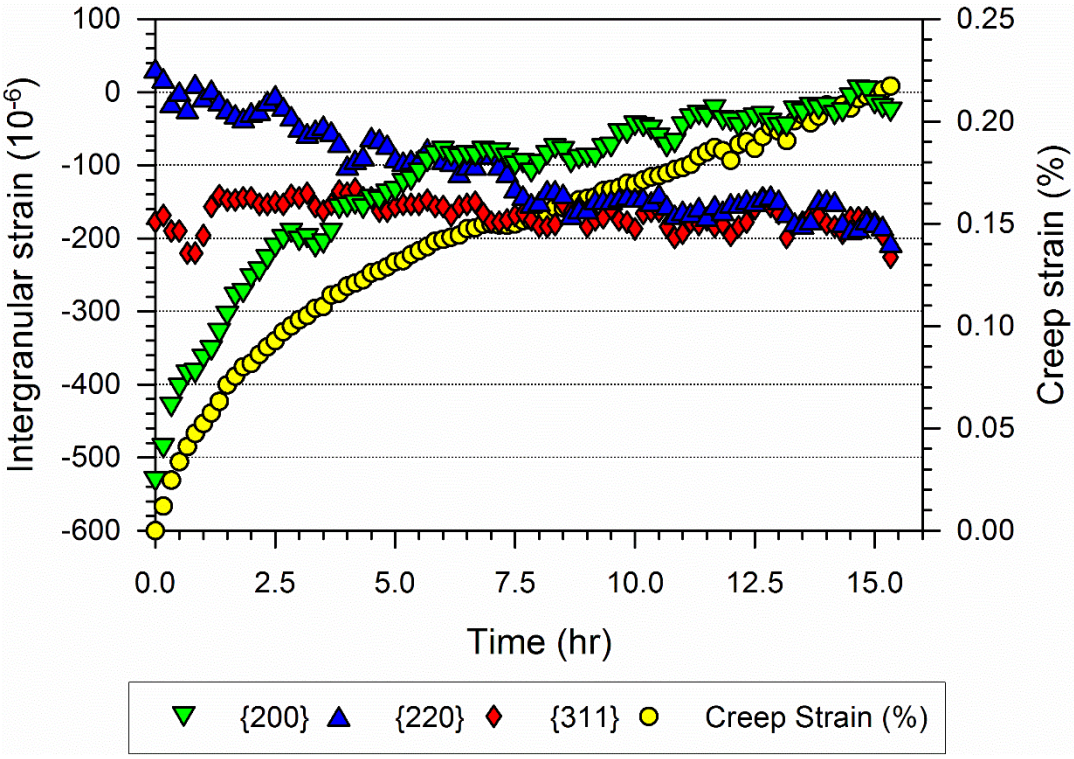

Figure 6-15 Evolution of IR strains during creep dwells of 316H stainless steel at 120 MPa and 650°C started at point C

Comparing with the other two dwells, it can be postulated that the large variations of IR strains observed in this dwell is because of the macroscopic material being in the elastic regime when the creep dwell was started. An important insight of the relative deformation of variously oriented grains can be obtained from the observed changes of the IR strains during this dwell. With increasing creep strain, the IR strains in the {200} grain family can

be observed to accumulate increasing tensile intergranular strains while the {220} grain family to accumulate increasing compressive intergranular strains. This implies, similar to that of the plastic deformation, the {220} grain family deforms in creep relatively quicker than other grain families, therefore, being under compressive strains while the {200} grain family creep deforms slower, being under tensile strains. It can then be postulated, in type 316H austenitic steel, the set of grains which are relatively plastically weaker and stronger are the same set of grains which are creep weaker and stronger respectively. However, this hypothesis may only be relevant for the dislocation based creep mechanisms.

BF TEM Micrographs of this specimen after 7 hours of dwells is shown in Figure 6-16. A random distribution of dislocations can be noticed in the microstructure without formation of any cell type structure.

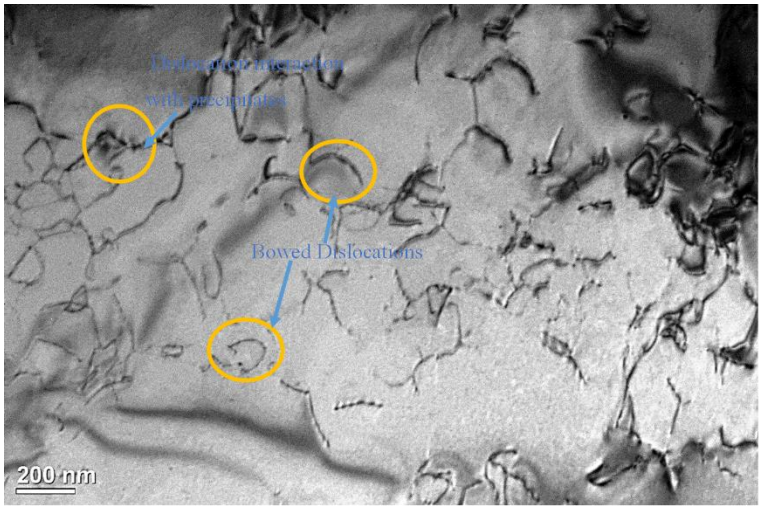

Figure 6-16 BF TEM micrographs after 7hrs of creep deformation of the dwell started at point C showing dislocations structures. There is no formation of cell type structures

In summary, the IR strains in some grain families (most prominent in the {200} grain family) were observed to increase during primary stage of creep deformation and remain nearly unchanged during the secondary stage. Such variation of IR strains is related to the difference in the mechanisms of creep deformation during primary and secondary regime. A deformation mechanism map [217], as shown in Chapter 2 suggests a dominant dislocation creep mechanism at the temperature ($T/Tm = 0.5$) and stress range ($\sigma/G \sim 10^{-3}s^{-1}$) of this test. In dislocation based creep deformation, the material first strain hardens due to generation of mobile dislocations upon application of the creep load. During primary creep, this

dislocation density increases with time up to a point at which the rate of hardening becomes equal to the rate of recovery [232, 233] which is the onset of secondary/steady-state creep. The increases of IR strains with increasing dislocation density, during primary creep and the near constant IR strains with constant dislocation density during secondary creep suggests a strong co-relation between the IR strains and the dislocation densities during load controlled creep deformation in type 316H stainless steel. The observations of unchanged IR strains during secondary creep is consistent with recent published works [216] [137]. However, this needs further verification by performing longer creep dwells under range of applied stress and temperatures.

No distinct dislocation cell type structures was observed in any of the creep interrupted specimens; only notion of such formation was observed in specimen B. Under the loading conditions studied here that is at the early stage of creep deformation, contribution of dislocation sub-structure generated intergranular stresses to the total back stress is not significant in this material. Other inhomogeneous distribution of dislocations, such as dislocations pile-ups near grain boundaries and dislocation tangling, are noticed in the specimens, which can also generate intragranular back stresses. However, it is difficult to quantify the magnitude of these intragranular stresses with respect to the total back stress in the material, as TEM investigations were conducted on a very small area compared to that of the bulk material. Difference of macroscopic creep deformation, for example, the loss of primary creep stage in the dwells started at point B, can be explained based on the observation of heavy dislocation tangling in this specimen prior to the creep loading.

6.2.5 Anelasticity and intergranular strain

In-situ neutron measurements were also obtained after the unload of the specimen from the creep load to record any anelastic recovery of strain and the corresponding changes in the intergranular strains, for the three creep dwells reported. This is done simply by unloading the specimen to 5 MPa at an unchanged temperature of 650 ℃ and then by measuring the macroscopic and corresponding lattice strains for ~2 hours. A small magnitude of anelastic recovery of strain and the corresponding changes of intergranular strains was recorded for each of the dwells during this unload period. However, due to the small creep strain in the material, the changes in intergranular strains were small in magnitude and with considerable

scatters in the data, a clear trend was difficult to observe in those. An alternative test at higher applied stress was conducted in order to generate higher magnitude of creep strain in the material before unloading. In this case, an identical specimen as used in the described tests was used. The specimen was loaded similar to the specimen B, except instead of unloading to 120 MPa upon reaching to 1% peak tensile strain in the second cycle, the applied load was increased to 180 MPa. The specimen was creep deformed at this load and temperature for ~12 hours. The specimen was then unloaded to zero macroscopic stress and measurements using in-situ neutron were continued for 2 hours with counting time of 10 mins for each measurements.

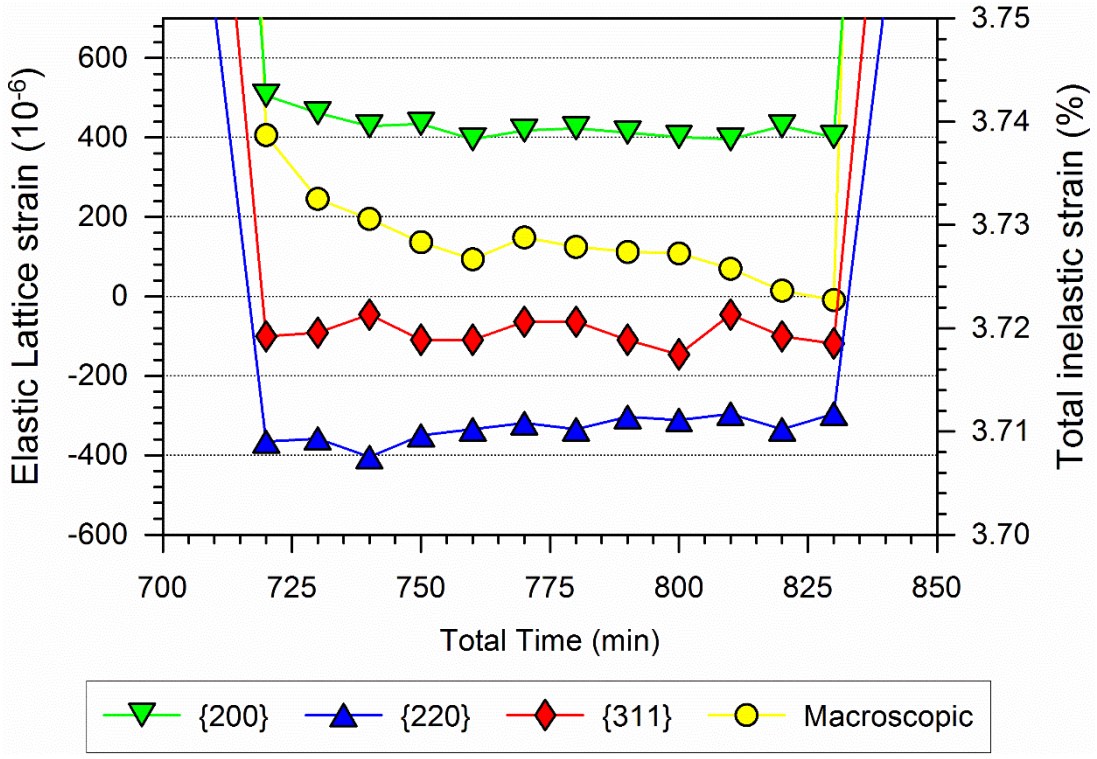

Figure 6-17 Evolution of IR strains in variously oriented grain families during anelastic recovery of creep strain upon unloading from 180 MPa at 650°C

The recovery of macroscopic strain (anelastic recovery) during this unloading period and corresponding changes in the IR strains of the three selected grain families is shown in Figure 6-17. A small magnitude of macroscopic strain can be observed to recover during this unload period. The tensile IR strains in the {200} grain family is observed to decrease and the IR strains in the {220} grain family is observed to increase during this period. The negligible IR strains in the {311} grain family is observed to remain nearly unchanged during the whole

period. The observed corresponding relaxation of IR strains during the anelastic recovery of creep strain supports the theory [81] of IR strains playing strong role in causing creep anelasticity in this material.

Generally speaking, this recovery of creep strain can be compared with compressive creep deformation, as because the recovery of strain is occurring due to a compressive stress (back stress) in the material. During this negative creep straining, the {220} grain family is observed to accumulate decreasing compressive residual strains while the {200} grain family is observed to accumulate decreasing tensile residual strains, which further support the above discussed postulation of the same grain sets which are relatively plastically weaker and stronger being the same sets of grains which are creep weaker and stronger respectively in this material.

6.3 Displacement controlled creep

Displacement controlled creep dwells were performed by fixing the displacement of the loading machine after cyclically deforming the specimen to a specific strain. The relaxation of stress in the displacement controlled dwell arise from the conversion of elastic strain to the creep strain. The tests were conducted at 650 ^{o}C following the same experimental procedures for the load controlled creep tests, described above. Specimens were heated to 650° C and then loaded cyclically at a strain rate of ~ $7 \times 10^{-6} s^{-1}$ over a total strain range of ±1%. Two identical specimens were used; the loading sequence for one specimen (Specimen E) was started in tension, while for the other specimen (Specimen F) was started in compression. In both the tests, the displacement controlled creep dwells were conducted at peak tensile strain. The motive for starting with tension in one specimen and in compression in another was to investigate, if the direction of first straining caused any difference in the development of the intergranular strains in different grain families and those subsequent effect on the creep deformation. The loading sequence of the specimens is illustrated below.

Specimen E: Three tension-compression cycles at 650°C in a strain range of ±1% were conducted starting in tension. In each cycle, a displacement-controlled dwell of 2 hours was conducted at the peak tensile strain, as illustrated in Figure 6-18.

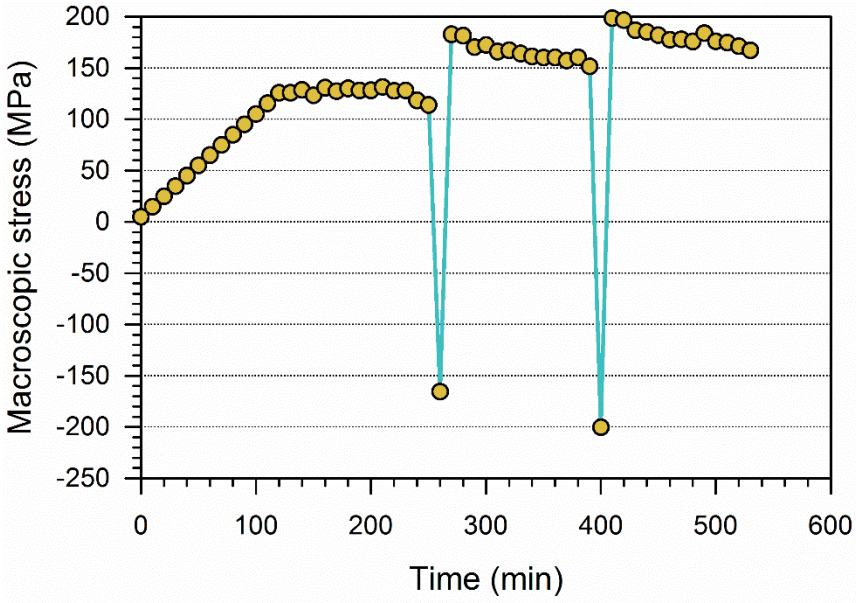

Figure 6-18 Loading sequence of specimen E, started in tensile loading. The test was conducted at 650° C and within ±1% strain range.

Specimen F: Four tension-compression cycles at 650°C in a strain range of ±1% were conducted starting in compression. In each cycle, a displacement-controlled dwell of 2 hours was conducted at the peak tensile strain, as illustrated in Figure 6-19.

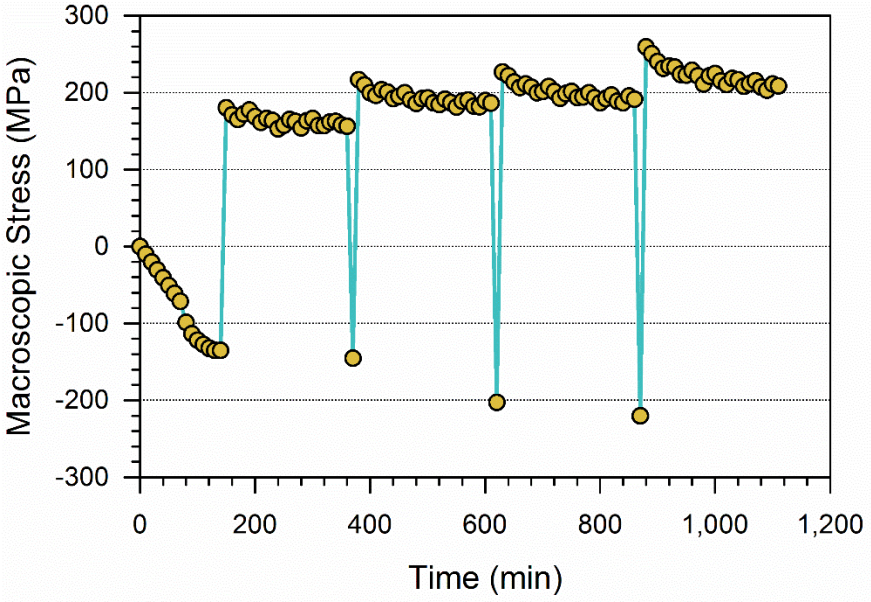

Figure 6-19 Loading sequence of the specimen (Specimen F) started in compressive loading. The test was conducted at 650° C and within ±1% strain range.

6.3.1 Specimen E: Loading started in tension

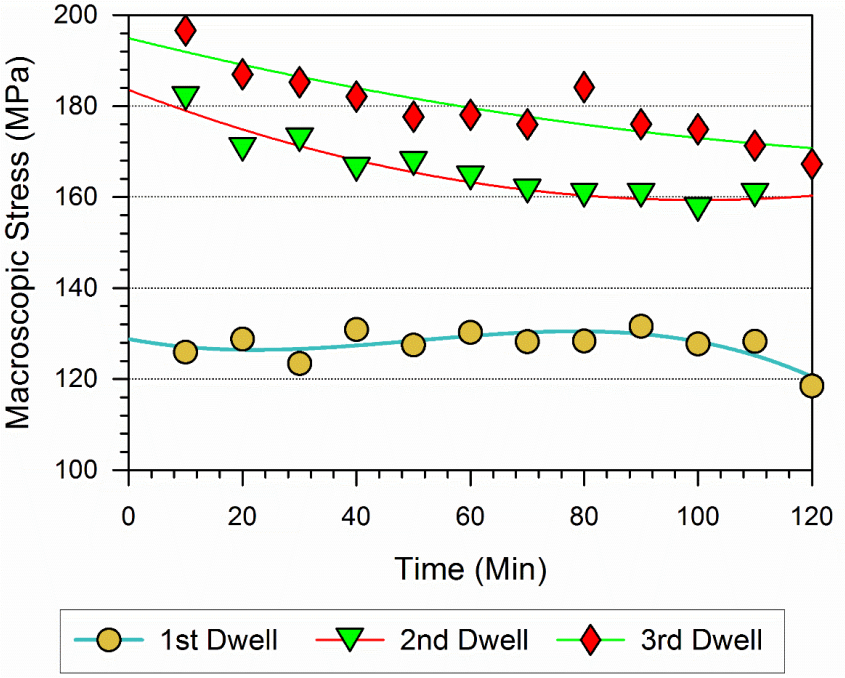

Figure 6-20 Relaxation of macroscopic stress during 3 displacement controlled creep dwells at peak tensile strain (1%) of Specimen E

Figure 6-20 shows the relaxation of macroscopic stress during the displacement controlled creep dwells at the peak tensile strain of specimen E at 650°C. The relaxation is almost negligible in the first dwell which is due to the low macroscopic applied stress reaching 1% strain. The stress required to reach to the 1% peak tensile strain in the 2nd cycle increases markedly due to strain hardening in the material during tension-compression cyclic loading. The dwell started at this point is therefore, at a much higher stress than the first dwell. The stress relaxation can also be observed much greater than the relaxation in the first dwell. An even higher magnitude of stress relaxation can be observed in the third dwell, although, the increment in the stress relaxation between the second and third dwells is much smaller than the increase between the first and second dwells, which is consistent with the increase of the initial dwell stress with respect to the number of cycles.

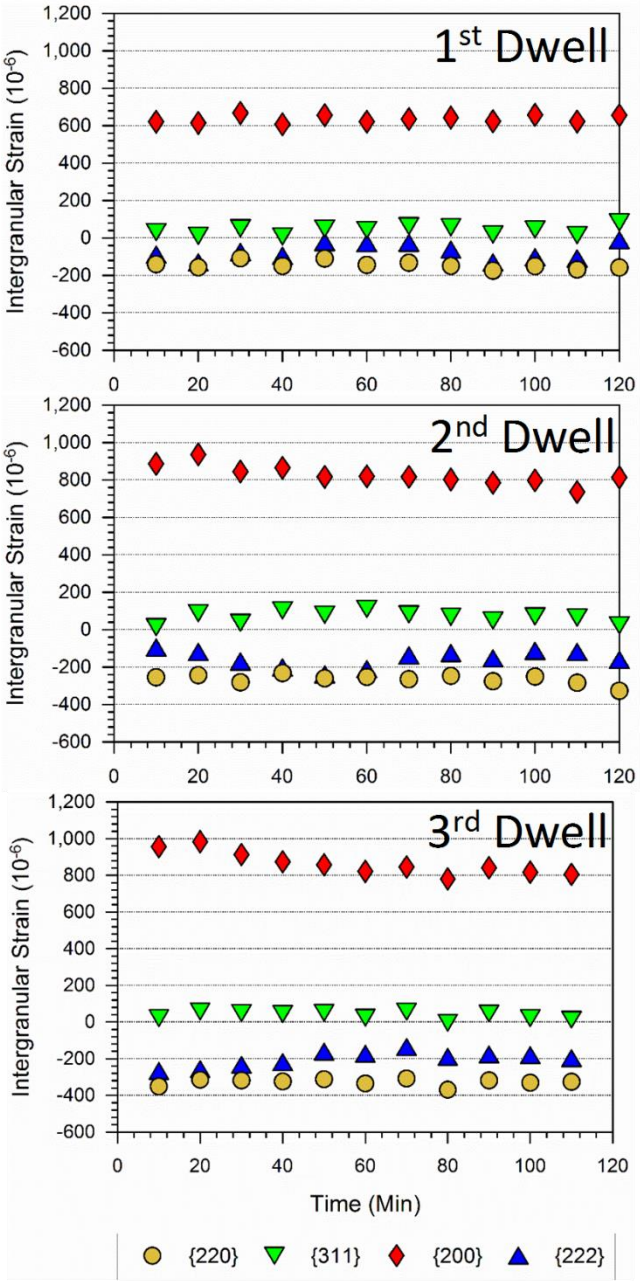

Figure 6-21 Variation of IR strains during 1st, 2nd, and 3rd dwells at tensile peak strain of cyclic loading at 650°C

The relaxation of intergranular strains during these three dwells is presented in Figure 6-21. Large tensile IR strains are observed to be accumulated in the {200} grain family and smaller compressive IR strains are observed to be accumulated in the {220} and the {222} grain families. It can also be observed that the magnitude of the IR strains at the start of dwell increases with repeated cycling, similar to the observation of macroscopic stress. The IR strains, particularly in the {200} grain family found to relax with time during the second and

third dwells. Interestingly, the trend of relaxation of the IR strains in the {200} grain family (as shown in Figure 6-22) is remarkably similar to the trend of the relaxation of macroscopic stress, suggesting that the relaxation of IR strains is a function of the relaxation of Macroscopic stress in this material during the displacement controlled creep dwells.

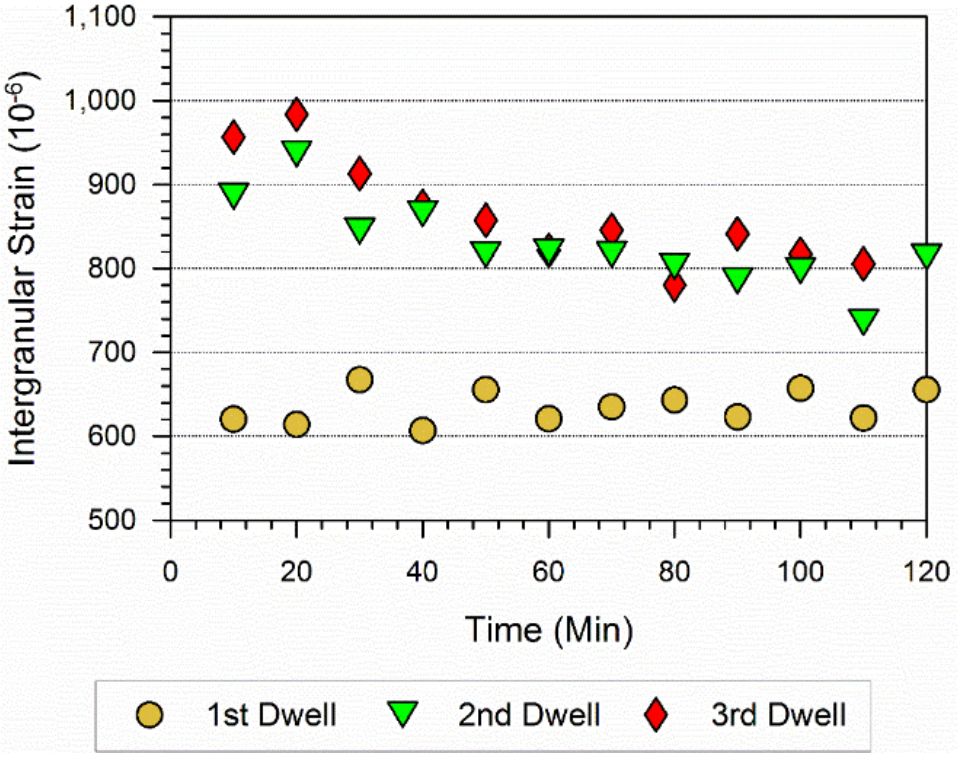

Figure 6-22 Relaxation of IR strain in the {200} grain family during displacement controlled creep dwells in 316H stainless steel specimen E at 650°C

Tensile and compressive IR stress must balance each other over a finite length scale in the material. So, if there is a decrease of tensile IR strains in some grains, there must be a decrease of compressive IR strains in other grains. Therefore with decrease of tensile IR strains in the {200} grain family, it is expected that the compressive IR strains in the {220} and the {222} grains will also decrease. However, in this experiment, owing to small excursion of deformation, the compressive IR strains in the {220} and {222} grain family are small. So, even though, with very careful observation, such trend of relaxation of compressive IR strains can be noticed in the {220} grain family, it is nowhere near as prominent as in the {200} grain family.

6.3.2 Specimen F: Loading started in compression

This specimen was loaded similarly to specimen E except that the loading started in compression. Figure 6-23 shows the relaxation of macroscopic stress during the 4 displacement controlled creep dwells that were performed at positive peak strain of 1%. Compared to specimen E, the stresses at the start of the dwells are higher. This is because when the 1st dwell was started at 1% tensile strain, the material has already strain hardened during the first compressive-tensile cyclic loading. It can also be seen that, compared to specimen E, the relaxation during the first dwell is clearer and larger. The stresses at the start of the subsequent dwells increase with each cycle and so does the relaxations of the macroscopic stresses.

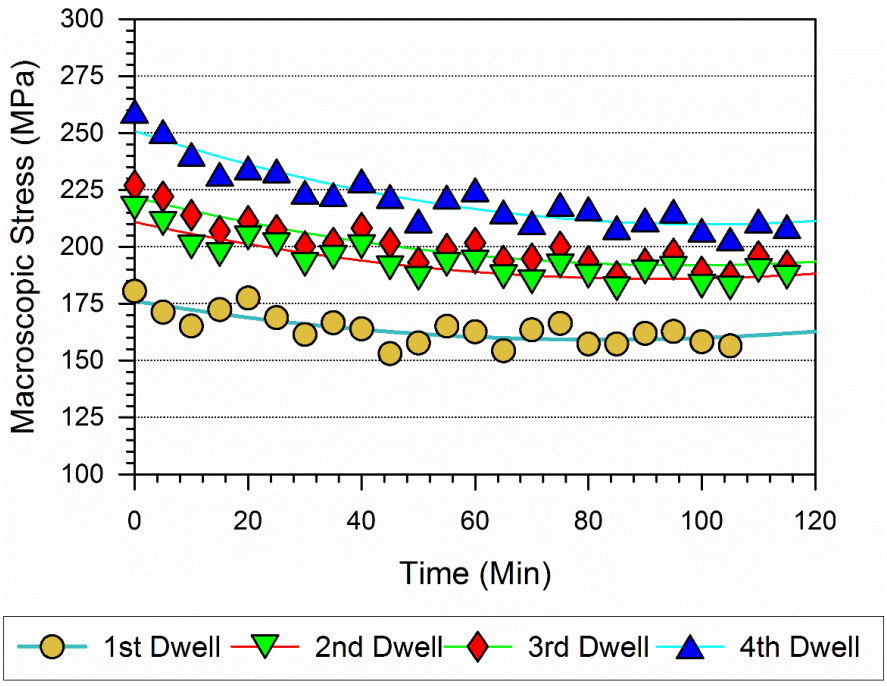

Figure 6-23 Relaxation of the macroscopic stress during displacement controlled dwells at positive peak strain of specimen F

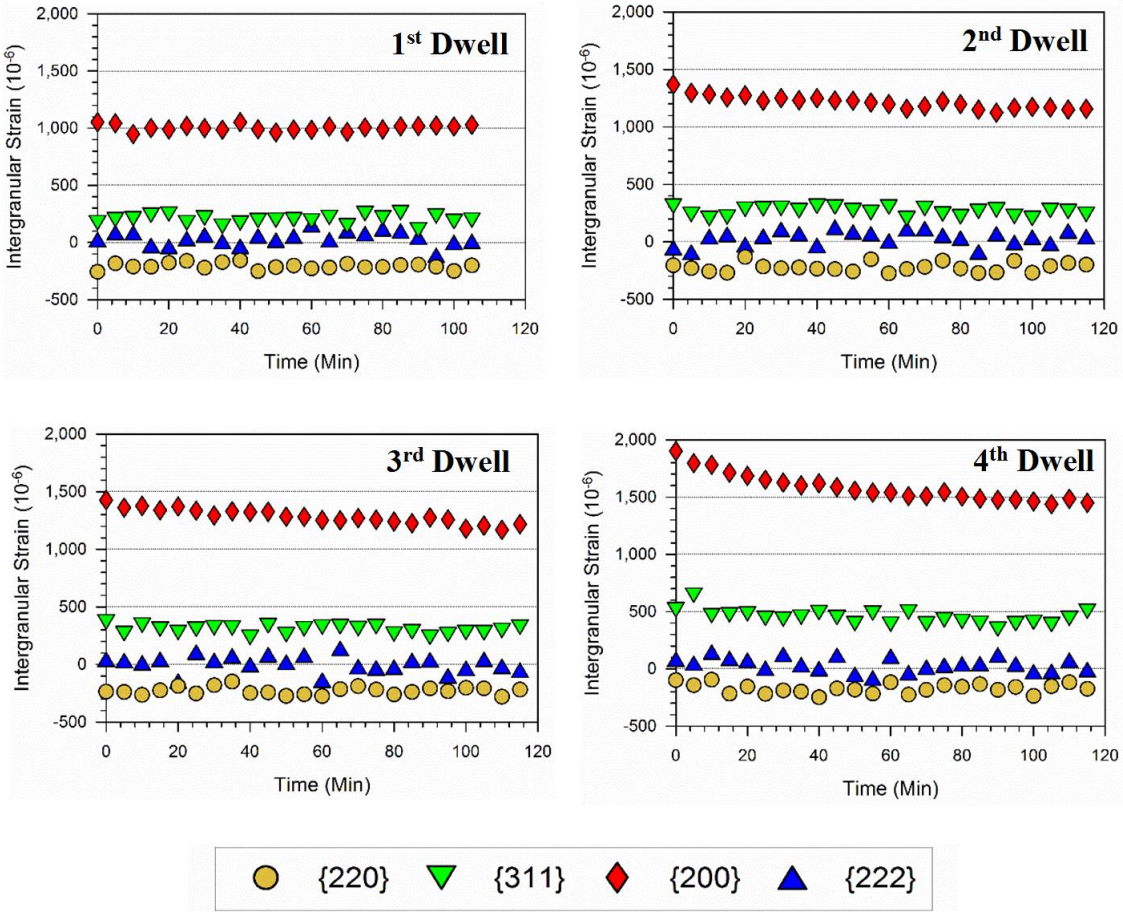

Figure 6-24 Variation of intergranular strains during dwells at peak stress of 1st, 2nd, 3rd and 4th dwells during cyclic loading sequence at 650 °C in specimen F

Figure 6-24 shows the relaxation of the IR strains during the dwells. The relative magnitude of the different IR strains generated in the different grain family is the same in specimen F as in specimen E. However, in specimen F the IR strains are higher in both the tensile and the compressive directions. Similar to the specimen E, large tensile IR strains are accumulated in the {200} grain family and smaller compressive IR strains are accumulated in the {220} and the {222} grain family. The relaxation of the IR strains during the first dwell is minimal and it gradually increases in second, third and fourth dwells with the increase of the initial dwell stresses. Most importantly, the trend of the relaxation in this specimen also supports the above mentioned co-relation between the relaxation of macroscopic IR stress and relaxation of microscopic strains in the {200} grain family as can been seen comparing Figure 6-23 and Figure 6-25.

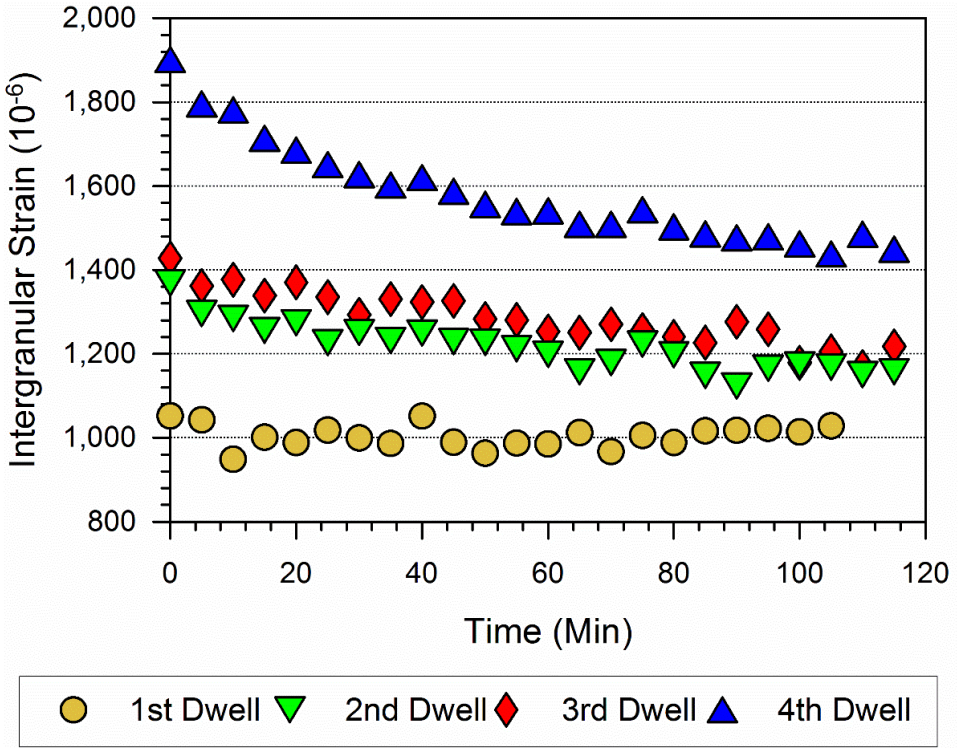

Figure 6-25 Relaxation of axial IR strains in the {200} grain family during displacement controlled creep dwells in 316H stainless steel in specimen F at 650°C

In contrast to the load controlled creep deformation, during displacement controlled creep dwells, IR strains relaxed with time. Stress relaxation is the time and temperature dependant decrease of stress in a solid due to the conversion of elastic strain into inelastic strain [234]. The results clearly show that, relaxation of IR strains is a function of the relaxation of the macroscopic stress. The significant relaxation of IR strains shows that the assumption of constant back stress in estimating stress relaxation in type 316H stainless steel [235] [236] is not realistic.

Finally, it is important to mention that the experimental results reported in this chapter are limited by the short period of the creep tests due to constraint in neutron beam time allocation. Further tests with much longer duration creep tests are required, particularly to confirm the findings about the evolution of IR strains during the creep dwells. Furthermore, these results only represent the earlier stages of creep deformation in 316H stainless steel, before significant precipitations has occurred.

6.4 Summary

1. IR strain originating from the plastic anisotropy is the dominant contributor to creep back stress in type 316H stainless steel at 650° C, particularly at the earlier stages of creep deformation when sub grains like dislocation structures are not formed.
2. During creep deformation of type 316H stainless steel, the back stress due to IR strains has a significant effect on the minimum creep rate in this material.
3. During load controlled creep dwells, IR strains developed during primary creep but remained almost unchanged during the short period of secondary creep in these tests.
4. Variation of the IR strains during creep dwells is closely related to the change in the dislocation density in the material. During primary creep, the dislocation density increases and so do the IR strains. During secondary creep, the dislocation density does not change and neither do the IR strains.
5. During anelastic recovery of creep strain, the IR strains in the creep weaker grain families were observed to increase and that in the creep stronger grain families were observed to decrease, suggesting that, the redistribution of IR strains during the recovery period play a strong role in causing the anelastic recovery in this material.
6. The observations of the relative deformation of grains during creep dwell and anelastic recovery of creep strain suggests that in this material the same set of grains which are relatively plastic weaker and stronger are the set of grains which are creep weaker and stronger respectively. This conclusion however is limited to the dislocation based creep only.
7. Transmission electron microscopy observations supported the hypothesis that intragranular stresses do not contribute significantly to back stress during the earlier stages of creep deformation in type316H stainless steel.
8. During displacement controlled creep deformation IR strains were observed to relax significantly with relaxation of the macroscopic stress. The similarity in the trends of relaxation of the microscopic IR strains and the macroscopic stress suggests, magnitude of IR strain relaxation to be a function of the magnitude of macroscopic stress relaxation.

Chapter 7 Assessment of creep damage and ex-situ intergranular strain measurement

7.1 Overview

The results of the creep studies presented so far in this thesis characterise the early stages of creep deformation in type 316H stainless steel. The creep experiments had to be unrealistically accelerated to fit within short periods of allocated neutron beam time. Even with such accelerations, the creep dwells, either in load or displacement controlled, had to be interrupted within the first few percent of creep deformation. With careful extrapolation of the findings for these short creep dwells, the effect of back stress on the overall creep life of the material can be estimated, however, a number of uncertainties remain. For example, the microstructure of the material evolves significantly during the later stages of creep deformation. Generally speaking, creep damage in the material occurs by nucleation and growth of creep cavities within the microstructure of the material; grain boundary microscopic cracks may then develop by the coalescing of creep cavities. The relationship between back stress evolutions, creep deformation and the onset and development of creep cavitation damage in the material are of particular interest.

This chapter presents novel experimental work investigating the evolution of back stress and creep cavitation in uniaxial creep rupture tests. The back stress is measured by neutron diffraction (ex-situ) and creep cavitation damage is characterised by SANS and HS-AFM techniques using a set of interrupted creep rupture test specimens. The measurements were conducted following the procedures described in Chapter 3. The creep damage characterization work using SANS and HS-AFM was conducted as part of a collaborative project led by Dr Hedieh Jazaeri of the Open University with assistance from the author in the acquisition and analysis of the SANS data, as well as in specimen preparation, acquisition

and analysis of the HS-AFM images. The HS-AFM imaging was conducted in collaboration with Dr Oliver Payton at the University of Bristol.

7.2 Experimental

Measurements of intergranular strains and evolution of creep damage were conducted on two sets of interrupted creep test specimens made from type 316H austenitic stainless steel. The creep tests were conducted at the OU high-temperature laboratory as part of a different PhD project [195] investigating the use of EBSD misorientations metrics for characterising accumulated inelastic (plastic and creep) strain in the material. Material for the creep tests was extracted from a serviced aged steam header designated as HRA 2B2/1, cast 69431, after over 10 years of service in an AGR. Details of the service history of the header and mechanical properties of the material (designated as material A) is described in Section 4.2.

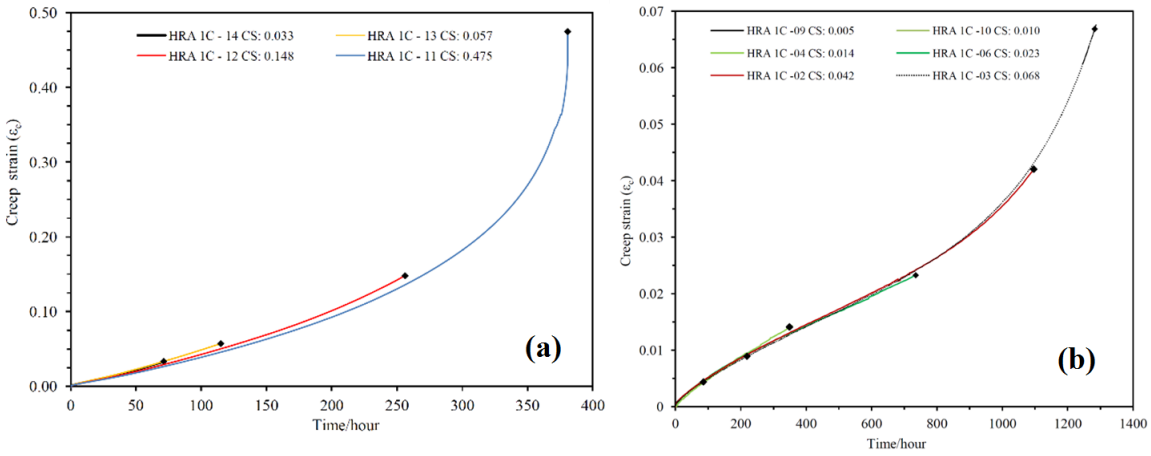

Figure 7-1 Creep curves of interrupted tests conducted on specimens extracted from an ex-service steam header made from type 316H austenitic stainless steel at two different loading conditions, (a) at 675 ℃ and 150 MPa and (b) at 550 ℃ and 320 MPa [195]

The two sets of load-controlled creep tests were conducted at 675℃ and 150 MPa and at 550℃ and 320 MPa using standard cylindrical specimen (as later presented in Figure 7 3). The specimens crept at 550℃ and 320 MPa were pre-strained to 7.9% true strain before the creep deformation. The pre-straining was conducted at 550℃ using a constant strain rate of 3.5x10-5 s-1. Upon reaching the intended plastic strain, the specimens were unloaded and cooled in the air to room temperature by opening the furnace. The loading was carried out

according to the procedures described in Chapter 3 using an Instron-8862 machine. The creep tests were conducted using standard fixed-load creep frames at the OU high-temperature laboratory. The specimens in both sets of tests were creep deformed to various strains covering the primary, secondary and tertiary regimes. Upon reaching to the intended creep strain, the test was interrupted by opening the furnace. The load was kept on during cool-down in order to preserve the specimen's deformation state microstructure by prohibiting recovery of the dislocation structures. The results of the creep tests for both sets of specimens are presented below in Table 7 1and Figure 7 2. Further details of the tests can be found in [195].

Table 7-1 Summary of the interrupted creep tests conducted at 550 ℃and 320 MPa and at 675 ℃and 150 MPa using ex-service type 316H austenitic stainless steel [195].

Loading conditions	Sample ID	Min strain rate	Plastic pre-strain	Plastic loading strain	Creep strain (%)	Creep stage
550 ℃and 320 MPa	HRA1C-**2**	7.5E-09	0.079	0.002	4.2	Secondary
	HRA1C-**3**	7.3E-09	0.079	0.003	6.8	Rupture (t_r=1287h)
	HRA1C-**4**	8.0E-09	0.079	0.003	1.4	Primary
	HRA1C-**5**	0.00	0.079	0.000	0.0	N/A
	HRA1C-**6**	7.5E-09	0.079	0.003	2.3	Secondary
	HRA1C-**9**	1.1E-08	0.079	0.003	0.5	Primary
	HRA1C-**10**	5.3E-09	0.079	0.002	1.05	Primary
675 ℃and 150 MPa	HRA1C-**11**	1.21E-07	0	0.002	47.5	Rupture (t_r=381h)
	HRA1C-**12**	1.04E-07	0	0.003	14.8	Tertiary
	HRA1C-**13**	1.13E-07	0	0.003	5.7	Secondary
	HRA1C-**14**	1.07E-07	0	0.003	3.3	Primary

Post-test the cylindrical specimens were first sectioned transverse to the loading axis and samples for EBSD analysis extracted from one-half of the specimen. The remaining halves of the specimens were used for the present work, from which disc-shaped samples were extracted from the gauge length and the grip section for SANS measurements (see Figure 7-2). The remaining part of the specimen was then used for intergranular strain measurements. The Engin-X neutron diffractometer was used for the measurement of

intergranular strains and the SANS2D instrument was used for the measurement of the evolution of creep damage in the material. These two instruments belong to the Rutherford Appleton Laboratory (RAL) of the ISIS pulsed neutron facility (see chapter 3 for the details of the instruments).

7.3 SANS measurement of creep damage

The SANS measurements were conducted following the procedure described in Section 3.6.7. An incident wavelength range of 0.42 to 1.25 nm was used achieving a scattering vector, Q, ranging from 0.015 to 1.1 nm^{-1}. The incident and scattered beam length of 12 m were used. This set-up enabled measurements of scattering from heterogeneities up to sizes of about 350 nm diameter. A circular aperture of 4 mm diameter was used for the measurements, making the gauge volume of the measurements approximately 12.5 mm^3. An average acquisition time of 60 mins was used for each measurement point. Two circular disc-shaped samples were extracted using wire EDM from each of the creep interrupted specimens for the measurements; one from the gauge length and the other from the grip section of the specimen. The diameter of the discs obtained from the gauge length (d1) and grip (d5) was ~6 mm and ~9 mm respectively. The thickness of all the samples was 1 mm. The approximate locations and dimensions of the discs are shown in a schematic in Figure 7-2.

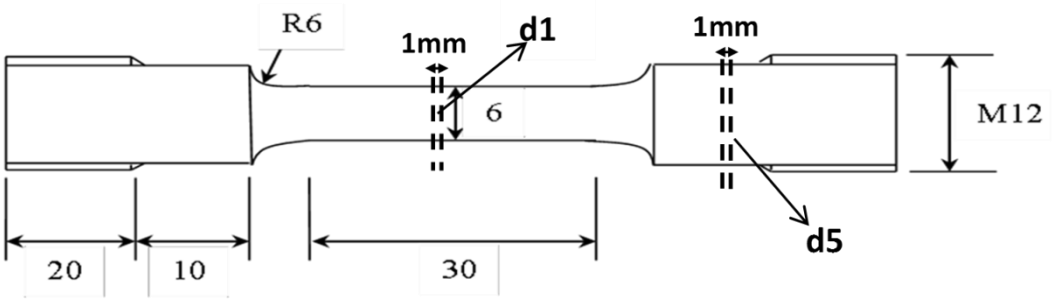

Figure 7-2 Schematic showing the approximate locations and dimensions of the disc samples obtained from the gauge length (d1) and grip section (d5) of the cylindrical creep specimens

7.3.1 Creep Interrupted specimen at 550℃ and 320 MPa

The experimental data was reduced and analysed following the procedure described in Section 3.6.7.1. Figure 7-3 shows the calculated V(D) in the gauge section (d1) samples of the specimens crept at 550℃ and 320 MPa. Two distinct population of defects can be observed, one with diameters in the range of 10-70 nm and the other with diameters in the range of 100-350 nm. The V(D) of the smaller diameter defects are observed to systematically increase with the increase of creep strain in the samples. No such trend can be noticed for the V(D) of the larger diameter defects. The ref. far field measurements show the lowest distribution of V(D). The measured V(D) of all the specimens are observed to reduce to zero for defects with a diameter bigger than the ~350 nm; which is due to the imposed limit of the lowest scattering vector [237] by the instrument.

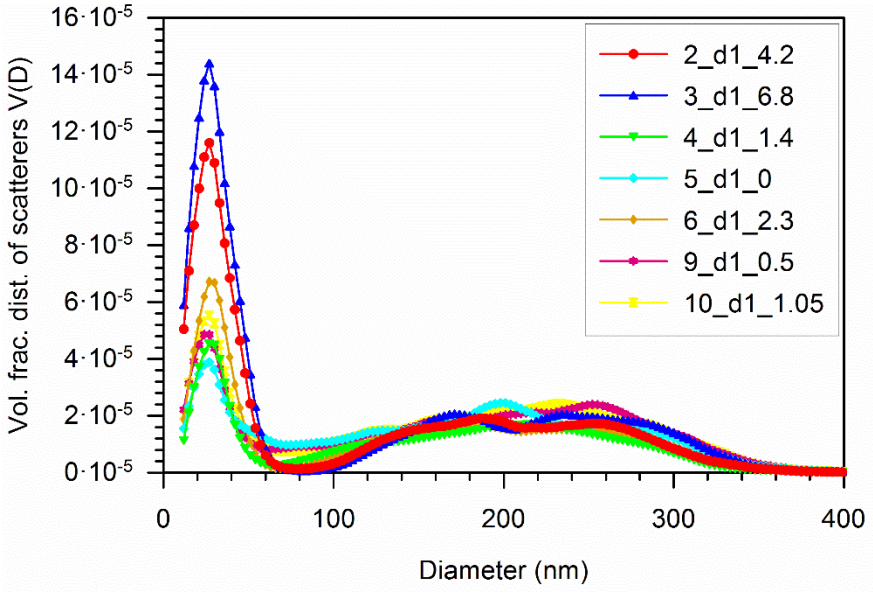

Figure 7-3 Volume fraction distribution of the scatterers from samples extracted from the gauge length of the creep interrupted specimens tested at 550℃ and 320 MPa. The measured V(D) shows a strong correlation with the creep strain in the material for the smaller population of the scatterers.

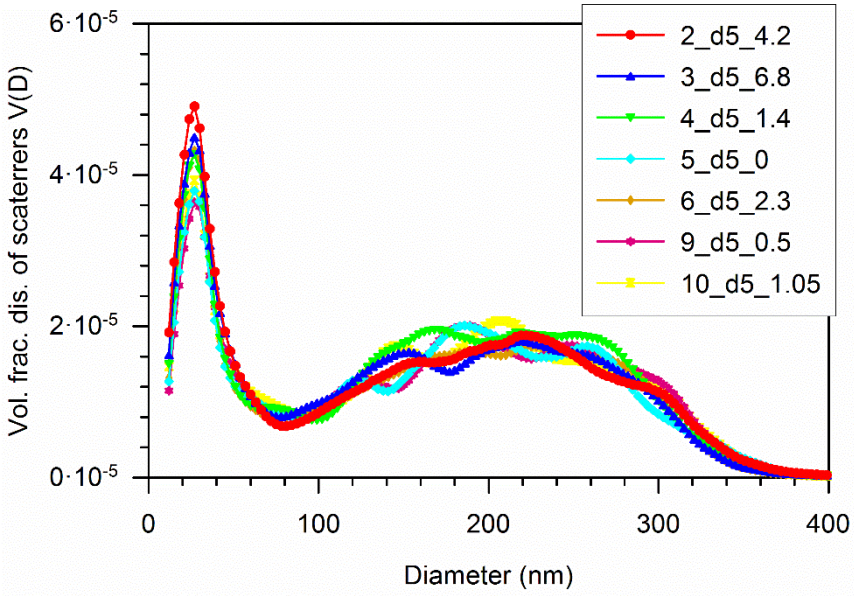

Figure 7-4 Volume fraction distribution of the scatters from the samples extracted from the grips of the creep interrupted specimens tested at 550℃ and 320 MPa

Figure 7-4 shows the results of the measurements conducted in the samples extracted from the grip section (d5) of the same set of specimens. Two distinct population of defects with a similar range of diameters can be observed for these samples too. The maximum peak of the V(D) for the smaller diameter defects is smaller by a factor of ~3 in the grip samples than that in the gauge length samples, but similar to that in the samples with low magnitude creep deformation. The difference in the distributions of V(D) between differently crept samples is also small and no systematic change of those with respect to the creep strains can be observed. The distributions of V(D) for the larger diameter scatters are found to be similar in magnitude to those of the gauge length samples. If these measurements of V(D) from the grips are used as reference measurements to obtain C(D) by subtracting those from the V(D) of the gauge length samples, negative magnitudes of C(D) will be observed in many of the crept specimens (particularly for the larger diameter cavities), which is unreasonable. On the other hand, as shown in Figure 7-3, the distribution of V(D) of the ref. far field measurement is lower than any crept samples for both the smaller and larger diameter cavities, this measurement was thus deemed more suitable to calculate the C(D) of all the samples.

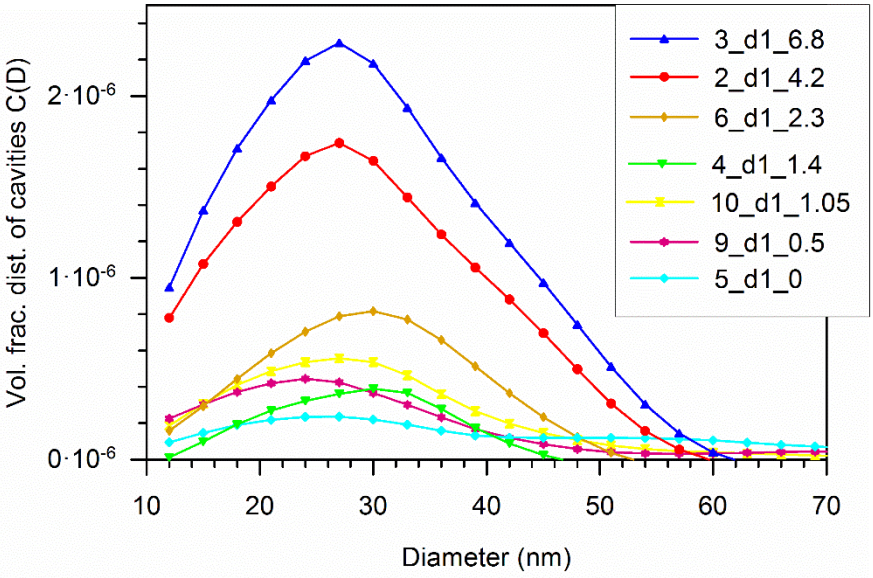

Figure 7-5 Distribution of C(D) from the smaller diameter creep cavities (less than 100 nm) measured in the samples extracted from the gauge length of the specimen crept at 550°C and 320 MPa.

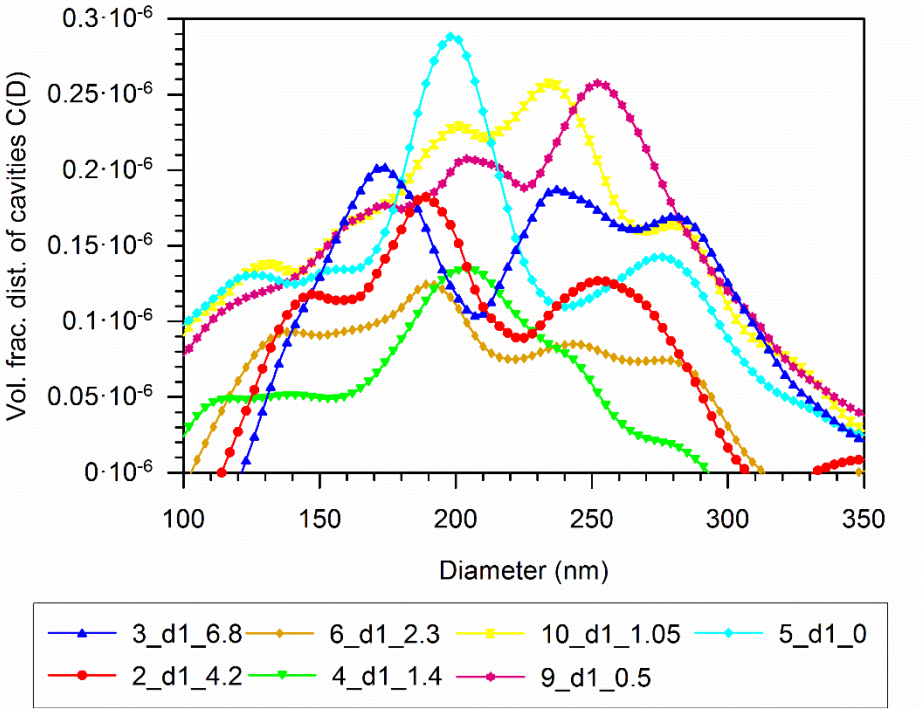

Figure 7-6 Distribution of the C(D) of the larger diameter (100-350 nm) creep cavities measured in the samples extracted from the gauge length of the specimen crept at 550°C and 320 MPa.

The C(D) of the two populations of creep cavities are plotted separately in Figure 7-5 and Figure 7-6. The smaller cavities and the larger cavities have diameters in the range of 10-60 nm and in the range of 100-350 nm respectively. The distribution of C(D) for the smaller

diameter cavities in Figure 7-5 shows that the scattering from the creep cavities is only a very small fraction of the total scattering from the samples. The volume fractions of the smaller sized creep cavities are observed to increase systematically with increase of creep strain in the samples; only the distribution for the sample 4_d1_0.5 does not follow the trend. The difference in C(D) between the samples with 1% or less creep strain is small. The magnitude of C(D) for some of the samples becomes negative due to uncertainties in the measured intensities which are interpreted as small peaks in the MAXE routine. These uncertainties are amplified when V(D) of the reference sample is subtracted giving negative C(D) magnitudes [238].

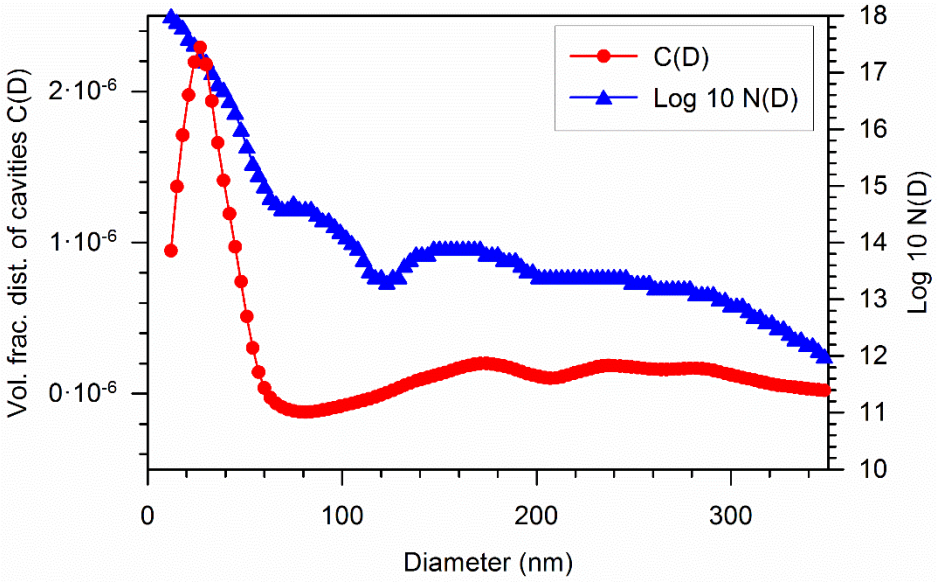

Figure 7-7 Distribution of the N(D) in sample 3_d1_6.8 with respect to increasing diameter of the creep cavities

Converse to the trend in size of smaller diameter cavities with creep strain, no significant difference can be observed in the distribution of C(D) of the larger diameter cavities, as shown in Figure 7-6. Moreover, the magnitude of C(D) of these cavities is smaller than those of the smaller sized cavities, therefore, according to Equation 8.2, the number distribution, N(D) of the larger diameter cavities will be much smaller than those with smaller diameters. An example of the variation of N(D) with respect to the diameter of the creep cavities is presented in Figure 7-7. It can be noticed that the smallest diameter cavities have the highest N(D); note how N(D) reduces rapidly with increasing diameter of the creep cavities for the

cavities up to ~80 nm diameter. Beyond that, the rate of decrease of N(D) with increasing diameter of the cavities reduces.

7.3.2 Creep interrupted specimen at 675℃ and 150 MPa

Figure 7-8 shows the distributions of V(D) for the samples extracted from the gauge length of the specimens crept at 675℃ and 150 MPa. Similar to the specimens crept at 550℃ and 320 MPa, two populations of scatters can be noticed, although, comparing Figure 7-3 and Figure 7-8, it can be observed that the peaks of the larger scatterers in this case are not as prominent as in the previous case. The peak values of V(D) for the smaller scatterers are noticed to increase systematically with increase of creep strain in the sample. The difference in the peak and distribution of V(D) is very small between the sample 13_d1_5.7 and the sample 14_d1_3.3. The same reference measurement obtained from the far-field measurement was used in this case, and is designated ref. far-field in the figure. The V(D) of the ref. far field measurement is again found to have the lowest distribution of V(D).

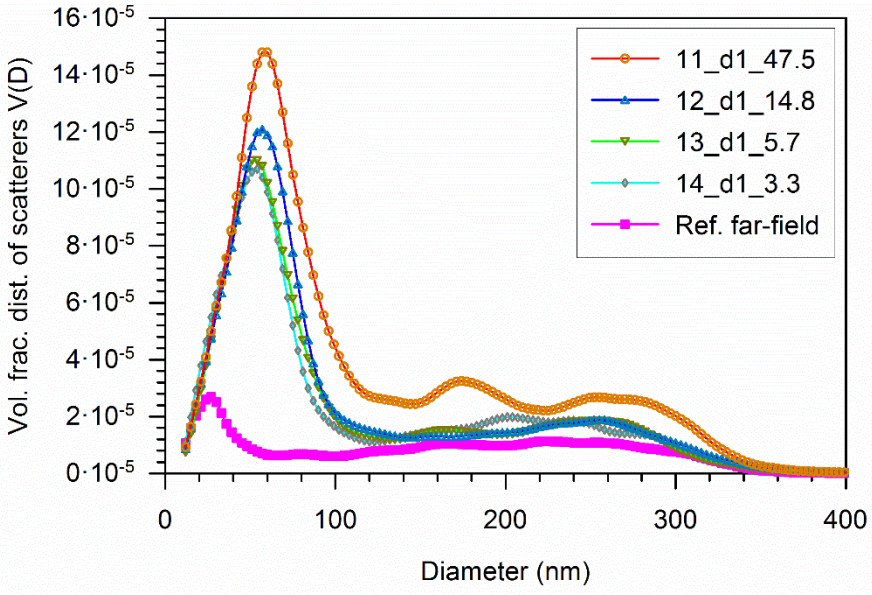

Figure 7-8 Volume fraction distribution of scatterers in samples extracted from the gauge sections of the creep interrupted specimens tested at 675℃ and 150 MPa.

The distribution of C(D) for the smaller and the larger cavities is plotted separately in Figure 7-9 (a) and (b) respectively. The C(D) of the smaller cavities can be observed to increase systematically with increase in creep strain in the samples. Unlike those observed in the previous set of samples, the C(D) of the larger cavities do not show any distinct peaks. No

systematic changes of these peaks with respect to the creep strain can be noticed, except that the sample 14_d1_47.5 shows the distinctively higher magnitude of C(D) than the rest of the samples.

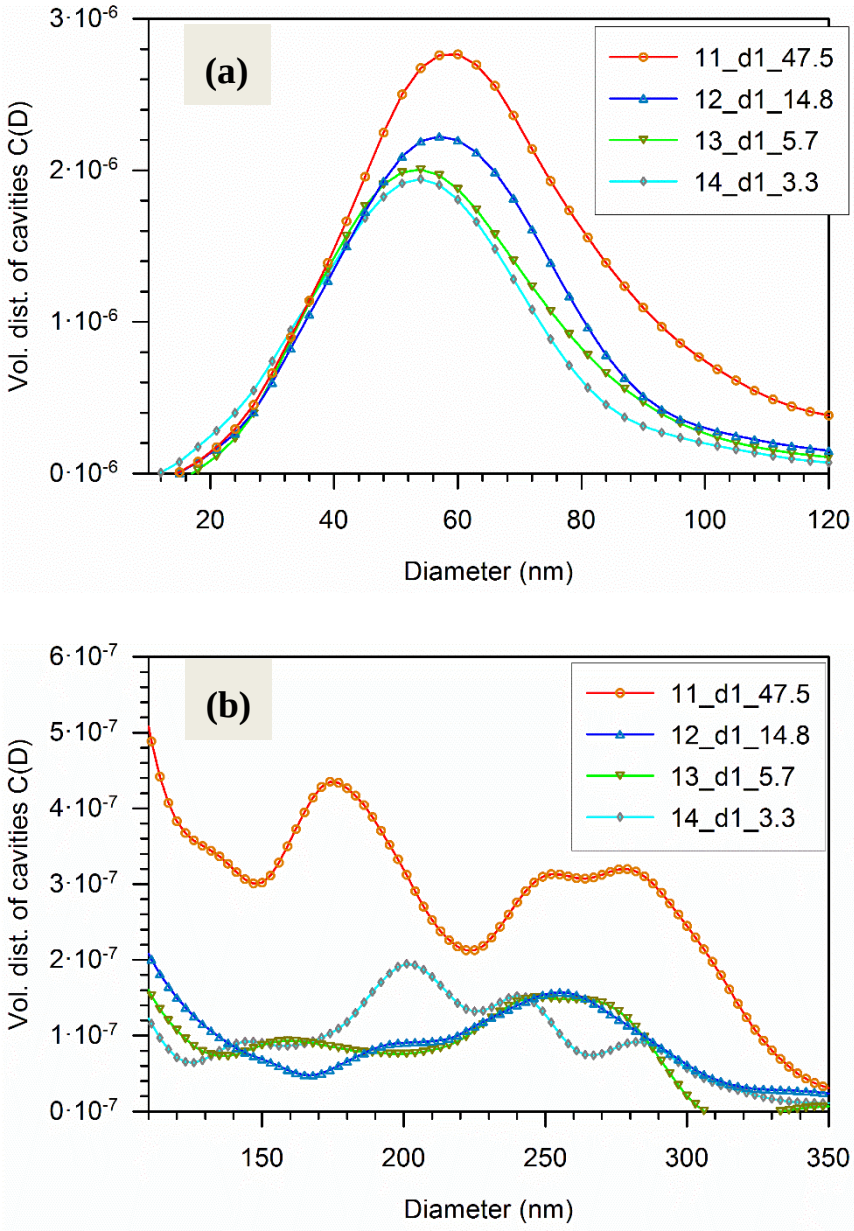

Figure 7-9 Distribution of C(D) of (a) the smaller and (b) the larger diameter creep cavities measured in the samples extracted from the gauge length of the specimen crept at 550℃ and 320 MPa.

Figure 7-10 shows a comparison of the distribution of C(D) of the smaller diameter cavities between the samples tested at 550℃ and 320 MPa and the samples tested at 675℃ and 150 MPa. A clear shift in the distribution of C(D) of the smaller cavities can be noticed between these two sets of samples. Samples tested at 550℃ and 320 MPa have much lower C(D) for

smaller sized cavities than those tested at 675℃ and 150 MPa. Moreover, the range of diameters of the cavities and the width of the peaks for the latter are bigger than the former. Interestingly, the differences in the distribution and magnitude of peaks of C(D) between the samples are smaller in the case of the specimen tested at 675℃ and 150 MPa despite having a much larger difference in the creep strain between the samples creep deformed at this condition. Moreover, differences can be observed in the positions of the peaks of C(D) between these two set of samples; the peak position for the samples tested at 550℃ does not change with increasing creep strain whereas that for the other set of samples shift to larger cavity size.

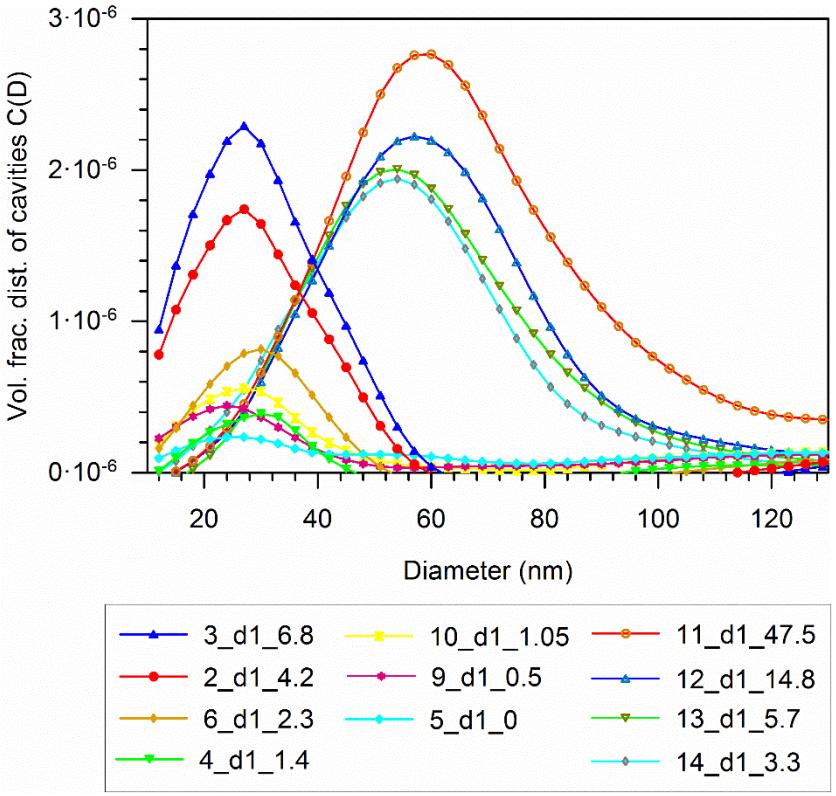

Figure 7-10 Comparison of the distribution of C(D) of the smaller diameter creep cavities between interrupted creep specimens tested in two conditions.

A direct comparison between the total volume fraction of the cavities can be obtained by plotting the integrals of the C(D) (area under the curve in Figure 7-10) of the two sets of the creep samples with respect to those creep life fraction. The results presented in Figure 7-11 show such a comparison. Due to the differences in the range of the diameters of the cavities in the two sets of samples, a separate limit of integration was used. The C(D) of the samples tested at 550℃ and 320 MPa were integrated over the range of 10-60 nm and those of the

samples tested at 675℃and 150 MPa were integrated into the range of 10-120 nm. The creep life fraction for the two sets of tests was determined by dividing the creep strain of each sample with a strain to reach failure in the respective cases, that is 6.8% for the samples tested at 550℃and 320 MPa and 47.5% for the samples tested 675℃and 150 MPa.

A systematic increase of total volume fraction of the smaller sized cavities with increasing creep life fraction can be noticed in both sets of creep test although an anomalous shift in case of sample 4_d1_1.4 can be noticed. The total volume fraction of cavities is a few times higher for the samples tested at 675℃and 150 MPa. The slope of the increase of the integrals of C(D) is steeper for the earlier stages of creep deformation in both the cases.

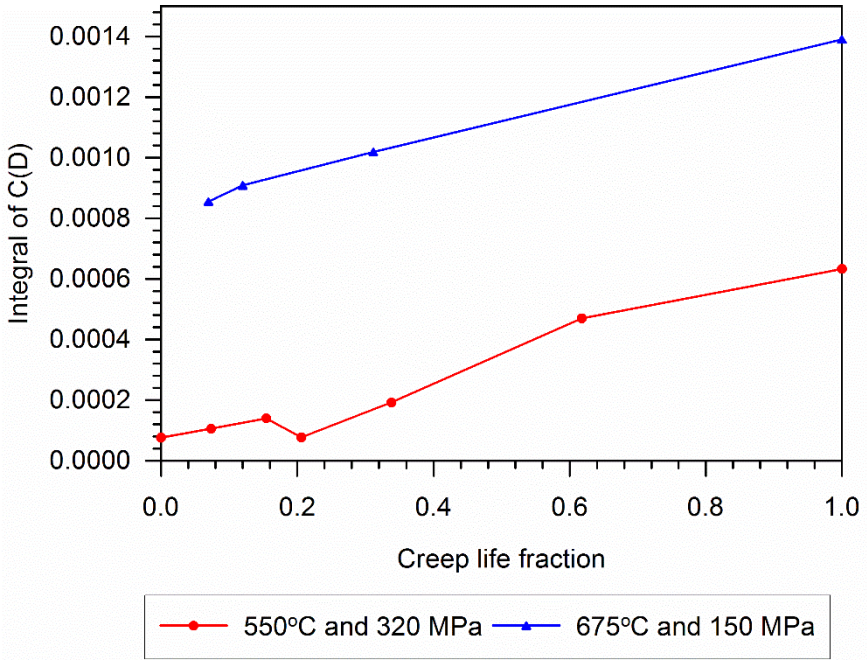

Figure 7-11 Comparison of the integrals of C(D) for the smaller diameter creep cavities between the interrupted creep specimen tested at two different conditions. The integrals were calculated within the limits of 10-60 nm for the specimens tested at 550℃ and 320 MPa and the within the limits of 10-120 nm for the specimens tested at 675℃ and 150 MPa

7.4 Microscopic investigations using HS-AFM

The results of the SANS experiments provided a wealth of quantitative data about the evolution of creep cavities in two sets of creep interrupted specimens of type 316H austenitic stainless steel. As mentioned previously, SANS can only measure cavities of certain size

limit (up to 350 nm diameter size, in this case) depending upon the instrument capability and set-up. Moreover, being purely quantitative in nature, information regarding the shape and spatial distribution of cavities cannot be obtained using SANS technique. Therefore, a complementary microstructural investigation using a High Speed Atomic Force Microscope (HS-AFM) was conducted on a number of selected creep interrupted samples. In comparison to the conventional electron microscope, the HS-AFM is capable to provide a 3D measure of cavities and carbides which ultimately can be compared with other volumetric measurement techniques such as SANS.

Three interrupted creep samples were chosen for the HS-AFM measurements, all these were deformed in creep at 550℃ and 320 MPa. The selected samples were 5_d1_0, 10_d1_1.05 and 3_d1_6.8. These samples were extracted from the other half of the gauge length of the specimens measured using SANS. The samples were previously analyzed using EBSD technique [195], therefore, those were available in mounted and electro-polished conditions. The specimens were further fine polished using 1/4 μm diamond paste on a nylon cloth and vibro-polishing for 24 hours at a rotational speed of 3 rpm using an oxide polishing suspension (OPS) solution. The steps of the specimen preparation were according to the procedures described in [163]. The specimens were first visually inspected using an optical microscope system attached to the HS-AFM system. Based on this inspection, a number of areas were chosen in each sample with particular interest on cavitated grain boundaries as many cavities are associated with intergranular carbides. Example images containing the observed features in the three samples investigated, are presented below.

7.4.1.1 Results

Specimen 5_d1_0

Figure 7-12 shows examples of images obtained from the sample 5_d1_0. In these images, carbides are shown as bright spots and the cavities are shown as dark spots, as designated in the Z scale as the right-hand Y axis. A random dispersion of small-sized carbides are observed all over the grains and larger sized carbides are observed mainly at the grain boundaries. The smallest measurable size (diameter) of carbides was in the range ~5-10 nm; a majority of the smaller dispersed carbides were observed to have diameters in the range of 20-60 nm. A majority of the larger size carbides had diameters in the range 150-250 nm.

Similar size distributions were also noticed in the other images (not presented here) obtained from this sample.

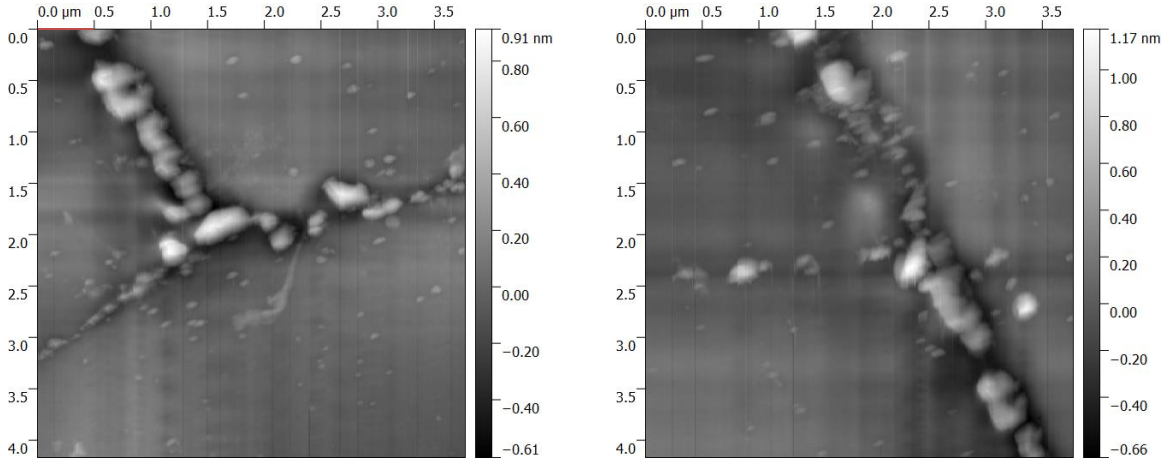

Figure 7-12 HSAFM images showing the size and spatial distribution of the carbides (bright colored) in the grain boundaries and in the matrix of sample 5_d1_0.

Specimen 10_d1_1.05

Figure 7-13 shows examples of images obtained from sample 10_d1_1.05. A similar distribution of smaller size carbides in the matrix of the microstructure and larger sized carbides in the grain boundaries can be noticed. Carbides with a diameter up to 500 nm can be observed in this sample. Such large carbides were not measured by SANS2D as these are out of measurement size scale of this instrument. Faceted creep cavities can be noticed in all the images, some of which are lying in between carbides in the grain boundaries, for example that in image (a). The largest sized cavities observed in the images, for example that in the image (c), is about 300 nm in length.

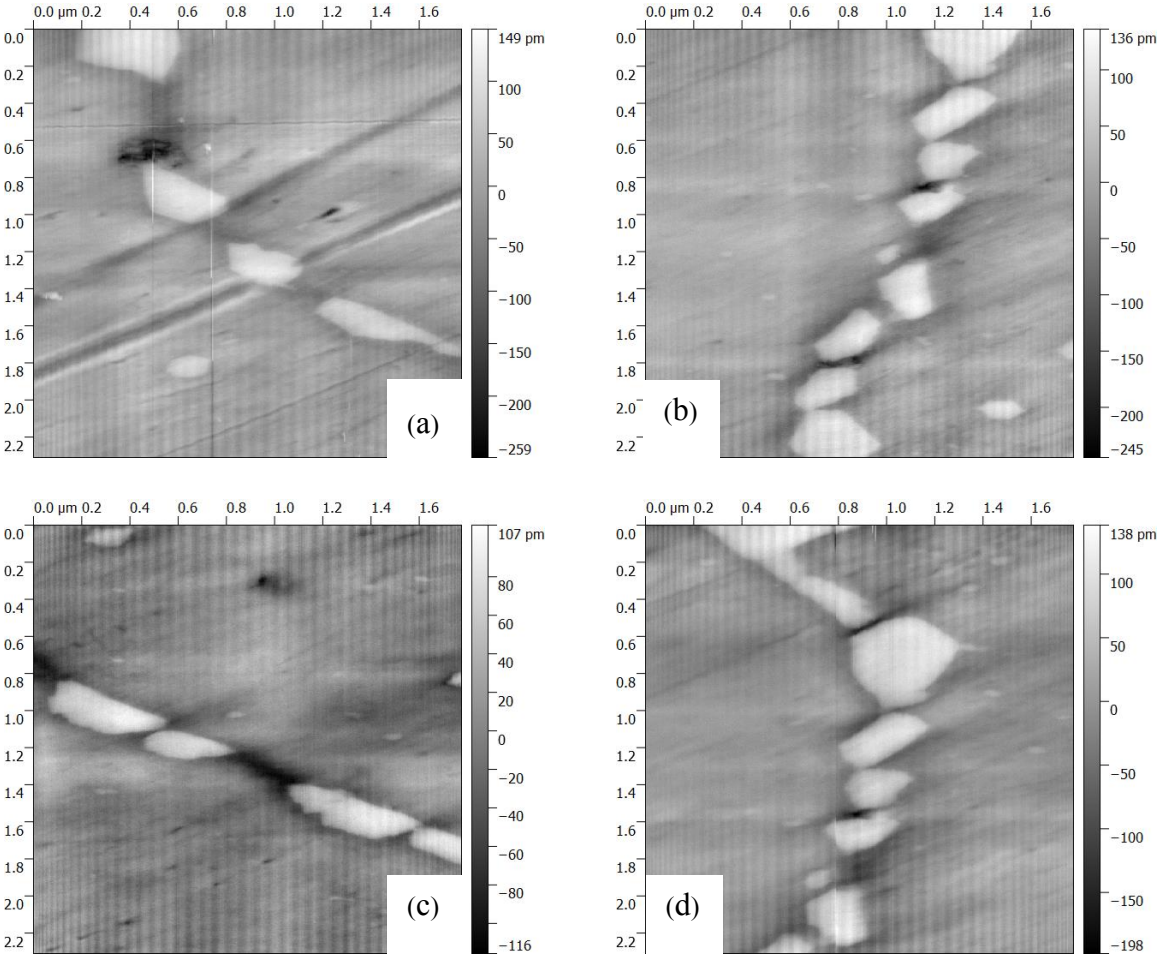

Figure 7-13 HSAFM images showing the size and spatial distribution of the carbides (bright colored) and cavities (dark colored) in sample 10_d1_1.05.

Specimen 3_d1_6.8

Figure 7-14 shows examples of images obtained from sample 3_d1_6.8. A similar distribution of smaller size carbides as seen in the other two samples can be noticed in the images. Carbides with a diameter as large as 1500 nm can be noticed. An increased density of cavities can be noticed in the matrix of the sample, most visibly in the images (a) and (d). Similar to sample 10_d1_1.05, cavities lying in between grain boundary carbides are noticed, for example in image (b). Small sized cavities with a diameter in the range 30-100 nm can be observed, which is similar to that observed in this sample with the SANS technique.

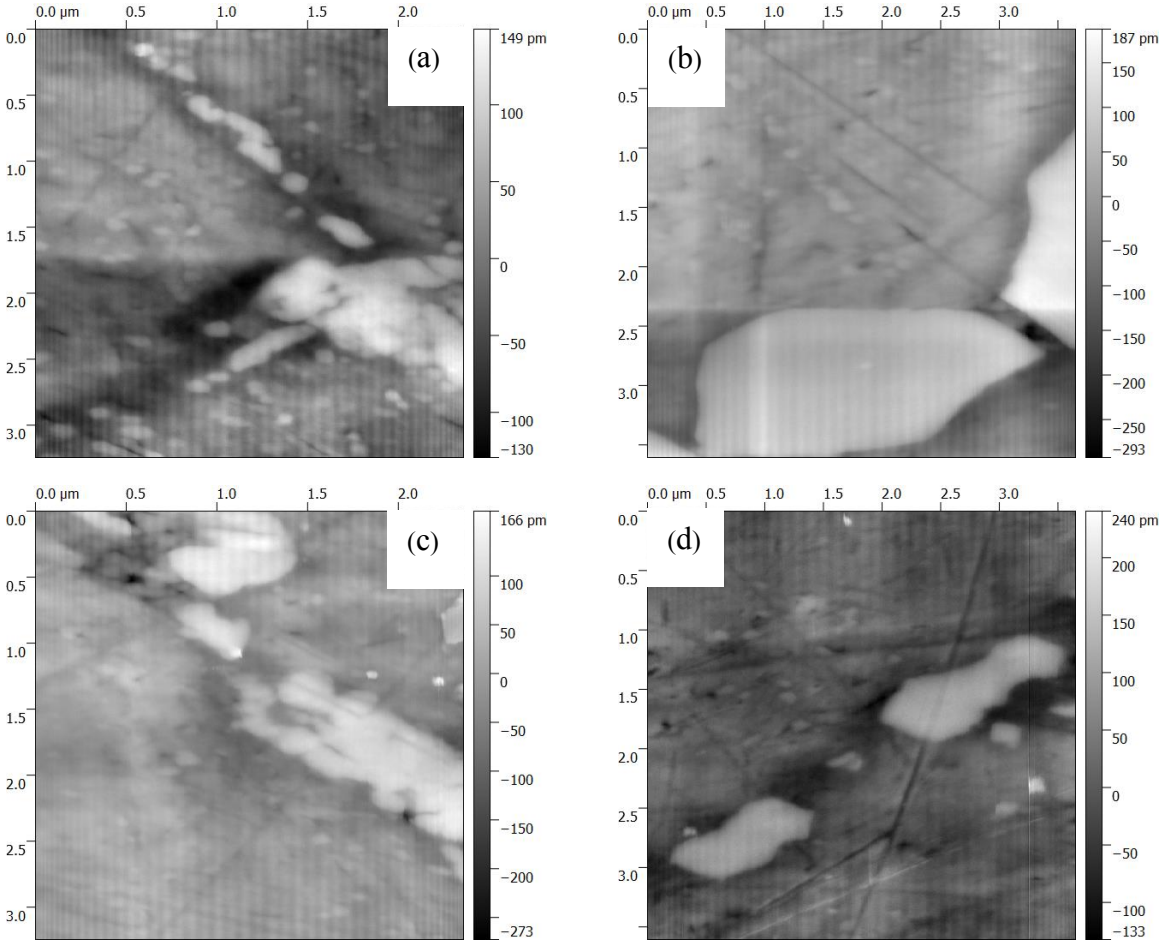

Figure 7-14 HSAFM images showing the size and spatial distribution of the carbides (bright colored) and cavities (dark colored) in sample 3_d1_6.8.

7.5 Evolution of intergranular strain

Lattice strains were measured using the neutron diffraction technique in the same two sets of interrupted creep test specimens used for the SANS measurement. The split half specimens were used for the measurements. The measurements were conducted using the Engin-X instrument following the procedures described in Section 3.6.6.1. The half specimen was screwed into one grip of stress rig on the Engin-X beamline and the position of the neutron beam aligned manually to the centre the positions of the measurement point in the specimen using a theodolite. At least 3 neutron measurements in the gauge length and 1 measurement in the grip section of each specimen were obtained. An average of the 3 measurements from the gauge length of the specimen was used for calculating the intergranular strain in the material.

The creep specimens were only available after the creep tests, therefore measurement of the absolute stress-free reference d_0 value in the undeformed specimen prior to the creep tests was not possible. As an alternative approach, an undamaged specimen extracted from the same steam-header was measured and the d_0 value of that specimen was used as a reference to calculate the intergranular strain in all 4 specimens. At least 3 neutron measurements in the gauge length and 1 measurement in the grip were conducted for each specimen. The magnitude of the strains measured in the gauge length showed good consistency with each other, for all the specimens, and an average of the 3 measurements was used for calculating the strain.

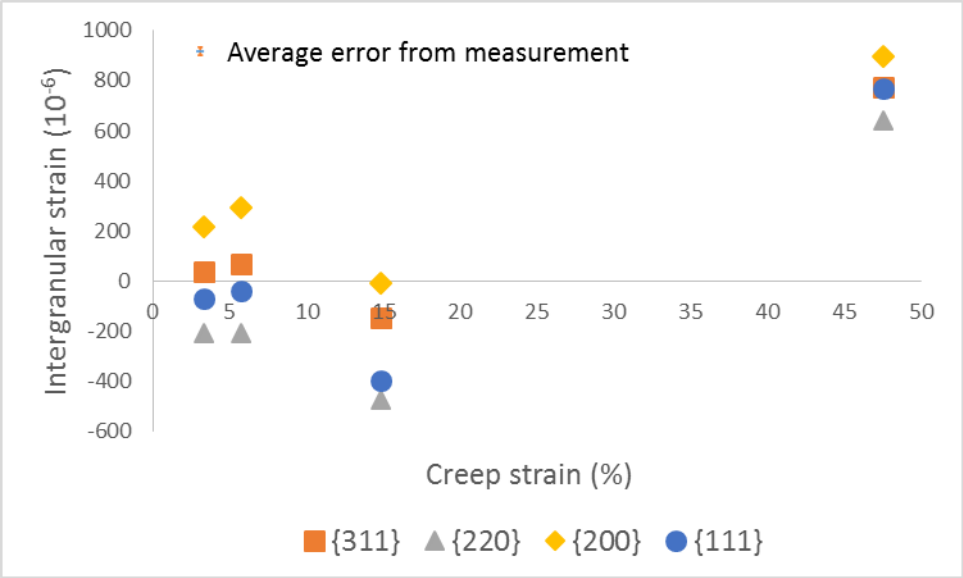

Figure 7-15 Variation of axial intergranular strains measured ex-situ in AISI type 316H austenitic steel specimens crept up to various life fractions at 675 ℃ under 150 MPa initial stress. The reference d_0 value for calculation of strain was measured from an undeformed specimen extracted from the same place of the steam header from where the creep specimen were extracted.

Figure 7-15 shows the calculated IR strains in the axial direction of the specimen, plotted as a function of the creep strain. The tensile IR strain can be observed to increase in the {200} and the {311} grain families and compressive intergranular strains can be observed to increase slightly in the {220} grain families with increasing creep strain from 3.3% (primary regime) to 5.7% (secondary regime). The measurements in the highly crept specimen, one at 14.8% strain (tertiary regime) and the other at 47.5% (rupture) show an unexpected large shift of the intergranular strains in compression and tension respectively. The range of intergranular strains between various grain families in the specimen crept to 14.8% is similar

to the specimen crept up to 5.7%, indicating that the apparent anomalous shift in this specimen could be due to the use of a generic d_0 value for calculating strain. This is because the spacing between lattice planes in the undeformed state of the material can differ slightly from specimen to specimen. The range of intergranular strain for the specimen crept to 47.5% is smaller than the other specimens.

Suspecting the anomalous shift of the magnitude of intergranular strains arose from the use of a generic d_0 value, an alternative approach was undertaken. In this approach, it was assumed that the deformation in the grips of the creep specimen was minimal compared to the deformation in the gauge length. Therefore, the d value measured from the grip of the individual specimen was used as the d_0 value to calculate strain in that respective specimen. The results obtained using this approach is shown in Figure 7-16. No clear correlation can be observed, neither between the measured intergranular strains with respect to macroscopic creep strain nor in the increase or decrease of the range of intergranular strains between the grain families.

Similar measurements (not presented here) were conducted in a few of the specimens from the set of creep interrupted specimens tested at 550℃and 320 MPa. Reference measurements from the grips of the individual specimen and from the undamaged specimen were used for calculating strains in various grain families in those specimens. No systematic variation of intergranular strains with respect to the creep strains were observed for this set of specimens as well. Moreover, the creep tests at 550℃ and 320 MPa were preceded by large plastic deformation (8% strain), which will affect the intergranular strain state of the material prior to the creep deformation. Without knowing the initial d_0 of the undeformed state of the material, it was not possible to quantify the changes of intergranular strains during the creep deformation process. In summary, no conclusive results could be obtained from the analysis of the results of the variation of intergranular strains during the creep process in this material.

During high temperature creep deformation, significant precipitation is expected in this material. Such precipitation may change the lattice spacing between crystal lattices, essentially introducing an error in strain calculation from neutron data. If any such pseudo strain errors are introduced in the calculation, it would be visible by decrease or increase of the Rietveld strain in the material. No such variation in the Rietveld strains were observed during the very short creep dwells presented in earlier chapters and therefore no corrections

were required for quantifying strain. However, significant precipitation is expected in the specimen discussed in this section, owing to their prolonged exposure to high temperature. Therefore, it is possible that the measured strain determined from the d value in the gauge length and d_0 value from the grip section changed due to pseudo-strain arising from precipitation.

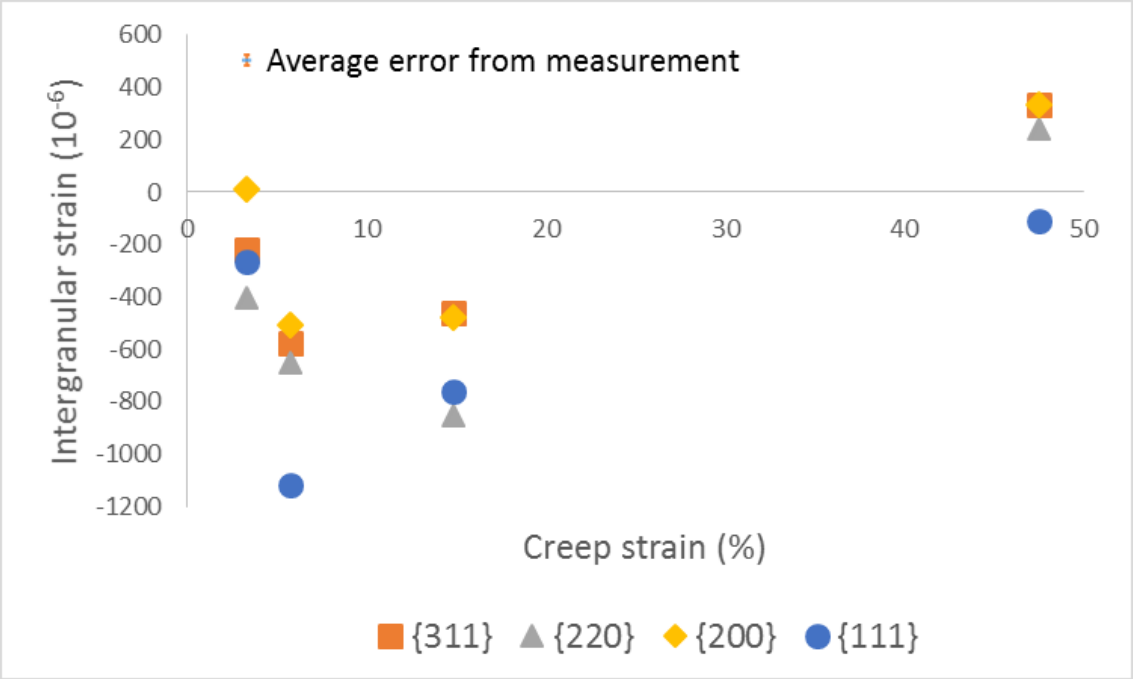

Figure 7-16 Variation of axial intergranular strains measured ex-situ in AISI type 316H austenitic steel specimen crept up to various percentage at 675 °C under 150 MPa. The reference d_0 value of each specimen for calculation of strain was measured from the grip section of the respective specimen.

In summary, no conclusive results could be obtained from the analysis of the above results in terms of variation of intergranular strains during the creep life of this material. However, from the discussion it is clear that ex-situ measurements of multiple specimens significantly increased the experimental uncertainties. Apart from uncertainties arising from the measurement of the d_0 value, uncertainties can also arise from the procedure aimed at preserving the internal stress state of the material after the creep tests. Published results [81] show that intergranular strains change following unloading during a creep test owing to anelastic recovery of creep strain. Therefore, the measured intergranular strain ex-situ may actually not be a true representation of the intergranular strain state at that creep strain. In contrast, in-situ measurements can provide a wealth of information in relation to the kinetics of internal stress evolution in the material during the deformation process. For example, with

ex-situ measurements, it wouldn't have been possible to observe the rate of relaxation of intergranular strains during the stress relaxation tests reported in this thesis.

7.6 Discussion

During creep deformation of austenitic stainless steel, mainly two types of microstructural changes occur in the material; 'precipitation' and 'nucleation and growth of creep cavities'. The former of these is mainly a consequence of temperature while the latter is a consequence of both stress and temperature. Quantitative metallography using optical / electron microscopy by repeated polishing and etching process is the most widely used technique for studying the evolution of microstructures of the material during the creep process. However, it is rarely possible to have high confidence data acquired about the size, shape, and volume of creep cavities using microscope based techniques [60] owing to operator dependence, and the limitations of it being a two-dimensional technique that samples a small area. In comparison, SANS can provide a volumetric measure of creep cavities and carbides, without the requirement for any specimen preparation. However, SANS measurements are usually limited to specific size ranges of scatterers and have to be supported by complementary techniques that can distinguish between the carbides and cavities.

The SANS results were interpreted using a suitable model based on a number of assumptions, including a uniform distribution of carbides in the material and spherical shape of the carbides and cavities. Measurements from far-field undamaged material of the steam header were used as the reference measure of the carbides in the creep damaged samples. It was assumed that the volume fraction of carbides measured in this sample is representative of the volume fraction of carbides post creep deformation in the creep interrupted samples that is no changes in volume fraction of carbides occurred in the specimens during the interrupted creep deformation process, which is not absolutely correct. Before the creep deformation in these specimens, the materials were in service for about ~10 years in the power plant at an average temperature of 525℃ and stress of 16 MPa. Therefore, it's a reasonable assumption that the precipitation in the microstructure of the material would have reached a saturated state during this period, that is any increase in volume fraction of precipitates would not be significant enough to affect the results. Such use of reference samples has also been reported in earlier SANS work by [73] [74] in separating cavities from

the carbides in creep deformed austenitic steel specimens. Nevertheless, the effect of stress on accelerating the precipitation in stainless steel is known [239], therefore, in reality during the creep deformation, the volume fraction of the carbides in these specimens may have increased slightly.

Two populations of scatters with different size distributions were observed for the measured C(D) in both sets of creep interrupted specimens. The diameters of the smaller sized cavities were found to be in the range of 10-120 nm. A similar size distribution of smaller creep cavities has also been measured using SANS in type 304 stainless steel [72] [240] post creep deformation at 593℃ and 134 MPa. The HS-AFM images of the interrupted creep samples tested here confirm the existence of this distribution of smaller sized carbides and cavities. Furthermore, a good correlation between SANS measurements of cavities up to this size and other microscope based measurements on 316H stainless steel, for example quantitative SEM metallography, have been reported in a number of recent publications [78, 192, 238]. However, in the case of the larger sized scatterers, the presence of larger carbides than those measured using SANS can be observed in some of the HS-AFM images. This is not unexpected because the SANS2D instrument cannot resolve scatterers larger than about 350 nm.

The C(D) of the smaller diameter cavities was found to increase systematically whereas the size of larger diameter cavities were almost unchanged with increasing creep strain in both sets of interrupted samples. This evidence indicates that the progression of creep damage in this material is by continuous nucleation of creep cavities. Exceptionally, in the case of sample 11_d1_47.5, a significant increase in the distribution of C(D) of the larger diameter cavities was observed, which can be attributed to the very high creep strain in this sample in comparison to the rest. The cavity nucleation rate in this material during the creep deformation process was reported to be nearly constant [75]. However, in this case it was observed that the increase in total volume fraction of the smaller sized cavities (integrals of C(D)) was higher at the early stages of creep deformation. It is possible that the smaller sized cavities at the earlier stages of creep deformation coalesced to larger sized cavities in the later stages of the creep test which would not be picked up by the SANS measurements (owing to the upper size limit of the SANS technique).

In the HS-AFM images, the smaller sized carbides were mostly found to be dispersed in the matrix of the microstructure, while larger sized carbides were observed mostly in the grain boundaries. Similar observations of intragranular and intergranular carbides have been made by using SEM and FIB serial sectioning respectively, of similar header materials by Jazaeri [192] and Burnett [241]. $M_{23}C_6$ is the most abundant type of carbide formed in this material (as described in chapter 2); this type of carbide is known to form at the early stage of creep deformation in grain boundaries, and therefore, it is likely that these carbides are sites for condensation of vacancies and initiation of creep cavitation [66] in the materials. In fact, most of the cavities were observed to be linked with carbides present either in the matrix or the grain boundaries of the microstructure. Such observed intimacy between the carbides and cavities suggests that these carbides are likely to control where, when and how the cavities form [241]. The cavities in the creep deformed samples were observed to mostly have irregular shapes, such as a needle, circular and faceted which is consistent with other recently published findings [241].

The ex-situ neutron diffraction measurements on the sets of interrupted creep specimens highlighted a number of limitations. The reason for including this work is to provide a basis for discussing the suitability of ex-situ neutron diffraction studies in relation to understanding the generation and evolution of intergranular strains during creep deformation. An accurate stress-free lattice parameter measurement is required for strain measurement using neutron diffraction. The measurement from an undamaged section/specimen of similar material is usually used for such purpose if the exact specimen can not be measured before deformation. However, the material for investigations being a service aged material with complex loading history, it was not possible to obtain a reasonably accurate measure of the d_0 value in this case.

Apart from the uncertainties arising from the measurement of d_0 value, uncertainties may also arise from preserving the internal stress state of the material post-tests. Intergranular strains in various grain families are reported to relax following an unload from a creep load to cause anelastic recovery of creep strain, as discussed in Section 6.2.5. This relaxation of intergranular strains in different grain families is different in magnitude and direction, therefore, the measured intergranular strain ex-situ may actually not be a true representation of the intergranular strain state at that creep strain. Moreover, during high temperature creep

deformation, the crystal lattice spacing is affected by precipitation which can introduce an error in strain calculation from neutron diffraction data [81] if not taken into account. Correction factor for such precipitations can be easily calculated for in-situ tests by recording the evolution of the Rietveld average strain, however, for ex-situ measurements it is difficult to account for. Finally, in the case of more complicated tests of creep deformation preceded by plastic deformation, like that conducted at 550℃and 320 MPa, the level of uncertainties' for the ex-situ measurements is very high and only in-situ tests can provide the complete picture of the evolution of intergranular strains during plastic and creep deformation interactions.

7.7 Summary

Creep cavity damage was measured in two sets of interrupted creep specimens of type 316H austenitic stainless steel using SANS and HS-AFM technique. Size and volume fraction of creep cavities was measured quantitatively using SANS and complementary qualitative imaging were conducted using HS-AFM.

1. In general two population of creep cavities were observed; one population with diameters in the range of 10-120 nm, and the other population with a diameter in the range of 130-350 nm. The results of this size distribution are found to be in good agreement with those observed in the HS-AFM images and the published results of quantitative metallography and other SANS measurements on this material. This demonstrates the excellent capability of the SANS technique in the mesurement of nanometer sized cavities in creep deformed materials.
2. The volume fraction of the smaller diameter cavities are found to increase systematically with the increase of the creep strain in the samples for both sets of creep interrupted specimens. This indicates a continous nucleation of creep cavities throughout the creep deformation of these samples.
3. Smaller sized carbides are found to be mostly dispersed in the matrix and the larger sized carbides are found to be dispersed in the grain boundaries of the microstructures in the samples. The creep cavities are found to be of irregular shapes and closely linked with the carbides in the grain boundaries.

4. Intergranular strains were measured ex-situ using same sets of interrupted creep specimens, however, no conclusive results were obtained due to the limitation of correct d_0 measurement of the stress-free sample and increasing uncertainties of the internal state of the specimen due to those complex service and loading history.

Chapter 8 General Discussions

8.1 Overview

This chapter is divided into two main parts. The first part discusses key findings presented in Chapter 4, Chapter 5 and Chapter 6 in the context of their broader applicability to creep models and life assessment methods. The second part of the chapter discusses the challenges of undertaking high-temperature in-situ creep studies using neutron diffraction instruments and presents ideas for developing a novel stress rig with a high-temperature furnace that would facilitate future studies of this kind.

8.2 Part 1: Discussion on key findings

8.2.1 Creep deformation and intergranular strain

The presented results on the evolution of intergranular strains during plastic and creep deformation in Chapter 4 and Chapter 6 respectively can be broadly discussed in the context of the effect of prior plastic deformation on the creep deformation in type 316H stainless steel. No creep tests were conducted in this project using pre-strained specimens, however, such experimental works reported in the literature can be directly correlated to findings of this thesis

There is a general agreement in the literature [228] [227] [229], that the creep ductility (strain at failure) of type 316H austenitic steel reduces due to room temperature tensile or compressive plastic pre-straining. On the other hand, minimum creep rate of this material is reported to decrease with increasing room temperature tensile pre-strain [227] and to increase with increasing room temperature compressive pre-strain [230]. Such decrease of the creep rate due to tensile pre-straining is usually explained in terms of the increase of

dislocation density during the pre-straining and also in terms of the effect of plastic deformation on the nucleation of cavities, for example by creating high residual stresses near an inclusion [242]. It is widely known that the dislocation density increases rapidly with increase of plastic strain; and a higher density of dislocations may not fully recover during the heating process prior to creep deformation creating more barriers to the movement of dislocations, resulting in a reduction of the minimum creep rate. However, a similar increase in the dislocation densities is also expected for compressive plastic pre-straining, after which the creep deformation rate is reported to increase in this material.

The role of plasticity generated back stress is mostly ignored in the context of the effect of plastic pre-straining on creep deformation rate. However, Wilshire et al. [227] have discussed the role of creep deformation generated back stress on the effect of the subsequent creep deformation rate. They [227] concluded that if the internal stresses developed during tensile creep can cause a negative creep rate to be recorded after a large stress reduction, then it seems reasonable to assume that the creep behaviour prior to the stress reduction is also dependent upon the magnitude of the internal stress. In this case, they assumed the internal stress (termed as back stress in this thesis) to be generated solely from the inhomogeneous distribution of dislocations, that is intragranular stresses. Nevertheless, the argument of creep deformation rate being governed by an effective stress (the difference between the applied stress and the back stress) [243] is highly relevant. Now, the results reported in Chapter 4 show that intergranular strains of significant magnitude are generated in type 316H austenitic stainless steel during room temperature tensile / compressive plastic deformation. It has also been shown in Chapter 6 that these plasticity generated intergranular strains affect the creep deformation rate. Moreover, the analysis of the dislocation structures prior and intermediate to the creep dwells, show no formation of dislocation cell type structures at the stage of creep deformation studied, yet significant anelastic recovery of strain in this material can be observed. The corresponding relaxation of intergranular strains during this anelastic recovery is also shown. Therefore, there is a strong basis to state that intergranular strain is the major contributor to back stress in this material, at least during early stages of creep deformation under load or displacement control. The dominating role of intergranular strains contributing to the total back stress of the material is also supported by published literature [81].

Having established this hypothesis, it is now possible to correlate the observed variation of intergranular strains during plastic deformation (presented in Chapter 4) with the published results of the effect of pre-straining on macroscopic creep rates. It can be observed that the total magnitude of intergranular strains in the material (calculated from the range of maximum tensile and maximum compressive intergranular strain) increases with increasing tensile and compressive plastic strain. Therefore, based on the previous argument of the 'effective stress' both tensile and compressive pre-straining is expected to reduce the creep deformation rate in this material. However, upon tensile pre-straining, the plastic weaker grain families accumulate compressive residual strain while those after compression pre-straining accumulate tensile residual strain. The plastic weaker grains are the same set of grains which are 'creep weaker' in this material [81]. Therefore, it is reasonable to postulate that the creep weaker grains with compressive residual strains (owing to tensile pre-straining) will creep more slowly during subsequent tensile creep loading than the same set of grains in virgin material; this will decelerate the minimum creep rate. Conversely, following compressive pre-strain, the plastic weaker grains accumulate tensile residual strain, and therefore these grains will creep faster during subsequent tensile creep loading than in virgin material, accelerating the creep deformation rate.

A similar interpretation of the results can also be extended to the high-temperature pre-strained specimen. Increasing tensile plastic pre-straining at 650 ℃ is reported to decrease the subsequent minimum creep strain of type 316H austenitic stainless steel [231]. In fact, pre-straining conducted at any temperature increases the creep resistance in this material [229] as long as the strain upon creep load is lower than the plastic pre-strain introduced [227]. An example of such effect of pre-straining at 650 ℃ on the minimum creep rate of type 316H austenitic steel at 650℃ and 140 MPa is presented in Figure 8-1. Moreover, Ohashi et al. [231] conducted creep tests followed by plastic pre-straining in tension-torsion for type 316H austenitic steel and by observing the reduction of the subsequent tensile creep deformation rate, they concluded that the 'decrease of the creep deformation rate' decreases with the increase of the difference between the direction of prior plastic deformation and subsequent creep deformation, which is consistent with the explanation of anisotropic deformation of grains provided above.

In the results of the evolution of intergranular strains during incremental plastic loading at 650°C (presented in Chapter 4), it was observed that the increase of intergranular strain with increasing plastic loading seems to saturate after ~8% of strain. It would be interesting to examine if the reduction in creep deformation rate due to prior plastic tensile strain remains unchanged with increasing pre-straining beyond this strain percentage. Unfortunately, no experimental results of creep rate measured after such high plastic pre-strain were found for this material in the literature. Nevertheless, with such high pre-straining, it would be difficult to separate the effect of the intergranular strains from the effect of cavity nucleation due to plastic strain. It is important to mention that the above general discussion is limited to dislocation based creep, and may not be applicable to diffusion based creep. This hypothesis is also based on the assumption that prior plastic straining does not create any creep cavities, nor significantly accelerate the creation of cavities. Thus the hypothesis is essentially limited to the effect of smaller levels of plastic pre-strain on creep deformation under high stress.

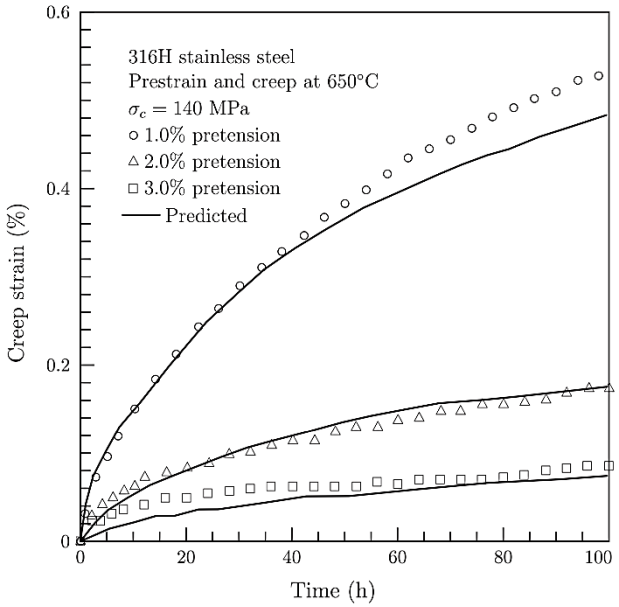

Figure 8-1 Tensile creep curves at 650°C and 140 MPa after various degrees of tensile pre-tension at 650°C in type 316H stainless steel, as presented in [229] from [231] and [244]

The effect of prior plasticity on subsequent creep deformation can be taken into account by, for example, incorporating a back stress term in the constitutive creep equations. Chapter 2 described the power law creep equation (Equation 8.1), which is widely used in estimating the secondary creep deformation rate of many metals under uniaxial loading.

$$\dot{\varepsilon}_s = A\,\sigma^n\,\exp\left(\frac{-Q}{RT}\right) \qquad (8.1)$$

Here, $\dot{\varepsilon}_s$ is the secondary creep rate, σ is the applied stress, A and n are the material constants, Q is the activation energy, T is the temperature and R is the universal gas constant.

The constants of this equation for a given material can be calculated by fitting experimental data from a matrix of creep tests conducted at different stress and temperature. Such estimation of creep deformation is not adequate for estimating the creep rate for dwells during tension-compression cyclic loading. This is because very different creep deformation rates under identical stress and temperature can be observed, due to the varying effective stress state at different positions of the tension-compression loading cycle (as shown for comparative load controlled creep dwells in Chapter 6). A modified power law accounting for the creep-plasticity interaction in terms of a back stress component can be used to predict the creep deformation rate better. Equation 8.2 has been used [236, 245] in improving prediction of stress relaxation of type 316H austenitic stainless steel for dwells with different initial dwell stresses at peak tensile strain of cyclic loadings.

$$\dot{\varepsilon}_s = A\,(\sigma-\beta)^n\,\exp\left(\frac{-Q}{RT}\right) \qquad (8.2)$$

Here, β is the back stress.

A fixed value of back stress was used in this analysis and no physical explanation for the chosen back stress magnitude was provided. In another approach [246] the back stress component was incorporated in the widely known Feltham equation, again for improving the stress relaxation prediction in type 316H austenitic steel. In this case, a magnitude of back stress equal to one-third of the initial dwell stress seemed to provide a good match between the prediction and experimental results. The results presented in this thesis show that the back stress state in the material varies significantly at different points around the tension-compression loading cycle and is not a function of the macroscopic applied stress. Therefore, neither of the approaches described above correctly captures the effect of plasticity for creep dwells introduced at any arbitrary point around the stress-strain cycle.

It may not be practicable to estimate the magnitude of back stress for individual dwells in practical applications. A simple model, such as shown in [247], can be implemented to obtain

the magnitude of the macroscopic back stress, essentially by back fitting the creep deformation rate to a matrix of test results. A maximum and minimum magnitude of back stress can be estimated from such a model for a set of strain and stress ranges, giving respectively realistic and conservative estimates of creep stress relaxation.

The effect of precipitation on strain hardening and creep resistance has not been discussed because tests were conducted on type 316H austenitic stainless steel in a solution treated condition. Moreover, at the early stages of creep deformation studied here, the formation of a dislocation sub-structure was not observed. However, in real service applications, the formation of both significant precipitation and dislocation cell sub-structures is expected in this material, which would further contribute to the back stress (i.e. an intragranular source of back stress) in the material. Nevertheless, it has been noted [117] that the influence of intragranular stress does not conflict with intergranular stress, that is both can simultaneously contribute to the total back stress in the material.

8.2.2 Evolution of IR strain during creep dwells

In Chapter 6, results showing the evolution of intergranular strains during load controlled and displacement controlled creep dwells are presented. The relaxation of macroscopic stress during displacement controlled deformation is a consequence of the creep deformation occurring in the material [248]. Constitutive relations based upon load controlled tests can be reformulated to calculate the rate of stress relaxation in a displacement controlled test. In practice, directly measured stress relaxation data reported in the literature are limited to a few test conditions (in terms of initial stress, temperature and time). More often, stress relaxation data are reported based upon analytical models derived from load controlled creep deformation data. Some of these analytical models predict the stress relaxation rate with good accuracy however only for limited loading conditions; for example for short term tests and not for longer term tests, or for tests at lower stress / temperature but not at a higher stress / temperature etc. [249].

One basic assumption taken in the models while converting the forward creep equation to stress relaxation rate is that the total stress relaxation during the displacement controlled test arises from the conversion of the elastic strain to creep strain in the material. The basis of

this assumption is that the total and plastic strain in the material remains constant during displacement controlled tests, that is

$$\begin{aligned} \varepsilon_t &= \varepsilon_{el} + \varepsilon_p + \varepsilon_c \\ \varepsilon_t &= 0; \varepsilon_p = 0 \\ \varepsilon_c &= -\varepsilon_{el} \end{aligned} \qquad (8.3)$$

Here, ε_t = total strain, ε_{el} = elastic strain, ε_p = plastic strain and ε_c = creep strain

Equation 8.3 can be translated into the following forms to define a correlation between the rate of creep and rate of stress relaxation.

$$\dot{\varepsilon}_c = - \dot{\varepsilon}_{el} \qquad (8.4)$$

$$\dot{\varepsilon}_c = -\frac{1}{E} \dot{\sigma} \qquad (8.5)$$

Here, E is the elastic modulus and $\dot{\sigma}$ is the rate of stress relaxation.

Now, from minimum creep data derived from experimental data, or by fitting a suitable creep rate equation (in terms of load, time and temperature) with necessary material constants, the minimum creep rate can be input into Equation 8.5 and the stress relaxation rate can be calculated. Results of the displacement controlled tests presented in Chapter 6 show that the simple assumption of creep strain arising only from the conversion of elastic strain is not correct. This is because, during stress relaxation in displacement controlled tests, the inelastic intergranular strains are found to relax with time. Therefore, the stress relaxation does not only arise from the conversion of elastic strain to creep strain but also from the changes in the inelastic internal strain in the material. In creep dwells with increasing intergranular strains after repeated cyclic loading, the relaxation of intergranular strains in some grain families is as large as 500 με for a macroscopic stress relaxation of 45 MPa. Therefore, a constitutive model that ignores relaxation of internal stresses during displacement controlled tests will significantly underestimate the rate of macroscopic stress relaxation. The relaxation of the intergranular strains in the grains was observed to follow the trend of the relaxation of the macroscopic stress, therefore, the changes of back stress during stress relaxation of type 316H austenitic steel can be modelled as a function of the macroscopic stress relaxation.

In the case of load controlled creep dwells, intergranular strains are observed to increase during primary creep and remain nearly unchanged during secondary creep. A similar variation of intergranular strains during primary and secondary creep has also been reported in other similar investigations in type 316H austenitic steel [81, 137]. The small increase of internal stress during primary creep will reduce the creep deformation rate and therefore a creep rate equation that ignores internal stress will overestimate stress relaxation during primary creep. The observations also show that separate constitutive equations for creep rates for the primary and secondary regime have to be considered to obtain the stress relaxation rates from load controlled creep data.

8.2.3 Creep damage assessment in plant operation

A number of high-temperature design standards such as ASME III [250], RCC-MR [251]) and high-temperature life assessment procedures such as CRIEPI [252] and R5 [7] outline procedures for quantifying creep deformation in metals during high-temperature creep-fatigue loading. In these codes, creep damage is either expressed in terms of time fraction to rupture or as a fraction of creep ductility exhaustion. A comprehensive review of these approaches can be found elsewhere [253], here some of the findings of the thesis are described in the context of the approaches used in the R5 life assessment code. Using the ductility exhaustion approach, the creep damage per cycle can be calculated using Equation 8.6.

$$d_c^{R5} = \int_0^{t_h} \frac{\dot{\varepsilon}_c}{\varepsilon_f(\dot{\varepsilon}_c, T)} dt \qquad (8.6)$$

Here $\dot{\varepsilon}_c$ is the instantaneous creep strain rate, ε_f is the corresponding creep strain at failure (i.e. the creep ductility) at temperature *T*, as a function of the creep strain rate.

Spindler [254, 255] [253] has conducted extensive creep-fatigue tests with creep dwells starting at various positions of the loading cycle in a few different grades of stainless steel. He reported that life estimation using a ductility exhaustion approach for creep dwells with low initial stresses is overly conservative. This over conservatism increases as the creep dwell initial stress reduces, implying that there is an effect of stress on creep damage which is not currently taken into account by the ductility exhaustion approach [253]. Spindler [253]

formulated a modified version of the ductility exhaustion approach, in which the effect of stress on creep damage is included by considering the creep ductility as a function of both stress and strain rate, as shown in equation 8.7.

$$d_c^{SM} = \int_0^{t_h} \frac{\dot{\varepsilon}_c}{\varepsilon_f(\dot{\varepsilon}_c, \sigma, T)} dt \qquad (8.7)$$

Moreover, it has been shown experimentally [256] that the uniaxial creep ductility of austenitic stainless steels can be represented by Equation 8.8

$$\varepsilon_f = A_1 \exp\left(\frac{P_1}{T}\right) \dot{\varepsilon}_c^{\,n_1}\, \sigma^{-m_1} \qquad (8.8)$$

Here A_1, n_1, m_1 and P_1 are material constants.

In summary, the ductility exhaustion approach calculates creep damage by taking into account the creep strain rate during a dwell and creep ductility as a function of strain rate and temperature. No account of back stress or variation of back stress during creep dwells is taken in the current R5 life assessment procedure. In the above sections, it has already been discussed how the varying back stress state in the material alters the effective stress under which creep damage is occurring. From Equation 8.8, it can be observed that the creep ductility of austenitic steel is a function of both stress and strain rate of the material that is a varying back stress state in the material may significantly affect the creep ductility of this material during creep-fatigue deformation. No experimental work was conducted in this project, quantifying the effect of back stress on the creep ductility due to the limitation of time; but this should form part of future work following this thesis.

Finally, in R5 high-temperature assessment procedure [7] the total damage due to creep-fatigue loading is estimated by linearly adding the damage caused by creep and fatigue, calculated separately. Failure is conceded when the sum of the fatigue and creep damages reaches some failure criterion; in R5 a linear damage summation is used and failure is conceded when $D_c+D_f \geq 1$ [253]. Experimental findings from the cyclic creep tests show that this linear summation approach implicitly ignores the changes in the creep strength and ductility of the material caused by the cyclic loading [257]. Again further investigation in

this area is required to quantify the effect and improve models that can be incorporated into modern high-temperature assessment procedures.

8.2.4 Bauschinger effect

Results of Bauschinger tests conducted using type 316H austenitic stainless steel at room and elevated temperatures are presented in Chapter 5. At various points of tension-compression cyclic loadings, the load was interrupted systematically followed by reloading of the specimen either in the same or the opposite direction. The macroscopic yield stress was found to vary systematically with the magnitude of the interruption strain and the direction of the re-loading. These findings are in good agreement with the published works of Skelton [87] where a number of different alloys (such as 316, IN718, CMSX4, SRR99, Ti-Al etc.) were similarly tested to a different strain range and temperature range (400-1025℃). Therefore, the macroscopic findings for type 316H austenitic steel in this project are transferrable to a number of other polycrystalline materials for a wide range of loading and temperatures. Skelton has also shown that the macroscopic yield stress variation during interrupted cyclic loadings can be roughly predicted using the widely known Ramberg-Osgood [258] power law (Equation 8.9) with careful determination of the constant β from the experimental data.

$$\Delta\sigma = A\Delta\varepsilon_p^{\beta} \qquad (8.9)$$

Here, $\Delta\sigma$ is the stress range, $\Delta\varepsilon_p$ is the plastic strain range and A and β are the constants defining the plastic strength and the strain hardening coefficient respectively.

A wide range of theories (see Chapter 2 for details), mostly phenomenological, have been developed considering the role of changing dislocation structures and inhomogeneous distribution of dislocations in the microstructure in explaining the Bauschinger effect. However, contrasting findings, such as that by Rauch [102] et al. shows that the observed macroscopic reduction of yield stress during reverse loading and corresponding changes of dislocation structures may not be uniquely correlated. The main aim of the experimental work presented in this thesis was to investigate the role of intergranular strain in causing the Bauschinger effect in type 316H austenitic stainless steel.

Intergranular strains were measured in a number of differently oriented grain families after various load interruptions in tension and compression. The residual intergranular strains in the plastically 'weaker' and 'stronger' grain families were correlated with the observed changes of macroscopic yield stress arising from the load interruptions. Yielding in the plastically weaker grain families initiated macroscopic yielding. It has been experimentally shown that, during tensile reloading, with the increase of compressive residual strains in this grain family, the macroscopic tensile yield stress increases. Conversely during compressive reloading, with the increase of tensile residual strains in the grain family, the macroscopic compressive yield stress increases and vice versa. This is because the applied stress has to first overcome the 'extra' residual strains in this grain family (compared to a virgin specimen) before starting to deform in the normal manner.

The role of intergranular strains of opposite sense in the plastically stronger grain families was also investigated. It has been shown that intergranular strains in this and other grain families contribute to the changing shape of the elastic to the plastic transition of the macroscopic stress-strain curve. This shape was found to be sharpened (grains with different orientations yielding within a shorter range of stress-strain change) with decreasing difference in the yield stress of the differently oriented grain families, for example due to accumulation of tensile residual strains in the plastically weaker grains and compressive residual strains in the plastically stronger grains, before a tensile reloading. On the other hand, this shape was found to be increasingly smoother (grains with different orientations yielding within a longer range of stress-strain change) with increasing difference of the yield stress, for example due to accumulation of tensile residual strains in the plastically weaker grains and compressive residual strains in the plastically stronger grains, before a compressive reloading. This finding is consistent with recently published work [118].

This interpretation of the intergranular strains playing a dominant role in causing the Bauschinger effect in type 316H stainless steel can be equally applicable to other polycrystalline materials with a FCC crystal structure and particularly material which deforms solely by slip. Measurement of intergranular strains in Aluminium [259] and Nickel superalloy [260] for example are reported to show the generation of a similar degree of intergranular strains during plastic loading. Moreover, intergranular strains were also investigated in detail in carbon steel with a BCC crystal structure [207], in which the

interpretation can be further extended to. Accurate prediction of the Bauschinger effect is considered a litmus test for the validity of strengthening theories [117]. The experimental data set for room and elevated temperatures presented in this thesis can be utilised to validate crystal plasticity and elastic plastic self-consistent models accounting for kinematic hardening of materials.

8.2.5 Creep cavitation studies

SANS and HS-AFM techniques were employed to study cavitation development in interrupted creep specimens of type 316H austenitic stainless steel. The SANS technique was found capable of non-destructively measuring creep cavities, evident from the measure of systematic increase in the number and volume fraction of creep cavities with the increase in the creep strain in the specimens. However, the measurements of cavities using SANS were limited to a size below 350 nm diameter which does not cover the total size range of cavities expected in this material. Nevertheless, it has been shown [75] that a large population of creep cavities of size ~500 nm diameter dominate the development of creep damage in type 316H austenitic steel for uniaxial creep deformation whereas the population of cavities in the size range of ~1000 nm to 2400 nm diameter is much smaller. The number density vs diameter plot presented in Figure 7-7 shows the similar decay in number of cavities with increasing diameter size. Therefore, the SANS results presented here provide a reasonably good measure of underlying creep damage [76]. This technique has great potential for quantitative measurement of the creep cavities which can be used to develop better creep damage models. However, in order to obtain the complete picture of creep cavity damage, complementary measurement techniques, for example FIB serial sectioning and Ultra-High Resolution SANS need to be applied.

HS-AFM was used to qualitatively observe the shape and size of creep cavities measured using the SANS. The observed irregular facetted shape of cavities associated with grain boundaries and secondary particles highlights the over-simplification of current models that are used to predict the lifetime of components based on nucleation and growth of spherical cavities [241].

8.3 Part 2: Limitations of experimental facilities

8.3.1 Creep-fatigue studies at central facility neutron beamlines

A major limitation of the creep results presented in this thesis is that the secondary or minimum creep rate for each test was calculated from data acquired during very short duration creep dwells. By keeping the loading parameters consistent, it was possible to observe the effect of intergranular strains on the creep deformation rate. But the short creep dwells examined may not represent the length of creep dwells experienced by operating power generating plant. In such engineering applications, structures are exposed to high-temperature conditions for tens of years (not days) and experience thousands (not tens) of complex load cycles. For practical reasons, test acceleration methods have to be applied where unrealistic high stresses are used or high temperatures or both. But when the duration of experiments is restricted to a few hours, there are strong grounds for challenging the credibility of the acceleration strategy.

The necessity of testing over short duration creep dwells was constrained by the beam time awarded for the neutron diffraction experiments (at most consecutive 5 days). Access to expensive neutron beam time at any Central Facility in the world is highly competitive. This limits the scope and relevance of creep tests that can be performed and investigated under complex load-history representative of plant components under service operating conditions. The remainder of this chapter discusses the engineering limitations of using neutron beamlines to carry out in-situ longer term mechanical studies of material at high temperature and proposes a solution to overcome the issues identified.

As described in Chapter 7, one way to overcome the issue of conducting overly accelerated creep tests is to conduct ex-situ creep tests in a conventional laboratory and then to measure the intergranular strains at various times (or life fractions), or the volume fraction of cavities, by interrupting the test, or by testing a set of identical specimens at different life fractions. Successful ex-situ measurements tracking the evolution of intergranular strains are reported in the literature, for example in [136, 137], and successful measurements of creep cavities are presented in chapter 7 of this thesis. However, ex-situ experiments have a number of limitations including, the preservation of the internal stress state upon load interruption and

the challenge of precisely measuring the stress-free lattice parameters in the case of materials with complex service loading history.

The study of intergranular strains poses additional challenges because to fully understand the generation and evolution of intergranular strains in a polycrystalline material, it is required to measure the strain response of multiple grain families simultaneously. This requirement limits the study of intergranular strains to polychromatic neutron diffraction instruments where simultaneous measurements of deformation in multiple oriented grains are possible. Moreover, in order to conduct in-situ measurements, a robust high-temperature testing rig is necessary. This essentially limited the work described in this thesis to polychromatic facilities offering suitable loading and heating facilities. In fact, the Engin-X neutron diffractometer is the only instrument in Europe which currently has such facilities available. Considering the limited availability of polychromatic neutron diffraction instruments, an alternative monochromatic instrument, SALSA was also used for experimentation in this project. The SALSA [261, 262] neutron strain analyzer is one of the 40 instruments belonging to the Institut Laue Langevin (ILL) central neutron facility.

In SALSA, the double focussing monochromator coupled with the ILL reactor provides high neutron flux and thus enables rapid measurements with excellent penetration [263] depth. Being monochromatic, at any frame of time, strain in the grains oriented only in one orientation can be measured using this instrument. However, unlike the Engin-X instrument, the detector in the SALSA instrument is movable; therefore, lattice strains in variously oriented grains can be measured one after another by moving the detector by known distances. A much shorter counting time of 2 minutes can be used to achieve a satisfactory diffraction peak compared to the time 5-6 minutes needed at the Engin-X instrument. Therefore, using this instrument, although the measurements in variously oriented grains cannot be collected simultaneously, they can be measured sequentially within a small time frame by moving the detectors. This gives the instrument the capability to study intergranular strain, particularly for slow deformation process, such as creep.

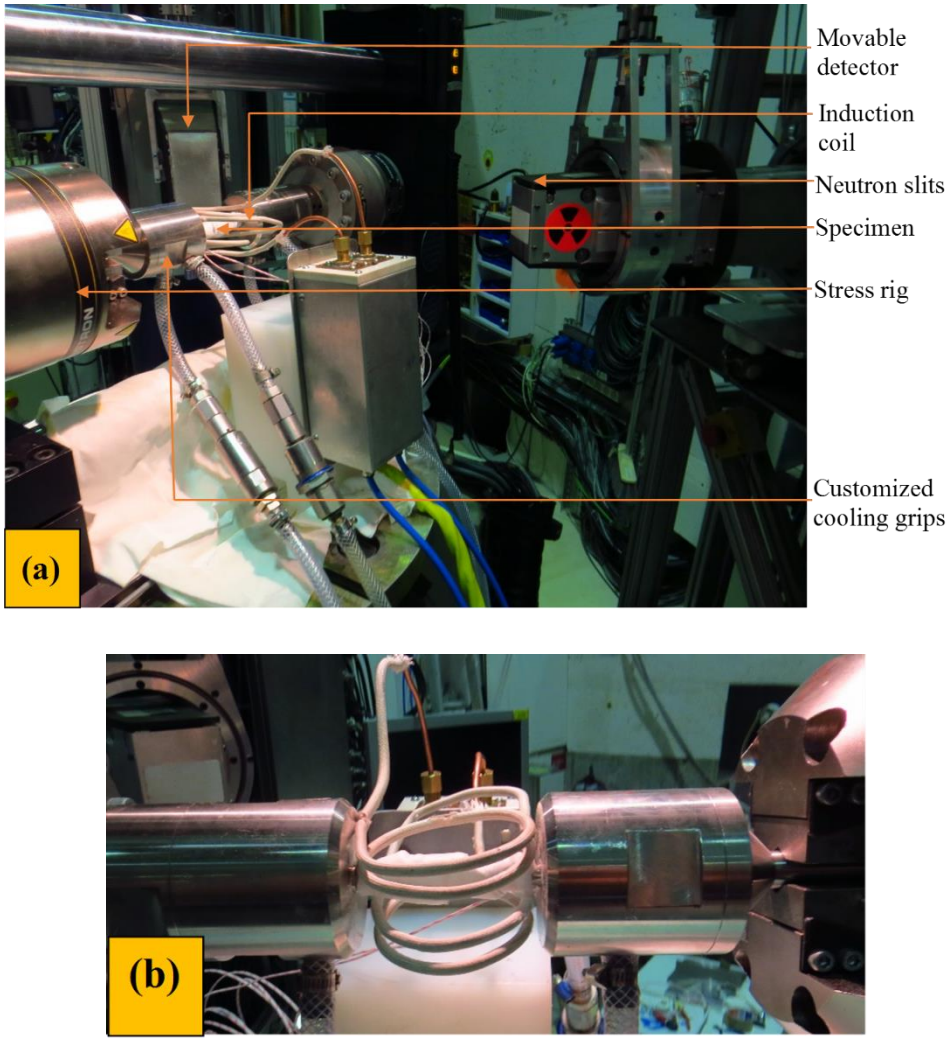

Figure 8-2 (a) Experimental set-up for high-temperature in-situ neutron diffraction testing at the SALSA instrument. (b) The induction coil around the specimen (covered in zirconia fibre for better thermal stability) shows the space limitation for extensometer attachment in the gauge length of the specimen.

A set of creep-fatigue tests was conducted using the instrument. The aim of the tests was to investigate the changes of intergranular strains during load control creep deformation during intermediate creep dwells. Responses from 3 different orientations of grains in the material (the {200}, {220} and {311} grain families), were recorded one after another by systematically moving the detector. In this section, the limitations of the in-situ testing facilities and their effects on the measured neutron data are discussed, rather than the actual findings from the experiment.

The SALSA instrument has a dedicated stress rig with the capability of conducting room temperature tension-compression cyclic loading. The instrument does not have any

dedicated furnace to conduct high-temperature tests. An in-house custom built induction coil was improvised by the experimental team for this particular set of tests. An image of the experimental set-up is shown in Figure 8-2 (a). The temperature of the specimen was monitored using 2 N-type thermocouples attached to the gauge length of the specimen. A PID controller was used to control the power output of the induction system to maintain the temperature of the specimen. The specimens were wrapped with zirconia fibre in order to achieve better temperature control. The maximum resolution of the temperature control achieved was ±5℃.

The results of the experiment showed that the high flux and resolution of this instrument makes it possible to study intergranular strains in differently orientated grains with reasonable accuracy compared with the Engin-X facility. However, large scatter in the data was observed due to the poor temperature control achievable using the induction heating system. Measurement of elastic strain in the material is highly sensitive to temperature, therefore a slight variation of temperature in the specimen can give rise to a significant variation in the scatter of neutron lattice strain measurements. In fact, this scatter was so large that any meaningful interpretation of the data in terms of change of intergranular strains during creep dwell was impossible to make. Moreover, as can be seen in Figure 8-2 (b), due to the limited space available adjacent to the specimen gauge length and the use of the zirconia fibre wrap, it was not possible to use an extensometer to measure the macroscopic strain directly from the gauge length of the specimen. Therefore, the strain in the specimen had to be measured from the recorded change of distance between the cross heads of the stress rig. This again increased the error in macroscopic strain measurement, because the change in the distance between the cross heads of the stress rig arises not only from the specimen's strain but also from the finite stiffness of the rest of the load train. In summary, with this experimental set-up in this instrument, it was not possible to acquire experimental data with reasonable accuracy due to large fluctuations in the temperature of the specimen and lack of suitable extensometry. Robust heating, temperature control, strain measurement and data recording systems are required in order to obtain meaningful test results from an in-situ high-temperature loading test.

8.3.2 Proposed Creep-fatigue rig for longer term tests at neutron beamlines

Based on the above discussion, it is clear that equipment currently available at central neutron facilities restricts the study of creep and creep-fatigue deformation to either ex-situ measurements of questionable accuracy or in-situ measurements of the overly accelerated tests. Changes of internal strains in the material during creep deformation are often slow, which means that continuous neutron measurement throughout a creep test is not necessarily required. Measurements at regular intervals or when a noticeable change occurs in macroscopic deformation can be sufficient to characterize the kinetics of internal stress evolution. Based on such a rationale, a specification for building a novel creep-fatigue stress-rig was developed by the author during the early part of the Ph.D. project, in close collaboration with the ISIS facility. A portable creep-fatigue stress rig was specified for longer term creep tests that could be conducted outside the neutron beamline, for example in a hutch next to the neutron instrument. The stress rig would then be moved intermittently into the neutron beamline using an overhead crane for in-situ measurements, whilst keeping the tests running. Details of the specification development work can be found elsewhere [264]. A short description of the work is provided here.

The proposed stress rig was configured for the Engin-X instrument and other instruments at the ISIS Facility where longer term high-temperature tests are of interest, for example, Sans2D [78, 237, 238, 265]. Small Angle Neutron Scattering (SANS) can be used to characterize the distribution and evolution of creep cavities and precipitates in engineering materials. A neutron imaging and diffraction instrument, IMAT, has recently been built at the ISIS facility to study engineering materials and processes. IMAT offers a combination of imaging and spatially resolved diffraction modes with capabilities of neutron radiography, neutron tomography, energy-selective imaging, neutron strain scanning, crystallographic structure, phase, and texture analysis [266]. IMAT has just come into operation and initially will use the in-situ testing capabilities of the Engin-X instrument. Another motivation for developing the new rig was to allow measurements on all three above mentioned neutron diffraction instruments, thereby enriching the scope of scientific output that could be delivered. For example, ENGIN-X was specifically designed for residual stress mapping but there is a growing demand for 3-dimensional tomography studies for which ENGIN-X is not

optimized [4] and therefore the ability to undertake such complementary measurements in the newly built IMAT instrument would be very useful.

The principal requirement for the stress rig was for it to be transported in and out of the beamline without affecting the stress, strain, and temperature of the live high-temperature test. The rest of the specification for the rig was developed considering a number of factors such as the users' requirements, the availability of technologies, the limited space in the beamlines etc. Table 8-1 summarizes the specifications developed for the rig for which more detail can be found in [264]. Potential suppliers were invited to tender to build the new rig but the budget available was insufficient to cover the design innovation and build requirements.

Table 8-1 Summary of the specifications developed for the novel testing rig in order to conduct intermittent measurement of intergranular strain by neutron diffraction during longer term creep-fatigue tests.

Specifications	**Minimum requirements**	**Optimum requirements**
Test facilities	Uniaxial tension and compression	Tomography capability
Max. loading capacity	10 KN	25 KN
Loading rate	Static loading rate 20 N/s to 1000N/s and max. cyclic loading rate 0.1 Hz.	Same as minimum
Control required	Stress, strain and displacement	N/A
Strain measurement	Non-contact laser extensometer	N/A
Max. temperature	1000^0 C	1500^0 C
Heating rate	0.03^{o}C/min to 60 ^{o}C/min	Same as minimum
Max. Frame dimension	As small as possible	800 × 600 × 500 mm

Max. Frame weight	As low as possible	50 kg
Other requirements	• The furnace and any parts of the heating system must not impede neutrons in or out of specimen • Removable Inert gas (e.g. argon) chamber or vacuum facility with capacity of 1 mbar vacuum or less • The furnace should be detachable from the stress rig	

In summary, development of a new custom designed "portable" rig would open opportunities for performing longer term creep-fatigue tests with intermittent in-situ material state monitoring at neutron beamlines. This capability would enable researchers to study the longer term behavior of engineering materials using more realistic test conditions. Moreover, the portable creep-fatigue stress rig could be used for measurements using a variety of neutron instruments thereby enriching the scientific outcomes. The instrument scientists of each of these three instruments were involved in this collaboration work between the RAL, ISIS, and the Open University. The author of this thesis has developed the specifications of the stress rig and authored the rationale, in the supervision of Professor John Bouchard of the Open University and Dr. Shu-Yan Zhang of the RAL, ISIS facility.

8.4 Summary

The first part of this discussion chapter has evaluated and discussed findings arising from the creep-fatigue studies presented in the thesis. The influence of varying back stress during tension-compression cyclic loading, relaxation of intergranular strains during displacement controlled stress relaxation tests, and an increase of intergranular strains during primary creep regime during load controlled creep deformation of type 316H austenitic steel have been reviewed in relation to creep rate and stress relaxation rate estimation. The significance of the findings is discussed in relation to widely used analytical creep equations and damage assessment procedures for creep deformation. The second part of the chapter discusses the challenges of conducting in-situ creep tests at neutron beamlines. The importance of having fully instrumented, well controlled, in-situ testing capabilities is also described. Finally, the

rationale for developing a novel creep-fatigue stress-rig is described and outline specifications are defined. Building such a new rig would increase UK capability for undertaking novel creep studies with in-situ monitoring in different types of neutron beamlines without having to excessively accelerate the tests.

Chapter 9 Overall conclusion and future work

9.1 Overview

The aim of this thesis is to enhance understanding of the generation and evolution of back stress in type 316H austenitic stainless steel during mechanical deformation at room and high temperature (up to 650 ^{o}C). In Chapter 1, the relevance of the work is described in relation to practical engineering applications such as improving life assessment procedures for power plant components in service. A thorough literature review of the field has been conducted and knowledge gaps highlighted. Plans for a set of experiments were formulated to address the research gaps. The experimental techniques and procedures used are described in detail in Chapter 3. In the first set of experiments, the generation and evolution of intergranular strains was measured in-situ by neutron diffraction during tension, compression, load-unload and cyclic loadings at room temperature and at 650 ^{o}C. Strain controlled symmetric loading cycles were chosen to represent those experienced by material in power generation plant components during real life service. The results obtained from this set of experiments formed the basis for later experimental investigations about the effect of intergranular strains on the creep and cyclic deformation of type 316H austenitic stainless steel. The test results from all the experiments are discussed in detail and their significance described. In this chapter, overall conclusions from the work are described, limitations highlighted and future research opportunities suggested.

9.2 Experimental techniques

Suitable techniques for measuring internal stresses in crystalline materials have been reviewed in Chapter 3. The suitability of a measurement technique to measure internal

stresses was found to depend on the length scale of measurement required, type of measurement (destructive or non-destructive), resolution of measurement and availability of the technique. Microscope-based techniques, for example, those based on TEM imaging are found to be more suitable for studying intragranular strains because of their high spatial resolution, but are limited by sampling small areas of material. Moreover, microscope based techniques are often laborious and prone to errors introduced by multi-step specimen preparation. Diffraction techniques on the other hand have the capability of measuring grain averaged internal strains in groups of grains with a similar orientation distributed through a gauge volume of tens of cubic millimetres. Neutron diffraction technique, in particular, has the unique capability of studying intergranular stresses in the bulk of the material.

9.3 Material characterisation

Most of the experimental work reported has been carried out using Type 316H stock bar (Material B). The material was solution heat treated at 1050℃ for 1 hour followed by water quenching before extracting test specimen from those. The material has an average grain size of 71 ± 4 μm and hardness of 120 ± 7 HV in the solution heat treated condition. The material is found to have a weak texture with a maximum MUD of 2.22. A few preliminary tests were conducted on Material A, extracted from an ex-service steam header supplied by the EDF Energy.

9.4 Generation and evolution of intergranular strain

The following conclusions relating to the generation of intergranular strains in type 316H austenitic stainless steel during mechanical deformations at room temperature and at 650℃ follow from the experimental work described in this thesis:

- During elastic deformation, grains with different orientations deform differently as a function of their specific crystallographic elastic stiffness. Intergranular strains generated purely from elastic deformation are small; however, elastic anisotropy of

grains play a strong role in the generation of intergranular strains during elastic-plastic transition and plastic deformation.

- Significant intergranular strains start to generate when slip systems in some grains get activated while other grains are still deforming elastically that is during transition from elastic to plastic deformation in the material.
- The magnitude of intergranular strains increases with increasing subsequent plastic deformation in the material, particularly in the {200} and {220} grain families. During room temperature deformation, the increase in intergranular strains was found to be almost a linear function of plastic strain (up to the maximum level of 17.5% tested); however, during similar tests conducted at 650°C, the increase of intergranular strains during tension and compression loading was found to saturate after about 8% of macroscopic strain.
- During uniaxial loading at room and high temperature, the {200} grain families accumulated maximum lattice strains and the {220} and {111} grain families accumulated least. The {311} grain families accumulated lattice strains similar to the average predicted by Rietveld refinement analysis; the resemblance being closer at room temperature tests than at high temperature.
- During tension loading, the {200} grain families were found to accumulate tensile intergranular strains and the {220} grain families to accumulate compressive intergranular strains and vice versa for compression loading.
- During isothermal strain controlled cyclic deformation (±1% strain range) at room and high temperature, intergranular strains were found to increase with repeated cycling, again, the increase being greatest for the {200} and the {220} grain families.
- During cyclic loading, intergranular strains for any specific grain family do not change sign (compression to tension and vice versa) at the same time as the macroscopic loading, rather, it starts changing when the material starts to plastically deform macroscopically in the reverse direction. The {200} grain family was found to be the most responsive of the grain families to these changes, accumulating

maximum tensile intergranular strain at macroscopic tensile peak strain and maximum compressive intergranular strain at macroscopic compressive peak strain.

- During tension-compression cyclic loading, the magnitude of intergranular strain is not a function of total strain / stress in the material, that is, at an identical stress / strain, the magnitude of intergranular strains could be very different depending upon the loading path history.

9.5 Effect of back stress on load controlled creep deformation

Effect of back stresses on the creep deformation of type 316H austenitic steel was studied at 650°C, by introducing 3 load-controlled creep dwells at different positions during a tension-compression cycle at an identical applied stress but with varying states of internal stress. The intergranular and intragranular component of back stresses were studied separately using in-situ neutron diffraction and transmission electron microscopy (TEM) respectively. The state of back stresses at the beginning of each creep dwell and subsequent evolution during the load-controlled creep dwell were recorded. The effect of different back stress states on the minimum creep deformation rate was quantified. The following conclusions can be reached from these studies:

- The back stress due to intergranular stresses has a significant effect on the macroscopic minimum creep rate of type 316H austenitic stainless steel; the minimum creep rate was found to decrease with an increase in magnitude of intergranular strain in the material at the beginning of the creep dwell.
- TEM observations showed that cell type dislocation substructures were not formed in the earlier stages of creep deformation in type 316H stainless steel tested, that is intragranular stresses do not contribute significantly to back stress during this earlier stage of creep deformation of this material at 650°C.
- During load controlled creep dwells, intergranular strains increased during the primary creep stage but remained almost unchanged during secondary creep deformation; this suggests that evolution of intergranular strains is related to the change in the dislocation density in the material, as dislocation density changes

significantly only during primary creep. However, the creep dwells conducted were indeed very short in duration and further observations during longer creep dwells is required to confirm the finding of the unchanged IR strains during the secondary creep regime.

9.6 Displacement controlled creep deformation

Displacement controlled creep dwells were introduced at peak tensile strains of tension-compression cyclic loadings (±1% strain range) at 650°C. Corresponding changes in the magnitude of stress and intergranular strains were recorded in-situ for a number of dwells with repeated cyclic loading. Moreover, the loading was started in compression in one test instead of tension to evaluate the effect of this variation on intergranular strain generation in various grain families. The following conclusions can be reached from the study.

- During displacement controlled creep deformation, intergranular strains relax significantly with relaxation of the macroscopic stress. Therefore, the simplistic assumption taken in calculation of load controlled creep properties from stress relaxation data that the creep strain during stress relaxation arising completely from the relaxation of elastic strain is not valid.
- The similarity in the trends of relaxation of the microscopic IR strains and the macroscopic stress suggests, magnitude of IR strains relaxation is a function of the magnitude of macroscopic stress relaxation. The relaxation of intergranular strains in the {200} grain families is significantly larger compared to other grain families.
- Starting loading in compression instead of tension does not have any significant effect on the generation of intergranular strains or orientation of the grain families which accumulate tensile and compressive intergranular strains.

9.7 Intergranular stresses during cyclic loading

The effect of intergranular strains on the change of yield stress during tension-compression cyclic loading f type 316H austenitic stainless steel was studied at room and high temperature (650° C). Strain-controlled cyclic tension-compression tests (strain range of ±1%) were conducted with systematic interruptions under compression and tension loads. The yield stress of the reverse cycle either in the same or opposite directions was measured and subsequent changes in the intergranular strains were recorded using in-situ neutron diffraction. The main findings from the experimental work are:

- During tension-compression cyclic loading of AISI type 316H austenitic stainless steel, only transient softening and no permanent softening was observed on the reverse loading for both room and high temperature deformation cases.
- The tensile yield stress of Type 316H stainless steel decreased with an increase in compressive interruption strain and increased with an increase in tensile interruption strain. Compressive yield behaviour showed similar history dependence in the opposite sense that is, it increased with an increase in compressive interruption strain and decreased with an increase in tensile interruption strain. The findings are similar for both room temperature and high temperature tests.
- The magnitude of intergranular strains in the plastically weaker, stronger and average grain families showed a strong correlation with the observed variation of the yield stress during the reloading. The correlation is worse for the high-temperature tests which can be attributed to activation of high temperature non-slip based deformation mechanisms and measurement variables such as, anelastic strain recovery and peak shape broadening during measurements.
- The intergranular strains at the peak macroscopic tensile and compressive strain tips of the cycle (±1%) reach a saturated magnitude irrespective of the interruption strains. This observation of near constant intergranular strain is consistent with the observation of zero permanent softening in the material at the peak strain irrespective of the interruption strains.

- These strong correlations imply that the intergranular strains generated due to the anisotropic deformation of the grains play the most dominant role causing the Bauschinger effect in this material. This differs from the classical dislocation based explanation of this phenomenon.
- Compared to the room temperature tests, the intergranular strains in various grain families are found to be more evenly distributed among differently oriented grain families at high temperature. This difference in the distribution of the intergranular strains can be attributed to the activation of different deformation mechanisms at high temperatures, such as dislocation glide or glide plus climb processes.
- An anelastic recovery was noticed for the high-temperature tests during the dwell time for neutron measurements in the unloaded state after various interruptions. The anelastic strain after compression interruption was positive and after tensile interruption was negative. The magnitude of the anelastic strains varied depending upon the degree of compressive or tensile plastic deformation before unloading.
- It was experimentally inferred that initiation of macroscopic yielding in type 316H stainless steel occurs by the yielding of the plastically weaker grain families, for example the {220} grain family. In the case of tension-compression cyclic loading the magnitude and sign of IR strains in these weaker grain families determines the macroscopic yield stress of the material under subsequent loading.
- During tension reloading, after tension interruptions, macroscopic yielding occurred sharply and after compression interruptions, it occurred smoothly. Sharp yielding occurred, when the differences between the yield stresses of various grain families are reduced due to the plastically weaker grain families possessing compressive IR strains and plastically stronger grain families possessing tensile IR strains. Conversely, smooth yielding occurs when the differences between the yield stresses of different grain families' increases due to possessing IR strains of opposite sense. A similar observation in the opposite sense was made during compression reloading.

9.8 Measurement of creep cavitation

1. Size and volume fraction of creep cavities were measured quantitatively in two sets of creep interrupted specimens of type 316H stainless steel using SANS.

2. In general two population of creep cavities were observed; one population with diameters in the range of 10-120 nm, and the other population with a diameter in the range of 130-350 nm. The volume fraction of the smaller diameter cavities are found to increase systematically with the increase of the creep strain in the samples for both sets of creep interrupted specimens.

3. Complementary qualitative imaging of few of the samples were conducted using HS-AFM. The size distribution of the carbides and cavities observed in these images are found to be in good agreement with the SANS results. The sets of results are also in good agreement with the published results of quantitative metallography and other SANS results on this material.

4. In HS-AFM images, smaller sized carbides are found to be mostly dispersed in the matrix and the larger sized carbides are found to be dispersed in the grain boundaries of the microstructures in the samples. The creep cavities are found to be of irregular shapes and closely linked with the carbides in the grain boundaries.

5. Intergranular strains were measured ex-situ using same sets of interrupted creep specimens, however, no conclusive results were obtained due to the limitation of correct d0 measurement of the stress-free sample and increasing uncertainties of the internal state of the specimen due to those complex service and loading history.

9.9 Suggestions for future work

The work reported in this thesis lays the foundation for studying the effect of back stress on the mechanical deformation of materials. The findings can be extended in a number of ways, as proposed below.

- The evolution of intergranular strains has been studied for Type 316H austenitic stainless steel with a FCC crystal structure. Similar studies could be conducted examining other materials, for example with a BCC crystal structure.
- The experimental work presented in this thesis shows how intergranular stresses affect the creep rate of Type 316H austenitic steel for the case of short duration creep dwells when the contribution of intragranular stresses to the back stress is not significant. However, in real life, plant is exposed to longer term creep deformation dwells, where if the high temperature is sufficiently high, dislocation structures can re-arrange themselves into cell type structures which can add to the magnitude of back stress. In order to assess the effect of back stress on overall creep life of materials, a combined effect of intergranular and intragranular stresses needs to be taken into account which requires further work characterising the evolution of back stress during longer duration creep dwells.
- Some life assessment methods (such as the R5 High Temperature Procedure) use creep ductility (strain at failure) to assess the remnant creep life of structures. In this project the effect of back stress on creep deformation rate alone has been investigated. We do not know how the creep ductility may have been modified, although it is well known that plastic history has a major influence. This needs to be quantified for back stress to be allowed for in new lifetime assessment methods. A programme of work is required to characterise creep ductility as a function of back stress.
- The creep deformation mechanism examined in this thesis is related solely to dislocation dynamics. Accelerated creep tests had to be conducted under much higher stress than material would experience under typical service operating conditions to facilitate in-situ neutron diffraction monitoring (at best 5 days of continuous neutron beam time can be accessed). If the proposed novel stress rig for the ENGIN-X neutron diffractometer is built (see Chapter 5), much longer creep tests under more realistic stress conditions could be conducted. This could widen the field of study to

include the evolution of intergranular and intragranular stresses during diffusion based creep.

- Constitutive models for kinematic hardening of materials could be improved that take into account the effect of intergranular strains on the yielding of material. The results of the cyclic interrupted tests at room and elevated temperature can be used to validate such models.
- The texture of material can have a significant effect on the generation of intergranular strains during plastic and creep deformation as well as the multi-axial stress state at the macroscopic level. These effects could be studied through a combination of in-situ neutron diffraction experiments and in-situ experiments in a scanning electron microscope using EBSD (to characterise grain orientations and dislocation structures) and digital image correlation (DIC) to map grain to grain inelastic strains. The experimental work would need to be supplemented by self-consistent elasto-plastic analysis and crystal plasticity modelling.

Chapter 10 Key Findings

- During isothermal strain controlled cyclic deformation (±1% strain range) at room and high temperature, intergranular strains were found to increase with repeated cycling, the increase being greatest for the {200} and the {220} grain families. The magnitude of this intergranular strain is not a function of total strain / stress in the material, that is, at an identical stress / strain, the magnitude of intergranular strains could be very different depending upon the loading path history.
- In both room and high temperature Bauschinger tests, a strong correlation was observed between the intergranular strains and the change of macroscopic yield and peak stresses. This implies that intergranular stress is the primary source of the origin of Bauschinger effect in type 316H austenitic steel.
- Magnitude and direction of intergranular strains can significantly affect the macroscopic creep deformation rate of type 316H stainless steel; the minimum creep rate was found to decrease with an increase in magnitude of intergranular strain in the material at the beginning of the creep dwell.
- The intergranular strains were observed to relax as a function of the macroscopic stress relaxation during displacement controlled creep. In case of load controlled creep, the intergranular strains were observed to increase during primary creep and remain almost unchanged during secondary creep.
- Small angle neutron scattering (SANS) and high-speed atomic force microscope (HS-AFM) are found to be two innovative new techniques, capable of quantifying creep damage in steel.

Bibliography

1. Statistics, N., *Energy Trends: electricity*, E.I.S. Department for Business, Editor. 2016.
2. *Nuclear Power in the United Kingdom*. 2016 [cited 2016 21/10/2016]; Available from: http://www.world-nuclear.org/information-library/country-profiles/countries-t-z/united-kingdom.aspx.
3. Houlton, N., *Life Extension of the EDF Energy Nuclear Fleet*. 2013, EDF Energy.
4. KCB, S.A.M., *Nuclear power in the UK*. 2016, National Audit Office.
5. Nix, W.D., J.C. Gibeling, and K.P. Fuchs *The role of long -range internal back stresses in creep of metals*. ASTM special technical publication, 1982. 301-321.
6. Feaugas, X., *On the origin of the tensile flow stress in the stainless steel aisi 316l at 300 k: back stress and effective stress.* Acta Materialia, 1999. **47**(13): p. 3617-3632.
7. *R5, Assessment Procedure for the High Temperature Response of Structures*. 2014, EDF energy nuclear generation Ltd.
8. Bhadeshia, H., *Steels: Microstructure and Properties*. 2006, Oxford: Elsevier Ltd.
9. Abe, F., T. Kern, and R. Viswanathan, eds. *Creep-resistant steels*. 2008, Woohead Publishing Limited: Washington DC.
10. Marshall, P., *Austenitic stainless steels: Microstructure and mechanical properties*. 1984, Essex: Elsevier Applied Science.
11. Higgins, R.A., *Engineering Metallurgy part I*. 1993, Great Britain: Arnold.
12. Weiss, B. and R. Stickler, *Phase instabilities during high temperature exposure of 316 austenitic stainless steel.* Metallurgical Transactions, 1972. **3**(4): p. 851-866.
13. McGuire, M.F., *Stainless steels for design engineers*. 2008, Ohio: ASM International.
14. Lai, J.K.L., *A study of precipitation in AISI type 316 stainless steel.* Materials Science and Engineering, 1983. **58**(2): p. 195-209.
15. Tsakiris, V. and D.V. Edmonds, *Martensite and deformation twinning in austenitic steels.* Materials Science and Engineering A, 1999. **273**(275): p. 430-436.
16. Schmid, E. and W. Boas, *Plasticity of crystals*. 1950: Hughes & Co.
17. Peierls, R., Pro. Phys. Soc., 1940. **52**(34).

18. Oliver, E.C., *The generation of internal stresses in single and two phase materials*, in *Materials Science Centre*. 2002, University of Manchester: Manchester.
19. Hull, D. and D.J. Bacon, *Introduction to dislocations*. 4th ed. 2001: Butterworth-Heinemann.
20. C.B.Carter, M.G.N., *Ceramic materials: science and engineering*. 2007: Springer.
21. jr., W.T.R., *Dislocations in crystals*. 1953, New York: Mcgraw-hill book company.
22. Warren, B.E. and E.P. Warekois, Acta Metall., 1955. **3**.
23. G.E.Dieter, *Mechanical metallurgy*. 3rd ed. McGraw-Hill series in materials science and engineering. 1986: McGraw Hill.
24. Washko, S.D. and G. Aggen, *Wrought Stainless Steels*, in *ASM Handbook: Properties and Selection of Irons, Steels and High Performance Alloys*. 1992, ASM International: Ohio. p. 2049.
25. Crampin, S., et al., *The calculation of stacking fault energies in close-packed metals.* j. Mater. Res., 1990. **5**(10).
26. Frank, F.C. and W.T.R. Jr, *Multiplication Processes for Slow Moving Dislocations.* Physical Review 1950. **79**(4): p. 722-723.
27. Schoeck, G. and R. Frydman, *The Contribution of the Dislocation Forest to the Flow Stress.* physica status solidi (b), 1972. **53**(2): p. 661-673.
28. Hirth, J.P. and J. Lothe, *Theory of Dislocations*. 2nd ed. 1982, Malabar, Florida: Krieger Publishing Company.
29. Tilley, R.J.D., *Understanding solids: the science of materials*. 2004: John Wiley & Sons Ltd.
30. Seeger, A., *Dislocations and Mechanical Properties of Crystals*. 1957, New York: John Wiley & Sons, Inc.
31. Mughrabi, H., *Dislocation wall and cell structures and long-range internal stresses in deformed metal crystals.* Acta Materialia, 1983. **31**: p. 1367-1379.
32. Sachs, Z., Ver. Dtsch. Ing., 1928. **72**.
33. Taylor, G.I., J. Inst. Metals, 1938. **62**.
34. Bishop, J.W.F., Phil Mag, 1953. **44**.
35. Bishop, J.W.F. and R. Hill, Phil. Mag., 1951. **42**.
36. Bishop, J.W.F. and R. Hill, Phil Mag, 1951. **42**.
37. Delannay, L., *Observation and modelling of grain interactions and grain subdivision in rolled cubic polycrystals*. 2001, Katholieke universiteit leuven.
38. Hutchinson, J.W., *Elastic-plastic behaviour of polycrystalline metals and composites.* Proc. Roy. Soc. Lond. A., 1970. **319**: p. 247-272.
39. Lin, T.H., *Analysis of elastic and plastic strains of a face-centered-cubic crystals* J. Mech. Phys. Solids, 1957. **5**: p. 143.

40. Clausen, B., T. Lorentzen, and T. Leffers, *Self-consistent modelling of the plastic deformation of f.C.C. Polycrystals and its implications for diffraction measurements of internal stresses.* Acta materialia, 1998. **46**(9): p. 3087-3098.

41. Kroner, E., *Zur plastischen verformung des vielkristalls.* Acta Metall., 1961.

42. Budiansky, B. and T.T. Wu. *Theoretical predictions of plastic strains of polycrystals*. in *Proc. 4th U.S. Nat. Congr. Appl. Mech.* 1962. New York: ASME.

43. Hutchinson, J.W., *Plastic stress-strain relations of F.C.C. polycrystalline metals hardening according to Taylor's rule.* J. Mech. Phys. Solids, 1964. **12**: p. 11-24.

44. Eshelby, J.D., *The determination of the elastic field of an ellipsoidal inclusion, and related problems.* Proc. R. Soc. Lond. A, 1957. **241**: p. 376-396.

45. Hill, R., J. Mech. Phys. Solids, 1965. **13**: p. 89-101.

46. R. W. Evans, B.W., *Introduction to creep*. 1993, London: The Institute of materials.

47. Lagneborg, R., *Int. Metall. Rev.* 1972. **17**: p. 130-146.

48. K. L. Murty, I.C., *J. Nucl. Mater.* 2008. **383**: p. 189-195.

49. Monkman, F.C., & Grant, N. J., Proc. ASTM, 1956. **56**: p. 593.

50. G. Sposito, C.W., P. Cawley, P. B. Nagy, C. Scruby, *A review of non-destructive techniques for the detection of creep damage in power plant steels.* NDT&E International, 2010. **43**: p. 555-567.

51. H. J. Frost, M.F.A., *Deformation mechanism maps*. 1982, Exeter: Pergamon.

52. Herring, C., *Diffusional Viscosity of a Polycrystalline Solid* Journal of applied physics, 1950. **21**(5): p. 437-445.

53. Coble, R.L., *A Model for Boundary Diffusion Controlled Creep in Polycrystalline Materials* Journal of applied physics, 1963. **34**(6): p. 1679-1682.

54. Kassner, M.E., *Fundamentals of Creep in Metals and Alloys*. 2nd ed. 2009: Elsevier.

55. Wilshire, B. and P.J. Scharning, *A new methodology for analysis of creep and creep fracture data for 9–12% chromium steels.* International Materials Review, 2008. **53**(2): p. 91-104.

56. Greenwood, J.N., J. Iron Steel Inst., 1954. **176**.

57. Greenwood, J.N., D.R. Miller, and J.W. Suiter, Acta Metall, 1954. **2**.

58. Boettner, R.C. and W.D. Robertson, Trans. Met. Soc., 1961. **221**.

59. Kassner, M.E. and T.A. Hayes, *Creep cavitation in metals.* International Journal of Plasticity, 2003. **19**: p. 1715-1748.

60. Chen, B., et al., *An improved method to identify grain boundary creep cavitation in 316H austenitic stainless steel.* Ultramicroscopy, 2011. **111**(5): p. 309-313.

61. Raj, R. and M.F. Ashby, *Intergranular fracture at elevated temperature.* Acta Metall., 1975. **23**(6): p. 653-666.

62. Riedel, H., *Cavity nucleation at particles on sliding grain boundaries. A shear crack model for grain boundary sliding in creeping polycrystals.* Acta. Metall., 1984. **32**(3): p. 313-321.

63. Dyson, B.F., *Continuous cavity nucleation and creep fracture.* Scripta Metall., 1983. **17**(1): p. 31-37.

64. Chen, I.W. and A.S. Argon, *Creep cavitation in 304 stainless steel.* Acta Metall., 1981. **29**(7): p. 1321-1333.

65. Chen, R.T. and J.R. Weertman, *Grain boundary cavitation in internally oxidized copper.* Mater. Sci. Eng. , 1984. **64**(1): p. 15-25.

66. Gill, T.P.S., et al., *Transformation of delta-ferrite during the postweld heat treatment of type 316L stainless steel weld metal.* Weld. Res. Suppl, 1986.

67. Hales, R., *The role of cavity growth mechanisms in determining creep-rupture under multiaxial stresses.* Fat Fract Eng Mater Struct, 1994. **17**: p. 579-91.

68. Cadek, J., *Creep in Metallic Materials*. 1988, Amsterdam: Elsevier.

69. Kassner, M.E., T.C. Kennedy, and K.K. Schrems, *The mechanism of ductile fracture in constrained thin silver films.* Acta Mater., 1998. **46**(18): p. 6445-6457.

70. Randle, V., *Strain-induced secondary recrystallization.* Materials Science Forum, 1993. **115**: p. 189-194.

71. Page, R., J.R. Weertman, and M. Roth, *Investigation of fatigue-induced grain boundary cavitation by small angle neutron scattering.* Scripta Metallurgica, 1980. **14**(7): p. 773-777.

72. Yoo, M.H., et al., *Small angle neutron scattering study of creep deformation and fracture of type 304 stainless steel*, in *6th international conference on the strength of metals and alloys*. 1982, ORNL: Melbourne, Australia,.

73. Boeuf, A., et al., *Small angle neutron scattering study of the damage induced by creep deformation in aisi 304 stainless steel* 1982, Commission of the European Communities nuclear science and technology: Brussels, Luxembarg.

74. E. R. Fuller, J., et al., *Characterization of Creep Damage in Metals Using Small Angle Neutron Scattering* Journal of research of the National Bureau of Standards, 1984. **89**(1).

75. Bouchard, P.J., F. Fiori, and W. Treimer, *Characterisation of creep cavitation damage in a stainless steel pressure vessel using small angle neutron scattering.* Applied Physics A, 2002. **74**: p. S1689-S1691.

76. Bouchard, P.J., et al., *Quantification of creep cavitation damage around a crack in a stainless steel pressure vessel.* Acta Materialia, 2004. **52**(1): p. 23-34.

77. Jazaeri, H., et al., *Application of small angle neutron scattering to study creep cavitation in stainless steel weldments.* Materials Science and Technology, 2015. **31**(5).

78. Jazaeri, H., et al., *Study of cavities in a creep crack growth test specimen*, in *21st European Conference on Fracture, ECF21*. 2016: Catania, Italy.

79. Crossland, I.G., R.B. Jones, and G.W. Lewthwaite, Journal of applied physics, 1973. **6**: p. 1040-1046.

80. Parker, J.D. and B. Wilshire, Metal Sci, 1978. **12**: p. 453-458.

81. Rao, A., et al., *Anelasticity in Austenitic Stainless Steel.* Acta Materialia 2012. **60**(19): p. 6851-61.

82. Bauschinger, J., *Mittheilung XV:On the changes of the elastic limit and the strength of iron by straining in tension and in compression.* Mittheilungen aus dem Mechanisch-Technischen Laboboratorium der Koniglichen Technischen Hochschule in Munchen, 1886. **13**(8): p. 1-115.

83. P. J. Withers, H.K.D.H.B., *Residual stress Part 1 – Measurement techniques.* Materials Science and Technology, 2001. **17**: p. 355-365.

84. Mughrabi, H., Mater. Sci. Eng, 1987. **85**: p. 15-31.

85. Humphreys, F.J. and M. Hatherly, *Recrystallization and related annealing phenomena*. 2nd ed. 2004: Elsevier Science.

86. Xiaoyu, H., et al., *The Bauschinger effect and the stresses in a strained single crystal* Scripta Metallurgica et Materialia 1992. **27**(7): p. 865-870.

87. Skelton, R.P., *Bauschinger yield in the range 400–1025°C during cyclic deformation of high temperature alloys.* Materials at high temperatures, 2013. **30**(3): p. 241-260.

88. Sleeswyk, A.W. and G.J. Kemerink, *Simillarity of the Bauschinger effect in Cu, Al and Ni.* Scripta Materialia, 1985. **19**(471-476).

89. Heyn, E., *Internal strains in cold-wrought metals and some troubles caused thereby.* Journal of the Institute of Metals, 1914. **12**: p. 3-37.

90. Wood, W.A. and N. Dewsnap, *Internal stresses in metals.* Nature, 1948. **161**: p. 617-628.

91. Rahlfs, P. and G. Masing, Metallk., 1950. **41**.

92. Sachs, G. and H. Shoji, Z. Phys., 1927. **45**.

93. Orowan, D.E., in *Int. Conf. on Stresses and Fatigue in Metals*. 1959, Elsevier: Amsterdam. p. 59-80.

94. Sleeswyk, A.W., et al., Acta Metall, 1978. **26**: p. 1265-71.

95. T. Ungar, et al., *X-ray line-broadening study of the dislocation cell structure in deformed [001]-orientated copper single crystals.* Acta Materialia, 1984. **32**: p. 333-342.

96. Nabarro, F.R.N., *Work hardening and dynamical recovery of F.C.C. metals in multiple glide.* Acta Mater, 1989. **37**(6): p. 1521-1546.

97. Argon, A.S. and P. Haasen, *A new mechanism of work hardening in the late stages of large strain plastic flow in f.c.c. and diamond cubic crystals* Acta Mater, 1993. **41**: p. 3289-3306.

98. Rauch, E.F. and J.H. Schmitt, *Dislocation substructures in mild steel deformed in simple shear.* Materials Science and Engineering: A, 1989. **113**: p. 441-448.

99. Hasegawa, T., T. Yako, and U.F. Kocks, *Forward and reverse rearrangements of dislocations in tangled walls.* Materials Science and Engineering, 1986. **81**: p. 189-99.

100. Wilson, D.V. and P.S. Bate, *Influences of cell walls and grain boundaries on transient responses of an if steel to changes in strain path.* Acta Metallurgica et Materialia, 1994. **42**(4): p. 1099-1111.

101. Nesterova, E.V., B. Bacroix, and C. Teodosiu, *Experimental observation of microstructure evolution under strain-path changes in low-carbon IF steel.* Materials Science and Engineering: A, 2001. **309-310**: p. 495-499.

102. Rauch, E.F., J.J. Gracio, and F. Barlat, *Work-hardening model for polycrystalline metals under strain reversal at large strains.* Acta Mater, 2007. **55**(9): p. 2939-2948.

103. Strauven, Y. and E. Aernoudt, *Directional strain softening in ferritic steel.* Acta Metallurgica, 1987. **35**(5): p. 1029-1036.

104. Peeters, B., et al., *Work-hardening/softening behaviour of b.c.c. polycrystals during changing strain:: Part II. TEM observations of dislocation sheets in an IF steel during two-stage strain paths and their representation in terms of dislocation densities.* Acta Mater, 2001. **49**(9): p. 1621-1632.

105. Peeters, B., et al., *Work-hardening/softening behaviour of b.c.c. polycrystals during changing strain paths: I. An integrated model based on substructure and texture evolution, and its prediction of the stress-strain behaviour of an IF steel during two-stage strain paths.* Acta Materialia, 2001. **49**(9): p. 1607-1619.

106. Bouvier, S., et al., *Modelling of anisotropic work-hardening behaviour of metallic materials subjected to strain-path changes.* Computational Materials Science, 2005. **32**(3-4): p. 301-315.

107. Thuillier, S. and E.F. Rauch, *Development of microbands in mild steel during cross loading.* Acta Metallurgica et Materialia, 1994. **42**(6): p. 1973-1983.

108. Hasegawa, T., T. Yakou, and S. Karashima, *Deformation behaviour and dislocation structures upon stress reversal in polycrystalline aluminium.* Materials Science and Engineering, 1975. **20**: p. 267-276.

109. Kocks, U.F., T. Hasegawa, and R.O. Scattergood, *On the origin of cell walls and of lattice misorientations during deformation.* Scripta Metallurgica, 1980. **14**(4): p. 449-454.

110. Kassner, M.E., A.A. Ziaai-Moayyed, and A.K. Miller, Metall. Trans. A, 1985. **16**(A): p. 1069-76.

111. Kassner, M.E. and M.A. Wall, Metall. and Mater. Trans., 1999. **30**(A).

112. Kassner, M.E., M.A. Delos-Reyes, and M.A. Wall, *Microstructure and mechanisms of cyclic deformation of aluminum single crystals at 77 K.* Metall. and Mater. Trans., 1997. **28A**(3): p. 595-609.

113. Vincze, G., et al., *A comparison of the mechanical behaviour of an AA1050 and a low carbon steel deformed upon strain reversal.* Acta Mater, 2005. **53**: p. 1005-1013.

114. Rauch, E.F., *The stresses and work-hardening rates of mild-steel with different dislocation patterns.* Materials science and Engineering A, 1997. **234**: p. 653-656.

115. Abel, A. and H. Muir, *The Bauschinger effect and discontinuous yielding.* Philosophical Magazine, 1972. **26**(2): p. 489-504.

116. Petegem, S.V., et al., *In-situ neutron diffraction during biaxial deformation.* Acta Materialia, 2016. **105**: p. 404-416.

117. Wollmershauser, J.A., B. Clausen, and S.R. Agnew, *A slip system-based kinematic hardening model application to in situ neutron diffraction of cyclic deformation of austenitic stainless steel.* International Journal of Fatigue, 2012. **36**: p. 181-193.

118. Chen, B., et al., *Role of the misfit stress between grains in the Bauschinger effect for a polycrystalline material.* Acta Materialia, 2015. **85**: p. 229-242.

119. Saleh, A.A., et al., *On the evolution and modelling of lattice strains during the cyclic loading of TWIP steel.* Acta Materialia, 2013. **61**: p. 5247-5262.

120. Mitra, S.K. and D. McLean, Proc. R. Soc. Lond. A, 1966. **295**.

121. Davies, C.K.L., P.W. Davies, and B. Wilshire, Phil. Mag., 1965. **12**.

122. Gibbs, G.B., Phil. Mag., 1966. **13**: p. 317.

123. Ahlquist, C.N. and W.D. Nix, Scripta Materialia, 1969. **3**.

124. Blum, W., J. Hausselt, and G. Kanig, *Transient creep and recovery after stress reduction during steady state creep of AlZn.* Acta metallurgica, 1976. **24**: p. 293-297.

125. Lagneborg, R., *Recovery creep in materials hardened by a second phase.* J. Mater. Sci., 1968. **3**: p. 596-602.

126. McLean, D., *Dislocation contribution to the flow stress of polycrystalline iron.* Can. J. Phys., 1967. **45**: p. 973.

127. Morris, D.G., *Creep in type 316 stainless steel.* Acta Metall, 1978. **26**: p. 1143-1151.

128. Hasegawa, T., Y. lkeuchi, and S. Karashima, *Internal stress and dislocation structure during sigmoidal transient creep of a copper-16 at.-% Aluminium alloy.* Metal Sci, 1972. **6**(1): p. 78-82.

129. Blum, W., et al., Mater Sci Eng, A, 1989. **112**.

130. Gibeling, J.C. and W.D. Nix, Acta Metall, 1981. **29**.

131. Biberger, M. and J.C. Gibeling, Acta Metall. Mater, 1995. **43**: p. 3247-3260.

132. Gibbons, T.B., V. Lupinc, and D. Mclean, Mater. Sci. Eng., 1975. **9**.

133. V.Lupinc and F.Gabrielli, Mater. Sci Eng, 1979. **37**: p. 143-149.

134. L.O.Bueno and R.L.Bell, Mater. Sci. Eng. A, 2005. **410-411**: p. 72-78.

135. Chen, B., et al., *A review of the changes to internal state related to high temperature creep of polycrystalline metals and alloys.* International Materials Reviews, 2015. **60**(1): p. 1-29.

136. Chen, B., et al., *Quantifying Internal stress and internal resistance associated with thermal ageing and creep in a polycrystalline material.* Acta Materialia (under review) 2013

137. Chen, B., et al., *Internal strains between grains during creep deformation of an austenitic stainless steel.* j. Mater. Sci., 2015. **50**(17): p. 5809-5816.

138. Chen, B., et al., *Effect of thermal ageing on creep and oxidation behaviour of Type 316H stainless steel.* Materials at High Temperatures, 2015. **32**(6): p. 592-606.

139. Greenough, G.B., *Residual lattice strains in plastically deformed metals.* Nature, 1947. **160**.

140. Allen, A., et al., *Measurement of internal stress within bulk materials using neutron diffraction.* NDT International, 1981: p. 249-254.

141. Allen, A.J., M.T. Hutchings, and C.G. Windsor, *Neutron diffraction methods for the study of residual stress fields.* Advances in physics, 1985. **34**(4): p. 445-473.

142. Pang, J.W.L., T.M. Holden, and T.E. Mason, *In situ generation of intergranular strains in an Al7050 alloy.* Acta Mater, 1998. **46**: p. 1503-1518.

143. J. W. L. Pang, et al., *The generation of intergranular strains in 309h stainless steel under uniaxial loading.* Acta Materialia, 2000. **48**: p. 1131-1140.

144. P.A. Turner, N.C., and C.N. Tom., *Modeling the mechanical response of rolled zircaloy-2.* Int. J. Plasticity, 1995. **11**(3): p. 251-265.

145. Clausen, B. and T. Lorentzen, *Experimental evaluation of a polycrystal deformation modeling scheme using neutron diffraction measurements.* Metallurgical and Materials Transactions A, 1997. **28**(12): p. 2537-2541.

146. Clausen, B., et al., *Lattice strain evolution during uniaxial tensile loading of stainless steel.* Mater. Sci. Eng, 1999. **a**(259): p. 17-24.

147. Lorentzen, T., et al., *Lattice strain evolution during cyclic loading of stainless steel.* Acta Mater, 2002. **50**: p. 1627-1638.

148. Korsunsky, A.M., K.E. James, and M.R. Daymond, *Intergranular stresses in polycrystalline fatigue: diffraction measurement and self-consistent modelling.* Engineering Fracture Mechanics, 2004. **71**(4-6): p. 805-812.

149. Wang, X.L., et al., *Inter- and intragranular stresses in cyclically-deformed 316 stainless steel.* Materials Science and Engineering A, 2005. **399**(1-2): p. 114–119.

150. wang, Y.-d., et al., *The development of grain-orientationdependent residual stressess in a cyclically deformed alloy.* nature materials, 2003. **2**: p. 101-106.

151. Daymond, M.R. and P.j. Bouchard, *Elastoplastic Deformation of 316 Stainless Steel Under Tensile Loading at Elevated Temperatures.* Metallurgical and Materials transactions A, 2006. **37**(A): p. 1863-1873.

152. Fajoui, J., et al., *Bauschinger Effect in an Austenitic Steel: Neutron Diffraction and a Multiscale Approach.* Metallurgical and Materials Transactions A, 2016. **47A**.

153. Ahmed, I.I., et al., *Deformation path effects on the internal stress development in cold worked austenitic steel deformed in tension.* Materials Science and Engineering: A, 2014. **614**: p. 326-337.

154. Gonzalez, D., et al., *Macro and intergranular stress responses of austenitic stainless steel to 90° strain path changes.* Materials Science and Engineering: A, 2012. **546**: p. 263-271.

155. Hu, J., et al. *Self-consistent Modelling and the Evaluation of Lattice Deformation in a Polycrystalline Austenitic Stainless Steel* in *Joint 3rd UK-China Steel Research Forum & 15th CMA-UK Conference on Materials Science and Engineering*. 2015.

156. Hu, J. and A.C.F. Cocks, *A multi-scale self-consistent model describing the lattice deformation in austenitic stainless steels.* International Journal of Solids and Structures, 2016. **78-79**(1): p. 21-37.

157. *Metallic materials - Tensile testing - Part 1: Method of test at ambient temperature*. 2009.

158. *Tensile testing of metallic materials - Part 5: Method of test at elevated temperatures.* 1992.

159. Githinji, D.N., et al., *An EBSD Study of the Deformation of Service-Aged 316 Austenitic Steel.* Metallurgical and Materials Transactions A, 2013. **44**(9): p. 4150-4167.

160. Binnig, G., C.F. Quate, and C. Gerber, *Atomic Force Microscope.* Physical review letters, 1986. **56**(9): p. 930-933.

161. Humphris, A.D.L., M.J. Miles, and J.K. Hobbs, *A mechanical microscope: High-speed atomic force microscopy.* Applied physics letters, 2005. **86**.

162. Payton, O.D., L. Picco, and T.B. Scott, *High-speed atomic force microscopy for materials science.* International Materials Review, 2016. **61**(8): p. 473-494.

163. Warren, X., et al., *Preparation of stainless steel surfaces for scanning probe microscopy techniques.* Microscopy Today, 2016.

164. B. Chen, P.E.J.F., A. C. F. Cocks, D. J. Smith, *A review of the changes to internal state related to high temperature creep of polycrystalline metals and alloys.* International Materials Review (accepted), 2013.

165. M.A. Morris and J.L. Martin, Acta Metall, 1984. **32** p. 1609-1623.

166. Martin, M.A.M.a.J.L., Acta Metall, 1984. **32**: p. 549-561.

167. Morris, D.G., Acta Metall, 1978. **26**: p. 1143-1151.

168. D. Mukherji, R.P.W., *On the measurement of lattice mismatch between γ and γ′ phases in nickel-base superalloys by CBED technique.* Scripta Materialia 1996. **35**(1): p. 117-122.

169. Salmon, J.C.W.a.P.S., *Structure of molten ScCl3 and ScI3 studied by using neutron diffraction* Journal of Physics: Condensed Matter, 1999. **11**(10).

170. Glaum, R., et al., *Neutron diffraction Study of the Nuclear and Magnetic Structure of the CrVO4Type Phosphates TiPO4and VPO4.* Journal of Solid State Chemistry, 1996. **126**(1): p. 15–21.

171. P. Šittner, P.L., V. Nováka, M.R. Daymond, G.M. Swallowe, *In situ neutron diffraction studies of martensitic transformations in NiTi polycrystals under tension and compression stress.* Materials Science and Engineering A, 2004. **378**: p. 97-104.

172. Daymond, M.R. and P.J. Withers, *In situ monitoring of thermally cycled metal matrix composites by neutron diffraction and laser extensometry.* Applied composite materials, 1997. **4**: p. 375-392.

173. Rao, A., *Creep and Anelastic Deformation in Austenitic Steels*, in *Department of materials engineering*. 2010, The Open University: Milton keynes, UK.

174. Choo, H., et al., *In situ neutron diffraction studies on the elevated-temperature deformation behavior of a TiAl–W alloy.* Applied physics letters, 2004. **85**(20).

175. Huang, S., et al., *In Situ Neutron-Diffraction Studies on the Creep Behavior of a Ferritic Superalloy.* Metallurgical and materials transactions A, 2011. **43**: p. 1497-1508.

176. M.T. Hutchings, P.J.W., T.M. Holden, T. Lorentzen, *Introduction to the Characterisation of Residual Stresses by Neutron Diffraction*. 2005, London: Taylor & Francis.

177. Pynn, R., *Neutron Scattering—A Non-destructive Microscope for Seeing Inside Matter*, in *Neutron Applications in Earth, Energy and Environmental Sciences*, L. Liang, R. Rinaldi, and H. Schober, Editors. 2009, Springer US. p. 15-36.

178. Fitzpatrick, M.E. and A. Lodini, eds. *Analysis of residual stress by diffraction using neutron and synchroton radiation*. 2003, Taylor and Francis: London.

179. Larson, A.C. and R.B.V. Dreele, *GSAS - General Structure Analysis System manual*. 2002.

180. Santisteban, J.R., et al., *ENGIN-X: a third-generation neutron strain scanner.* Journal of Applied Crystallography, 2006. **39**: p. 812-825.

181. Rietveld, H.M., *Line profiles of neutron powder-diffraction peaks for structure refinement* Acta Cryst., 1967. **22**: p. 151-152.

182. Daymond, M.R., et al., *Use of Rietveld refinement for elastic macrostrain determination and for evaluation of plastic strain history from diffraction spectra.* Journal of applied physics, 1997. **82**(4): p. 1554-1562.

183. Oliver, E., et al., *ENGIN-X User Manual*. 2004.

184. Johnson, M.W. and M.R. Daymond, *An optimum design for a time-of-flight neutron diffractometer for measuring engineering stresses.* Journal of applied crystallography, 2002. **35**(1): p. 49-57.

185. Jorgensen, J.D., et al., *Electronically focused time-of-flight powder diffractometers at the intense pulsed neutron source.* Journal of Applied Crystallography, 1989. **22**(4): p. 321-333.

186. Rustichelli, F., *Applications of small angle neutron scattering in material science and technology.* Mettalurgical science and technology, 1993. **11**(3): p. 118-141.

187. Guinier, A. and G. Fournet, *Small Angle Scattering of X-rays*. 1955, New York: John Wiley.

188. Heenan, R.K., et al., *Small angle neutron scattering using Sans2d.* Neutron News, 2011. **22**: p. 19-21.

189. Heenan, R.K., J. Penfold, and S.M. King, *SANS at pulsed neutron sources: present and future prospects.* J. Appl. Cryst., 1997. **30**: p. 1140-1147.

190. Arnold, O., et al., *Mantid—Data analysis and visualization package for neutron scattering and μ SR experiments.* Nuclear Instruments and Methods in Physics Research Section A: Accelerators, Spectrometers, Detectors and Associated Equipment, 2014. **764**: p. 156-166.

191. Potton, J.A., G.J. Daniell, and B.D. Rainford, *A new method for the determination of particle size distribution from small-angle neutron scattering measurements.* J. Appl. Crystallogr, 1988. **21**: p. 891-897.

192. Jazaeri, H., et al. *Study of creep cavitation in a stainless steel weldment using small angle neutron scattering and scanning electron microscopy*. in *ASME Pressure Vessels & Piping Conference*. 2014.

193. Hutchings, M.T., *The use of small angle neutron scattering for mapping creep cavitation damage in an ex-service steam header*. 2012, The Open University. p. 1-26.

194. Heenan, R.K., et al., *SANS2d at the ISIS Second Target Station*, in *ICANS-XVII 17th Meeting*. 2005: Santa Fe, New Mexico.

195. Githinji, D.N., *Characterisation of Plastic and Creep Strains From Lattice Orientation Measurements*, in *Engineering and Innovation*. 2013, The Open University: Milton Keynes, UK.

196. *Stainless steel grade datasheets*. 2011.

197. *Metallic materials - Vickers hardness test - Part 1: Test method*. 2005.

198. Hall, E.O., Proc. Phys. Soc. , 1951. **64**.

199. Petch, N.J., J. Iron Steel Inst., 1953. **174**.

200. ASTM, *Standard test methods for determining average grain size*, in *E112-12*.

201. Intenational, A., *Standard Practice for Determining Average Grain Size Using Electron Backscatter Diffraction (EBSD) in Fully Recrystallized Polycrystalline Materials*, in *E2627−13*.

202. Ferreira, T. and W. Rasband, *ImageJ User Guide*. 2012.

203. Humphreys, F.J., *Review Grain and subgrain characterisation by electron backscatter diffraction.* Journal of Materials Science, 2001. **36**.

204. Kocks, U.F., C.N. Tome, and H.R. Wenk, eds. *Texture and Anisotropy*. 1998, Cambridge University Press.

205. Randle, V. and O. Engler, *Introduction to Texture Analysis: Macrotexture, Microtexture and Orientation Mapping*. 2000, Amsterdam: Gordon and Breach science.

206. Daymond, M.R., C.N. Tome, and M.A.M. Bourke, *Measured and predicted intergranular strains in textured austenitic steel.* Acta Materialia, 2000. **48**: p. 553-564.

207. Oliver, E.C., M.R. Daymond, and P.J. Withers, *Interphase and intergranular stress generation in carbon steels.* Acta Materialia, 2004. **52**: p. 1937-1951.

208. O'Donnell, M.P., et al., *Use of conventional stress-strain data to develop parameters for an advanced constitutive model.* Mater. High Temp, 2002. **19**: p. 215-223.

209. Stoltz, R.E. and R.M. Pelloux, *The Bauschinger effect in precipitation strengthened aluminum alloys.* Metallurgical and Materials Transactions, 1976. **7**(8): p. 1295-1306.

210. Setoodeh, A.R. and H. Attariani, *Nanoscale simulations of Bauschinger effects on a nickel nanowire.* Materials Letters, 2008. **62**(27): p. 4266-4268.

211. Mataya, M.C. and M.J. Carr, *The Bauschinger effect in a nitrogen-strengthened austenitic stainless steel.* Materials Science and Engineering, 1983. **57**(2): p. 205-222.

212. Schwartzbart, H., M.H. Jones, and W.F.B. Jr., *Observations on Bauschinger effect in copper and brass*. 1951, National Advisory Committee for Aeronautics: Washington.

213. Skippon, T., B. Clausen, and M.R. Daymond, *Effect of loading mode on lattice strain measurements via neutron diffraction.* Materials Science & Engineering A, 2013. **577**: p. 169-178.

214. Llyod, G.J. and R.J. McElroy, Acta Metall., 1974. **22**.

215. Gibeling, J.C. and W.D. Nix, Acta Metall., 1980. **28**.

216. Rao, A., Bouchard, P. J., Northover, Shirley M., and Fitzpatrick, Michael E., *Anelasticity in Austenitic Stainless Steel.* Acta Materialia 2012. **60**(19): p. 6851-61.

217. Frost, H.J. and M.F. Ashby, *Deformation mechanism maps*. 1982, Exeter: Pergamon.

218. Altenbach, H. and K. Naumenko, *Modelling of creep for structural analysis*, ed. V.I. Babitsky and J. Wittenburg. 2007: Springer.

219. Ishikawa, H. and K. Sasaki. *Unified approach to constitutive modeling -plasticity and creep*. in *Advances in engineering plasticity and its applications*. 1996. Hiroshima, Japan.

220. Dobes, F., *The back stresses in creep of a Fe–30Al–4Cr intermetallic alloy with addition of Zr.* Scripta Materialia, 2008. **59**(1): p. 59-62.

221. Takagi, H., et al., *Experimental and computational creep characterization of Al–Mg solid-solution alloy through instrumented indentation.* Philosophical Magazine, 2003. **83**(35): p. 3959-3976.

222. Coleman, M.C., D.A. Miller, and R.A. Stevens. *Reheat cracking and strategies to assure integrity of Type 316 weld components*. in *Proceedings of the International Conference on Integrity of High Temperature Welds*. 1998. London: PEP Ltd.

223. Monkman, F.C. and N.J. Grant, Proc. ASTM, 1956. **56**: p. 593-620.

224. Predeleanu, M. and P. Gilormini, eds. *Advanced Methods in Materials Processing Defects*. 1997, Elsevier: Amsterdam.

225. Yoda, R., T. Yokomaku, and N. Tsuji, Materials characterization, 2010. **61**.

226. Tanaka, H., et al., *Microstructural evolution and change in hardness in type 304H stainless steel during long-term creep.* Materials science and Engineering A, 2001. **319**: p. 788-91.

227. Wilshire, B. and M. Willis, *Mechanisms of Strain Accumulation and Damage Development during Creep of Prestrained 316 Stainless Steels.* Metallurgical and Materials Transactions A, 2004. **35A**.

228. Mehmanparast, A., et al., *The influence of pre-compression on the creep deformation and failure behaviour of Type 316H stainless steel.* Engineering Fracture Mechanics, 2013. **110**: p. 52-67.

229. Li, D.F., et al., *A review of the effect of prior inelastic deformation on high temperature mechanical response of engineering alloys.* International Journal of Pressure Vessels and Piping () 2010. **87**: p. 531-542.

230. Davies, C.M., D.W. Dean, and K.M. Nikbin, *The influence of compressive plastic prestrain on the creep deformation and damage behaviour of 316H stainless steel.*, in *International conference on engineering structural integrity assessment* 2009, EMAS Publishing: Manchester, UK.

231. Ohashi, Y., M. Kawai, and T. Momose, *Effects of prior plasticity on subsequent creep of type 316 stainless steel at elevated temperature.* J Eng Mater Technol-Trans, 1986. **108**(1): p. 68-74.

232. Riedel, H., *Fracture at high temperatures*. 1987.

233. Bampton, C.C., I.P. Jones, and M.H. Loretto, *Stacking fault energy measurements in some austenitic stainless steels.* Acta Metallurgica, 1978: p. 26-39.

234. Fox, A., ed. *Stress relaxation testing*. 1979, American Society for Testing and Materials: Baltimore.

235. Fookes, A., et al., *Stress Relaxation during Dwells for Creep and Fatigue Cycling of Type 316H Stainless Steel at 550°C*, in *2nd International ECCC Conference*. 2009: Switzerland.

236. Douglas, J., R. Dennis, and M. Spindler, *DEVELOPMENT OF AN ADVANCED CREEP MODEL FOR TYPE 316 STAINLESS STEEL*, in *Eighth International Conference on Creep and Fatigue at Elevated Temperatures*. 2007: San Antonio, Texas.

237. Jazaeri, H., et al., *Application of small angle neutron scattering to study creep cavitation in stainless steel weldments.* Materials Science and Technology, 2014. **31**(5).

238. Jazaeri, H., et al., *Study of creep cavitation in stainless steel weldment.* Materials Science and Technology 2014. **30**(1).

239. Swindemann, R.W., et al., *Substructures developed during creep and cyclic tests of type 304 stainless steel (heat 9t27961)*. 1977, ORNL.

240. Yoo, M.H., J.C. Ogle, and J.H. Schneibel, *Sans and tem studies of carbide precipitation and creep damage in type 304 stainless steel*. ORNL.

241. Burnett, T.L., et al., *Multiscale 3D analysis of creep cavities in AISI type 316 stainless steel.* Materials Science and Technology, 2015. **31**(5): p. 522-534.

242. Shiozawa, K. and J.R. Weertman, *Studies of nucleation mechanisms and the role of residual stresses in the grain boundary cavitation of a superalloy.* Acta Metall, 1983. **31**(7): p. 993-1004.

243. Williams, K.R. and B. Wilshire, Met. Sci. J, 1973. **7**: p. 176-179.

244. Peleshko, V.A., *Applied creep theory for bodies with anisotropy due to plastic prestrain.* Mech Solids, 2007. **42**(2): p. 307-320.

245. A. Fookes, et al., *Stress Relaxation during Dwells for Creep and Fatigue Cycling of Type 316H Stainless Steel at 550°C*, in *2nd International ECCC Conference*. 2009: Switzerland.

246. Chen, B., et al., *Constitutive equations that describe creep stress relaxation for 316H stainless steel at 550° C.* Materials at High Temperatures, 2011. **28**(3).

247. Mamun, A.A., R.J. Moat, and P.J. Bouchard, *Origin and effect of back stress on cyclic creep deformation of 316H stainless steel*, in *ASME 2015 Pressure vessels and piping conference*. 2015: Boston, USA.

248. Kuhn, H., *Mechanical testing and evaluation*, in *ASM Handbook*. 2000, ASM International.

249. Wang, Y.Q., et al., *Critical analysis of the prediction of stress relaxation from forward creep of Type 316H austenitic stainless steel.* Materials & Design, 2016. **95**: p. 656-668.

250. *ASME, Section III Div. 1 Sub-Section NH*. 2001, ASME: New York USA.

251. *RCC-MR, Design and Construction Rules for Mechanical Components of FBR Nuclear Islands*. 2002, AFCEN: Paris, France.

252. Takahashi, Y., *Development of Structural Integrity Assessment Guideline for FBR components*, in *ASME PVP*. 1998. p. 207-214.

253. Spindler, M.W., *An improved method for calculation of creep damage during creep-fatigue cycling.* Materials Science and Technology, 2007. **23**(12): p. 1461-1470.

254. Spindler, M.W. *An Improved Method to Calculate the Creep-Fatigue Endurance of Type 316H Stainless Steel*. in *Proc. 8th Liege Conf*. 2006. Forschungszentrum Jülich GmbH, Germany.

255. Spindler, M.W. *Effects of Dwell Location on the Creep-Fatigue Endurance of Cast Type 304L*. in *Proc. Creep & Fracture in High Temperature Components - Design & Life Assessment Issues*. 2005. Lancaster, USA: DEStech Publications.

256. Spindler, M.W., *The Multiaxial and Uniaxial Creep Ductility of Type 304 Steel as a Function of Stress and Strain Rate.* Mater. at High Temps, 2004. **21**: p. 47-52.

257. Takahashi, Y., *Effect of cyclic loading on subsequent creep behaviour and its implications in creep–fatigue life assessment.* Materials at high temperatures, 2015. **32**(5): p. 492-501.

258. Ramberg, W. and W.R. Osgood, *Description of stress-strain curves by three parameters*. 1943, NACA.

259. Korsunsky, A.M., M.R. Daymond, and K.E. James, *The correlation between plastic strain and anisotropy strain in aluminium alloy polycrystals.* Materials Science and Engineering, 2002. **A334**: p. 41–48.

260. Daymond, M.R., M. Preuss, and B. Clausen, *Evidence of variation in slip mode in a polycrystalline nickel-base superalloy with change in temperature from neutron diffraction strain measurements.* Acta Materialia, 2007. **55**(9): p. 3089-3102.

261. Hughes, D.J., et al., *First Impressions of SALSA: The New Engineering Instrument at ILL.* Neutron News, 2006. **17**(3): p. 28-32.

262. Pirling, T., G. Bruno, and P.J. Withers, *SALSA - A New Instrument for Strain Imaging in Engineering Materials & Components.* Mat. Sci. Eng. A, 2006. **437**(1): p. 139-144.

263. Pirling, T., D. Hughes, and J.S. Robinson, *Precise Determination Of Residual Stresses In Large Specimens By Neutron Diffraction.* Materials Science Forum, 2010. **652**: p. 80-85.

264. Mamun, A.A., et al., *Rationale for scoping the design of the creep-fatigue rig for ISIS*. 2013, The Open University.

265. Jazaeri, H., et al., *Study of creep cavitation through creep life*, in *13th International Conference on Creep and Fracture of Engineering Materials and Structures,*. 2015: Toulouse, France.

266. W. Kockelmann, E.C.O., P. G. Radaelli, *IMAT- An imaging and materials science & engineering facility for TS-II*, in *IMAT – draft proposal for discussion*. 2007, STFC.